N° d'ordre NNT : **2020LYSEC03** **ANNÉE 2020**

THÈSE de DOCTORAT DE L'UNIVERSITÉ DE LYON
opérée au sein de l'École Centrale de Lyon

École Doctorale N° 162
Mécanique, Énergétique, Génie civil, Acoustique

Spécialité de Doctorat : Acoustique

Soutenue publiquement le 29/01/2020, par :

Miguel PESTANA

Effets d'un stator hétérogène sur le bruit d'interaction rotor-stator : étude analytique, expérimentale et numérique

Impact of a heterogeneous stator on the rotor-stator interaction-noise: an analytical, experimental and numerical investigation

---

Jury

Pr.	CASALINO	Damiano	TU Delft (NL)	Rapporteur
Pr.	CINNELLA	Paola	Arts et Métiers ParisTech (FR)	Président du jury
Pr.	FRÉCHETTE	Luc	Université de Sherbrooke (CA)	Rapporteur
Dr.	GRUBER	Mathieu	Safran Aircraft Engines (FR)	Invité
Pr.	MOREAU	Stéphane	Université de Sherbrooke (CA)	Directeur de thèse
Pr.	ROGER	Michel	École Centrale de Lyon (FR)	Directeur de thèse
Pr.	SANJOSÉ	Marlène	École de Technologie Supérieure (CA)	Examinateur

Laboratoire de Mécanique des Fluides et d'Acoustique, UMR CNRS 5509
École Centrale de Lyon

Abstract

The present study aims to quantify by means of analytical modelling, experiments and numerical simulations, the impact of a heterogeneous stator on the rotor-stator noise in axial turbomachines. This study starts with the first observations on an axial low-speed fan at École Centrale de Lyon, the *LP3* stage. It has been observed that the first two blade passing frequencies (BPF) were radiating at high levels while they were expected to be cut-off by the duct according to Tyler & Sofrin's criterion. An experiment is then carried out with the heterogeneous stator configuration which makes it possible to characterize the spectral and modal contents. To ensure that no inflow distortion is present at the inlet, a Turbulence Control Screen is used. Modal decomposition techniques are used with pseudo-random antennas to obtain the predominant acoustic modes. Results show a strong acoustic radiation of the first two BPFs and evidence some dominant modes. The same experiment is then simulated numerically using the lattice Boltzmann method. The simulations show a good physical behaviour of the turbomachine but predict a lower pressure-rise compared with the experiment. The comparison between homogeneous and heterogeneous stators allows quantifying directly the impact of the heterogeneity. The heterogeneity is responsible for a level increase of more than 10 dB at the first two BPFs. The modal content from the numerical simulations on the heterogeneous configuration is also in good agreement with the experiment. In addition, the analysis of the flow in the inter-stage made it possible to highlight the impact of the heterogeneity on the potential field. Finally, the analytical modelling is focused on two dominant sources: wake-interaction noise and potential-interaction noise. Results put in evidence a minor contribution of the latter despite the short rotor-stator spacing. The same dominant modes are found in certain propagation directions in accordance with what is measured in the experiment. Finally, an optimisation of the modified vanes angular position is carried out. One of the optimal configurations showing a great noise attenuation is numerically validated by the LBM. The numerical results show that the optimisation of the azimuthal positioning of the modified vanes makes it possible to obtain a significant reduction of the levels at the first two BPFs. Thereby, the comparison of the analytical, experimental and numerical investigations allows achieving a better understanding of the modification of noise mechanisms caused by the heterogeneity of the stator.

Keywords: aeroacoustics, turbomachinery, rotor-stator interaction, heterogeneous stator, analytical modelling, Lattice-Boltzmann Method, experimental.

Résumé

La présente étude vise à quantifier par une modélisation analytique, des essais et des simulations numériques, l'impact d'un stator hétérogène sur le bruit d'interaction rotor-stator dans les turbomachines axiales. Le travail développé s'appuie sur des premières observations sur un ventilateur axial à basse vitesse à l'École Centrale de Lyon, l'étage *LP3*. Il a été observé que les deux premières fréquences de passage des pales (FPP) rayonnaient à des niveaux élevés alors qu'elles devaient être coupées par le conduit selon le critère de Tyler & Sofrin. Une campagne expérimentale est alors réalisée sur la configuration de ventilateur hétérogène qui permet la caractérisation des contenus spectral et modal. Afin de s'assurer qu'aucune distorsion d'entrée d'air n'est présente, un écran pour le contrôle de la turbulence est utilisé. Des techniques de décomposition modale sont utilisées sur des antennes pseudo-aléatoires afin d'obtenir les modes acoustiques prédominants. Les résultats montrent un fort rayonnement acoustique des deux premières fréquences de passage des pales et mettent en évidence des modes dominants. La même expérience est ensuite simulée numériquement en utilisant la méthode de Boltzmann sur réseau. Les simulations montrent un bon comportement de la turbomachine mais prédisent une augmentation de pression inférieure à celle de l'expérience. La comparaison entre un stator homogène et hétérogène permet de quantifier directement l'impact de l'hétérogénéité. L'hétérogénéité est alors responsable d'une augmentation du niveau tonal de plus de 10 dB aux deux premières FPP. Le contenu modal mesuré sur la configuration hétérogène est bien retrouvé par les simulations numériques. En outre, l'analyse de l'écoulement dans l'espacement inter-rotor-stator a permis de mettre en évidence l'impact de l'hétérogénéité sur le champ potentiel. Finalement, la modélisation analytique est axée sur deux sources dominantes : le bruit d'interaction de sillages et le bruit d'interaction potentielle. Les résultats montrent une contribution mineure de ce dernier. Les mêmes modes dominants sont retrouvés dans certaines directions de propagation en accord avec ce qui est observé expérimentalement. En dernier lieu, une étude d'optimisation de la position des bras support est présentée. Une des configurations optimales montrant une forte atténuation du niveau de bruit tonal est validée numériquement par des simulations numériques. Les résultats montrent que l'optimisation du positionnement angulaire des aubes structurelles permet d'obtenir une réduction significative des niveaux aux deux premières FPP. L'étude des différentes composantes (analytique, expérimentale et numérique) fournit ainsi une meilleure compréhension des mécanismes de bruit modifiés par l'hétérogénéité du stator.

Mots-clés : aéroacoustique, turbomachines, interaction rotor-stator, stator hétérogène, modélisation analytique, méthode de Boltzmann sur réseau, expérimental.

Remerciements

Cette thèse a été réalisée dans le cadre de la chaire industrielle ADOPSYS entre l'École Centrale de Lyon et Safran Aircraft Engines, en cotutelle avec l'Université de Sherbrooke au Canada. Je souhaite remercier l'ANR, l'ANRT et Safran Aircraft Engines pour leur soutien financier sans lequel ce doctorat n'aurait pas pu être réalisé.

En premier lieu, je tiens à remercier sincèrement mes directeurs de thèse, Michel Roger et Stéphane Moreau, pour leur soutien et encadrement tout au long de la thèse. Merci à Michel pour sa pédagogie, sa créativité scientifique et sa légèreté, avec qui travailler est un réel plaisir. Merci à Stéphane pour son dévouement, sa grande disponibilité, ses nombreux enseignements et de m'avoir accueilli chaleureusement au pays du grand froid. Leur encadrement fut essentiel à l'aboutissement de cette thèse et je leur en suis très reconnaissant.

Je souhaite également remercier Mathieu Gruber pour son implication, son encadrement et ses conseils qui m'ont permis de conserver un lien fort avec Safran et à toujours mieux appréhender les enjeux industriels à l'origine du sujet de thèse. Je le remercie pour l'accueil bienveillant au sein de l'équipe acoustique R&T de Safran Aircraft Engines et de m'avoir aidé à construire et réaliser mon projet professionnel.

J'exprime toute ma gratitude à Marlène Sanjosé pour son accueil à l'Université de Sherbrooke, sa disponibilité et son aide pendant ces années de thèse. Son soutien m'a permis de surmonter un grand nombre de difficultés et de toujours valoriser mon travail au sein de la communauté scientifique.

Je remercie également le professeur Paola Cinnella, le professeur Damiano Casalino et le professeur Luc Fréchette pour leur évaluation de mon travail et pour leurs retours et corrections qui m'ont permis d'améliorer le travail réalisé.

Mes remerciements vont naturellement à toute l'équipe expérimentale du LMFA et à tous ceux ayant participé aux essais pour leur aide et leurs enseignements. Je pense notamment à Antonio Pereira, Johan Thisse, Edouard Salze, Pascal Souchotte, Emmanuel Jondeau, Jean-Michel Perrin et Pierre Roland, je leur en suis très reconnaissant. Je souhaite également remercier Laurent Pouilloux et Dan-Gabriel Calugaru pour leur aide fondamentale sur tous les aspects informatiques et de calcul.

Un grand merci à Marie-Gabrielle Perriaux pour son aide et promptitude sur tous les aspects administratifs contribuant au bon déroulement de la thèse. Je souhaite remercier également Dominique Berthet et Michel Teissieux pour l'attention portée aux doctorants.

Cette thèse restera marquée par d'innombrables rencontres en France et au Canada, qui ensemble ont formé un entourage de thèse unique et familier. Je remercie mes premiers collègues de bureau Nassim, Simon, Benjamin, Gyuzel et Justine pour leur accueil chaleureux et pour toutes les discussions existentielles sur l'aéroacoustique. Merci à Johan (à nouveau) pour les quelques lendemains difficiles mais justifiés mais surtout pour son amitié et sa bonne humeur. Du côté Québécois, j'aimerais remercier Aurélien, Aurélien, Bastien, Bruce, Bruno, Carlos, Chaofan, Dipali, Dominic, Emmanuel, Gabriele, Hao, Julien, Manqi, Maud, Michael, Prateek, Quentin, Safouane, Timothée et Yann d'avoir fait de cette expérience à la belle province un souvenir inoubliable. Merci à mes nouveaux collègues de bureau (a.k.a. the muppet show) Danny, Léo et Gabriele de m'avoir accueilli lors de mon retour en France, pour toute leur aide et d'avoir supporté mon humour ! Merci à Paul pour tout le bon temps passé ensemble et pour son coaching sportif de poids ! Merci à Antoni, Bertrand, Damien, David, Elina, Étienne, Georgios, Marion, Mathieu, Mohcene, Pierre, Rafael, Sarah, Simon, Thomas, Vianney, Vincent, Virginie, Yann et Yuanyuan pour tous les bons moments, gâteaux et la bonne ambiance au bureau. Je souhaite aussi remercier tous les permanents du laboratoire pour leur accueil et les nombreux moments de partage agréables. Un grand merci à l'équipe acoustique de Safran pour leur super accueil et aide à chaque passage à Villaroche.

Enfin, je tiens à remercier ma famille, mes amis et Fanélie pour tout leur soutien, confiance et de m'avoir donné tous les moyens pour réussir.

Obrigado !

Contents

Nomenclature & Abbreviations

Latin characters

$\mathbf{S_{pp}}$	Cross-spectral matrix	[Pa^2]
$\mathcal{P}$	Acoustic power	[W]
$\vec{V}$	Flow velocity components	[m s^{-1}]
$\vec{x}$	Oberver position also written x_i or (x_1, r, φ), also absolute coordinate system	[m]
$\vec{y}$	Source position, also written y_i or $(y_1, r', \tilde{\varphi})$	[m]
$\vec{z}$	Airfoil coordinate system (z_1, z_2, z_3)	[m]
A_{mn}	Modal amplitude of the mode (m, n)	[Pa]
B	Number of rotor blades	
c	Airfoil chord	[m]
c_0	Speed of sound of the uniform flow	[m s^{-1}]
C_p	Pressure coefficient	
E	Fresnel integral	
f_i	Components of pressure force vector	[Pa]
f_{mn}	Radial shape function	
G	Green's function	
J_m	Bessel function of the first kind of order m	
k_0	Acoustic wavenumber $(k = \omega/c_0)$	[rad m^{-1}]
K_1, K_2	Chordwise and spanwise hydrodynamic wavenumbers	[rad s^{-1}]
k_a	Damping coefficient	[rad m^{-1}]

K_{mn}	Duct eigenvalues	$[\mathrm{rad\,m^{-1}}]$
k_{mn}	Wavenumber defined as $k_{mn} = \sqrt{k_0^2 - \beta^2 K_{mn}^2}$	$[\mathrm{rad\,m^{-1}}]$
M	Mach number	
n	Rotational frequency harmonic order	
P	Hydrodynamic pressure	[Pa]
p	Acoustic pressure	[Pa]
p_{atm}	Atmospheric pressure	[Pa]
Q	Monopole source term	$[\mathrm{kg\,s^{-4}}]$
Q_m	Mass flow rate	$[\mathrm{kg\,s^{-1}}]$
R_H, R_T	Hub and tip radius of the duct respectively	[m]
s	BPF order	
$S(\vec{y})$	Blade/vane surface	
t	Observer time	[s]
T_{ij}	Lighthill's tensor	$[\mathrm{kg\,m^{-2}\,s^{-2}}]$
u	Upwash function	$[\mathrm{m\,s^{-1}}]$
U_0	Axial velocity of the uniform flow	$[\mathrm{m\,s^{-1}}]$
u_a	Upwash amplitude	$[\mathrm{m\,s^{-1}}]$
V	Number of stator vanes	
$V^{(h)}$	Number of modified stator vanes	
w	Wake velocity gust	$[\mathrm{m\,s^{-1}}]$
Y_m	Bessel function of the second kind of order m	

Greek characters

β	Compressibility parameter ($\sqrt{1-M^2}$)	
χ_B, χ_V	Stagger angle of rotor blades and stator vanes respectively	[rad]
ΔP	Pressure jump over the airfoil	[Pa]
γ_{mn}	Axial wavenumber of the mode (m, n)	$[\mathrm{rad\,m^{-1}}]$
$\mathbf{\Phi}$	Modal basis in a matrix form	
Ω	Rotor rotational speed	$[\mathrm{rad\,s^{-1}}]$
ω	Angular frequency	$[\mathrm{rad\,s^{-1}}]$

Ω_s	Spinning phase speed of the mode m	$[\mathrm{rad\,s^{-1}}]$
Φ	Error function	
ϕ, ψ, Ψ	Potentials	$[\mathrm{m^2\,s^{-1}}]$
Π	Fan-OGV pressure rise	[Pa]
ρ	Fluid density	$[\mathrm{kg\,m^{-3}}]$
σ	Hub to tip ratio ($\sigma = R_H/R_T$)	
τ	Emission time	[s]
θ_{mn}	Emission angle (2D) of mode (m, n)	[rad]

Indices

0	Mean flow values
B	Refers to the rotor blade geometry
k	Vane index, varies from 0 to $V - 1$
m	Azimuthal order of the duct mode (m, n)
n	Radial order of the duct mode (m, n)
p	p^{th} Fourier's series index
s	BPF order
V	Refers to the stator vane geometry

Superscripts

$\pm$	Downstream $(+)$ and upstream $(-)$ propagation direction

Acronyms

BPF	Blade Passing Frequency
BPR	ByPass Ratio
CAA	Computational Aero-Acoustics
CFD	Computational Fluid Dynamics
CSM	Cross-Spectral Matrix
HBR	High Bypass Ratio
HVAC	Heat, Ventilation and Air Conditioning
LBM	Lattice-Boltzmann Method
LES	Large Eddy Simulation

MPT	Multiple Pure Tones
OGV	Outlet-Guide-Vanes
PWM	Pulse-Width Modulation
SPL	Sound Pressure Level
SWL	Sound Power Level
TCS	Turbulence Control Screen
UHBR	Ultra High Bypass Ratio
URANS	Unsteady Reynolds Averaged Navier Stokes

Introduction

Since the first developments of Sir James Lighthill in the early 1950s, aeroacoustics has become a discipline of major interest. Aeroacoustics is by definition: *the branch of physics that deals with the production of noise as a result of aerodynamic forces or turbulent airflow*[(a)]. In fact, the sound generated by a flow interacting or not with a solid surface can be found in many different situations; starting from the nature with the aeolian sound of the wind passing through tree branches to the more recent technologies as wind turbines or aircraft engines. Because most of the time a reduction of the noise level is valued, aeroacoustics became an important source of scientific research.

This PhD project focuses on one particular aeroacoustic application, turbomachinery noise. Turbomachines are found in several applications such as in HVAC[(b)] systems or in aircraft propulsion. In the case of air ventilation, fan noise is contributing to the ambient noise in a given confined space and can be disturbing for people exposed for long periods of time. In the case of aircraft engines, the noise generated at takeoff and landing phases is likely to disturb nearby dwellings. Both of them represent cases of noise pollution. The Madeira island airport shown in Figure 1 is an example among others, where populated areas are close to the airport and where a reduction of the acoustic footprint would be much appreciated.

The ACARE[(c)] has set the following goal within Flightpath 2050 targets [1]: "*The perceived noise emission of flying aircraft is reduced by 65%*". With the stricter noise regulations evolving over the years, it is then of great importance to reduce the noise emissions.

As a matter of fact, the first turbojet engines that entered commercial service in the 1950s had a very extended noise footprint. At that time, the engine thrust was generated by high exhaust speeds leading to an important jet noise. Indeed, Lighthill demonstrated [2, 3] that the total radiated acoustic power of a jet stream was related

[(a)] Online Oxford dictionnaries
[(b)] Heat, Ventilation and Air Conditioning
[(c)] Advisory Council for Aviation Research and Innovation in Europe

Figure 1: Madeira island airport in Portugal.

to the exhaust flow velocity to the eighth power. That meant having significant ejection speeds would lead to important noise levels. On the other hand, it also meant that a small reduction of the flow outlet velocity would considerably reduce noise emissions. Years later, in search of more fuel-efficient engine architectures, turbofans were developed, see Figure 2. These new bypass engines had higher mass flow rates for generating the necessary thrust. Thus, the reduction of the exhaust velocity that came along contributed to a significant noise reduction. Turbofans remain today the main propulsive systems used in commercial air transport and the bypass ratio[(d)] (BPR) has been increasing since then.

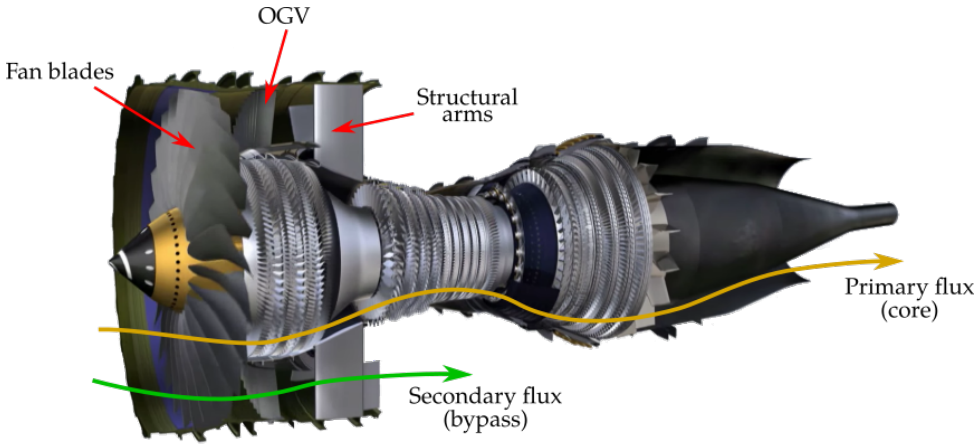

Figure 2: CFM56 turbofan. Entered service in 1982.

In terms of acoustics, turbofans also changed the relative contributions of noise sources. In Figure 3 are presented the various noise sources of an engine configuration with low and high BPR. Whereas in low BPR engines (comparable to turbojet) the downstream jet is dominating, in turbofans with higher BPR, fan noise becomes very significant upstream and downstream of the engine. For this reason, the research presented hereafter will be focused on this source.

[(d)] Ratio between the mass flow rate of the bypass flux and the mass flow rate of the core flux

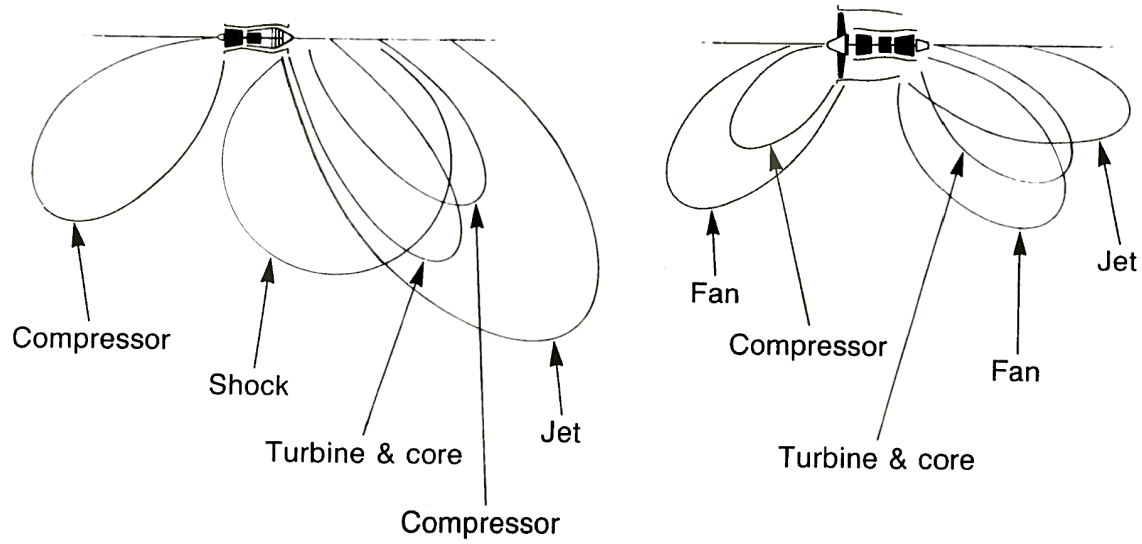

(a) Low bypass ratio (b) High bypass ratio

Figure 3: Noise radiation patterns for low and high bypass ratio engines, from Smith [4].

In the fan stage, the rotating part (fan) is coupled with a stationary part, the stator or more commonly, the OGV[(e)] (see Figure 2). The stator allows increasing the aerodynamic performance by straightening the flow exiting the rotor. This allows removing the flow swirl, for which the tangential velocity component would not contribute to the total axial thrust of the turbo-engine. However, from the acoustic standpoint, this interaction is at the origin of the so-called rotor-stator interaction noise.

In order to further develop turbofans, future architectures such as Ultra-High-Bypass-Ratio (UHBR) engines have the potential for reductions in fuel consumption. These engines are expected to have bypass ratios of 12 to 20 compared to 11 for current engines [5]. However, the increase in the bypass ratio implies larger fan diameters. Thus, to avoid higher drag due to the increased wet surface and to avoid mass increase, one option is to consider shorter nacelles. Consequently, the contribution of rotor-stator noise mechanisms could be increased due to reduced fan-OGV spacing. Moreover, because of the required compactness, structural elements will be included in the stator row yielding geometrical heterogeneities. This occurs already in modern turbofan configurations. In previous turbofan generations, the nacelle was held to the engine through structural struts placed downstream of the OGV as shown in Figure 2. However, in modern and future engines, the stator can play a structural role and some of the vanes are modified accordingly, see Figure 4. The lack of vane to vane periodicity in the stator is expected to have an important impact in terms of noise emissions.

This PhD project is focused on improving the understanding of the physics of rotor-stator interaction noise mechanisms with heterogeneous stators and quantify their impact. For engine manufacturers, a better understanding of these new noise sources is essential. In the long term, it will help to define innovative design strategies for quieter engines that

[(e)] Outlet-Guide-Vanes

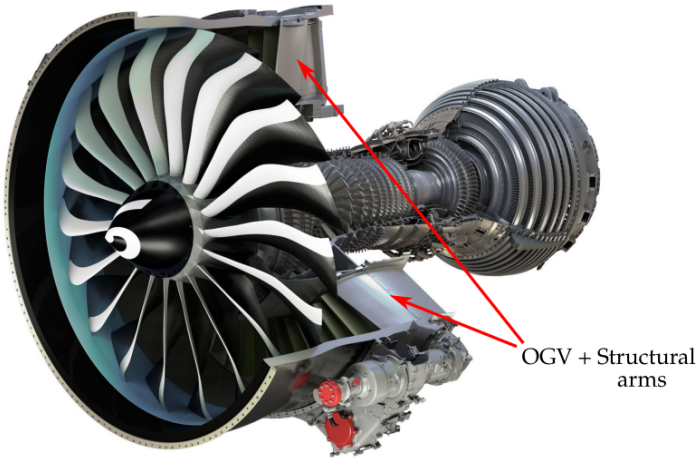

Figure 4: CFM LEAP engine. Entered service in 2016. In this engine, Outlet-Guide-Vanes have a structural role.

lie within future noise regulations.

The study of low-speed fans

In the present study, a low-speed ducted fan will be investigated. The study of low-speed fans is relevant in this context because physical phenomena occurring in those configurations are in many ways similar to those in turbofans. The low hub to tip ratio of the studied configuration allows having a significant modal content which can be retrieved by detailed analyses of the acoustic field. The flow velocity in both turbomachines is the major difference. Whereas in a turbofan transonic Mach numbers are reached at maximum power, in HVAC systems the maximum tip Mach number is generally subsonic (high limit of the incompressible regime). However, for a better understanding of rotor-stator mechanisms, the investigation of low-speed fan is legitimate. Moreover, some low-speed fan configurations have inhomogeneous stators, in accordance with future turbofan architectures. In addition, a ducted fan test-rig facility at École Centrale de Lyon is available for the experimental characterization of the sound field. Finally, the relatively low tip Mach number allows performing numerical simulations of the experimental setup using the Lattice-Boltzmann Method (LBM) in its experienced domain of application and where it is remarkably computationally-efficient. The simulation of the full geometry installed in its experimental environment is essential if one wants to account for installation effects and for the full heterogeneous stator geometry.

The investigated configuration is a ducted low-Mach number axial-flow fan (labelled LP3) from Safran Ventilation Systems. This fan is used in cargo hold and galley cooling of aircraft. It has the particularity of possessing a heterogeneous stator and having a short rotor-stator distance, two major characteristics of future turbo-engines. As mentioned above, an experimental facility of this fan is available at École Centrale de Lyon and fully

instrumented in order to perform aerodynamic and in-duct acoustic measurements. In addition to that, LBM simulations will be performed.

Finally, the LP3 will be analytically investigated. Analytical modelling offers an interesting alternative for the noise prediction. In this kind of approaches, drastic simplifications must be made in order to derive closed-form analytical solutions. However, the latter provides a first approximation of the sound generated and principally gives a physical insight into the mechanisms that are at the origin of the sound radiation. These methods are useful and widely used in pre-design phases where fast results are needed for parametric studies and where high accuracy is not required. In this case, analytical models have to be extended to account for heterogeneous stators as was first proposed by Roger et al [6]. It is important to highlight that all approaches (analytical, numerical and experimental) are complementary, necessary and often compared.

To sum-up, this PhD project aims at investigating the impact of heterogeneous stators in terms of acoustic emissions. For that goal, a combined analytical, experimental and numerical investigation will be carried out, focussed on the *LP3* low-speed ducted fan.

In chapter 1, the state of the art on turbomachinery noise and all the necessary theoretical background are presented. The experiment carried out on the *LP3* stage is then described in chapter 2. Next, the numerical simulations of the experimental apparatus using the Lattice-Boltzmann Method are given in chapter 3. Finally, analytical models are investigated in chapter 4 in which an acoustic optimisation of the stator is provided and general conclusions on the stator heterogeneity are summarized.

The list of published papers is given in appendix A and the AIAA journal published on another investigated configuration (the ANCF) which is not presented in the manuscript is given in appendix B.

1 State of the art

Contents

At the origin of turbomachinery noise are complex phenomena occurring from the interaction of the flow with rigid surfaces. As introduced before, the present study will be focused on rotor-stator interaction noise mechanisms. This chapter aims at giving a literature review of them. The studies available in the literature on the stator heterogeneity are presented. Firstly, a description of the operation of an axial turbo-engine is given. Then, the identified noise mechanisms are presented and described in detail. Secondly, the different investigation methods are described from which we can retain the analytical modelling, the numerical simulation and experiments on a fan test-rig. For each approach (analytical, numerical and experimental), the necessary theoretical background and the most relevant studies in the literature will be introduced. Their coupling will also be discussed in order to build the guiding thread for this research endeavour.

1.1 Axial turbomachines

Turbomachines can be classified in three main categories: axial, radial and mixed flow machines [7]. This categorization is based on the flow nature encountered through the rotor. In the framework of this study, axial turbomachines will be investigated where both the air intake and the outflow are axial. The rotor is in charge of accelerating and compressing the incoming fluid and generate an axial thrust. The rotation of the fan establishing the axial flow in the duct represents an energy transfer from the rotor to the fluid. A sectional representation in a meridian plane of a modern turbofan is shown in Figure 1.1. The flow path along the engine can now be described. The air enters the duct via an inlet designed to obtain the cleanest flow intake. Then, the majority of it goes through the secondary stream. Here, the air is compressed by the fan, straightened by the OGV and ejected through the exhaust (cold jet). This flow is in charge of more than 80% of the engine thrust in High Bypass Ratio engines and is characterized by high mass flow rate. On the other hand, a small portion of the air goes through the primary stream. The air is first compressed through low-pressure and high-pressure compressor stages, mixed with the fuel where the combustion occurs, expanded through turbine stages where the energy is partially recovered and finally ejected by the core exhaust (hot jet). The main role of the primary stream is to drive the compressor and fan rotating stages with the energy recovered by the turbine. This stream is characterized by hot temperatures, high exhaust speeds and low mass-flow rate.

In terms of noise, several sound-generating mechanisms can be found from the interaction of the flow with the different elements in the core and bypass streams. Compressor noise, combustion noise, turbine noise, jet noise and fan noise can be distinguished. Because the relative contributions of the sources have changed for recent engines as explained in the introduction, the focus will be given on noise sources associated with the fan and

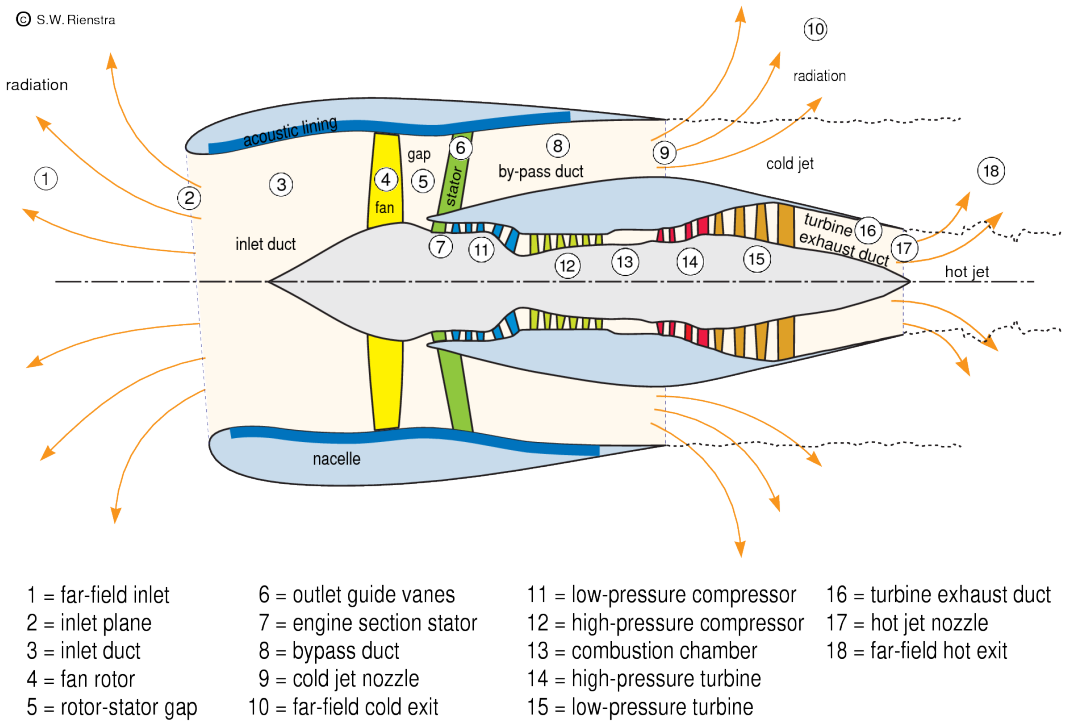

Figure 1.1: Turbofan representation from Rienstra [8]

OGV in the bypass flow. It has become a relevant and dominant source both at approach and take-off conditions [9]. Moreover, for HVAC fans, the rotor is driven by an electrical motor and is thus a single-stream machine. For these reasons, it is then relevant to study in detail sources located on the fan and OGV.

1.2 Heterogeneous stators

The objective of this PhD thesis is to investigate heterogeneous stators. The heterogeneity is defined as the non-periodic geometry from vane to vane. It is the case of recent and future engine generations where structural elements are now included in the stator row. This includes struts as well as bifurcations usually placed at 6 and 12 o'clock within the duct section. The impact of such technological options has not been extensively studied in the literature in terms of excitation and source related modifications.

In terms of analytical modelling, the paper of Roger & Caule [6] represents an interesting starting point. A preliminary study of the effect of a inhomogeneous stator has been performed. The studied configuration is the HVAC fan from Safran Ventilation Systems investigated in this PhD project, the *LP3*. According to the Tyler & Sofrin rule based on purely periodic blade/vane rows, the first two BPFs should be cut-off by the duct. With a simplified analytical approach, it has been shown that the heterogeneity could be causing the regeneration of the first two BPFs. In this paper, some experiments have also been conducted. The increase in the heterogeneity of the stator (increased thickness and

longer chord of one vane) has evidenced an increase of the first BPF shown in Figure 1.2.

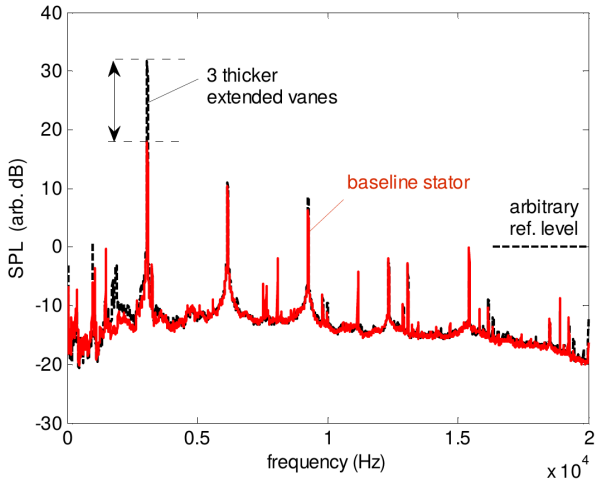

Figure 1.2: Spectrum of the LP3 configuration from Roger et Caule [6]. Baseline configuration (heterogeneous stator) in red and the modified stator (increased heterogeneity) in black.

However, some questions are still unanswered. Possible inflow distortions entering the fan could also be contributing and re-generate the first two BPFs. Furthermore, the presence of a power-supply cable downstream of the OGV could be source of another heterogeneity and also contribute to the appearance of the first BPFs. Finally, how the modal content of this configuration is influenced by these geometrical modifications? This PhD aims at providing a detailed investigation and quantification of the impact of the heterogeneity.

In terms of numerical investigations, the works of Bonneau et al. [10], Holewa et al. [11] and more recently Kozlov et al. [12] can also be mentioned.

In a recent study by Bonneau et al. [10], a turbofan configuration which includes struts and bifurcations has been numerically investigated, see Figure 1.3. In this research, it has been shown that the first BPF which should be cut-off by the duct radiates at high levels. The BPF spectrum shown in Figure 1.3b compares results for homogeneous and heterogeneous stators. Because the simulation has only been performed on a heterogeneous stator, a homogeneous stator has been artificially re-created by taking one vane, either a strut, a bifurcation or a baseline vane, and by duplicating it periodically in the azimuthal direction. In this case, the first BPF is seen to be cut-off because of the vane-to-vane periodicity. However, the computation on the real heterogeneous stator evidences a high level of the first BPF.

The work of Holewa et al. [11] is focused on the bypass bifurcations impact on tonal noise radiation. The authors compare a rotor-stator stage alone with the addition of bifurcations. The modal spectrum is found to be extended including all orders instead of only the orders predicted by the Tyler & Sofrin's rule, as also evidenced by Roger & Caule [6].

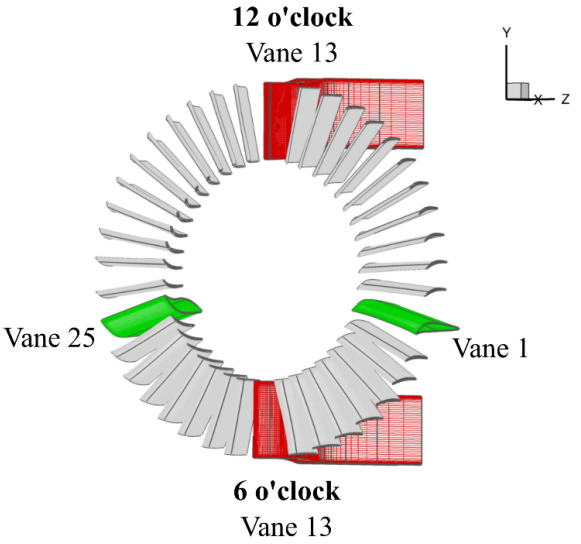

(a) Heterogeneous OGV with struts and bifurcations.

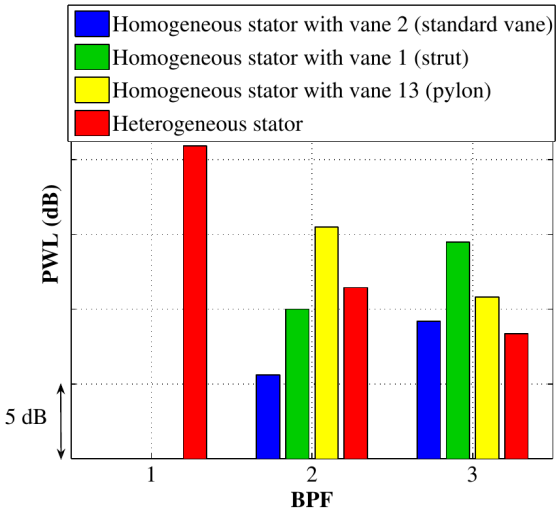

(b) Noise predictions for homogeneous and heterogeneous configurations.

Figure 1.3: Configuration investigated by Bonneau et al. [10] and respective radiation predictions.

More recently, during the course of this PhD, Kozlov et al. [12] have investigated the rotor noise generated from downstream disturbances. These perturbations are generated by mounting structures downstream of the stator row. The authors have shown that even if potential distortions attenuate rapidly upstream, they generate low acoustic circumferential mode orders, very efficient in sound transmission. The generated sound level has been compared with the classical wake-interaction noise and shown to be comparable.

The numerical investigation of complex geometries including heterogeneous stators is becoming more and more accessible. However, most of the time it requires simulating the full 360 degrees geometry, which represents a high computational cost. Most of the available studies treat the tonal noise case by using URANS simulations. If the broadband noise is to be simulated by using methods like LES, the simulation cost on a full 360° geometry is often prohibitive. In this PhD, it is proposed to use the Lattice-Boltzmann Method applied to the full rotor-stator geometry and to account for installation effects for an accurate comparison with experiments. This method is introduced in section 1.5.

Aside from the previous cited works, the detailed characterization of source and excitation modifications due to the heterogeneity has not been done. The weak stator heterogeneity investigated in this PhD prevents from changing the operating conditions of the machine and allows for easier comparisons with the homogeneous case. Moreover, the combination of the analytical, numerical and experimental analyses should give a more comprehensive interpretation of the underlying physical phenomena.

Heterogeneous stators — **Summary**

The impact of the stator heterogeneity has not been extensively investigated in the literature. Some recent studies have demonstrated that the presence of massive bifurcations or struts in modern turbofan configurations may have an important impact on the noise levels. However, a fair comparison with an equivalent homogeneous stator has not been done and a detailed analysis of the modal content modification is still lacking.

1.3 Fan noise mechanisms

The typical far-field noise spectrum of a fan-OGV configuration is shown in Figure 1.4. Two major noise components can be observed: broadband noise and tonal noise. On the one hand, the broadband noise component extends within a wide range of frequencies. It is related to the turbulence in the flow and its interaction with solid surfaces. On the other hand, pure tones arise at discrete frequencies. These tones are caused by periodic interactions between the rotor and the stator or by the interaction of flow distortions with the rotor. They appear at the blade passing frequency (BPF) $f_s = sB\Omega/60$ and its harmonics, where s is the harmonic order, B the number of rotor blades and Ω the rotational speed in rpm.

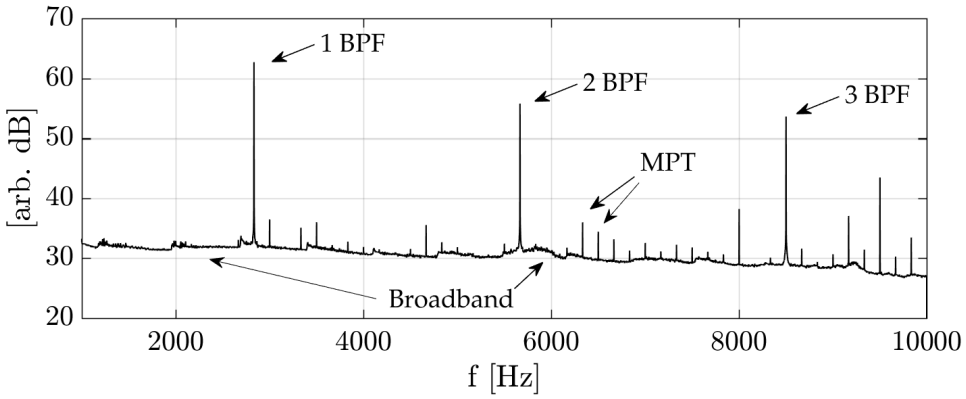

Figure 1.4: Typical noise spectrum of a low-speed fan-OGV configuration.

Finally, another tonal source can be observed emerging from the broadband level. It is a series of multiple pure tones (MPT) at multiples of the rotational shaft frequency $n\Omega/60$. They are caused by geometrical or flow discrepancies between rotor blades. In the particular case of turbofans, this phenomenon has been recently investigated for Buzz Saw Noise (shock wave noise) in transonic conditions by Thisse [13]. Because the rotor is considered perfectly periodic from blade to blade in the present work, this component will be ignored. It is worth noting that manufacturing uncertainties on the rotor in the actual experiment are not excluded, which could yield inhomogeneity and generate MPTs. The

same MPT can also be generated by mechanical or electromagnetic imbalance.

At a given frequency, either tonal or broadband, several sources contribute to the noise. Because of that, it is often complicated to separate the contribution of each individual source in numerical simulations or experiments. Within an analytical modelling strategy, each source is modelled independently and can be summed up based on linear acoustics and an assumption of independent noise sources. In the following, a detailed description of the identified noise mechanisms is given for tonal and broadband noise.

1.3.1 Sources of tonal noise

Tonal noise mechanisms are described in this section. Along with the description, the possible impact of an inhomogeneous OGV is discussed. The rotational speed of the engine defines the radiating tonal frequencies and because rotor blades are assumed identical, all presented mechanisms are contributing to the acoustic spectrum at the BPFs. Four major sources of tonal noise were identified in the fan-OGV stage [14]: wake and potential interactions, inflow distortion and fan self-noise.

1.3.1.1 Wake-interaction noise

A schematic representation of the wake-interaction noise is shown in Figure 1.5 for both homogeneous and heterogeneous stator configurations. The viscous flow occurring on rotor blades gives rise to downstream velocity deficits, the wakes. Rotating at the rotational speed and being convected axially by the flow, wakes impinge on the OGV. In consequence, stator vanes experience lift fluctuations because of the passage of those velocity disturbances.

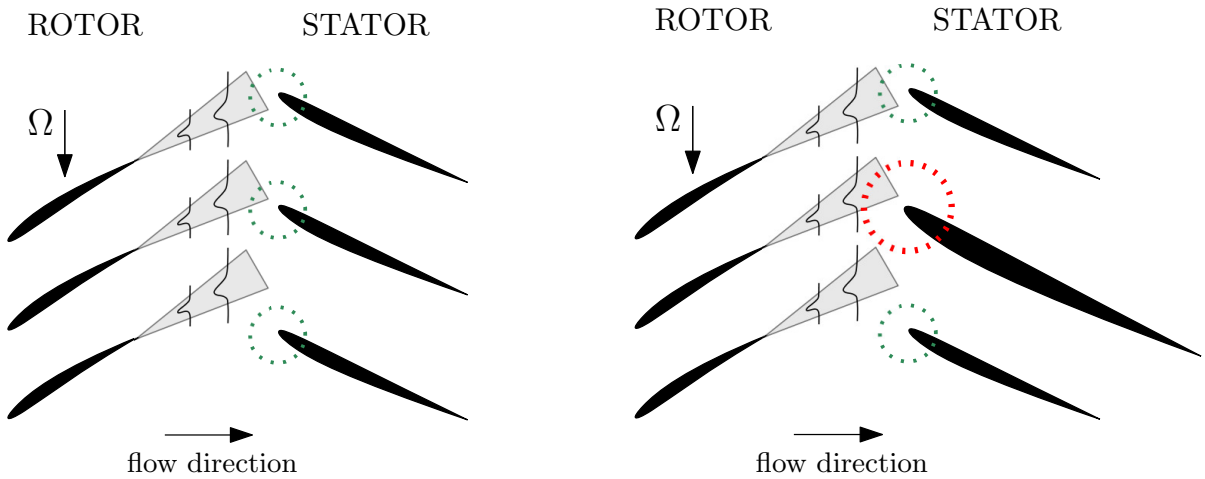

(a) Homogeneous (b) Heterogeneous

Figure 1.5: Two-dimensional representation of the wake-interaction noise mechanism for a homogeneous and heterogeneous stators.

As explained in section 1.4, pressure fluctuations on airfoils are at the origin of noise radiation. The interaction of B-periodic wake deficits with the stator row constitutes a

periodic interaction phenomenon and radiation will appear at the BPFs. In the case of a periodic stator, each vane responds identically to each blade wake. Now, in the presence of modified vanes, the aerodynamic response to the same excitation (wakes) is not identical from vane to vane. The break in the stator periodicity is expected to generate duct modes that would not be created from destructive interferences between the B blade wakes and the V stator vanes for a periodic OGV. The wake-interaction noise mechanism can be seen as a leading edge perturbation problem with the sources being mainly located in this region (dotted circles in Figure 1.5).

1.3.1.2 Potential-interaction noise

Potential interaction is described and sketched in Figure 1.6. This noise mechanism is generated by the interaction of the rotor blades with the potential field of downstream obstacles. In fact, the potential flow on the stator is responsible for a disturbed field in the upstream vicinity of the vanes. Rotor blades passing through this downstream field experience pressure fluctuations. In theory, it is known that the potential decreases fast upstream [15]. It would mean that if a sufficient fan-OGV separation distance could be ensured, the source weight would be minimized and the source made negligible compared to the wake-interaction. However, in future engine architectures, the reduced length of the engine requires a shorter fan-OGV spacing. In consequence, the contribution of the potential interaction noise is increased. The potential noise was analytically investigated by Parry [16] for counter-rotating open rotor configurations and by Roger et al. [17] for the rotor interaction with a downstream radial cylinder.

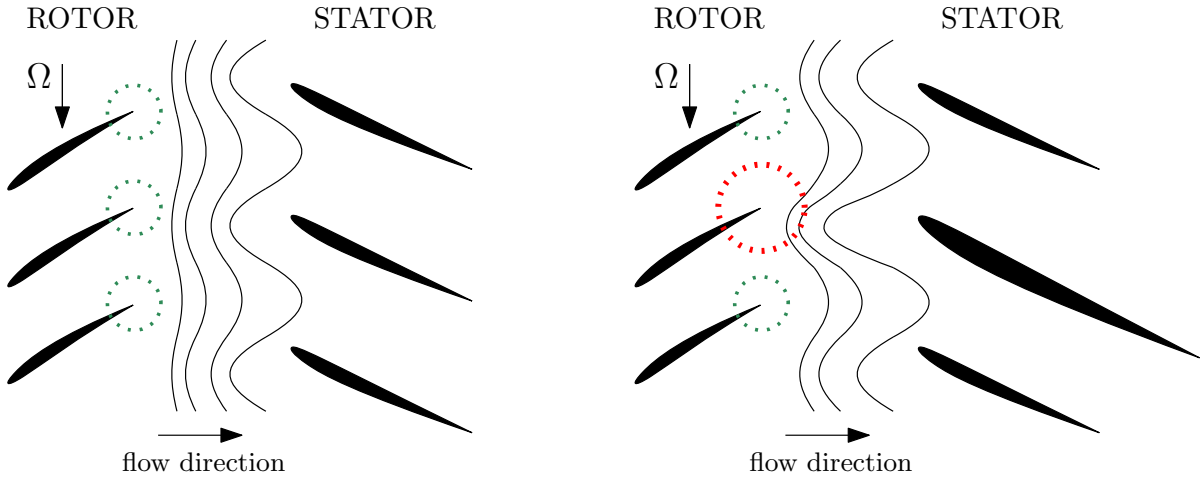

(a) Homogeneous (b) Heterogeneous

Figure 1.6: Representation of the potential interaction noise mechanism for a homogeneous and heterogeneous stators.

In the case of a heterogeneous stator, the upstream distorted field is stronger and loses its periodicity from vane to vane as shown in Figure 1.6b. In a analogue way as for wake-interaction, the rotor blades will experience non-periodic excitations. In terms of

source location, this mechanism can be seen as a trailing-edge interaction.

1.3.1.3 Inflow distortion

An inflow distortion is characterized by an asymmetry of the flow. It can be caused by an asymmetric inlet geometry as was investigated by Daroukh et al. [18] or by other atmospheric flow inhomogeneities entering an axisymmetric inlet as evidenced by Sturm [19], see Figure 1.7. In these conditions, rotor blades experience unsteady pressure fluctuations by crossing azimuthal flow disturbances. The passage accross steady or quasi-steady flow disturbances will generate sound around the BPFs. However, if the inflow distortion has random fluctuations, broadband noise will also be radiated. The heterogeneity is not expected to impact this noise mechanism. This source mechanism can be seen as a leading edge mechanism on the rotor blades.

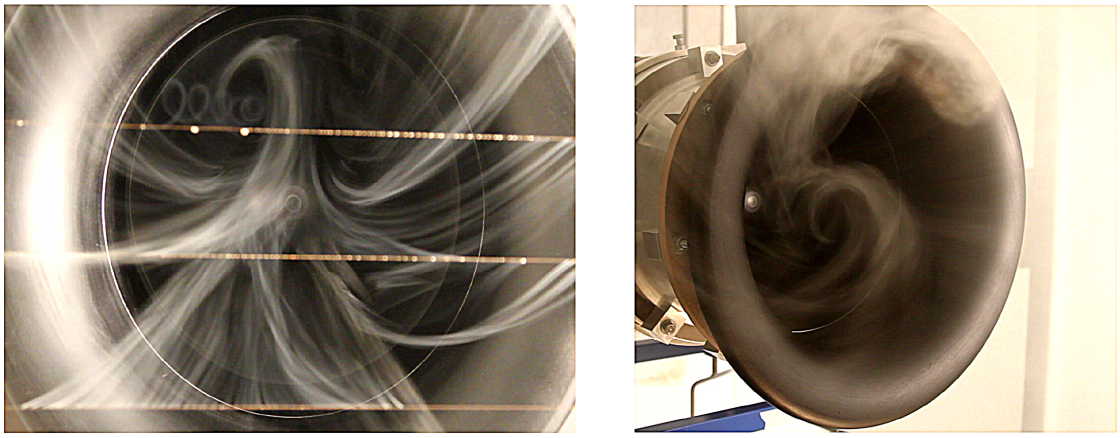

(a) View 1 (b) View 2

Figure 1.7: Inflow distortion visualization with a smoke generation technique by Sturm et al. [19].

1.3.1.4 Fan self-noise

The fan self-noise is caused by the steady volume-displacement effect exerted by the rotor blades on the fluid. However, this noise mechanism has been shown to be negligible at low-Mach numbers [20] as is the case of the studied configurations.

1.3.2 Sources of broadband noise

In Figure 1.8 are sketched different sources of broadband noise.

1.3.2.1 Blade/vane self-noise

The boundary layers developing on blades and vanes generate noise by the interaction with the trailing edge [21, 22, 23, 24]. The trailing edge represents a singular point location

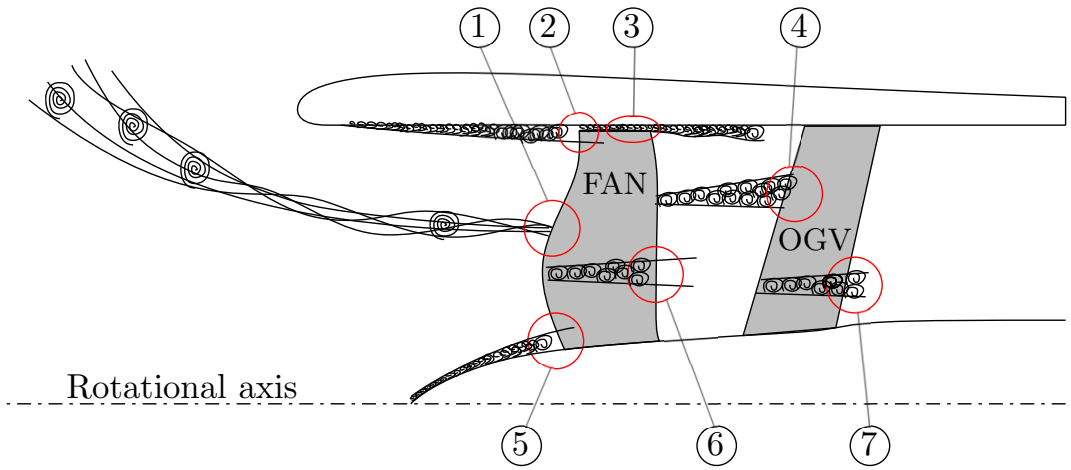

Figure 1.8: Schematic representation of various broadband noise sources in axial turbomachines. (1) inflow turbulence ingestion, (2&5) duct boundary layer interaction, (3) tip flow, (6,7) blade/vane boundary layer scattering (self-noise) and (4) turbulent wake-interaction.

where pressure side and suction side flows merge. If the the trailing edge is thick enough with respect to the boundary layers, the vortex shedding occurring at the trailing edge is also a source of tonal noise as investigated by Roger et al. [17].

1.3.2.2 Wake-interaction noise

Wake interaction can also be a broadband noise source. In fact, the important flow shear occurring at the blade walls and at the shear layers of the wake creates convected turbulent structures. The interaction of these structures (at different scales) with the stator generates broadband noise. This source must not be confused with the self-noise induced by the scattering of turbulent structures on the airfoil itself.

1.3.2.3 Duct boundary-layer interaction with blades

The interaction of the duct turbulent boundary layers developing from the inlet with the rotor and the stator is source of broadband noise. In a turbulent boundary layer, the shear at the wall is important and responsible for the generation of turbulent structures. Thicker boundary layers are expected to increase this noise component.

1.3.2.4 Tip flow

The tip flow occurring within the tip clearance of the rotor is at the origin of coherent structures. Vortices are formed by the flow from the pressure to the suction side around the blade tip, see Figure 1.9. Because of the mixing of the tip vortices with other turbulent structures, the sound spectrum features humps around the BPFs or at slightly lower shifted frequencies [25, 26, 27, 28]. In fact, the coherent structures generated at the blade

tip within high shear layers between the blade tip and the duct wall give rise to highly turbulent flow.

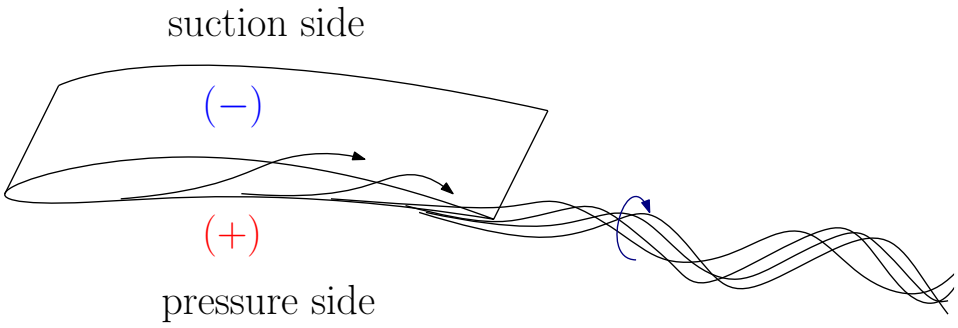

Figure 1.9: Formation of the tip (or leakage) vortex.

The size of the vortex generated at the tip is related to the gap size. Thus, bigger tip clearances should increase this source caused by strong interactions of tip vortices with the stator.

1.3.2.5 Turbulence ingestion

In the case of a turbulent inflow distortion, the sound emitted will be broadband [29]. Atmospheric turbulence entering the duct is expected to interact with the fan blades and generate broadband noise. These disturbances can be attributed in some cases to installation effects (ground or obstacles).

Fan noise mechanisms — Summary

In this section, the various noise sources occurring in a rotor-stator configuration have been presented. Regarding the tonal noise, two main sources of interest have been retained: the potential interaction noise and the wake-interaction noise. Among these two noise sources, the heterogeneous stator is expected to have a considerable impact. It is important to note that any possible inflow distortion must be removed if one wants to investigate the impact of the stator heterogeneity. In fact, this noise source contributes at the same frequencies as those of rotor-stator interaction noise mechanisms and constitutes an undesirable contribution for any precise quantification of the stator impact.
On the other hand, in terms of broadband noise sources, the wake-interaction contribution is expected to dominate. However, the impact of a heterogeneous stator on this source is hard to assess.

1.4 Analytical modelling of ducted fan noise

In this section, the analytical theory for modelling turbomachinery noise is introduced. First, the general noise-prediction methodology is detailed. Then, the general solution of the wave equation in a infinite duct is given and the cut-off condition is introduced. Goldstein's acoustic analogy is then presented. This analogy used in turbomachinery noise, expresses the acoustic field in the duct as a function of the unsteady loads on the blades or vanes. Airfoil response models are thus introduced. These models aim at providing the unsteady lift distribution as input of Goldtein's analogy. Finally, the analytical modelling of the aerodynamic excitation is given. These models are the necessary inputs for airfoil response models.

1.4.1 Noise prediction methodology

The classical analytical solving methodology adopted to investigate this problem is sketched in Figure 1.10. It is separated into sub-steps, the combination of which provides the noise radiation as sketched by Hubbard [30]. It can be separated in two major parts: unsteady aerodynamics modelling and acoustic analogy.

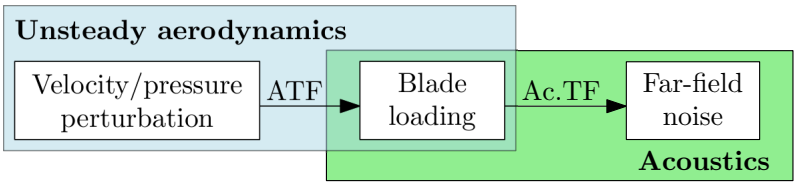

Figure 1.10: Noise prediction methodology scheme

The first step is part of unsteady aerodynamics and its objective is to evaluate the blade/vane response using an aerodynamic transfer function (ATF). This transfer function relates a velocity perturbation to the unsteady lift of the blade/vane. Then, the unsteady load is related to its far-field radiation through an acoustic transfer function (Ac.TF). In the present work, the acoustic analogy formulated by Goldstein [31] for axial duct flows will be used. In the case of the numerical simulation, all those steps are intrinsically combined when solving the unsteady flow.

In this study, the involved velocity perturbations can be analytically or numerically evaluated for each mechanism. The unsteady loading given by analytical models can also be compared to the numerical loads. On the other hand, experiments conducted in this thesis only allow to evaluate the noise upstream and downstream of the fan. From this noise-prediction methodology, one can see that the various investigation methods can be coupled differently. It should allow either improving models or either qualifying them. For instance, numerical unsteady loads can be used as the input of the analytical acoustic analogy as done by Casalino et al. [32] and Arroyo et al. [33].

1.4.2 Solution of the wave equation in a duct

The convected wave equation is obtained by linearisation of the Euler equations. Its solution in a rigid duct under the assumption of a uniform axial flow yields the general form of the acoustic pressure. The reference frame is shown in Figure 1.11.

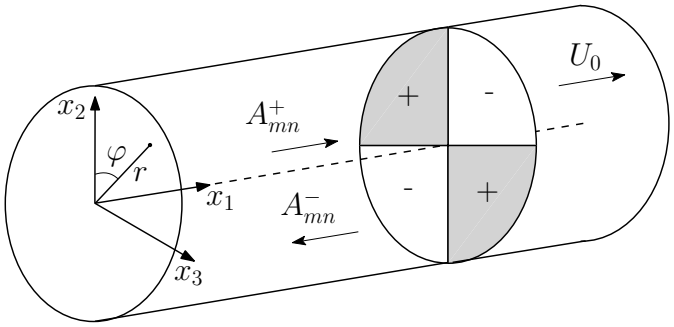

Figure 1.11: Duct reference frame. Schematic pattern of the mode $(m, n) = (2, 0)$ is shown for illustration.

The in-duct acoustic pressure can then be expanded as a sum of modes as follows:

$$p(x_1, r, \varphi, t) = \sum_{m=-\infty}^{+\infty} \sum_{n=0}^{+\infty} f_{mn}(r) \left[A^+_{mn} \mathrm{e}^{\mathrm{i}\gamma^+_{mn} x_1} + A^-_{mn} \mathrm{e}^{\mathrm{i}\gamma^-_{mn} x_1} \right] \mathrm{e}^{\mathrm{i}m\varphi} \mathrm{e}^{-\mathrm{i}\omega t} \tag{1.1}$$

The sum includes azimuthal modes of order m and radial modes of order n. The reader can refer to specialized acoustic books for a more detailed description [8, 34]. In the expression, constants $A^{\pm}_{mn}$ are complex-valued unknowns related to the source terms, often called the modal coefficients. Their calculation can be achieved analytically, numerically or via measurements. They represent the modal content of a given configuration. Regarding tonal noise in homogeneous rotor-stator stages, only some azimuthal modes of order m are expected from the rule first recognized by Tyler & Sofrin [35].

In the framework of this PhD, these coefficients will be computed by using isolated airfoil-response models as detailed later. They can also be obtained by matrix inversion from measured pressures by an array of microphones or from the numerical simulation.

The radial shape functions in the form proposed by Rienstra [8] are used here:

$$f_{mn}(r) = N_{mn} \left[\cos(\tau_{mn}) J_m(K_{mn} r) + \sin(\tau_{mn}) Y_m(K_{mn} r) \right] \tag{1.2}$$

where the normalization factors N_{mn} and the parameters τ_{mn} are defined as:

$$N_{mn} = \frac{\frac{1}{2}\sqrt{2}\pi K_{mn}}{\left\{ \dfrac{1 - m^2/K^2_{mn}}{J'_m(K_{mn})^2 + Y'_m(K_{mn})^2} - \dfrac{1 - m^2/K^2_{mn}\sigma^2}{J'_m(K_{mn}\sigma)^2 + Y'_m(K_{mn}\sigma)^2} \right\}^{1/2}} \tag{1.3}$$

$$\tau_{mn} = \arctan \left\{ \frac{J'_m(K_{mn})}{Y'_m(K_{mn})} \right\} \tag{1.4}$$

with $\sigma = R_H/R_T$. The axial wavenumber $\gamma_{mn}^{\pm}$ is given by

$$\gamma_{mn}^{\pm} = -\frac{M_0 k_0}{\beta^2} \pm \frac{k_{mn}}{\beta^2} \tag{1.5}$$

with $\beta = \sqrt{1 - M_0^2}$, $k_0 = \omega/c_0$, $M_0 = U_0/c_0$ and

$$k_{mn} = \sqrt{k_0^2 - \beta^2 K_{mn}^2} \tag{1.6}$$

where K_{mn} are the duct eigenvalues only depending on the duct geometry.

1.4.3 Duct cut-off condition

When studying duct propagation, the cut-off condition is an important notion. In fact, in a confined space as a duct, some of the modes of equation (1.2) are not transmitted. In order to better understand this notion, we can investigate the nature of the axial wavenumber k_{mn} given in equation (1.6). This wavenumber becomes imaginary when the following condition is satisfied:

$$\beta K_{mn} > k_0 \tag{1.7}$$

This case corresponds to evanescent waves known to decay exponentially along the axis. Modes fulfilling this condition are said to be cut-off modes since they do not propagate in the duct and this condition is known as the cut-off condition. Oppositely, other modes are said cut-on. Since eigenvalues K_{mn} increase with the mode order, all modes with orders above that of the first cut-off mode are also cut-off. This property is crucial when investigating duct propagation because the duct geometry itself will set a finite number of possible cut-on modes along the duct. In fact, this condition can be put in an other form where a spinning velocity of the mode is introduced. It can be demonstrated that the smallest value of K_{mn} for a given order m is equal to mB/R_T. Then the condition becomes:

$$M_t = \frac{R_T \Omega}{c_0} < \beta \tag{1.8}$$

$$M_0^2 + M_t^2 < 1 \tag{1.9}$$

with r_t the tip radius of the blade. This condition is now easier to interpret since it states that for low axial Mach numbers ($M_0 \approx 0$), only supersonic spinning modes will propagate. It is important to note that the mode $(m, n) = (0, 0)$ is known as the plane-wave mode and will propagate at any frequency if generated. The eigenvalue associated with this mode is null and thus the wavenumber is not anymore dependant on the Mach number. This mode has an infinite equivalent spinning velocity and corresponds to the case of a plane wave propagating along the axis.

A schematic representation of cut-on and cut-off modes is also given in Figure 1.12. For each mode, a propagation angle can be calculated. Its two-dimensional approximation is given by:

$$\theta_{mn} = \arctan\left(\frac{m}{rK_{mn}}\right) \tag{1.10}$$

The mode becomes cut-off when its angle θ_{mn} with the duct axis reaches 90°.

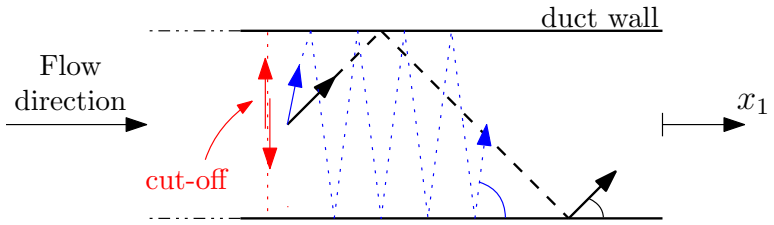

Figure 1.12: Two dimensional representation of cut-on and cut-off modes. Modes approaching cut-off have emission angles tending to $\pi/2$ rad. At cut-off, modes have a perpendicular emission direction with respect to the duct axis and thus are not transmitted axially. They are trapped radially.

1.4.4 Goldstein's analogy for duct flows

In the previous section, a general solution of the homogeneous convected wave equation has been introduced. Here, we propose to solve the inhomogeneous equation corresponding to the presence of sources in the duct by applying the acoustic analogy. The focus is here given on tonal noise but the problem can be approached for broadband noise in a similar way. The coordinate system used in this section is defined in Figure 1.13.

The acoustic analogy is based on a re-arrangement of the gas dynamics equations in order to obtain a non-homogeneous wave equation of the form:

$$\frac{\mathrm{D}^2 p}{\mathrm{D}\tau^2} - c_0^2 \nabla^2 p = \mathcal{S}(\vec{y}, \tau) \tag{1.11}$$

All aerodynamic sources are contained in the term $\mathcal{S}(\vec{y}, \tau)$. According to the acoustic analogy reformulated by Ffowcs-Williams and Hawkings [36] in the presence of rigid surfaces in the fluid, the source term can be expressed in the form of mono-, di- and quadrupolar sources [37]:

$$\mathcal{S}(\vec{y}, \tau) = \underbrace{\frac{1}{c_0^2} Q(\vec{y}, \tau) + \frac{\partial f_i(\vec{y}, \tau)}{\partial y_i}}_{\text{surface effects}} + \underbrace{\frac{\partial^2 T_{ij}(\vec{y}, \tau)}{\partial y_i \partial y_j}}_{\substack{\text{turbulence of the} \\ \text{flow and mean-flow} \\ \text{distortions (gradients)}}} \tag{1.12}$$

with the following definitions:

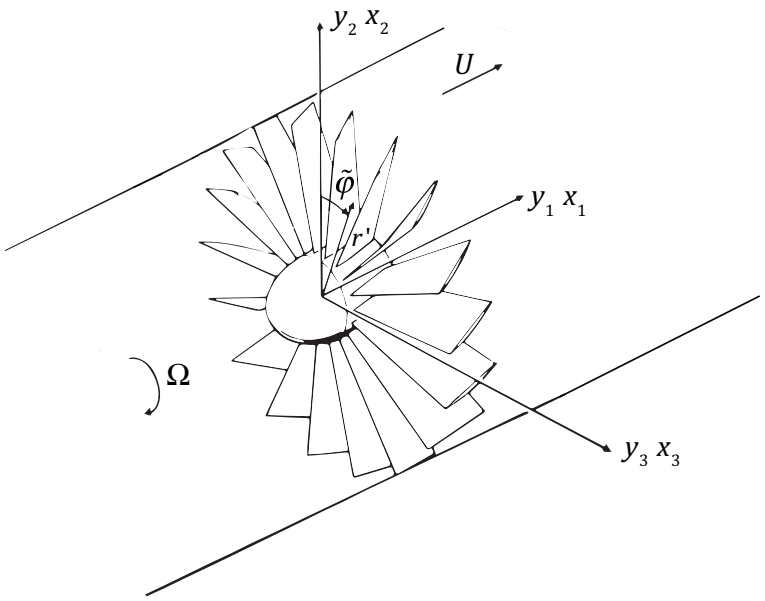

Figure 1.13: Coordinate system for a fan installed in an infinite duct [31].

1. $\frac{1}{c_0^2}Q(\vec{y},\tau)$: this term corresponds to a monopole source and is at the origin of the so-called thickness noise [38]. In the case of thin airfoil theory with small camber and thickness, it can be neglected ;

2. $\frac{\partial f_i(\vec{y},\tau)}{\partial y_i}$: this term corresponds to a dipole source. All unsteady aerodynamic loads are included in this contribution. In the framework of this study, by investigating unsteady loads induced by upstream/downstream gusts, this will be the dominant term [36] ;

3. $\frac{\partial^2 T_{ij}(\vec{y},\tau)}{\partial y_i \partial y_j}$: this term corresponds to a quadrupole source. All random phenomena like turbulence will be included here, as well as mean-flow gradients (related to Lighthill's tensor T_{ij}). In the present case, for low speed applications this term can be neglected as shown by Morfey [39].

The monopole and dipole sources result from the presence of surfaces in the flow. In absence of surfaces, the original Lighthill's analogy is recovered. Then, by only keeping load terms, the equation becomes:

$$\frac{\mathrm{D}^2 p}{\mathrm{D}\tau^2} - c_0^2 \nabla^2 p = \frac{\partial f_i(\vec{y},\tau)}{\partial y_i} \tag{1.13}$$

The solution of this inhomogeneous wave equation can be obtained using the Green's function method and is given by the convolution product of the source term with a tailored

Green's function. After some manipulations, the solution is written as:

$$p(\vec{x},t) = \int_{-T}^{T}\int_{S(\tau)} \frac{\partial G}{\partial y_i} f_i \,\mathrm{d}S(\vec{y})\,\mathrm{d}\tau \tag{1.14}$$

where S now denotes the blade surface. The exact Green's function for a duct flow is given by Goldstein [31] as

$$\begin{aligned} G(\vec{x},t \mid \vec{y},\tau) &= \frac{\mathbf{i}}{4\pi}\sum_{m,n} \frac{f_{mn}(K_{mn}r')e^{-\mathbf{i}m\tilde{\varphi}} f_{mn}(K_{mn}r)e^{\mathbf{i}m\varphi}}{\Gamma_{mn}} \\ &\quad \times \int_{-\infty}^{\infty} \frac{\exp\left\{\mathbf{i}\left[\omega(\tau-t)+\frac{Mk_0}{\beta^2}(y_1-x_1)+\frac{k_{mn}}{\beta^2}\mid y_1-x_1\mid\right]\right\}}{k_{mn}}\,\mathrm{d}\omega \end{aligned} \tag{1.15}$$

The cylindrical coordinates of the source $\vec{y}$ and of the observator $\vec{x}$ are

$$r' = \sqrt{y_2^2+y_3^3} \qquad \tilde{\varphi} = \tan^{-1}(y_3/y_2) \tag{1.16}$$

$$r = \sqrt{x_2^2+x_3^3} \qquad \varphi = \tan^{-1}(x_3/x_2) \tag{1.17}$$

By using the Green's function for duct flows, Goldstein [31] first provides an expression of the duct modes for sources located on the rotor with B identical blades. The pressure at the blade passing frequency ($sB\Omega$) writes:

$$p_{sB}^{\pm}(\vec{x}) = \frac{B}{2}\sum_{p=-\infty}^{+\infty}\sum_{n=1}^{+\infty} \frac{f_{mn}(K_{mn}r)}{\Gamma_{mn}k_{mn}} \mathrm{e}^{\mathbf{i}(m\varphi-\gamma_{mn}^{\pm}x_1)} \times \left(mD_{mn}^{\pm}-\gamma_{mn}^{\pm}T_{mn}^{\pm}\right) \tag{1.18}$$

where T_{mn} and D_{mn} are blade loading factors given by:

$$D_{mn}^{\pm} = \int\int_{\mathcal{A}_0} f_{mn}(K_{mn}r')\mathrm{e}^{\mathbf{i}(\gamma_{mn}^{\pm}y_1^c-m\varphi')}F_{D_0}^{(p)}\,\mathrm{d}r'\,\mathrm{d}\varphi' \tag{1.19}$$

$$T_{mn}^{\pm} = \int\int_{\mathcal{A}_0} f_{mn}(K_{mn}r')\mathrm{e}^{\mathbf{i}(\gamma_{mn}^{\pm}y_1^c-m\varphi')}F_{T_0}^{(p)}\,r'\,\mathrm{d}r'\,\mathrm{d}\varphi' \tag{1.20}$$

$\mathcal{A}_0$ being the surface of a single blade and $\pm$ denoting the modes propagating downstream $(+)$ or upstream $(-)$. These expressions can be put in the form:

$$D_{mn}^{\pm} = \int_{R_H}^{R_T} f_{mn}(K_{mn}r')\left\{\int_{\mathrm{LE}}^{\mathrm{TE}} \mathrm{e}^{-\mathbf{i}(\gamma_{mn}^{\pm}r'\mathrm{cotan}\chi_B+m)\varphi'}F_{D_0}^{(p)}(r',\varphi')\,\mathrm{d}\varphi'\right\}\mathrm{d}r' \tag{1.21}$$

$$T_{mn}^{\pm} = \int_{R_H}^{R_T} f_{mn}(K_{mn}r')\left\{\int_{\mathrm{LE}}^{\mathrm{TE}} \mathrm{e}^{-\mathbf{i}(\gamma_{mn}^{\pm}r'\mathrm{cotan}\chi_B+m)\varphi'}F_{T_0}^{(p)}(r',\varphi')\,\mathrm{d}\varphi'\right\}r'\,\mathrm{d}r' \tag{1.22}$$

where y_1^c was projected according to Figure 1.14. Only unsteady forces perpendicular

to the airfoil are considered in this study. The unsteady parallel forces are negligible in far-field noise as pointed out by Roger in the Part 2 of [40] for instance.

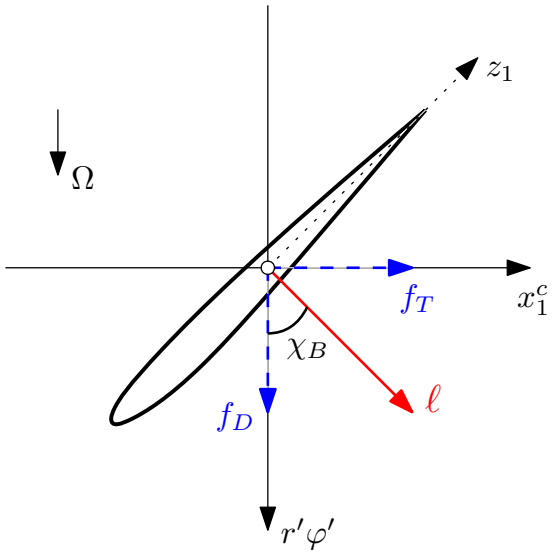

Figure 1.14: Reference frame for the blade loading

The following projections are used:

$$x_1^c = z_1 \cos\chi_B = -r'\varphi' \text{cotan}\chi_B \tag{1.23}$$

$$r'\varphi' = -z_1 \sin\chi_B = -\frac{c}{2}\sin\chi_B z_1^* \qquad \text{with} \quad z_1 = \frac{c}{2}z_1^* \tag{1.24}$$

$$\mathrm{d}\varphi' = -\frac{c}{2r'}\sin\chi_B \,\mathrm{d}z_1^* \tag{1.25}$$

so that

$$\begin{aligned} -(\gamma_{mn}^{\pm} r' \text{cotan}\chi_B + m)\varphi' &= \frac{c}{2r'}\left[\gamma_{mn}^{\pm} r' \text{cotan}\chi_B + m\right]\sin\chi_B z_1^* \\ &= \frac{c}{2}z_1^*\left[\gamma_{mn}^{\pm}\cos\chi_B + \frac{m}{r'}\sin\chi_B\right] \\ &= A_{mn}\, z_1^* \end{aligned} \tag{1.26}$$

with

$$A_{mn}(r') = \frac{c}{2}\left[\gamma_{mn}^{\pm}\cos\chi_B + \frac{m}{r'}\sin\chi_B\right] \tag{1.27}$$

The aerodynamic load components can then be projected according to Figure 1.14 as:

$$f_T = \Delta P \sin\chi_B \qquad f_D = \Delta P \cos\chi_B \tag{1.28}$$

Finally, the chordwise integral is expressed with the new projections as

$$\int_{\mathrm{LE}}^{\mathrm{TE}} \mathrm{e}^{-\mathbf{i}(\gamma_{mn}^{\pm} r' \mathrm{cotan}\chi_B + m)\varphi'} F_{T,D}(r', \varphi')\, \mathrm{d}\varphi' = - \begin{pmatrix} \sin\chi_B \\ \cos\chi_B \end{pmatrix} \cdot \frac{\sin\chi_B}{2r'} \times c \int_{-1}^{1} \Delta P(z_1^*) \mathrm{e}^{\mathbf{i} A_{mn}(r') z_1^*} \mathrm{d}z_1^* \quad (1.29)$$

In equation (1.29), the unsteady lift ΔP corresponds to the airfoil response and can be retrieved analytically or from numerical simulations. Within the scope of analytical modelling, this term will be obtained using the Amiet-Schwarzschild approach.

Finally, once load terms are determined, the far-field noise can be computed from equation (1.18). In the case of infinite duct propagation, the directivity makes no sense because the sources are shrouded. More commonly, the upstream and downstream radiated acoustic powers are computed. They are given by Goldstein [31] as:

$$\boxed{\mathcal{P}_{sB}^{\pm} = \frac{B^2\beta^4}{2\rho_0 c_0} \left(\frac{sB\Omega}{c_0}\right) \sum_{m=-\infty}^{+\infty} \sum_{n=1}^{+\infty} \frac{|mD_{mn}^{\pm} - \gamma_{mn}^{\pm} T_{mn}^{\pm}|^2}{\Gamma_{mn} k_{mn} \left[\frac{sB\Omega}{c_0} \pm M k_{mn}\right]^2}} \quad (1.30)$$

Previous sum on p was replaced by a sum on the azimuthal order which is given by the relation $m = sB \pm p$. This sum is made only on cut-on modes which have a non-zero radiated power. In other words, only modes verifying the following cut-off condition contribute to the power transmission:

$$\beta^2 K_{mn}^2 < \left(\frac{sB\Omega}{c_0}\right)^2 \quad (1.31)$$

The case presented in this section is formulated for rotor noise but can be written similarly for stator noise.

1.4.5 Tyler & Sofrin's rule

In the previous section, we introduced the acoustic power due to the interaction of disturbances with the rotor. We propose now to apply the previous methodology for rotor-stator interaction. In fact, the presence of a stator with V vanes downstream of the rotor will impose a new modal structure. In the case of wake-interaction noise, sources are located on the stator. In the case of potential interaction, sources are located on the rotor. However, in both cases, the $2\pi/B$ periodicity of the rotor and the $2\pi/V$ periodicity of the stator restrict the azimuthal orders that can be generated. This is known as the Tyler & Sofrin's rule [35] written as:

$$m = sB - pV \qquad s \in \mathbb{N}, \quad p \in \mathbb{Z} \quad (1.32)$$

In the case of the rotor alone operating in arbitrary distortion, the azimuthal order is only constrained by multiples of the number of blades B plus an integer meaning that all mode orders can be generated *a priori*. Here, the presence of the stator constrains this integer allowing only multiples of the number of vanes. This rule allows to carefully choose the number of blades and vanes in order to avoid generating low mode orders that are cut-on and that are very efficient in the noise transmission.

An illustration of the rule for two rotor-stator configurations is shown in Figure 1.15 and Table 4.6.

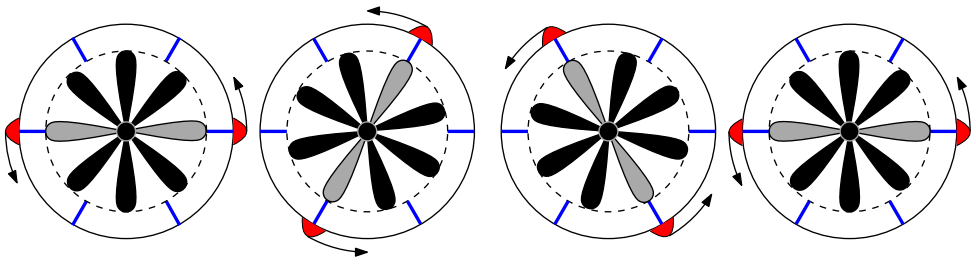

(a) $B = 8$ and $V = 6$

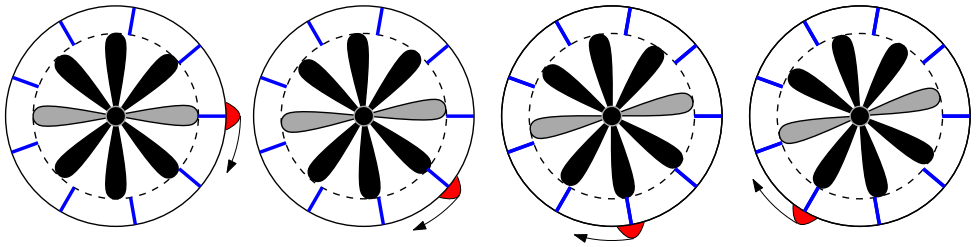

(b) $B = 8$ and $V = 9$

Figure 1.15: Illustration scheme of the Tyler & Sofrin rule [35]. Stator vanes are highlighted in blue and rotor blades in black (with two reference blades in grey). The coincidence of a stator vane and a rotor blade is highlighted in red. The rotor rotates in the counter-clockwise direction.

This illustrates how the patterns are generated and how they rotate. For a given number of vanes and blades a m-lobe pattern is observed if we highlight (in red) when stator vanes are coincident with rotor blades. Thus, a sense of rotation appears for consecutive positions of the rotor. For the case 1.15a, a 2-lobe pattern appears with a counter-clockwise motion. In this case, each time a vane coincides with a rotor blade, the vane in the opposite side will also be coincident. The second example 1.15b features a 1-lobe pattern with a clockwise spinning motion. These identified (dominant) modes can then be easily retrieved with the rule as shown in Table 4.6.

p	-4	-3	-2	-1	0	1	2	3	4	
m	32	26	20	14	8	**2**	-4	-10	-16	Figure 1.15a
m	44	35	26	17	8	**-1**	-10	-19	-28	Figure 1.15b

Table 1.1: Tyler & Sofrin's rule for the first BPF ($s = 1$) and for the case presented in Figure 1.15

The spinning phase speed Ω_s of each mode $sB - pV$ is then defined with the rule as:

$$\Omega_s = \frac{sB\Omega}{sB - pV} \tag{1.33}$$

The fundamental mode ($m = 0$) is not always generated if the number of vanes and blades is chosen carefully. This is important because it has been shown that the radial order $n = 0$, the mode $m = 0$ will always propagate. It must be noted that the rule is valid in the case of equally spaced sources of equal intensity, thus only for a homogeneous rotor and stator.

1.4.5.1 Sources located on the stator

For the case of sources located on the stator as for the wake-interaction noise, the previous power expression given by Goldstein reads:

$$\mathcal{P}^{\pm}_{sB} = \frac{V^2\beta^4}{2\rho_0 c_0}\left(\frac{sB\Omega}{c_0}\right)\sum_{m=-\infty}^{+\infty}\sum_{n=1}^{+\infty}\frac{|mD^{\pm(sB)}_{mn} - \gamma^{\pm}_{mn}T^{\pm(sB)}_{mn}|^2}{\Gamma_{mn}k_{mn}\left[\frac{sB\Omega}{c_0} \pm Mk_{mn}\right]^2} \tag{1.34}$$

In the case of a homogeneous stator, each stator vane reacts identically to each rotor wake. However, if the stator is heterogeneous, some of the vanes will respond differently to the impinging wakes due to the geometrical difference. It is then necessary to separate each vane response. This can be done by using an interference sum on the vane index k:

$$\mathcal{P}^{\pm}_{sB} = \frac{V\beta^4}{2\rho_0 c_0}\left(\frac{sB\Omega}{c_0}\right)\sum_{m=-\infty}^{+\infty}\sum_{n=1}^{+\infty}\sum_{k=0}^{V-1}\mathrm{e}^{\mathrm{i}k(sB-m)\frac{2\pi}{V}}\frac{|mD^{\pm(sB)}_{mn,k} - \gamma^{\pm}_{mn}T^{\pm(sB)}_{mn,k}|^2}{\Gamma_{mn}k_{mn}\left[\frac{sB\Omega}{c_0} \pm Mk_{mn}\right]^2} \tag{1.35}$$

When the stator is homogeneous, the interference sum simplifies:

$$\sum_{k=0}^{V-1}\mathrm{e}^{\mathrm{i}k(sB-m)\frac{2\pi}{V}} = V \tag{1.36}$$

$T^{\pm}_{mn,k}$ becomes $T^{\pm}_{mn}$, $D^{\pm}_{mn,k}$ becomes $D^{\pm}_{mn}$ and the previous expression is recovered.

1.4.5.2 Sources located on the rotor

In the case of potential interaction noise, sources are located on the rotor because the blades respond to the downstream potential field generated by the stator vanes. In the case of an inflow distortion, sources are also localized on the rotor from the impingement of upstream velocity disturbances. In the case of a heterogeneous stator, the sources (rotor) remain homogeneous and the acoustic power is written:

$$\mathcal{P}_{sB}^{\pm} = \frac{B^2\beta^4}{2\rho c_0}\left(\frac{sB\Omega}{c_0}\right)\sum_{m=-\infty}^{+\infty}\sum_{n=1}^{+\infty}\frac{|mD_{mn}^{\pm(p)} - \gamma_{mn}^{\pm}T_{mn}^{\pm(p)}|^2}{\Gamma_{mn}k_{mn}\left[\frac{sB\Omega}{c_0} \pm Mk_{mn}\right]^2} \tag{1.37}$$

The heterogeneity has been introduced by considering loading harmonics of orders $p\Omega$ and not only $pV\Omega$ (a consequence of the stator cascade irregularity). For the case of a homogeneous stator, these terms become $T_{mn}^{\pm(p)} \rightarrow T_{mn}^{\pm(pV)}$.

1.4.6 Airfoil response models

In the previous section, the acoustic analogy was introduced. The only remaining terms to be calculated are the blade/vane loading terms. In this section, the analytical modelling of unsteady loads is thus presented. Airfoil response models relate an upstream or downstream disturbance to the unsteady lift. Two main model categories exist: isolated airfoil response and cascade response models.

The isolated airfoil response considers a single blade or vane and does not account for the effect of adjacent blades/vanes. The first model considering an incompressible response was proposed by Sears [41] in 1941. In 1975, Amiet [42] proposed a compressible airfoil response, further extended for finite chord effects in 1976 [43]. These models were then also used to deal with the case of trailing-edge noise [21]. More recently, Roger et Moreau [22] and Moreau et Roger [23] proposed an extension of the model for trailing-edge noise by performing a back-scattering iteration. This extension allowed integrating finite chord effects relevant at low frequencies.

On the other hand, cascade models account for the adjacent vanes and thus the airfoil response is modified by the associated confinement. Different models were developed with increasing complexity, see Ventres et al. [44], Hanson et al. [45], Glegg [46], Posson et al. [47, 48] and more recently with a novel approach, based on a mode-matching technique, see Bouley et al. [49]. Note that some of these models can directly provide the radiated acoustic pressure as opposed to isolated airfoil responses which must be coupled to an acoustic analogy.

Significant differences between isolated and cascade models are expected when the spacing between adjacent blades or vanes is low and when the stagger angle is small, see Figure 1.16. In fact, because the equivalent sources are dipoles perpendicular to the chord, the interaction with the adjacent blades is stronger when the overlap is higher and when the inter-blade spacing is small. Otherwise, isolated-airfoil response models give a good approximation of the unsteady lift. They are used for their simplicity and because they can be more easily integrated in the extension of the homogeneous theory to account for heterogeneous stators by using Goldstein's analogy.

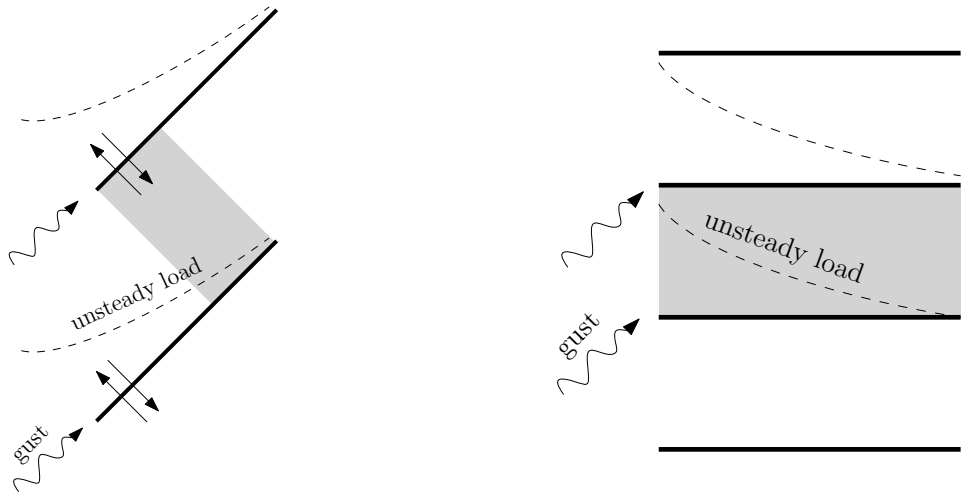

(a) Weak cascade effect.

(b) Strong cascade effect.

Figure 1.16: Sketch of weak and strong cascade effects.

1.4.6.1 Leading-edge impingement

In the framework of this study, aerodynamic loads on the blades and/or vanes will be calculated with Amiet's theory [42, 43]. The method considers an isolated blade or vane. It has been widely used and is in good agreement with experimental and numerical simulations of thin airfoils with small camber [23].

The theory describes the response of the airfoil to an incident gust (velocity disturbance), see Figure 1.17. The airfoil is assimilated to a flat plate with zero thickness and incidence. These geometry simplifications may seem abusive. However, the airfoil geometry mainly influences the mean loading and thus the steady lift and drag. In the framework of unsteady aerodynamics, the flat plate assumption is a good approximation when dealing with thin and weakly cambered airfoils. As a counterexample, highly cambered turbine blades are a case where the flat plate assumption would not be relevant.

The considered velocity perturbation (or gust) is the upwash, the normal velocity component with respect to the airfoil. It is defined as:

$$u = u_a \exp\left[\mathbf{i}(K_1 z_1 + K_2 z_2 - \omega t)\right] \tag{1.38}$$

where ω is the angular frequency, $K_{1,2}$ the chordwise and spanwise hydrodynamic wavenumbers respectively and u_a is the gust amplitude. The resulting unsteady lift fluctuations, responsible for noise radiation, behave like equivalent dipoles. The aerodynamic problem is recast in order to solve it as an equivalent wave scattering problem keeping in mind that the response of the airfoil to vortical disturbances is a potential field. The velocity potential ϕ satisfies the convected Helmholtz equation:

$$(1 - M^2)\frac{\partial^2 \phi}{\partial z_1^2} + \frac{\partial^2 \phi}{\partial z_2^2} + \frac{\partial^2 \phi}{\partial z_3^2} - 2\mathbf{i}kM\frac{\partial \phi}{\partial z_1} + k^2\phi = 0 \tag{1.39}$$

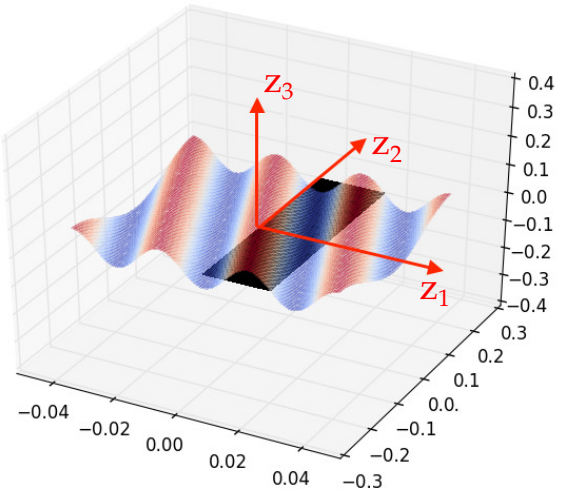

Figure 1.17: Two-dimensional gust convected past an airfoil of infinite span

This equation has to be solved with three boundary conditions:

$$\begin{cases} \phi = 0 & \text{for} \quad z_1 < 0\,, \quad z_3 = 0 \\ \dfrac{\partial \phi}{\partial z_3}(z_1, 0) = -u & \text{for} \quad 0 < z_1 < c\,, \quad z_3 = 0 \\ \Delta P = 0 & \text{for} \quad z_1 \geq c\,, \quad z_3 = 0 \end{cases} \tag{1.40}$$

The first boundary condition cancels the velocity potential upstream of the airfoil. The second one corresponds to the rigid-wall boundary condition on the airfoil where the normal velocity goes to zero. The third one is the Kutta condition which forces the pressure jump to zero at the trailing edge.

A direct solution of the potential compliant with all boundary conditions is not possible. Instead, the resolution relies on the so-called Amiet-Schwarzschild technique. It consists in an iterative method where corrections are consecutively applied by considering semi-infinite flat plates extending upstream or downstream. Details are found in the references and only the key steps are outlined here. A potential which cancels the incident upwash over the entire plane by virtue of the rigidity condition is first determined as an initial solution.

Then the first iteration consists in considering a semi-infinite airfoil extending downstream of the leading edge and cancelling the potential upstream from it. To introduce the finite-chord effect, a second boundary-value problem is then formulated from the trailing edge. This second iteration applies the Kutta condition defined as a zero pressure jump at the trailing edge and along the wake.

We now present in more details the classical Amiet's result for the leading edge. The first iteration consists in solving a first boundary value problem where the airfoil is artificially extended downstream. It is a sufficient approximation only for high frequency applications since the chord is infinite and the equivalent source distrbution is not compact.

In order to include finite-chord effects, a second iteration is performed. The resolution can be summarized as follows:

1. State a boundary value problem in order to apply the rigidity condition and cancel the potential upstream of the airfoil;
2. Convert the potential into pressure;
3. Define a new boundary value problem on pressure and cancel the pressure jump downstream of the trailing edge.

In this section, only the final results will be presented. For more details in this theory, please refer to [42, 43]. After a change of variables, the Helmholtz equation is written in a canonical form. The system of interest for the first iteration is:

$$\begin{cases} \nabla^2\Psi + \kappa^2\Psi = 0 & \\ \dfrac{\partial\Psi}{\partial z_3^*} + u = 0 & \text{for} \quad z_1^* > -1 \\ \Psi = 0 & \text{for} \quad z_1^* \leq -1 \end{cases} \tag{1.41}$$

where

$$\mu = \frac{K_1^* M}{\beta^2}, \qquad z_{1/3}^* = \frac{2z_{1/3}}{c} - 1, \qquad z_2^* = \frac{2z_2\beta}{c}, \qquad \kappa = \mu\sqrt{1 - \frac{1}{\Theta^2}}, \qquad K_{1/2}^* = \frac{K_{1/2}c}{2}$$

and $\Theta = MK_1^*/(\beta K_2^*)$ is Graham's parameter defining whether a gust is sub-critical ($\Theta \leq 1$) or super-critical ($\Theta > 1$). Super-critical gusts are often only considered because their contribution to the far-field radiated noise is higher.

Schwarzschild solution. *Given the following boundary value problem:*

$$\begin{cases} \nabla^2\Psi + \mu^2\Psi = 0 & \\ \dfrac{\partial\Psi}{\partial y}(x,0) = 0 & \textit{for} \quad x < 0 \\ \Psi(x,0) = f(x) & \textit{for} \quad x \geq 0 \end{cases} \tag{1.42}$$

The Schwarzschild problem states that the solution $\Psi(x,0)$ is given by :

$$\Psi(x,0) = \frac{1}{\pi}\int_0^\infty L(x,\xi,0)f(\xi)d\xi \tag{1.43}$$

with

$$L(x,\xi,0) = \sqrt{\frac{-x}{\xi}}\frac{e^{-i\mu(\xi-x)}}{\xi - x} \tag{1.44}$$

The potential solution of the previous system can then be related to the pressure and thus the unsteady lift. The final result is written as

$$\Delta P^{(1)} = 2P^{(1)} = \frac{-2\rho u_a U e^{\mathbf{i}\pi/4}}{\sqrt{\pi(K_1^* + \beta^2\kappa)(1+z_1^*)}} \exp\left[-\left\{(\kappa + \mathbf{i}\mu M)(1+z_1^*) + \mathbf{i}K_2^* z_2^*\right\}\right] \quad (1.45)$$

This result shows that the unsteady lift is singular at the leading edge and decreases when going away from it. In this first iteration, an infinite chord is considered so that the source is not compact. In order to include the finite-chord effect, a second iteration is performed. In this iteration, a semi-infinite airfoil is then considered starting from the trailing edge and being extended upstream. The following system is then solved:

$$\begin{cases} \nabla^2 P^{(2)} + \kappa^2 P^{(2)} = 0 & \\ \dfrac{\partial P^{(2)}}{\partial z_3^*} = 0 & \text{for} \quad z_1^* < 1 \\ P^{(2)} = -P^{(1)} & \text{for} \quad z_1^* \geq 1 \end{cases} \quad (1.46)$$

The final integral which appears in the resolution has no exact analytical solution. For that reason, a relevant approximation is performed in order to derive a closed-form solution. This approximation is well detailed in [22, 50]. By considering that the unsteady pressure fields on the suction and pressure sides have opposite phases, the integral yields:

$$\Delta P^{(2)} = 2P^{(2)} = \frac{2\rho u_a U e^{\mathbf{i}\pi/4}}{\sqrt{2\pi(K_1^* + \beta^2\kappa)}} \exp\left[-\left\{(\kappa + \mathbf{i}\mu M)(1+z_1^*) + \mathbf{i}K_2^* z_2^*\right\}\right] \times \left\{1 - (1-\mathbf{i})E[2\kappa(1-z_1^*)]\right\} \quad (1.47)$$

where $E[x]$ is the Fresnel function given by:

$$E[x] = \int_0^x \frac{\mathrm{e}^{\mathbf{i}t}}{\sqrt{2\pi t}} \mathrm{d}t \quad (1.48)$$

Finally, the corrected pressure jump (unsteady lift) is provided by the sum of the previous two contributions.

$$\Delta P = \Delta P^{(1)} + \Delta P^{(2)} \quad (1.49)$$

which leads for super-critical gusts to:

$$\Delta P = \frac{2\rho u_a U e^{\mathbf{i}\pi/4}}{\sqrt{2\pi(K_1^* + \beta^2\kappa)}} \exp\left[-\left\{(\kappa + \mathbf{i}\mu M)(1+z_1^*) + \mathbf{i}K_2^* z_2^*\right\}\right] \times \left\{1 - \sqrt{\frac{2}{1+z_1^*}} - (1-\mathbf{i})E\left[2\kappa(1-z_1^*)\right]\right\} \quad (1.50)$$

This summation ensures that the pressure jump at the trailing edge is zero as required

by the Kutta condition. In the case of sub-critical gusts κ must be replaced by $\mathbf{i}\kappa' = \mathbf{i}\mu\sqrt{1-1/\Theta^2}$ and the term $(1-\mathbf{i})E$ is replaced by the error function $\Phi\left[\sqrt{2\kappa'(1-z_1^*)}\right]$. Φ is the complex-valued error function.

As an iterative process, Amiet's theory increases in accuracy with the number of iterations considered. However, the practical application of this process shows that only two iterations are required for a good level of accuracy [43].

In Figure 1.18, the chordwise unsteady lift is plotted for several values of Graham's parameter. Generally, two characteristics are observed: the pressure jump is singular at the leading edge (with the integrable inverse square-root singularity) and is cancelled at the trailing edge (Kutta condition). Loads are essentially concentrated at the leading edge and decrease far from it. This is an expected result since the impingement location of the gust is at the leading edge. For sub-critical gusts ($\Theta \leq 1$), the pressure-jump is monotonically decreasing much faster being almost null at the mid-chord, thus not highly contributing to the far-field radiation. For super-critical gusts ($\Theta > 1$), the unsteady load is higher and extends over the whole chord.

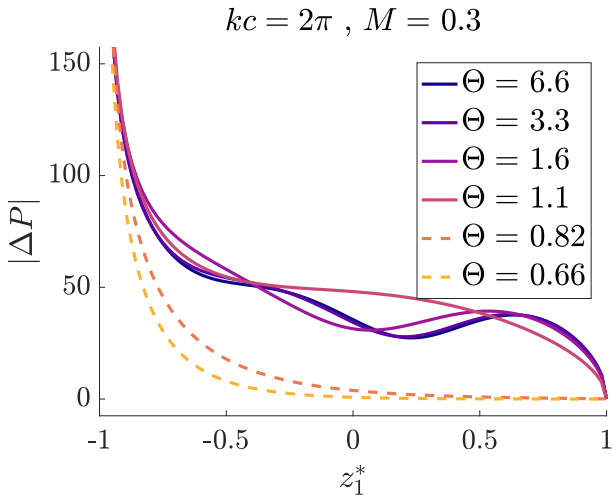

Figure 1.18: Pressure jump amplitude given by Amiet's theory for leading-edge gust impingement

To sum-up, this kind of airfoil response can be used for interaction of rotor wakes with the stator vanes or for the impingement of an upstream distortion on the rotor blades, both of them constituting a leading-edge interaction problem.

1.4.6.2 Trailing-edge interaction

When dealing with trailing-edge interactions, the previous modelling is not adapted. In this section, the focus is given to the modelling of the trailing-edge noise from the downstream potential field. We propose here to review the reversed Sears' model formulated by Roger et al. [17] and applied then for complex wavenumbers by Conte et al. [51]. This approach is based on the classical Amiet's approach where basically the problem is set first at the trailing edge for a semi-infinite plate extending upstream. The problem

is solved on the potential and finally related to the pressure to achieve the chordwise pressure distribution. The input gust is given by

$$u = u_a \exp\left[\mathbf{i}(K_{\text{pot}} z_1 + K_2 z_2 - \omega t)\right] \tag{1.51}$$

where $K_{\text{pot}} = K_1 + \mathbf{i}k_i$ is complex, with the imaginary part corresponding to potential damping upstream of the stator vanes. This upwash is then introduced in a reversed Amiet problem. After a change of variables to restore a canonical Helmholtz equation, the following boundary value problem can be formulated

$$\begin{cases} \nabla^2 \Psi + \mu^2 \Psi = 0 & \\ \dfrac{\partial \Psi}{\partial \bar{z}_2} + u = 0 & \text{for} \quad \bar{z}_1 < 0 \\ \Psi = 0 & \text{for} \quad \bar{z}_1 \geq 0 \end{cases} \tag{1.52}$$

where $\bar{z}_1 = z_1 - c$. A first potential solution is calculated from the Helmholtz equation with the first rigidity condition applied on an infinite airfoil artificially extended from $-\infty$ to $+\infty$ in the chordwise direction. Then, a new boundary value problem is defined where downstream the trailing edge the potential is chosen in order to cancel the previous potential. The main differences with the classical Amiet's approach are :

- The frame of reference is placed at the trailing edge first;
- The upwash wavenumber is complex;
- No Kutta condition is imposed at the trailing edge;
- The first iteration is performed in direction opposite to the flow.

In a simplified form, the potential solution writes:

$$\boxed{\Psi(\bar{z}_1, 0) = A e^{B\bar{z}_1} \Phi\left[\sqrt{(C\bar{z}_1}\right]} \tag{1.53}$$

with A, B and C being constants which can be complex-valued. This final potential is then related to the pressure by

$$P = -\rho \frac{D\phi}{Dt} \tag{1.54}$$

By considering that oscillations are in phase opposition on both faces at the trailing-edge, the pressure jump is twice the pressure, and finally the pressure jump distribution on the airfoil is given in a simplified form as

$$\Delta P = \mathcal{A}\left\{\mathcal{B}\mathrm{e}^{\mathcal{C}\bar{z}_1}\Phi\left[\sqrt{(\mathcal{D}\bar{z}_1}\right] + \frac{\mathcal{E}\mathrm{e}^{\mathbf{i}\mathcal{F}\bar{z}_1}}{\sqrt{\mathcal{G}\bar{z}_1}}\right\}\mathrm{e}^{\mathbf{i}\omega t} \tag{1.55}$$

where $\mathcal{A}$ to $\mathcal{G}$ are constants depending on the parameters of the problem. One can see that this result is singular at the trailing edge and decreases upstream. The typical pressure jump is plotted in Figure 1.19. Parameters of the LP3 cooling fan were chosen for the

test. Since the Kutta condition is not applied, the pressure jump goes to infinity at the trailing edge. Results also show that loads concentrate in the last quarter of the airfoil as expected for this kind of interaction.

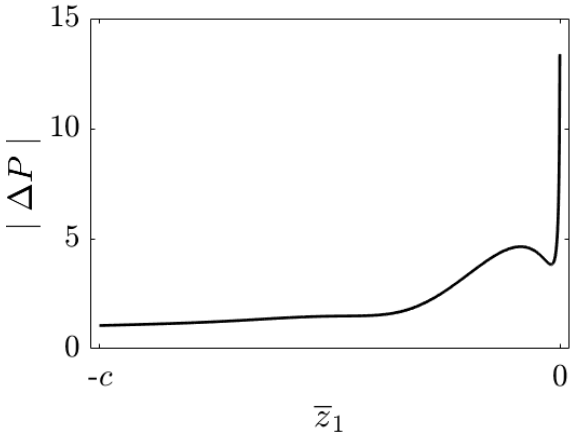

Figure 1.19: Typical pressure jump obtained with the Reversed Sears model.

Another model can be also found in Parry's Ph.D dissertation [16]. This model accounts for the Kutta condition at the trailing edge. In this case, the solved problem is the following:

$$\begin{cases} \nabla^2\Psi + \mu^2\Psi = 0 & \\ \dfrac{\partial\Psi}{\partial\bar{z}_2} + u = 0 & \text{for} \quad \bar{z}_1 < 0 \\ \Delta p = 0 & \text{for} \quad \bar{z}_1 \geq 0 \end{cases} \tag{1.56}$$

The problem is first formulated on the potential and a solution which fullfills the rigidity boundary condition is found. Then the potential is related to the pressure and the Kutta condition is applied. Parry solves this problem using the Wiener-Hopf technique. The final solution writes in a simplified form:

$$\Delta P = \mathcal{H}\left\{\mathcal{I}\mathrm{e}^{\mathcal{J}\bar{z}_1}\Phi\left[\sqrt{(\mathcal{K}\bar{z}_1}\right]\right\}\mathrm{e}^{\mathrm{i}\omega t} \tag{1.57}$$

where $\mathcal{I}$ to $\mathcal{K}$ are constants depending on the parameters of the problem. Compared with the reversed Sears problem, the pressure jump is no longer singular at the trailing edge by virtue of the Kutta condition. This model will be investigated from another standpoint. An alternative solving procedure will be investigated by using the formalism of Amiet-Shcwarzschild introduced before and is presented in Chapter 4.

1.4.7 Aerodynamic excitation models

In the previous section, the airfoil response models for leading edge and trailing edge interactions were presented. In those models, the remaining unknown is the velocity

perturbation. In this section, the objective is to introduce simple modelling for both wake and potential fields, the expected main noise sources of rotor-stator interaction.

1.4.7.1 Wake modelling

A wake is a velocity deficit observed downstream of an object immersed in a viscous flow due to the no-slip condition. To approximate the wake velocity profile, several analytical models are available. A simplified modelling can be achieved with a series of Gaussian pulses defined as

$$w\left(t\right) = \sum_{n=-\infty}^{+\infty} w_a \, \exp\left\{-\xi \left(t - nT\right)^2 / \tau^2\right\} \tag{1.58}$$

with $T = 2\pi/B\Omega$ the wake passing period, $\xi = \ln(2)$, τ the half-wake passage time, b the half-width and r the radius. An estimate of the wake parameters can be found in the work of Philbrick and Topol [52]. The estimate is made from some aerodynamic and geometrical parameters of a given configuration. In Figure 1.20 the wake velocity deficit is shown as a function of time for a case with $B = 14$ blades. A Gaussian profile is seen to be repeated at each blade-passing period.

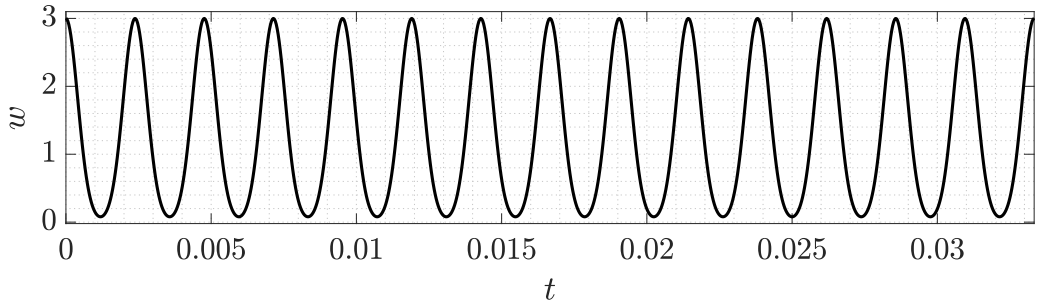

Figure 1.20: Wake velocity profile function of time $t \in [0\,,\, BT]$

Wakes are periodic and can then be expressed with Fourier series.

$$w(t) = \sum_{s=-\infty}^{+\infty} w_s \exp\left\{-\mathbf{i}\omega st\right\}\,, \qquad \text{with} \qquad w_s = \frac{1}{T}\int_0^T w(t)\, \exp\left\{\mathbf{i}\omega st\right\} \mathrm{d}t \tag{1.59}$$

where $T = 2\pi/B\Omega$. After some derivation, the Fourier coefficients can be expressed as:

$$w_s = \frac{w_a B\Omega}{2\pi} \int_{-\infty}^{+\infty} \exp\left\{-\xi\left(t/\tau\right)\right\} \cos\left(sB\Omega t\right)\, \mathrm{d}t \tag{1.60}$$

According to Gradshteyn and Ryzhik [53], the integral becomes:

$$w_s = \frac{w_a B\Omega}{2\pi} \sqrt{\frac{\pi}{\xi}} \exp\left\{-\left(sB\Omega\tau\right)^2 / (4\xi)^2\right\} \tag{1.61}$$

With the previous expression, we can see that only orders multiple of the number of blades B will contribute to the sum. The previous expression can also be expressed in space coordinates by introducing an axial convection speed U and by expressing t as a function of φ ($t = \varphi/\Omega$). The final wake expression in space coordinates is written:

$$w(x_1, \varphi) = \sum_{s=-\infty}^{+\infty} w_s \exp\left\{-\mathbf{i}\frac{sB\Omega}{U}x_1\right\} \exp\{-\mathbf{i}sB\varphi\} \tag{1.62}$$

This spatial representation is shown in Figure 1.21. A phase shift due to the rotation and axial convection is observed.

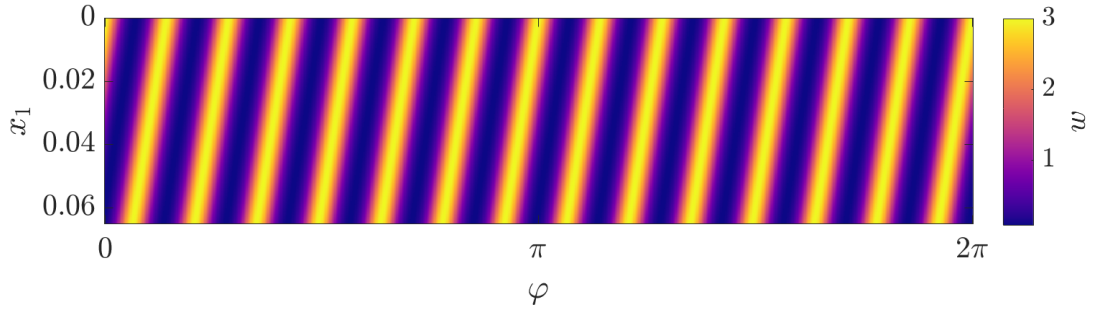

Figure 1.21: Modulus of the wake velocity w in spatial coordinates with $B = 14$.

This velocity variation w will induce an unsteady load on the stator vanes and thus a noise emission. For this noise mechanism, the problem can be stated as a classical Amiet's problem where wakes impinge on the leading edge of the stator vanes. The previous upwash form is injected in the expression presented in section 1.4.6. The disturbance is considered frozen (constant amplitude) and convected with the flow at the velocity U. This means that the upwash must be known only at the leading edge of the stator vane since the disturbance is considered frozen in the chordwise direction.

1.4.7.2 Potential modelling

The modelling of the potential field can be achieved with the classical potential theory [54, 55] or by extracting computational fluid dynamics (CFD) data. Potential inviscid theories for two-dimensional flows are presented here.

The potential flow solution is based on the following hypotheses:

- stationary flow: $\partial(\cdot)/\partial t = 0$
- incompressible flow: $\vec{\nabla} \cdot \vec{V} = 0$ ($\vec{V}$ is the velocity vector)
- irrotational flow: $\vec{\Omega} = \vec{\nabla} \times \vec{V} = 0$ ($\vec{\Omega}$ is the vorticity vector)

Under these hypotheses, a function ϕ exists such that

$$\vec{V} = \vec{\nabla}\phi \tag{1.63}$$

Combining equation (1.63) with the hypothesis of an incompressible flow, we obtain:

$$\nabla^2 \phi = 0 \tag{1.64}$$

The potential φ is therefore the solution of the Laplace equation (1.64). Since the Laplace equation is linear, the summation (superposition) of several solutions is also solution. Thus, the potential flow around a cylinder can be obtained by the superposition of several elementary flows such as a uniform flow and a doublet, see Figure 1.22.

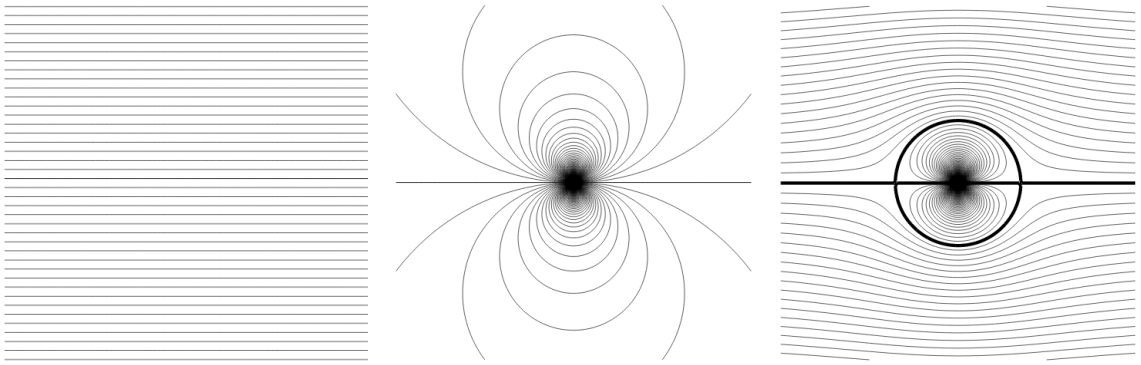

(a) Uniform flow (b) Doublet (= source + sink) (c) Uniform flow + doublet

Figure 1.22: Streamlines of elementary potential field solutions and their combination.

Finally, using a conformal mapping, the uniform flow around a cylinder can be transformed into the flow around an isolated airfoil. The mapping reads

$$T_k : z \longmapsto z + \frac{k^2}{z} \tag{1.65}$$

where $z = x_1 + \mathbf{i} r\varphi$ are the coordinates in the complex plane. Different conformal mappings T_k are investigated that transform the cylinder into a flat plate, an ellipse and a thin Joukowski airfoil. The parameter k of the conformal mapping and the origin of the complex plane are related to the vane chord, thickness and camber of the transformed geometry [16, 55]. As for the sum of elementary solutions, the potential flow over a cascade of elements can be built by performing a shifted sum of potential solutions, see Parry [16]. With this solution, it is then possible to extract the potential field upstream of the stator vanes and use it as the perturbation on the rotor blades. These disturbances are then put in the form of gusts which are the inputs of the airfoil response models.

Analytical modelling of ducted fan noise — Summary

In this section, the aeroacoustics theory has been introduced. First the duct modes have been presented along with the duct cut-off condition. The solutions of the homogeneous and then inhomogeneous convected wave equation achieved with Goldstein's analogy have been also introduced. Finally, the airfoil response models and the aerodynamic excitation modelling have been presented. The

chaining of the previous elements (acoustic analogy, airfoil response model and excitation model) is necessary in order to analytically predict the sound generated by a rotor-stator configuration. In this chain, some elements can also be provided by numerical simulations or experiments described in the next sections.

Points to remember and methodological choices retained for the study:

- Golstein's analogy for duct flows:
  - More general formulation to account for heterogeneous stators (by an interference sum)
- Isolated airfoil responses:
  - Amiet's response for leading-edge interaction
  - Parry's response for trailing-edge interaction
- Aerodynamic excitations:
  - Gaussian model for the wake modelling
  - Potential theory (with conformal mapping) for the potential field

1.5 Numerical simulation and modelling techniques

With the development of numerical approaches like CFD and CAA, the characterization of complex flows like those encountered in the industry is becoming possible. Compared to the analytical modelling, numerical simulation ensures a more realistic representation of the flow. However, because acoustic waves are generated by unsteady pressure fluctuations, highly accurate unsteady computations are necessary. This induces high computational costs and if the turbulence is to be partially solved by using methods like LES, the investigation of industrial configurations with high Mach and Reynolds numbers is often too costly.

1.5.1 Review of available numerical modelling techniques

The numerical flow simulation has been highly developed in the last decades. The increase in power of HPC[(a)] has allowed the simulation of increased geometrical complexity. Different methodologies can be used in order to model the flow behaviour. Most of them are based on the resolution of the Navier-Stokes equations, derived simultaneously in the early 1800s by G. G. Stokes in England and M. Navier in France. Within the past decade, a novel numerical method has emerged, the Lattice-Boltzmann method solving the Boltzmann equation on a lattice. To summarize the possible methods, a hierarchy of CFD methods [56] is shown in Figure 1.23.

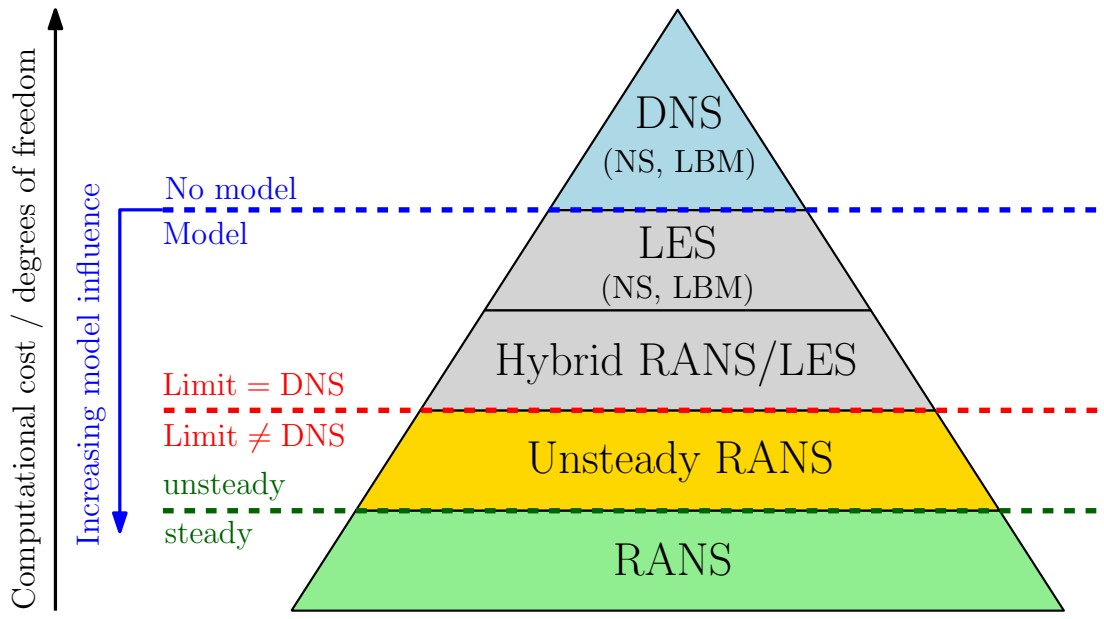

Figure 1.23: Hierarchy of Computational Fluids Dynamics (CFD) methods, Sagaut et al. [56]

At the bottom of the pyramid is the Reynolds-Averaged-Navier-Stokes (RANS) method. It is a stationary method based on the Reynolds- or Favre-decomposition for compressible

[(a)] High-Performance-Computers

flows and allows the calculation of the mean turbulent quantities. The resolution of these equations relies on the modelling of the symmetric Reynolds-stress tensor (6 additional unknowns). Different models of one, two or more additional equations are then used in order to model this tensor. One can mention Spalart-Allmaras one-equation model [57], the $k-\epsilon$ [58] or $k-\omega$ [59] two-equations models and the Reynolds-Stress-Model [60] (RSM) modelling each tensor component. RANS simulations are widely used in the industry because of their low-cost, long-term experience and good reliability for well known stationary flows. However, acoustic waves are generated by fluctuations. These methods being stationary, they have to be coupled with a Computational Aero-Acoustics (CAA) solver or analytical models in order to obtain an estimation of the noise levels.

On top of RANS is the Unsteady-RANS simulation (URANS). This method is based on the RANS theory but with a filtered time-dependent resolved mean flow. It allows having a mean turbulent flow evolving in time. It is particularly adapted for turbomachinery simulations where the flow is periodic in time at least over a revolution. URANS simulations have been extensively used in order to perform simulations of complex turbomachines. However, these methods only allow the extraction of the tonal noise generated by periodic interactions of the flow with the rotor/stator. If the broadband noise is to be calculated, unsteady simulations like Large-Eddy-Simulation (LES) or Direct Numerical Simulation (DNS) must be used.

The LES method is a turbulence modelling approach which solves large turbulent structures and models small ones. The method resolves turbulence up to a given wavenumber (scale), upon which a sub-grid scale (SGS) model is used to reach the Kolmogorov scale where the energy is dissipated into heat. In practice, the cell size of the mesh and the stress tensor intensity define the activation of the SGS model. Two well-known models widely used have been proposed by Smagorinsky [61] and Nicoud and Ducros [62].

The extension of the LES grid requirements from Chapman [63] by Choi and al. [64] gives an estimated grid size for a wall resolved-grid or a wall-modelled simulation on an airfoil, see Table 1.2.

Reynolds	N_{wm}	N_{wr}
10^6	3.63×10^7	5.23×10^7
10^7	8.20×10^8	7.76×10^9

Table 1.2: Approximate number of grid points required for the numerical simulation of the flow over an airfoil (with an aspect ratio of 4) without separation, using the wall-modelled and wall-resolving LES [64].

From the previous estimate, it can be deduced that wall-modelled simulations of a 360° geometry with several blades and vanes are very computationally demanding because of the mesh size required to simulate a 360° rotor-stator geometry.

The Direct Numerical Simulation (DNS) is at the top the pyramid. It is a numer-

ical method that solves all the turbulent scales up to the Kolmogorov scale and does not include any modeled turbulence. Only the numerical implementation (discretization schemes, boundary condition implementation or parallelization) can cause a reduction of the simulation accuracy. However, this method is only possible at reasonable costs for relatively low Reynolds number simulations and relatively simple geometries. It is not an option for the simulation of a full three-dimensional fan-OGV stage.

Finally, the Lattice-Boltzmann method uses a different modelling methodology based on the resolution of the Boltzmann equation on a lattice. The fundamentals of this method rely on the statistical physics by considering an ensemble of particules (mesoscopic level) described by a distribution function. A DNS type resolution can be used in order to solve low Reynolds-number cases. However, in turbulent cases with high Reynolds-number, a Very Large Eddy Simulation (VLES) likewise modelling is used. Bigger scales are solved and smaller scales modeled based on a transport model of the turbulent quantities.. At low Mach numbers, the numerical cost of this method is very interesting compared to the classical methods. In fact, this method uses a vary fast and local algorithm and all macroscopic quantities can be computed from a single equation. For this reason, the method is highly efficient for parallel computing. Moreau [65, 66] made a comparison of the CPU-times required for a simulation using the URANS and LBM methods, see Table 1.3.

Numerical method	Grid size (million cells)	Cores	Time/BPP[(b)] for 1 core
URANS	7.9	128	941 days
VLES LBM	72.2	480	12.8 days

Table 1.3: Comparison of solver performance for URANS (Turb'flow) method and LBM (PowerFLOW) for H380EC1 low-speed rotor-stator simulations [65].

The LBM simulation is about 74 times faster than the URANS simulation despite having larger grid size. In the case of aeracoustic simulations, it is necessary to reach spectrum convergence, which will be attained faster using LBM. Also, because a LBM solver is naturally transient, the broadband noise can also be directly extracted from the simulation. Finally, it allows accounting for the experimental setup domain which should allow more accurate comparisons between numerical and experimental results. For these reasons, the Lattice-Botzmann method was chosen in the present work and its theoretical background is introduced in the next section.

1.5.2 Lattice-Boltzmann Method (LBM) theory

The Lattice-Boltzmann method founding is different from the one of the Navier-Stokes equations. Navier-Stokes equations are based on the continuum mechanics and account for fluid particles at the macroscopic scale, see Figure 1.24. Each fluid particle incorporates

billiards of molecules ($\sim 10^{16}$ molecules in 1 mm^3 of air at 25°C). At this level, the macroscopic quantities (density, speed, pressure and temperature) are naturally defined. On the other hand, the Lattice-Boltzmann method relies on a mesoscopic approach, as exemplified in Figure 1.24.

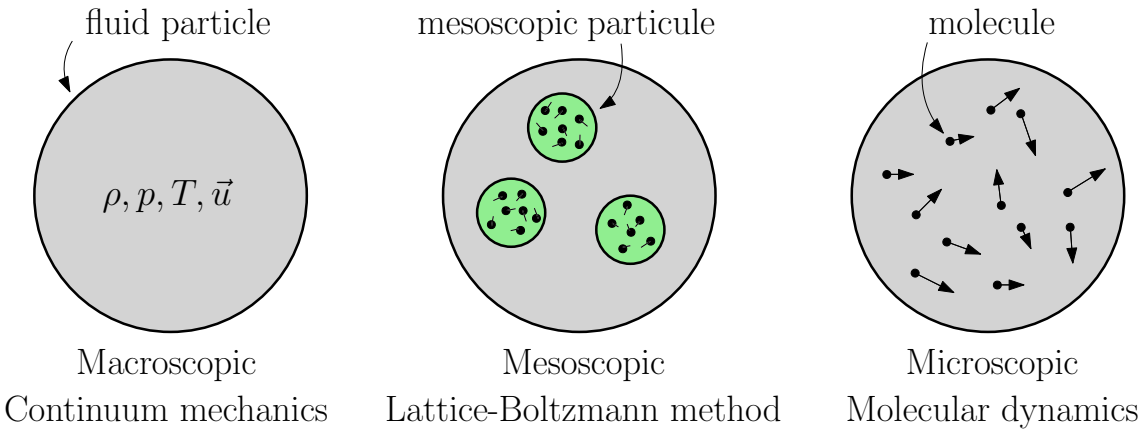

Figure 1.24: Difference between molecular dynamics, Boltzmann approach and continuum mechanics. Micro- meso- and macroscopic scales respectively.

The mesoscopic scale lies in-between the macro- and microscopic scale part of molecular dynamics. Tracking each molecule has been proven to be too costly for the investigation of complex cases except at very low density (rarefied gases). The Boltzmann approach considers an ensemble of particles described by a probability density (or distribution function) $f(\mathbf{x}, \mathbf{c}, t)$. This function represents the probability of having molecules with a velocity $\mathbf{c}$ at the position $\mathbf{x}$ and the time t. The evolution of the distribution function is given by the Boltzmann equation (1872) [67]:

$$\frac{\partial f}{\partial t} + c_i \frac{\partial f}{\partial x_i} + \frac{F_i}{m} \frac{\partial f}{\partial c_i} = \left(\frac{\partial f}{\partial t} \right)_{\text{coll}} \tag{1.66}$$

This equation is an advection-type equation. m is the molecular mass of the gas. It describes the advection of the quantity f at the velocities c_i under an external force F_i (e.g. gravity) with an additional source term called the collision operator. This operator represents the effect of particle collision. If zero, particles are solely advected under the external force without any change in direction. One of the major difficulties of the method is the modelling of the collision operator (right-hand side of equation 1.66). In 1953, Bhatnagarn, Gross and Krook [68] introduced a simplified model for the collision operator, the so-called the BGK collision model. The model reads:

$$\left(\frac{\partial f}{\partial t} \right)_{\text{coll}} = -\frac{1}{\tau} \left(f - f^{\text{eq}} \right) \tag{1.67}$$

where τ is a relaxation time related to the viscosity. In this model, particles are considered as pointwise rigid spheres that interact with each other. By considering elastic collisions,

this operator has conservative properties useful in the framework of fluid mechanics by conserving mass, momentum and energy. This model translates a relaxation process to an equilibrium state described by the Maxwell-Boltzmann velocity distribution:

$$f^{\mathrm{eq}}(\mathbf{x},\mathbf{c},t) = \rho\left(\frac{m}{2\pi k_B T}^{3/2}\right)\exp\left[-\frac{m}{2k_B T}\left(\mathbf{c}-\mathbf{u}\right)\right] \tag{1.68}$$

with k_B the Boltzmann constant and T the thermodynamic temperature. To obtain the main macroscopic quantities, f is integrated over the velocity space. The integration of the distribution function on all the possible velocities gives the density, momentum and kinetic energy as follows:

$$\rho = \int_{\mathbb{R}^3} f \,\mathrm{d}\mathbf{c} \tag{1.69}$$

$$\rho\mathbf{u} = \int_{\mathbb{R}^3} \mathbf{c} f \,\mathrm{d}\mathbf{c} \tag{1.70}$$

$$\rho e + \frac{1}{2}\rho\mathbf{u}^2 = \frac{1}{2}\int_{\mathbb{R}^3} |\mathbf{c}|^2 f \,\mathrm{d}\mathbf{c} \tag{1.71}$$

$$\tag{1.72}$$

In the case of isothermal conditions (as in low-Mach number flows), the density can be related to the pressure with the ideal gas law:

$$p = \rho R T \tag{1.73}$$

By neglecting external forces and by considering the BGK collision model, the Boltzmann equation becomes:

$$\frac{\partial f}{\partial t} + c_i\frac{\partial f}{\partial x_i} = -\frac{1}{\tau}\left(f - f^{\mathrm{eq}}\right) \tag{1.74}$$

It is known as the Boltzmann-BGK equation. Its integration allows to recover the Navier-Stokes equations by considering a second order expansion of the distribution function on the Knudsen number [69]. The Boltzmann-BGK equation can be re-written as an ordinary differential equation as:

$$\frac{\mathrm{d}f}{\mathrm{d}t} + \frac{1}{\tau}f = -\frac{1}{\tau}f^{\mathrm{eq}} \tag{1.75}$$

where

$$\frac{\mathrm{d}}{\mathrm{d}t} = \frac{\partial}{\partial t} + c_i\frac{\partial}{\partial x_i} \tag{1.76}$$

The integration over a timestep Δt leads to the final discrete form given by He and

Luo [70]:

$$f(x_i + c_i\Delta t, c_i, t + \Delta t) - f(x_i, c_i, t) = -\frac{1}{\tau}\left[f(x_i, c_i, t) - f^{\text{eq}}(x_i, c_i, t)\right] \tag{1.77}$$

In order to account for rotational elements, this discrete equation can be re-written by adding an additional source term including all additional forces, see Guo et al. [71]:

$$f(x_i + c_i\Delta t, c_i, t + \Delta t) - f(x_i, c_i, t) = \frac{1}{\tau}\left[f(x_i, c_i, t) - f^{\text{eq}}(x_i, c_i, t)\right] + F(x_i, t) \tag{1.78}$$

where F accounts for the centrifugal, Coriolis and Euler pseudo-forces:

$$F(x_i, t) = \underbrace{-\Omega(t) \times (\Omega(t) \times r(\mathbf{x}, t))}_{\text{centrifugal}} \underbrace{-2\Omega(t) \times u(\mathbf{x}, t)}_{\text{Coriolis}} \underbrace{-\frac{\mathrm{d}\Omega(t)}{\mathrm{d}t} \times r(\mathbf{x}, t)}_{\text{Euler}} \tag{1.79}$$

Finally, the fluid kinematic viscosity can be related to the relaxation time by:

$$\nu_0 = (\tau - 1/2)T \tag{1.80}$$

where T is the fluid temperature. For the case of turbulent flow, the turbulence modelling can be directly incorporated in the relaxation time in the collision operator. The notion of an eddy viscosity ν_t is introduced. A new expanded relaxation time is written as:

$$\tau_{\text{eff}} = \tau + \underbrace{C_\mu \frac{k^2/\epsilon}{T(1+\eta^2)^{1/2}}}_{\text{turbulent relaxation time}} \tag{1.81}$$

where $\nu_t = C_\mu k^2/\epsilon$ and where η is a local strain, vorticity and helicity parameter. The turbulent kinetic energy k and the turbulent dissipation rate ϵ are computed from the Renormalization Group (RNG) theory [72]. This new relaxation time can be seen as an equivalent sub-grid scale model in LES where turbulent scales below the grid resolution are modeled.

In terms of wall modelling, the method relies on a hybrid wall function that transitions from a turbulent wall function (logarithmic profile) to a viscous wall function (linear profile). The adverse pressure gradient is also accounted for.

The resolution of the Boltzmann-BGK equation over all possible velocities in $\mathbb{R}^3$ is out of reach in a numerical manner. For that reason, the velocity space has been reduced to a fixed discrete number of velocities. The chosen discrete velocities must verify a set of symmetry conditions in order to ensure an acceptable lattice isotropy to correctly recover macroscopic partial differential equations [73]. The equation is then written for a given velocity direction α:

$$f_\alpha(\mathbf{x}+\mathbf{c}_\alpha\Delta t,\mathbf{c}_\alpha,t+\Delta t)-f_\alpha(\mathbf{x},\mathbf{c}_\alpha,t)=-\frac{1}{\tau}\left[f_\alpha(\mathbf{x},\mathbf{c}_\alpha,t)-f_\alpha^{\mathrm{eq}}(\mathbf{x},\mathbf{c}_\alpha,t)\right] \tag{1.82}$$

The increase in the number of velocities improves the resolution accuracy but also increases the computational cost. A well-known discretization is the D3Q19. D3 stands for three-dimensional and Q19 for the number of considered possible velocity directions, see Figure 1.25. All possible velocities are summarized in Table 1.4.

α	1	2-7	8-19
$c_{\alpha,i}$	$(0,0,0)$	$(\pm1,0,0)$ $(0,\pm1,0)$ $(0,0,\pm1)$	$(\pm1,\pm1,0)$ $(0,\pm1,\pm1)$ $(\pm1,0,\pm1)$

Table 1.4: D3Q19 discrete velocities.

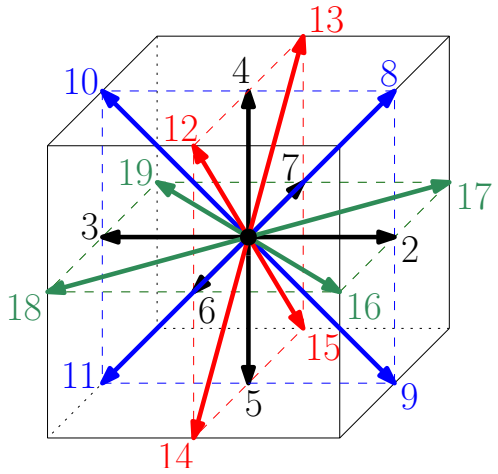

Figure 1.25: D3Q19 discrete velocity space.

For this discretization, the equilibrium function developed up to the second order in terms of Hermite polynomials yields the simplified f^{eq}:

$$f^{\mathrm{eq}}=\rho w_\alpha\left(1+\frac{\mathbf{u}\cdot\mathbf{c}_\alpha}{rT}+\frac{(\mathbf{u}\cdot\mathbf{c}_\alpha)^2}{2(rT)^2}+\frac{|\mathbf{u}|^2}{2rT}\right)+\mathcal{O}(\epsilon^3) \tag{1.83}$$

This discretization has been shown to be enough to recover the Navier-Stokes equations in low Mach-number isothermal conditions. In the case of high-speed flows, the number of discrete velocities has to be increased.

The Boltzmann equation is solved on a Cartesian grid, the lattice. This is imposed by the choice of the discrete velocities, in this case within a cubic cell. However, in order to obtain reasonable computational costs, only zones of interest of the domain are refined with smaller mesh cells. The work of Filippova et al. [74] presents a model for the grid refinement using the BGK model. This modelling is used by PowerFLOW and allows refining the mesh by factors of two, see Chen et al [75]. An example is shown in

Figure 1.26. This example illustrates a refinement done close to the regions of interest, in this case, the solid boundary of an airfoil. It must be noted that refining by a factor two increases considerably the mesh size because the same refinement must be done in the three directions of space.

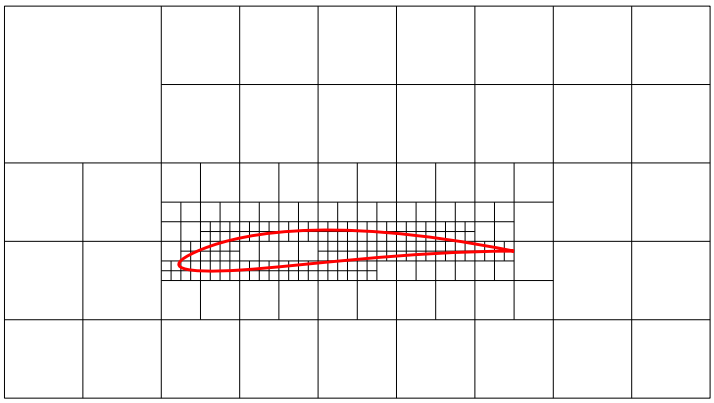

Figure 1.26: Example of grid refinement around a region of interest.

Note that in the present LBM formulation, time and space are coupled and the local resolution Δx imposes the timestep Δt. It means that the timestep is local and will be smaller for smaller voxels translating the fact that particles are moving at characteristic velocities c_α in the lattice. In order to obtain an increased resolution in time, the mesh has to be spatially refined. In practice, ensuring enough points per wavelength will also ensure enough points per period.

In PowerFLOW, the geometry is accounted for by using immersed boundary conditions. The use of this kind of boundary conditions allows considering complex geometries as the ones investigated in this work. A scheme of an immersed boundary is shown in Figure 1.27. The voxel (volume cell) intersection with the geometry (facets) gives what is called a surfel. At those surfels, special bounce back boundary conditions are applied in order to achieve a no-slip condition, see the work of Li et al. [76] for more details.

The acoustic properties of the LBM were extensively studied by Marié [77, 78] and Bres et al. [79]. In Figure 1.28 the spatial dissipation of a planar pulse is shown. One can see that the dissipation rate increases in frequency but remains low if the grid resolution is sufficient.

Because the method is compressible, of second order accuracy, with low dispersion (change in propagation speed) and dissipation (change in amplitude), it is an adequate method for the study of aeroacoustic problems. The Lattice-Boltzmann method then provides an accurate method for the simulation of low-speed fans allowing both accurate aerodynamic and acoustic analyses.

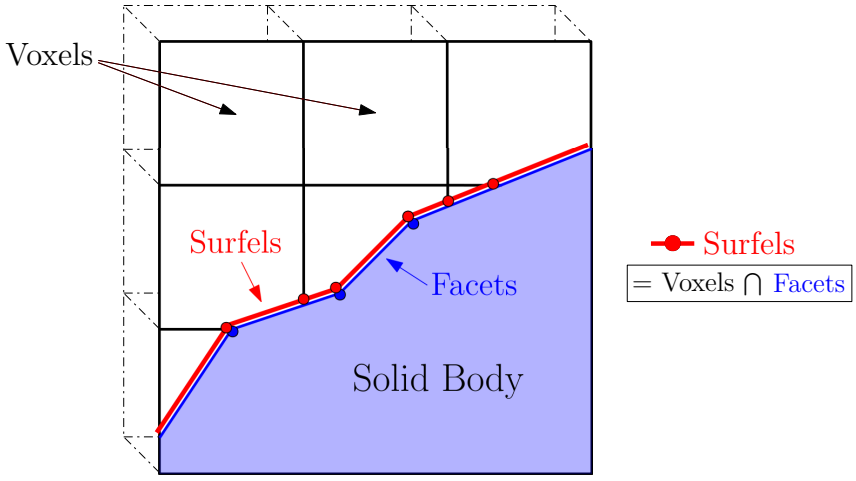

Figure 1.27: Intersection of the volume mesh (voxels) with the discrete geometry (facets) leading to the surfels.

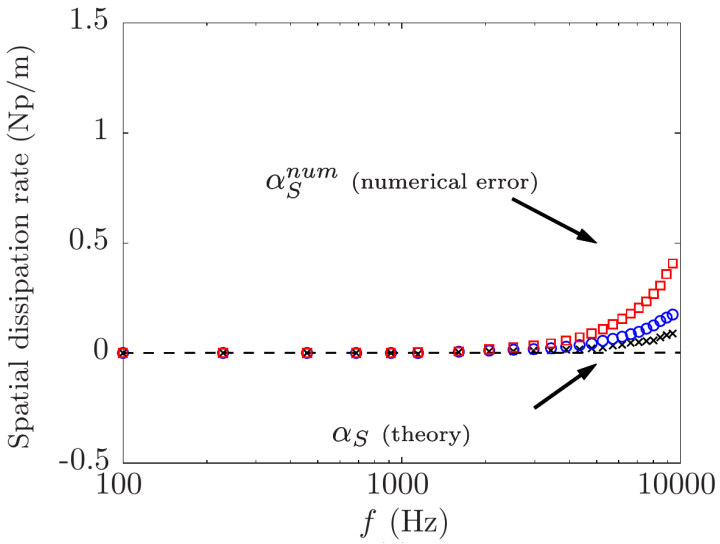

Figure 1.28: Spatial dissipation rate (in neper/m) of a planar pulse for different grid resolutions: $\Delta x = 0.001$ m in black, $\Delta x = 0.002$ m in blue and $\Delta x = 0.004$ m in red. Theory showed in black dashed line. VLES mode of the PowerFLOW solver used. Figure extracted from Bres et al. [79].

1.5.3 Simulation of low-speed fans

Several applications of rotating machines with the LBM method have been done in the recent years. Simulation cases go from low-speed fan configurations [26, 27, 28, 80, 81, 82, 83, 84] to axial turbofan configurations as the SDT from NASA [85, 86]. The method has demonstrated good agreement with experiments and has been able to simulate the main acoustic physical phenomena, either broadband or tonal.

The simulation of full experimental setups as the one studied by Sturm [83] is close to the simulations to be performed in this PhD for axial-flow turbomachines. The full experimental room is included in the computational domain for better comparison with experiments and for the study of inflow distortions, see Figure 1.29.

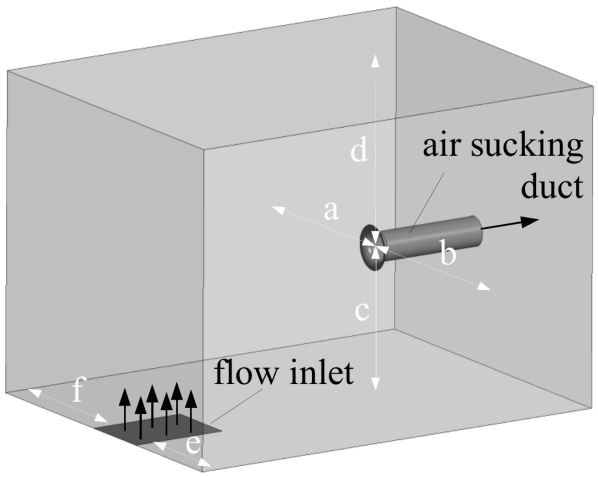

Figure 1.29: Numerical simulation domain from Sturm et al. [83].

The air is introduced in the room by an inlet placed in the floor upstream of the fan and ejected through an in-duct outlet condition. It has been shown that the simulation time had to be long enough in order to retrieve the correct flow development in the room. In other words, the long time simulated using LBM had allowed to capture an inflow distortion due to the flow establishment in the room. In terms of noise, contrary to previous simulations with shorter simulated times and performed by Zhu et al., the present simulations correctly reproduced the first BPF tones observed in experiments and attributed to inflow distortions, see Figure 1.30. This study highlighted the importance of taking into account the experimental environment and a long simulation time for better comparisons with the experiment.

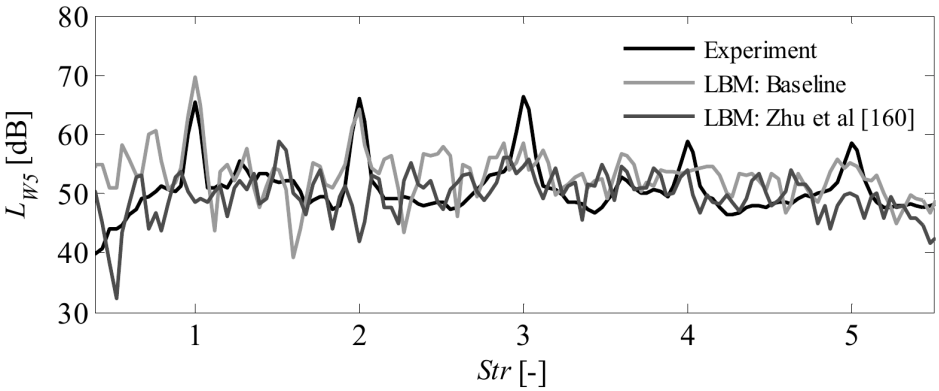

Figure 1.30: Power spectrum comparison of LBM simulations with experiments where $\mathrm{Str} = f/sB\Omega$. From Sturm et al. [83].

Another low-speed fan configuration was first investigated by Moreau & Sanjosé [27] and later by Lalliers-Daniels et al. [28]. The configuration is a 7-blades automotive cooling fan. In the simulation, the tip clearance is accounted for and results are compared to experiments. These studies highlighted the major contribution of the tip noise in this low-speed fan. In terms of spectra in Figure 1.31, sub-harmonic humps from the dimensionless

frequencies 10 and 14 and due to tip noise are seen. Because the fan has 7 blades, only tonal noise with harmonics multiple of 7 would be expected. These tones are mainly generated from an inflow distortion due to the rectangular shroud and from the rotor-wake interaction with the stator.

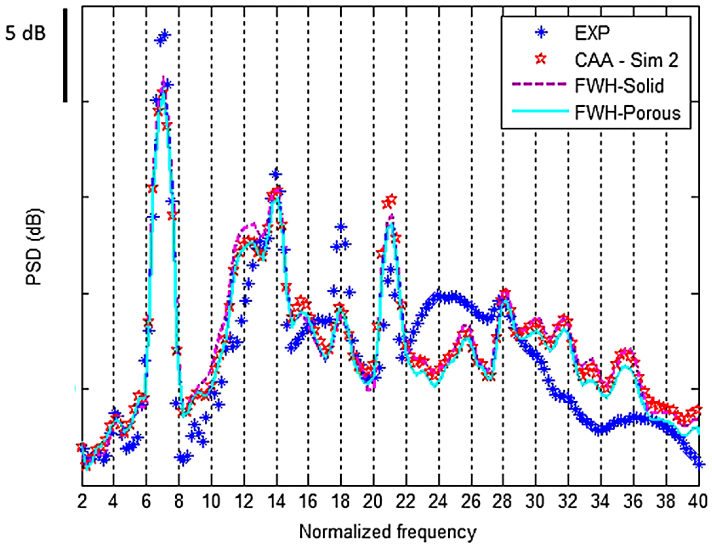

Figure 1.31: LBM acoustic spectrum from Lalliers-Daniels et al. [28].

Finally, the Active Noise Control Fan (ANCF) from NASA was investigated by Perot et al. [80] and by Sanjosé et al. [84]. This is one of the investigated configurations in this PhD not presented in the main text but provided as an additional material in Appendix B. From the simulations performed by Perot, modal decompositions were performed in order to retrieve the modal content at the different BPFs. As shown in Figure 1.32, the same dominant modes as in experiments are retrieved at the first three BPFs despite absolute levels are not reproduced. Because the stator is homogeneous, these tones are expected from the Tyler & Sofrin rule, see Table 1.5. Simulations successfully reproduced the tonal modal content of the configuration.

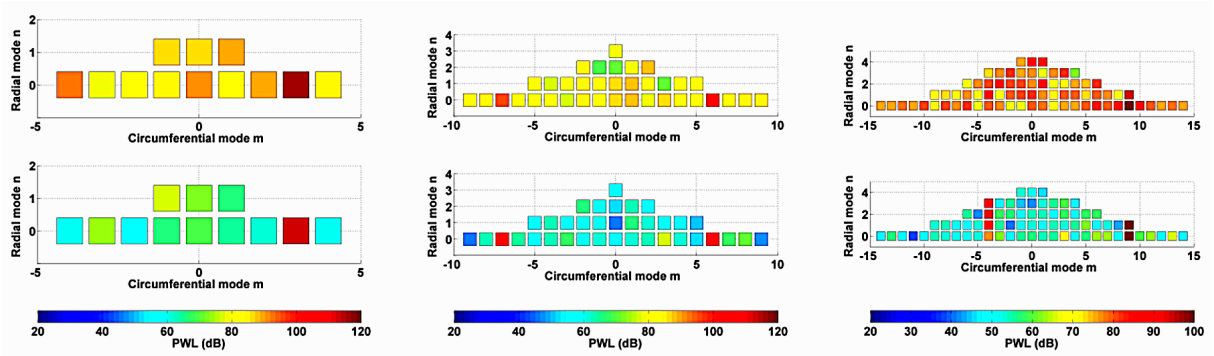

Figure 1.32: Comparison of experimental (top) and numerical (bottom) modal contents at the first three BPFs (left to right) of the ANCF configuration. The configuration has $B = 16$ blades and $V = 13$ stator vanes. From Perot et al. [80].

	Azimuthal mode $m = sB - pV$
BPF 1	$m = 1 \times 16 - 1 \times 13 = 3$
BPF 2	$m = 2 \times 16 - 2 \times 13 = 6$
	$m = 2 \times 16 - 3 \times 13 = -7$
BPF 3	$m = 3 \times 16 - 3 \times 13 = 9$
	$m = 3 \times 16 - 4 \times 13 = -4$

Table 1.5: Azimuthal dominant modes given by the Tyler & Sofrin rule for the first three BPFs. s is the BPF number, B the number of blades and V the number of vanes in the ANCF.

In the study performed by Sanjosé et al. [84], various stator configurations are simulated with different rotor-stator spacings and stator vane counts. This is expected to change the relative contribution of rotor-stator interaction noise mechanisms. A good agreement was found in terms of spectra and directivity plots with the experimental results. Numerical extraction planes were also projected onto duct modes in order to retrieve the modal content. Finally, aerodynamic excitations taken from the simulation were also used, coupled with Amiet's airfoil responses and propagated using Goldstein's analogy. With this, the direct projected modal content could be compared to the one achieved by an analytical approach as described in the previous section. Results had a good agreement in terms of direct modal projections from the simulation but evidenced some discrepencies when propagating with Golstein's analogy. This study provided interesting possible analyses for investigating different noise mechanisms and assessed the LBM capabilities for simulating low-speed fans.

Numerical simulation and modelling techniques ——— Summary

In this section the LBM theory has been introduced. This method relies on the resolution of the Boltzmann equation on a lattice. The turbulence is modeled by modifying the relaxation time to equilibrium computed using the RNG k-ϵ model. This modelling is referred to as VLES (Very Large Eddy Simulation) where large turbulent structures are resolved and smaller ones modeled (not captured by the mesh). This method has been chosen for its high computational performance, because it allows a direct extraction of acoustics and because it allows accounting for the experimental environment. Moreover, the investigation of the stator heterogeneity requires full 360° simulations made achievable with the LBM. Several studies of low-speed fans have showed good agreement compared to experimental results. Because of its transient nature, several acoustic analyses can be performed in the simulation allowing a detailed characterization of the sources.

Points to remember and methodological choices retained for the study:

- CFD method used: Lattice-Boltzmann Method (LBM)

- Solver: PowerFLOW by Dassault Systèmes
- Mode: Very Large Eddy Simulation
- Turbulence modelling: RNG $k - \epsilon$
- Direct propagation of acoustics in the solver
- Full experimental environment accounted for

1.6 Experimental investigations on fan noise

In the previous chapter, numerical simulations of low-speed fans were introduced. In the framework of this study, these simulations aim at reproducing the experimental setup of the investigated configurations. Experimental methods for fan noise will be described below. An experimental fan test rig is intended to provide a detailed aerodynamic and acoustic characterization. Because there are no models, a better physical description should be retrieved. However, in experiments, the difficulty changes from the fluid flow modelling to the measurement capabilities. One other difficulty is the ability to avoid measurement pollution by additional undesired aerodynamic or acoustic phenomena.

Figure 1.33a shows the LEAP-1A from CFM being ground tested at Peebles, USA. This kind of test-rig allows performing different types of measurements in order to test the engine prior to flight testing. One can mention aerodynamic performances or acoustic measurements but also blade failure, water ingestion or bird strike simulations. In order to mimic the real flight operating conditions, a turbulence control screen (TCS) can be added upstream of the engine, see Figure 1.33b. This screen allows homogenizing the turbulence entering the fan and removes inflow distortions related to ground effects.

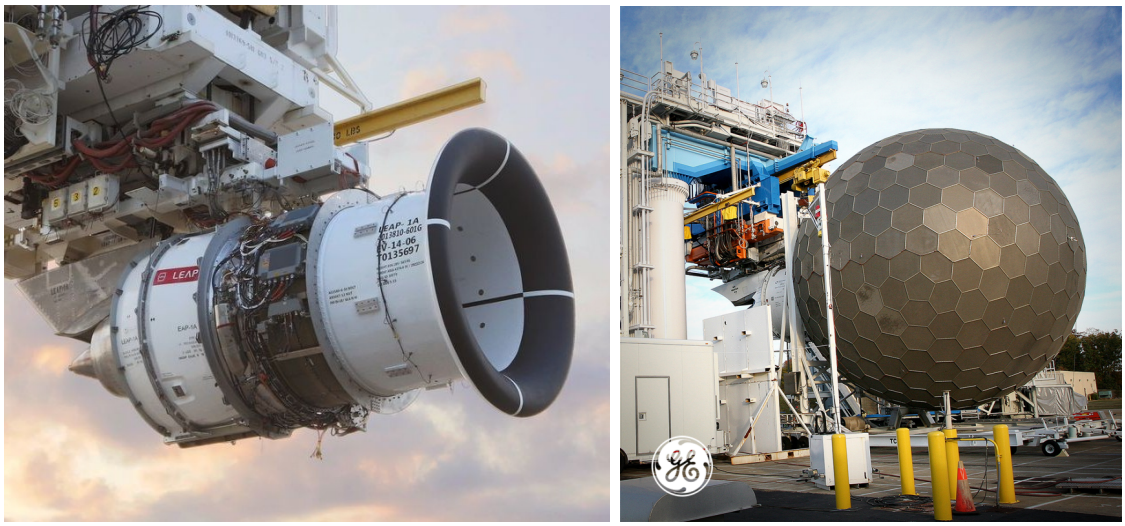

(a) LEAP-1A engine test. (b) Turbulence Control Screen.

Figure 1.33: Engine test-rig of General Electrics at Peebles, USA. Pictures from CFM.

Even though realistic, this kind of test-rig is of high complexity and very costly. Moreover, full engine tests include all noise sources of the primary and secondary streams, complicating the task of isolating noise sources. In order to perform experiments adapted for a research investigation, mock-up models and low-speed fans allow having manoeuvrable and versatile test-rigs where modifications of the setup can be done rapidly. From this standpoint, these test-rigs are better suited for research studies.

1.6.1 Fan noise test-rig

The type of experimental test-rig used in this PhD is sketched in Figure 1.34. The fan-OGV module is installed in a long duct of constant section. Using a constant duct section makes the comparison with analytical models accounting for cylindrical ducts with constant section easier. When the fan is running, the air enters the duct via an inlet, the geometry of which is designed to obtain the cleanest entering flow. The air is thus compressed by the fan and straightened by the OGV grid. The compression is measured by duct wall static pressure taps upstream and downstream of the fan. The air goes through a long duct section until reaching a Venturi tube, used to measure the mass-flow rate. The air is then ejected into an anechoic settling chamber in order to absorb acoustic waves. Finally, the flow is re-introduced inside the room through a curved duct portion forming thereby a closed loop cycle.

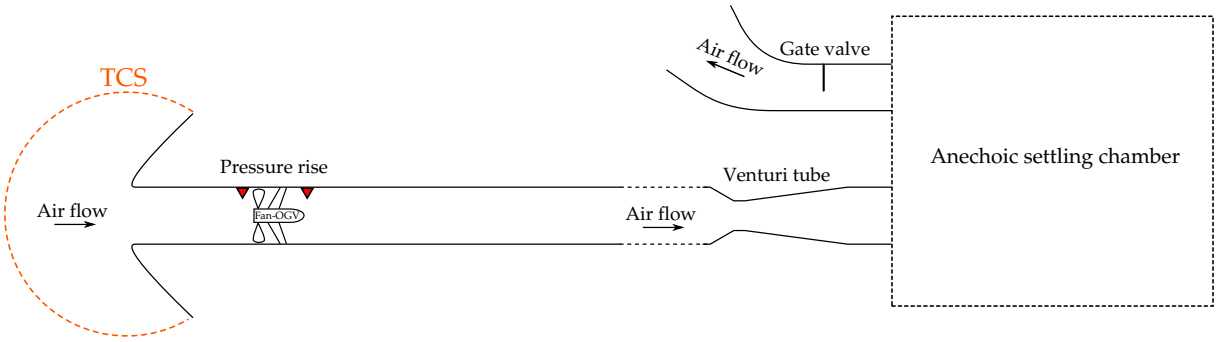

Figure 1.34: Ducted fan-OGV test-rig of LMFA-ECL.

The operating point of the turbomachine can be modified by adjusting the rotational speed and the flow rate. The adjustment of the mass-flow rate can be achieved by generating pressure losses. Different systems can then be used as a conical plug or a gate valve. The latter is used in the framework of this study and the mass-flow rate is adjusted by modifying the position of the valve in the duct.

The pressure rise and flow rate characteristic curves are sketched in Figure 1.35 for a typical axial turbomachine. At a given rotational speed, a reduction of the mass-flow rate increases the pressure rise up to a certain limit. By increasing the rotational speed, the performance curve is translated to the region of higher pressure rise/mass-flow rate. The limit of high compression rate defines the so-called surge limit. Above this limit, there is a complete flow disruption over the rotor. The cause for such phenomenon can be in some cases attributed to stall occurring on the blades. Aside from drastically reducing the performance of the machine, this phenomenon adds new acoustic sources and vibrations. For these reasons, acoustic measurements will be performed at the design point, assumed the best-efficient operating point.

Such an experimental setup has been investigated in the literature for the detailed characterization of fan-OGV noise, see [87, 88, 89, 90, 91]. For instance, in Figure 1.36 is shown a similar low-speed test bench investigated by Tapken et al. [91] at DLR. This kind

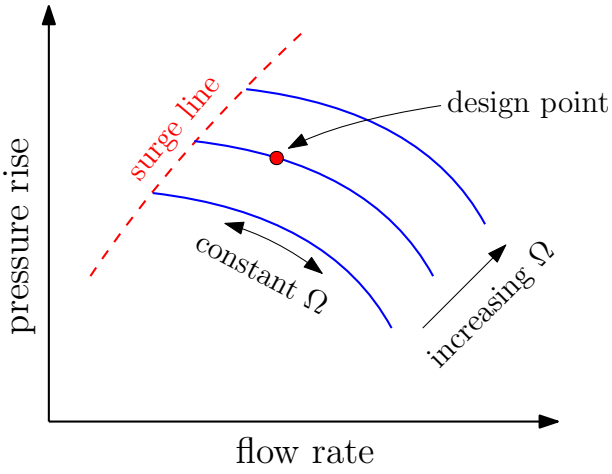

Figure 1.35: Schematized axial turbomachine performance curve.

of setup is used in order to retrieve the fan spectral and modal content of the fan from an upstream acoustic array shown in orange. A different ducted anechoic termination is used instead with treated duct walls to avoid reflections. The operating point is here controlled by a conical plug placed at the duct termination. Finally, the inlet is equipped with a Turbulence Control Screen not shown in the figure. This type of test bench is very similar to the one used in the present study. Its main features are: a long duct of quasi-constant cross-section, flush-mounted acoustic arrays, an anechoic termination and a TCS at the inlet.

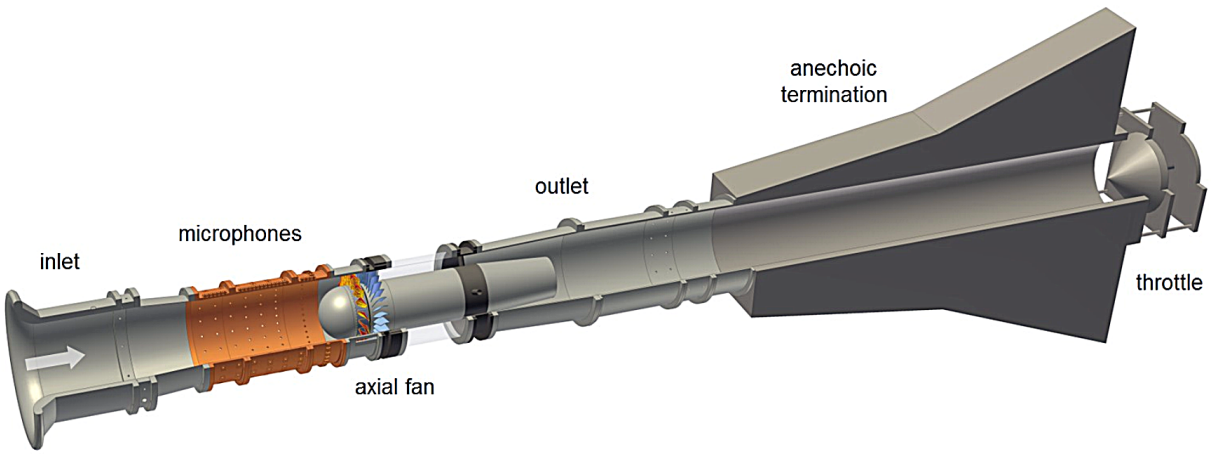

Figure 1.36: Low-speed test bench at DLR [91].

In this study, a TCS can also be added at the duct inlet in order to homogenise turbulence and remove possible inflow distortions. This screen is essential if one wants to isolate rotor-stator noise mechanisms. Different types of control screens were investigated by Sturm et al. [90], see Figure 1.37.

It has been shown that hemispherical screens were more efficient in the reduction of tonal noise associated with inflow distortions. In Figure 1.38 the spectrum is shown for different inflow conditions. The investigated configuration is an isolated fan made of 5

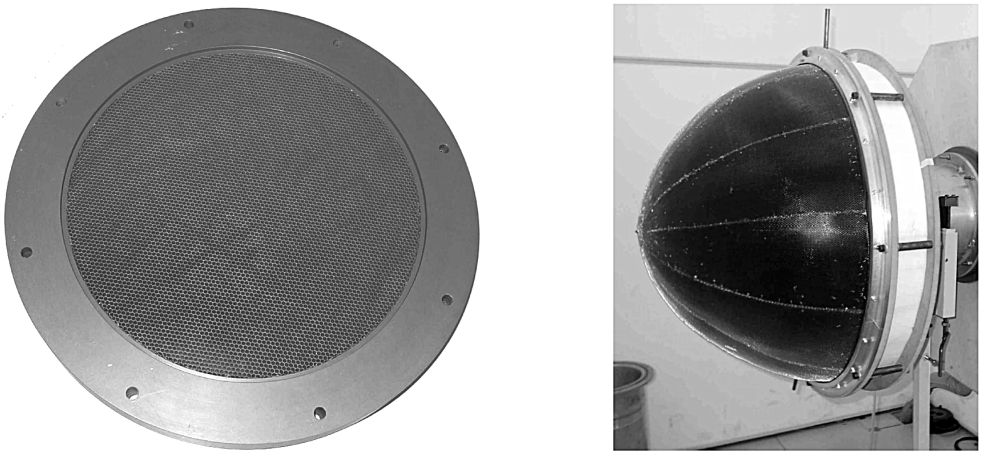

(a) Tubular flow conditioner (TFC). (b) Hemispherical flow conditioner (HFC).

Figure 1.37: Turbulence control screens from Sturm et al. [90].

blades. In theory, no discrete tones should appear at the blade passing frequencies for a nominal operating condition. However, tones clearly emerge for the free inflow case where an inflow distortion was identified, see Figure 1.6. One can see that the use of hemispherical control screens is more efficient in the reduction of the first BPF tones. For higher frequencies, BPFs with screen are also narrower. Therefore, this type of screen is used in the present study. In terms of broadband noise, the reduction is not significant for all screens. This may be explained by the fact that the inflow distortion is not highly turbulent. Thus, the breakdown of turbulent structures through the screen does not consequently modify the residual turbulent flow features impinging on the fan.

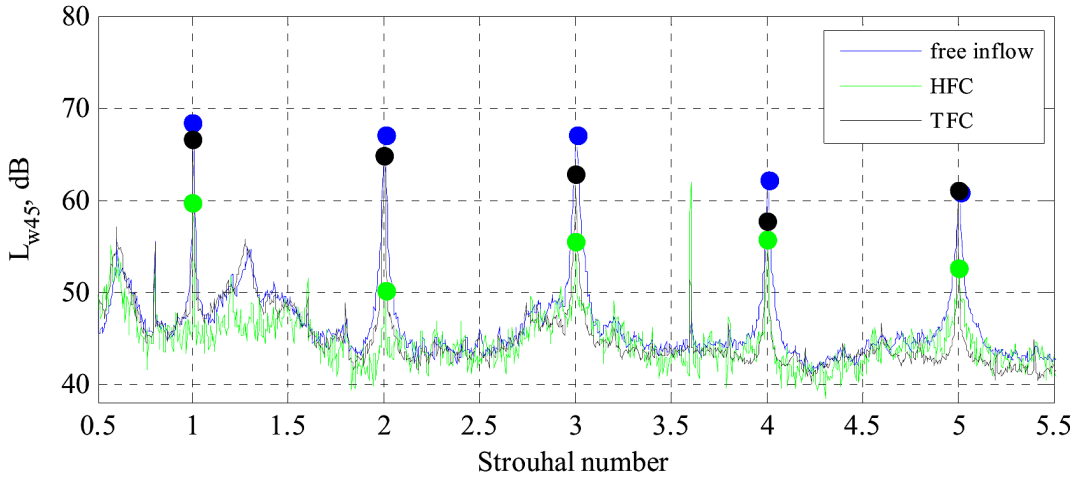

Figure 1.38: Acoustic spectrum with free inflow, HFC or TFC by Sturm et al. [90].

1.6.2 Aerodynamic and acoustic measurements

In order to characterize the machine and the test-bench, different aerodynamic and acoustic measurements can be done. In terms of aerodynamic measurements, velocity profiles

can be measured inside the duct. Different probe types allow characterizing both the mean and fluctuating parts of the velocity. In this study, hot-wire measurements will be used to characterize the flow entering the fan. Total pressure probes can also be used in order to have mean velocity profiles downstream of the fan-OGV module.

In terms of acoustic measurements, in-duct acoustic arrays will be used. Acoustic arrays with flush mounted microphones under pin-holes are used to measure the wall-pressure [92]. Because the objective is to retrieve the modal content of the fan, a large number of microphones is needed. The distribution of microphones in the acoustic array can be optimised for modal decompositions as proposed by Tapken et al. [93]. The optimisation is based on minimizing the condition number of the transfer matrix to be inverted in the modal decomposition process. To recall, the condition number for matrix inversion expresses the sensibility of the inverse to its inputs. The lower the condition number, the lower the sensibility of the results and thus the better the inversion. This analysis is based on the geometrical parameters of the duct and the frequency range to be analyzed. The optimisation performed by Tapken et al. [93] for different array configurations (but with constant spacing) can also be applied for randomly placed microphones. This is done by Pereira et al. [88] by optimising a fixed number of microphones at different azimuthal and axial positions. In Figure 1.39 is shown the condition number for different pseudo-random microphone distributions. The red curve indicates the optimal configuration and it can be seen that the condition number at high frequency is lower than the others. This type of acoustic arrays allows obtaining the azimuthal but also the radial modal content as opposed to azimuthally distributed arrays. It is therefore used in this study.

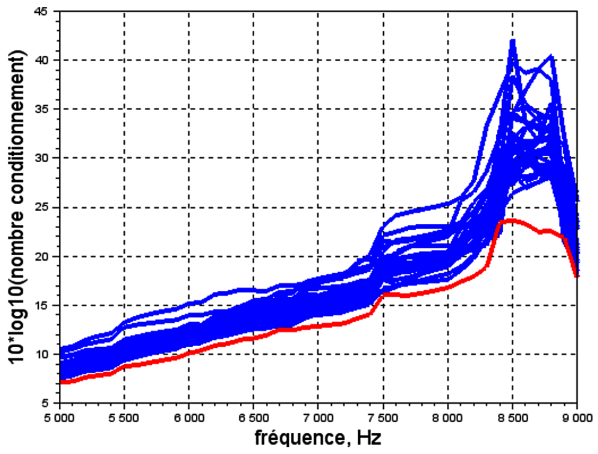

Figure 1.39: Acoustic array optimisation by Pereira et al. [88]

In the framework of this study, microphones are mounted behind a pinhole cap as shown in Fig. 1.40. This mounting was chosen because the protection grid of the microphones could not be removed. A small cavity between the microphone membrane and the pinhole is created and this will be at the origin of acoustic resonances at some frequencies. For this reason, a calibration process is essential in order to retrieve a correct transfer function for each microphone. It will relate the actual measured pressure by the

microphone to the pressure of interest at the duct wall.

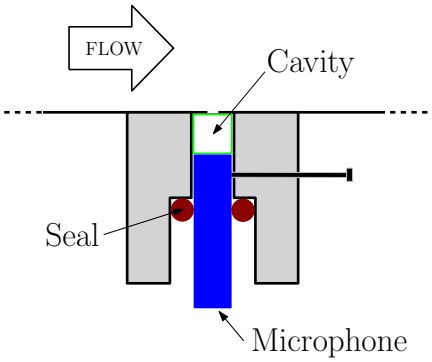

Figure 1.40: Microphone slot scheme.

To perform the microphone calibration, two methods are compared: an individual local method and a global non-local one, see Leclere et al. [94]. Both methods are compared for the investigated case in chapter 2.

1.6.3 Modal content from acoustic measurements

The objective is to investigate which modes are predominant [95, 96, 97, 98, 99, 100, 101, 102, 103, 104]. Considering a hard-walled duct of circular cross-section, the acoustic pressure at any point inside the duct can be expressed as a sum of modes as introduced in equation (1.2). At positions relatively far from sources or duct discontinuities, this infinite sum may be well-approximated by taking only those terms related to cut-on modes. Considering that the array is made of M microphones and assuming that there are N cut-on modes, equation (1.2) may be conveniently expressed in a matrix form as:

$$\mathbf{p} = \mathbf{\Phi c}. \tag{1.84}$$

This formulation is better suited for numerical resolutions in which a matrix inversion must be performed. The solution is then given by

$$\hat{\mathbf{c}} = \mathbf{\Phi}^{\dagger}\mathbf{p}, \tag{1.85}$$

where the notation $\square^{\dagger}$ stands for the pseudo-inverse of $\mathbf{\Phi}$. Microphone measurements can be assembled in a matrix called the Cross-Spectral Matrix (CSM) defined as follows

$$\mathbf{S_{pp}} = \mathbb{E}\left\{\mathbf{p}(\omega)\mathbf{p}(\omega)^{H}\right\}, \tag{1.86}$$

where $\square^{H}$ is the Hermitian operator and the notation $\mathbb{E}\{\square\}$ stands for the expected-value operator. equation (1.84) and equation (1.85) along with the definition in equation (1.86) yield:

$$\hat{\mathbf{S}}_{\mathbf{cc}} = \mathbf{\Phi}^{\dagger}\hat{\mathbf{S}}_{\mathbf{pp}}\mathbf{\Phi}^{\dagger H}, \tag{1.87}$$

where the matrix $\hat{\mathbf{S}}_{\mathbf{cc}}$ is a cross-spectral matrix of modal amplitudes. Diagonals contain auto-spectra of individual modes and off-diagonals terms are cross-spectra between all pairs of modes. In some cases, such as near cut-off frequencies, as well as frequencies at which the number of cut-on modes is large when compared to the number of microphones, the matrix $\mathbf{\Phi}$ may be ill-conditioned. In this case more involved techniques must be used to compute its inverse [105]. The method relies on a Bayesian regularization that has shown numerous benefits for inverse acoustic problems.

1.6.3.1 Hydrodynamic denoising

A difficulty in the analysis of fan broadband noise using wall flush-mounted probes is the fact that pressure fluctuations are largely dominated by a contribution of so-called hydrodynamic nature associated with wall-bounded turbulence (also called pseudo-sound). For the tonal noise component, this problem is minor since the fan-related noise largely emerges from the hydrodynamic component, often by at least 20 dB. In contrast, for the broadband component, the signal of interest might be about 10 dB lower. Thus, to perform a modal decomposition of the broadband noise component, an additional treatment is needed to extract the fan-associated noise.

At low Mach numbers, the turbulence length scales are much smaller than the separation distance between two neighbouring microphones, contrary to the theoretically infinite correlation length of acoustic waves. This implies that the hydrodynamic contribution is mainly contained in the diagonal of the cross-spectral matrix, whereas off-diagonal terms contain information about the sound waves.

To remove this hydrodynamic contribution, different methods are proposed in the literature [92, 106, 107, 108]. A common practice consists in removing the cross-spectral matrix diagonal, by setting diagonal entries to zero. Nevertheless, this approach removes the properties of a CSM matrix and can lead to non-physical negative modal amplitudes. To avoid this issue, another method is adopted in this study allowing to decompose the CSM into acoustic and hydrodynamic parts, as shown by Finez et al. [89]. The idea of the method is to exploit the different structures of the CSM associated with acoustic and hydrodynamic parts to help their separation. The chosen method is named Sparse & Low-Rank Decomposition (SLRD) and detailed in [89]. The CSM decomposition writes:

$$\hat{\mathbf{S}}_{\mathbf{pp}} = \mathbf{L} + \mathbf{S}, \tag{1.88}$$

where $\mathbf{L}$ is a low-rank matrix and $\mathbf{S}$ a sparse matrix. The low-rank approximation is based on the fact that only a finite number of cut-on modes contribute to the acoustic energy. On the other hand, the sparsity of the matrix $\mathbf{S}$ is based on the assumption that turbulent fluctuations are uncorrelated from microphone to microphone (if the separating distance is large enough). In consequence, these fluctuations should be mainly present in the matrix diagonal. To sum-up, $\mathbf{L}$ should include acoustics and $\mathbf{S}$ the pseudo-sound

part. The computation of $\mathbf{L}$ is formulated as an optimisation problem:

$$\text{minimize } \|\mathbf{L}\|_* + \lambda \|\mathbf{S}\|_1 \qquad \text{subject to } \mathbf{L} + \mathbf{S} = \hat{\mathbf{S}}_{\mathbf{pp}} \tag{1.89}$$

with $\|\square\|_*$ the nuclear norm, $\|\square\|_1$ the L1-norm and λ a regularization parameter. This optimisation is based on the assumption that the low-rank matrix solution of the physical problem should minimize the acoustic energy. With this, the in-duct acoustic spectra and the modal decompositions at broadband frequencies can be performed on the de-noised matrix $\mathbf{L}$.

1.6.4 Modal content interest

The characterization of the modal content of a given configuration is very instructive. In fact, as shown by Envia [109], active control systems can be used in order to cancel specific identified modes. The objective of such active control systems is to synthesize acoustic modes with the same amplitude but with opposite phase in order to cancel modes emitted by the configuration.

Figure 1.41 shows a system of active Helmholtz actuators placed upstream of the fan in order to attenuate specific emitted modes.

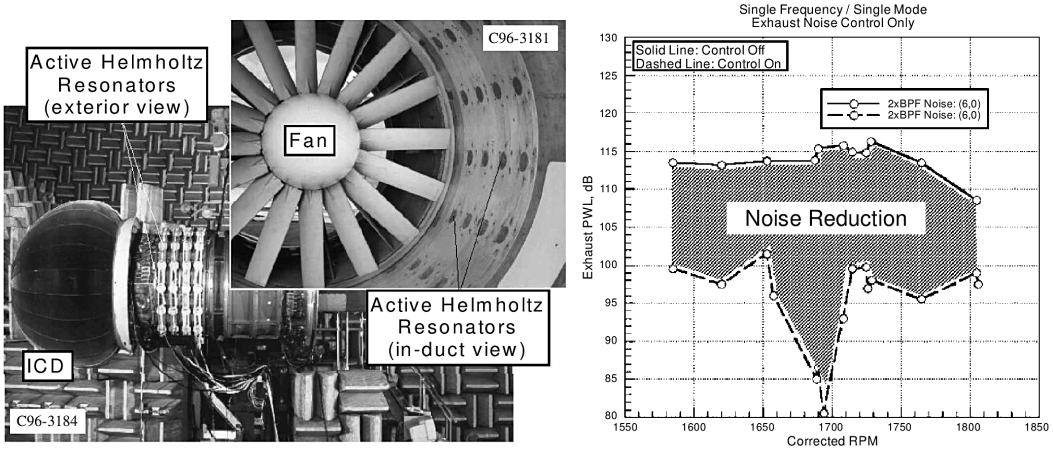

(a) Active Helmholtz resonators.

(b) Reduction of fan duct mode power level due to active noise control over a typical range of fan speeds tested in the ANCF rig.

Figure 1.41: Active noise control on the ANCF configuration from NASA [109].

In the study, other active noise actuators were also used as embedded actuators on the stator vanes or plate radiator drivers. The overall noise reduction using active noise control is shown in Figure 1.41b. A considerable reduction of up to 35 dB can be observed at around $\sim$ 1700 rpm.

A second example is shown in Figure 1.42. The configuration is a contra-rotating propfan investigated in a test stand at DLR. The noise control strategy consists in firstly

measuring the sound-field by an array of microphones. Secondly, the measured sound-field is azimuthally decomposed in modes at a given frequency and used to feed the noise reduction algorithm. Finally, a set of loudspeakers is then activated in order to cancel the measured sound field. As shown in Figure 1.42, the mode of order $m = -2$ is attenuated by more than 10 dB.

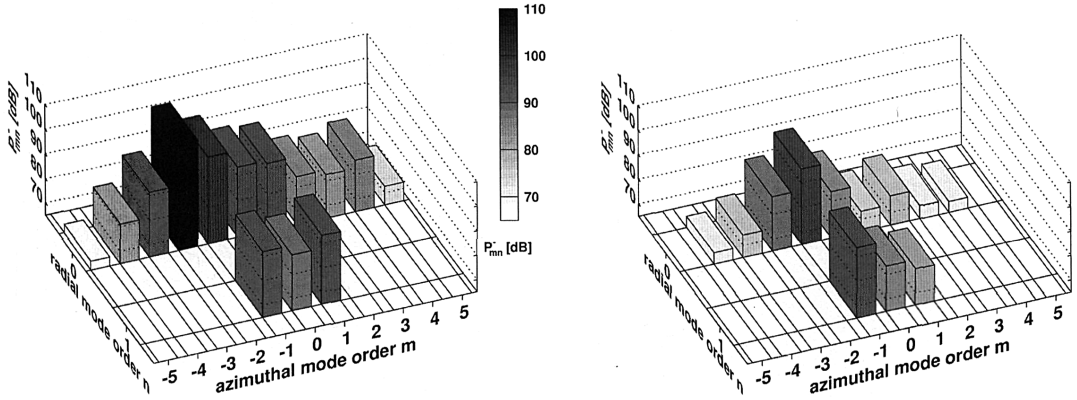

(a) Without active noise reduction.

(b) With active noise reduction.

Figure 1.42: Mode attenuation by active noise control, Enghardt et al. [110].

The importance of knowing the modal content of a turbomachine is also related to a possible better understanding of the impact of heterogeneous stators on rotor-stator noise. In fact, one can investigate whether radiated modes are predicted by the Tyler & Sofrin rule or if they are attributed to geometrical non-uniformities as the stator heterogeneity. In the study of Tapken et al. [87] of a UHBR configuration with homogeneous stator, a Tyler & Sofrin dominanting mode $m = 6$ is identified, see Figure 1.43. In this case, because the stator is homogeneous, no other significant modes are identified.

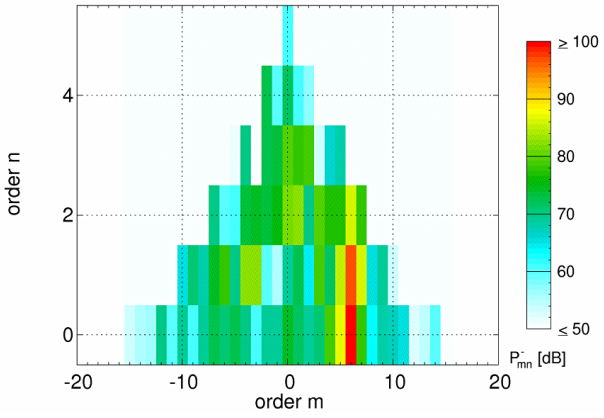

Figure 1.43: Modal content of a mock-up UHBR configuration [87] with homogeneous stator at 2BPF. Tyler & Sofrin mode observed, $m = 2B - pV = 2 \times 22 - 1 \times 38 = 6$.

The same modal analysis can also be done with the numerical simulation results. If experiments assess the numerical modal content, detailed analyses of the volume data can be done in the simulation in order to explain the impact of the heterogeneity. In the case

of additional noise radiation with non-periodic stators, the modal analysis will also allow investigating the acoustic energy is distributed over the modes. It should tell whether the energy is spread into a forest of modes or if it is concentrated in some dominant modes. In the latter case, the objective is to determine the generating mechanisms of such modes by the deterministic interaction of the rotor and stator.

Experimental investigations on fan noise — Summary

In this section, experimental methods for the characterization of fan noise have been presented. Compared to numerical simulation, experiments allow having realistic characterization of the noise and flow of a given configuration. In the framework of this study, the in-duct modal content will be investigated. For that mean, flush-mounted microphones upstream and downstream of the fan will allow characterizing either the tonal or broadband noise. Because the measurements are done at the duct-wall, a specific treatment in order to remove the pseudo-sound is applied. Finally, measurements can be compared to the numerical simulations of the same experimental setup. This comparison should first allow assessing the simulation results and if so, allow performing more detailed analyses in the volume data provided by the simulation.

Points to remember and methodological choices retained for the study:

- Long duct of constant section with an anechoic termination
- Flush-mounted acoustic arrays made of tens of microphones
- Optimised acoustic arrays for full modal decompositions
- Hemispherical Turbulence Control Screen for effective removal of inflow distortions

1.7 Conclusion

In this first chapter, all the necessary background for the investigation of turbomachinery noise has been introduced. The state of the art for the three aspects (experimental, numerical and analytical) has been presented along with some recent studies on the stator heterogeneity.

In terms of analytical modelling, Goldstein's analogy for duct flows is used. This analogy is coupled with an isolated airfoil response function given by Amiet's model for leading edge interactions or by Parry's model for downstream interactions. Finally, Goldstein's analogy is extended for a heterogeneous stator as proposed by Roger et al. [6].

In terms of numerical simulations, the Lattice-Boltzmann method is chosen. The method allows taking into account the full annulus geometry at a reasonable cost. Because the solver is naturally transient, it also provides the duct acoustic propagation directly in

the simulation and eases the noise computation by placing the same experimental probes in the simulation.

Finally, experimental methods have been described. The chosen test-bench is made of a long duct and equipped with a Turbulence Control Screen and flush-mounted acoustic arrays. The ability to retrieve the in-duct modal content from the measured wall-pressure fluctuations represents an essential feature for this investigation. Some studies have evidenced the potential to reduce the noise by attenuating some identified dominant modes.

2

Experimental characterization of the LP3

Contents

In the previous chapter, the state of the art provided all the necessary bibliography and theoretical background to investigate the noise of a heterogeneous turbomachine. The first step in our investigation is to characterize the noise of the *LP3* stage, that is to say, evaluate precisely the acoustic spectrum and modal content of the *LP3* stage at a given operating point that will be simulated afterwards in Chapter 3. The objective is to ensure that the measured tonal noise is only due to rotor-stator interaction mechanisms and not to inflow distortions or other spurious sources. In practice, this will allow evaluating whether the emitted noise is due or not to the stator heterogeneity.

2.1 The *LP3* configuration

The *LP3* is a low-speed electrical HVAC fan manufactured by Safran Ventilation Systems. It is used in the air conditioning of different compartments of an aircraft. This

configuration is an well-suited test-bed for the investigation of turbomachinery noise in particular for the investigation of modern and future technological features of turbofans. Hereafter, a few items justifying the choice of the *LP3* fan for this research project are listed:

1. The rotor-stator spacing is small (as for future turbofans):
   - The rotor-stator interaction is increased
   - The potential-interaction may become important
2. The stator is heterogeneous (as in present and even more future turbofans architectures):
   - The vane modification is moderate, avoiding strong flow modifications
   - It allows isolating the heterogeneity impact numerically
3. The first two BPFs should be cut-off by the duct (in theory for a homogeneous stator):
   - It allows evaluating the impact of the stator heterogeneity on tonal noise
4. The *LP3* is already installed for experiments at École Centrale de Lyon:
   - Modal detection techniques are available
5. The physical phenomena are representative if a real turbofan:
   - The hub-to-tip ratio is low: the modal content is increased
   - Same physical rotor-stator interaction phenomena are expected
6. The tip Mach number and Reynolds number are relatively low:
   - Unsteady LBM numerical simulations can be performed at a reasonable cost accounting for the experimental environment
7. The duct is of constant cross-section:
   - The analytical solution for the duct propagation is exact

In a realistic turbofan, some additional effects may appear. Among them, one can mention the high flow compressibility at transonic regimes, asymmetric air inlets, complex duct geometries and an increased degree of heterogeneity of the stator cascade. These together would add additional sources and would modify the acoustic propagation in the duct. Firstly, transonic regimes would increase the computational cost of numerical simulations and would add an additional contribution, the buzz saw noise. Secondly, the complex inlet and duct geometries would make any analytical modelling attempt very difficult. In addition, the inherent inlet distortion generated by an asymmetric inlet would not allow the isolation of rotor-stator interaction mechanisms. Finally, the high degree of heterogeneity of the stator cascade could compromise the quantification of its impact on the noise. In fact, a fair comparison with an equivalent homogeneous cascade would be difficult because of the expected modifications in the operating conditions. This is why this study is focused on a low-speed fan having some representative characteristics of a modern turbofan and being suited for a research investigation.

The *LP3* fan is shown in Figure 2.1. It is composed of a unique fan-OGV stage. The

fan is made of $B = 17$ blades and the stator of $V = 23$ vanes, 3 of which are modified (see Figure 2.1b). Compared to a baseline vane, the modified vane geometry consists of a radial thickening towards the tip, see Figure 2.2.

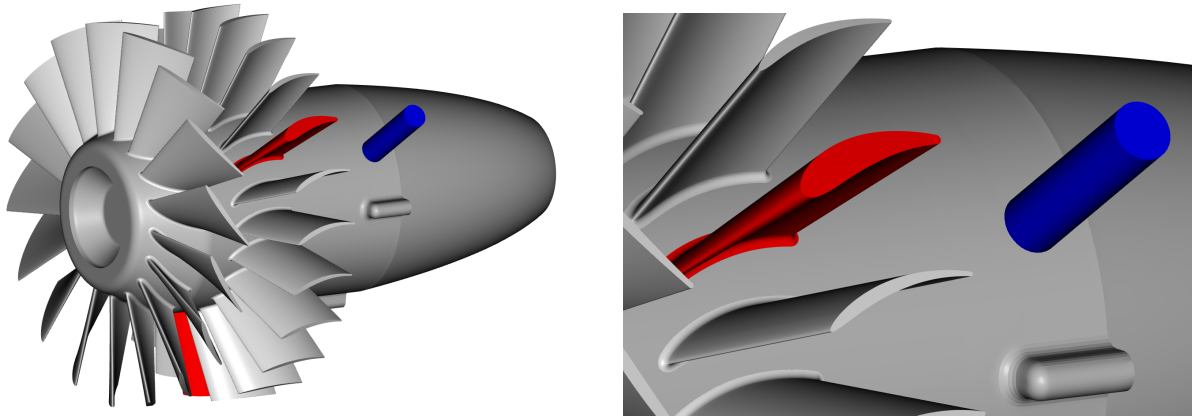

(a) Rotor-stator geometry.

(b) Zoom on a thickened stator vane in red and the power-supply cable in blue.

Figure 2.1: Safran Ventilation Systems *LP3* geometry.

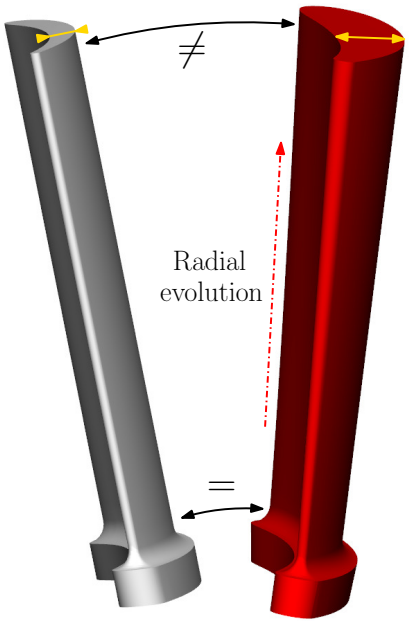

Figure 2.2: Comparison of a baseline vane (left) and a modified vane (right).

At the hub, both vane geometries are identical and at the tip, the modified vane is thicker by a factor of about 3. Compared to recent turbofans configurations, the heterogeneity degree of this stator can be considered as weak. The maximum rotational speed is of 10,000 rpm providing a tip Mach-number of about 0.3, the limit of the incompressible flow regime. The duct diameter is 17.1 cm and the hub-to-tip ratio at the stator position is equal to about 0.55. Parameters of the *LP3* are summarized in Table 2.1.

Rotational speed range	Ω	2000 - 10,000 rpm
Rotor blade number	B	17
Stator vane number	V	23
Heterogeneous stator vanes	$V^{(h)}$	3
Angular position of the thickened vanes	$\varphi/2\pi$	$1/23, 8/23, 16/23$
Blade, vane stagger range (hub to tib)	χ_B, χ_V	35.3° to 58.75°, 33°
Blade, vane chord	c_B, c_V	2.1, 3.0 cm
Diameter	$\oslash$	17 cm
Rotor-stator spacing (at midspan)	d_{RS}	$0.7 \times c_B$
Hub to tip ratio (at the stator position)	σ	0.55
Tip Mach number	M_{tip}	~ 0.3
Maximum mass flow rate	Q_m	~ 1 kg.s^{-1}
Maximum mean axial flow velocity	U_0	~ 40 m.s^{-1}

Table 2.1: *LP3* parameters summary table

The *LP3* configuration — Summary

1. Maximal rotational speed: $\Omega = 10000$ rpm
2. $B = 17$ rotor blades and $V = 23$ stator vanes
3. Low Mach-number configuration (tip Mach-number of about 0.3)
4. Heterogeneous stator: 3 thickened vanes (weak heterogeneity)
5. Ducted configuration (constant section)

2.2 Test bench presentation and qualification

The experiments were conducted in a test facility at École Centrale de Lyon (ECL). All the experimental apparatus was already available for this PhD but some improvements developed by the experimental team at ECL have been assessed during the course of this PhD. This includes the evaluation of the Turbulence Control Screen (TCS) effectiveness and the validation of the global calibration method, both described hereafter. The *LP3* is inserted in a ducted environment as sketched in Figure 2.3.

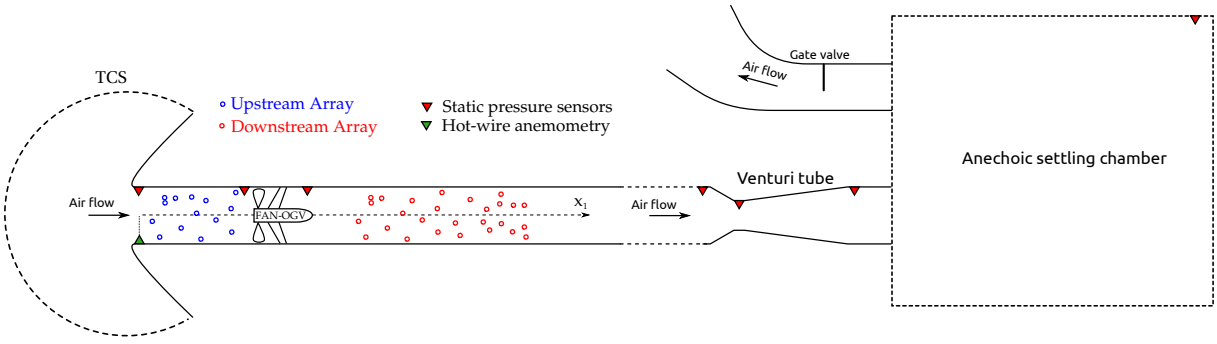

Figure 2.3: Sketch of the experimental facility at École Centrale de Lyon.

The air is introduced through an axi-symmetric inlet and travels down a long duct of constant section. The *LP3* stage is placed at about 20 cm downstream of the inlet. Its rotational speed is controlled by a pulse-width modulation (PWM) controller. Further downstream, a Venturi tube is used to measure the mass flow rate. Finally, the air is introduced in an anechoic settling chamber of $1.5 \times 1.5 \times 2$ m^3. This chamber is covered with foams and aims at absorbing the downstream propagating waves to avoid reflections in the duct. Duct-end reflections generate acoustic waves which would make the analysis less accurate. The air is finally ejected in the same room through an ejection system which has a gate valve that allows modifying the mass flow rate and in consequence the operating point of the *LP3*.

At the duct inlet, a Turbulence Control Screen (TCS) can be added as shown in Figure 2.4. The purpose of the TCS is to reduce free stream turbulence [29], to straighten the flow direction and to remove distortions at the fan inlet. The radius of the TCS is 0.5 m. It covers a portion of three quarters of a sphere centred on the duct inlet. It is made of tens of 2-cm thick plane facets of aluminum honeycomb, stuck together to approach a sphere, see Figure 2.4b.

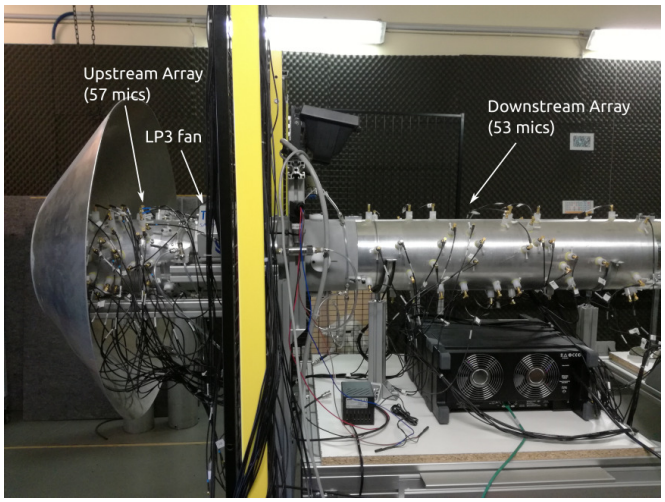

(a) Inlet (without the TCS) and instrumented duct.

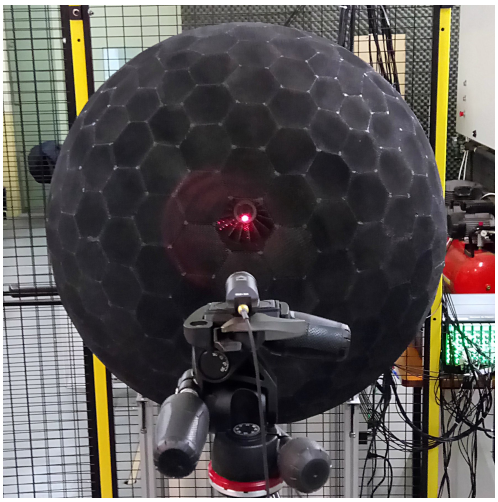

(b) Turbulence Control Screen (TCS). The laser beam is pointing at the fan through the honeycomb.

Figure 2.4: Test-facility photos.

In order to obtain a more precise rotational speed measurement during the experiments, a Brüel & Kjær type 2981 laser tachometer is used. The tachometer is placed outside the TCS, the laser beam going through one cell of the honeycomb, so that the inflow conditions are not altered. It produces a voltage pulse for each revolution of the rotor.

In terms of noise measurements, two acoustic arrays are placed upstream and downstream of the fan-OGV module. The upstream array is made of 57 microphones and is 20 cm long. The downstream array is made of 53 microphones and is 80 cm long. These

antennas allow performing detailed spectral and modal analyses. They have been designed and investigated in a previous study in the framework of the SEMAFOR project [88, 89]. Both are equipped with 1/4" Brüel & Kjær type 4957/8 microphones. Each microphone is mounted under a pin-hole configuration as shown in Figure 2.5.

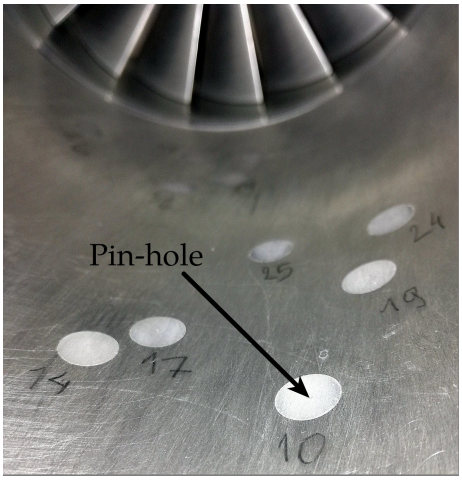

(a) Pin-hole in the experimental setup.

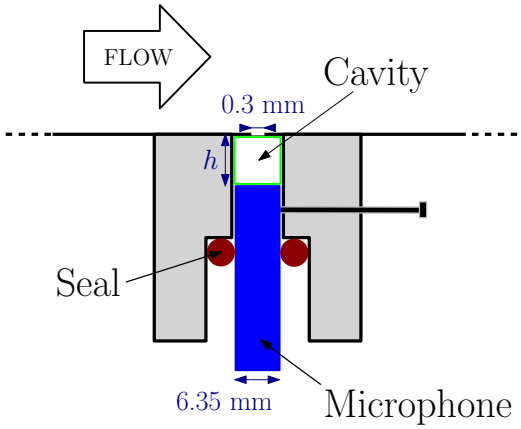

(b) Two-dimensional representation of the cylindrical pin-hole setup (not to scale). h varies from microphone to microphone but is of the order of the millimetre.

Figure 2.5: Pin-hole setup for the microphone installation.

This type of installation notably allows having a smooth duct surface and a non-intrusive measurement but also provides a point measurement (pin-hole of about 0.3 mm, the diameter of a B string in a standard guitar string set). However, because the microphone communicates with the flow region via a small cavity, a calibration step is necessary. The small cavity can be interpreted as a small Helmholtz resonator meaning that some resonances may appear at given frequencies depending on the cavity size. The installation of the microphone is made as shown in Figure 2.5b. The microphone is inserted in a slot at a given distance from the duct wall, fixed with a tightening screw; a plastic seal is added to ensure the sealing. Because the distance of the microphone to the wall may vary for each microphone, the calibration function is necessary for all microphones. Calibration methods and results are presented in sub-section 2.2.1. Pressure signals are recorded using 18 Brüel & Kjær type 3050 Lan-XI modules. The signals are simultaneously sampled over the 106 microphones at a frequency of 65.6 kHz.

The test-rig is also instrumented with 6 static pressure probes at different locations (see Fig. 2.3). The mean static pressure has been measured with Validyne DP15 transducers and Druck Unik5000 transducers. These measurements have allowed the determination of the pressure rise caused by the fan and the determination of the mass flow rate at the Venturi tube.

Hot-wire anemometry has also been performed at the inlet (see Fig. 2.3). A streamline anemometer combined with a single Dantec 55P01 hot-wire operating in constant voltage

mode provides the streamwise velocity, together with the velocity fluctuations. Parameters for the acoustic measurements are summarized in Table 2.2.

Record time	T	5 min (50,000 revolutions per operating point)
Sampling frequency	F_s	65536 Hz
Microphone		B&K 1/4-inch, Type 4957/58
Upstream array		$N_{\text{mic}} = 57$, $L = 20$ cm
Downstream array		$N_{\text{mic}} = 53$, $L = 80$ cm

Table 2.2: Acoustic measurements summary table.

The total record time of 5 min per operating point provides 599 averages considering 1 s windows with 50% of overlap. The sampling frequency F_s allows recovering a maximal study frequency of 25600 Hz well above the range of interest of 10 kHz.

2.2.1 Acoustic sensor calibration

Before performing any acoustic measurement, a calibration step must be performed. Each microphone of the acoustic antennas communicates with the flow through the pin-hole device introduced previously. This indirect communication makes a calibration required. To perform this calibration, two different methods are used, namely:

1. Individual method (local): each microphone is calibrated individually
2. Global method (non-local): all microphones are calibrated simultaneously

The individual method is illustrated in Figure 2.6. It must be performed for each microphone of the antenna using a calibrator. A loudspeaker (compression chamber) is used to generate a white noise excitation. The source is then deported using a hose at the end of which is the calibrator. In the calibrator is inserted a reference microphone that will be used for the calibration. As this calibrator is placed above the pin-hole, the signal is recorded in the cavity and at the reference microphone. Finally, the transfer function between these two signals (in other words, the frequency response of the pin-hole cavity) is obtained.

Nevertheless, this calibration method has some disadvantages. One of them is related to the repeatability of the calibration procedure which is very sensitive to the positioning of the calibrator on the pin-hole. Secondly, some microphones may become inaccessible after the installation of the antenna. This can be an issue if the microphones are calibrated before installing the duct portion. In fact, a small displacement of the microphone occurring during the installation of the antenna will modify the frequency response microphone-cavity system.

For this reason, a preferable method named global is now presented. This calibration consists in placing a white noise source at the entrance of the duct and in recording the signals of all microphones simultaneously as depicted in Figure 2.7.

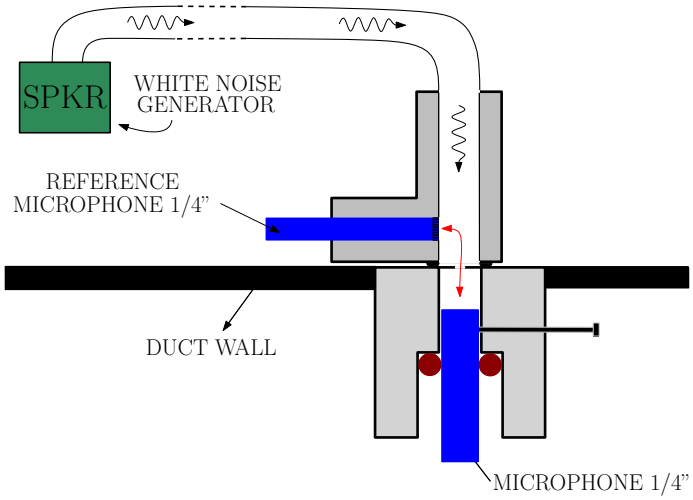

Figure 2.6: Individual calibration system.

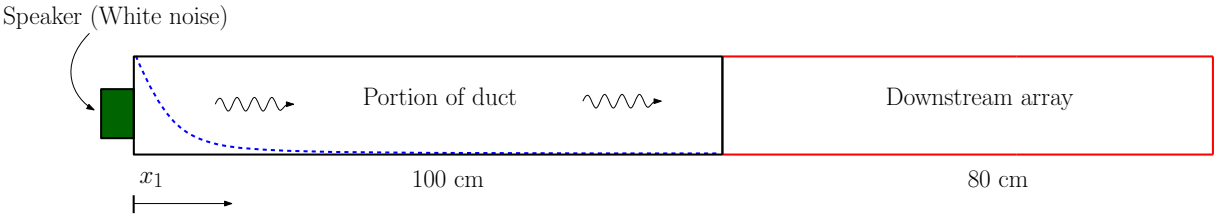

Figure 2.7: Global calibration method.

A portion of the duct is added between the source and the antenna to ensure that cut-off modes are fully damped so that only cut-on modes are measured by the antenna. Then, with the so-called global method developed by Q. Leclère et al. [94], the frequency response is calculated. This method can be summarized in three steps:

1. Projection of the measured pressure on the modal basis: $\tilde{\mathbf{c}} = \mathbf{\Phi}^{\dagger}\mathbf{p}$
2. Reconstruction of the pressure from the modal amplitudes resulting from the projection: $\mathbf{p}_{\text{rec}} = \mathbf{\Phi}\tilde{\mathbf{c}}$
3. Calculation of the frequency response from the difference between measured and reconstructed fields: $\mathbf{p}_{\text{err}} = \mathbf{p} - \mathbf{p}_{\text{rec}}$

Two comparisons between the global and individual methods are presented in Figure 2.8. The results provided by the two methods are very similar in amplitude and phase up to 10 kHz.

Regarding the shape of the response, we can observe two bumps at about 1 and 3 kHz. This type of resonance is related to the cavities present between the microphone and the pin-hole. The position of this resonance has been observed to be directly related to the size of the cavity. For this reason, a procedure for installing the microphones have been defined in order to obtain similar cavity sizes and consistency of mounting. At high frequency (above 10 kHz), some discrepancies are observed with the global method when compared with the individual method. At these frequencies, the number of modes is larger than the number of microphones and regularization steps are necessary. Despite

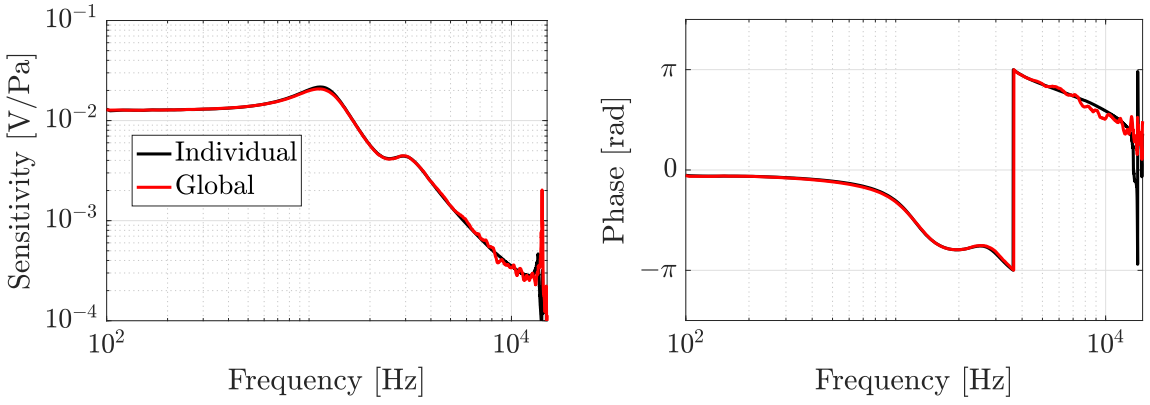

(a) Microphone 14 amplitude

(b) Microphone 14 phase

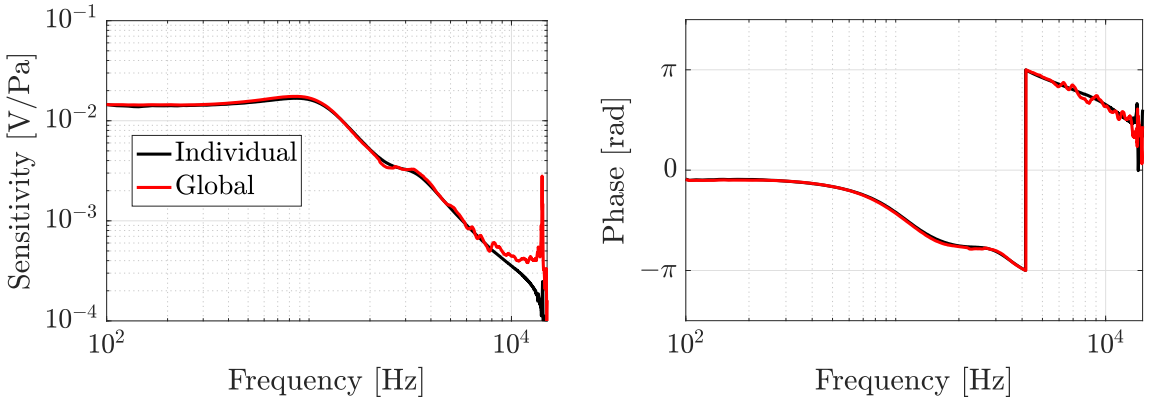

(c) Microphone 29 amplitude

(d) Microphone 29 phase

Figure 2.8: Comparison of the frequency responses of the individual method and the global method for two microphones (14 and 29 respectively) of the upstream array.

this regularization, some differences can still be observed. Finally, it should be noted that even for the individual method, a frequency limit is reached when the associated wavelength is smaller than the distance separating two microphones. This limit is only related to the installation and cannot be extended by post-processing methods. The global calibration is validated and therefore retained for the study. This method ensures that the installed calibration responses are correctly retrieved for each microphone, independently of any microphone displacement during the installation of the antenna.

Test bench presentation and qualification — Summary

Test-bench:

1. Two acoustic arrays with around 50 microphones each upstream and downstream of the fan
2. Microphones installed under pin-holes
3. Hemispherical Turbulence Control Screen available

Calibration:

1. Individual and global methods in good agreement

2. Global method selected for its rapidity and because it can be used with the installed antennas
3. High-frequency limitation above the frequency range of interest (∼10 kHz)

2.3 Inflow distortion and Turbulence Control Screen (TCS)

After ensuring the calibration of the test-bench probes, aerodynamic and acoustic measurements can be done. As introduced earlier, if one wants to investigate the impact of the heterogeneity on rotor-stator noise, it is necessary to remove any inflow distortion. In fact, this noise mechanism contributes at the same frequencies as rotor-stator interactions. Previous studies have evidenced the presence of distortions at the inlet in this configuration, see Figure 2.9. From two successive time snapshots, a different flow pattern is observed. The presence of inlet vortices is clearly evidenced by a smoke technique. Because of that, a Turbulence Control Screen is added in the current experiments to clean the inflow from these vortices. The effectiveness of such device is investigated in the following sections.

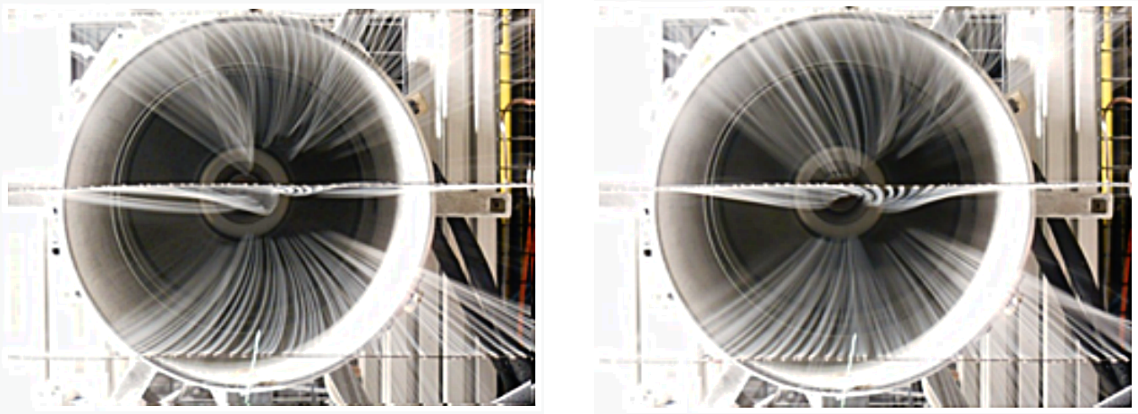

(a) Intant 1 (b) Instant 2

Figure 2.9: Two successive time snapshots of an inflow distortion made visible on the *LP3* facility using a smoke generation technique. Visualization obtained in the framework of previous investigations by K. Kucukcoskun at the LMFA.

The TCS has been first characterized aerodynamically at Université de Sherbrooke. This characterization, consists in measuring the pressure losses through a small TCS sample shown in Figure 2.10. From these pressure losses, the resistivity can be calculated [111]. Results have shown very low values of resistivity (from 75 to 100 $kg.m^{-1}.s^{-1}$) for a wide range of flow conditions. The measurements were at the lower limit of the measurement capabilities of the setup.

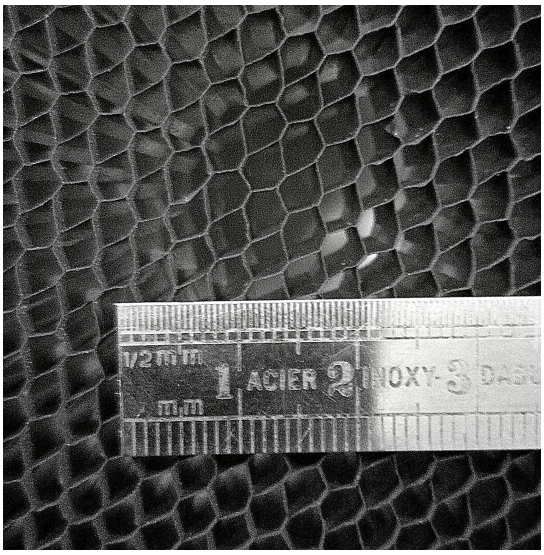

Figure 2.10: Turbulence Control Screen (TCS) honeycomb grid.

For the velocity values estimated at the TCS location for the *LP3* stage, pressure losses can thus be neglected. As for acoustics, a characterization done at École Centrale de Lyon showed an acoustic transparency for the investigated frequency range. For this reason, no significant reflections are expected at the TCS boundary.

In the following sections each measured operating point will be performed with and without TCS. This will allow verifying whether the flow conditions and/or the noise are modified or not.

Inflow distortion and Turbulence Control Screen (TCS) —— Summary

Inflow distortion:

1. Previous study evidenced inflow distortions at the inlet (unsteady vortices)

Turbulence Control Screen (TCS):

1. Objective: remove inflow distortions and homogenize turbulence
2. Acoustically transparent
3. Generates negligible pressure-losses

2.4 Aerodynamic analysis

The aerodynamic analysis presented in this section is separated in two parts. First, the operating conditions of the *LP3* stage are detailed. The impact of the TCS on the mass flow rate, pressure rise and rotational speed variations is discussed. Secondly, inflow conditions are investigated with hot-wire measurements. This will allow concluding on the removal of the inflow distortion by the TCS.

2.4.1 Operating conditions of the *LP3* stage

First, the performance curve of the *LP3* stage is retrieved for two different rotational speeds, see Figure 2.11. For each rotational speed, adjusting the position of the gate valve allows exploring several operating points of the fan. At a constant speed, the maximum mass flow rate point (and lowest Π accordingly) corresponds to the fully opened gate valve. At this condition, the fan provides a relatively small amount of work and is off-design. In contrast, the point at minimum mass flow rate corresponds to a nearly closed gate valve position and is the limit before surge. The intermediate points (distant from both limits) correspond to the conditions for which the fan has been designed (nominal operation).

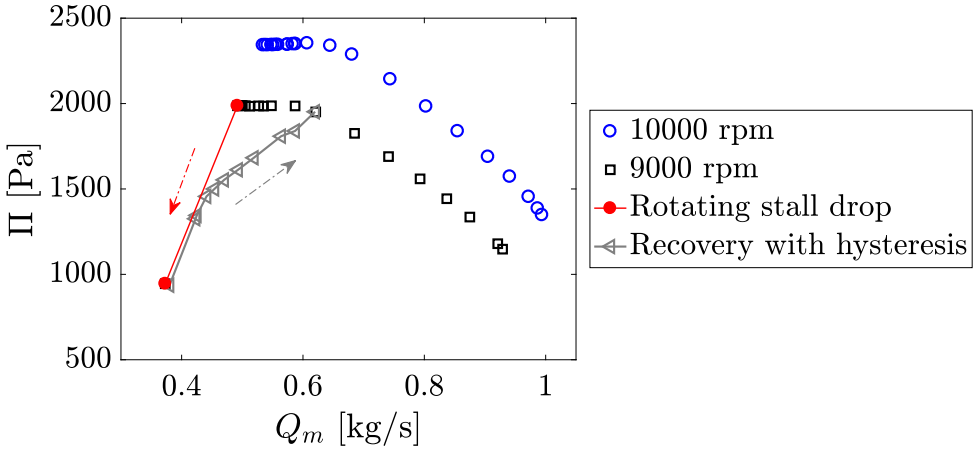

Figure 2.11: Performance curve of the LP3 stage for two rotational speeds.

When closing the gate valve, a plateau is observed for low mass flow rates where the reduction of the mass flow rate does not produce any Π increase. Then, an important drop of the pressure rise is observed, as featured by the red line in Figure 2.11. This drop can be attributed to the rotating stall phenomenon. In fact, a previous aerodynamic characterization of the *LP3* stage evidenced a rotating pattern on pressure signals at the duct wall for these conditions (the rotational speed of the pattern being different from the rotational speed of the rotor). In order to recover the normal operating conditions of the fan, the gate valve is gradually re-opened. A hysteresis cycle is then observed before joining the normal performance curve (gray line in Figure 2.11).

Acoustic measurements of the *LP3* stage were performed far from these conditions to avoid the addition of spurious acoustic sources and vibrations. The *LP3* stage performance is recorded every 30 s during the acoustic measurements. Results are shown in Figure 2.12 with and without the TCS. To compare both cases, the rotational speed and gate-valve position in the duct are fixed. It is clear that variations without TCS are higher than with the TCS (higher data scatter).

This is expected since the TCS should remove any inflow distortion at the inlet. The presence of unsteady vortices at the inlet causes variable inflow conditions and thus an increased variation of the operating point with time. A zoom on the nominal operating

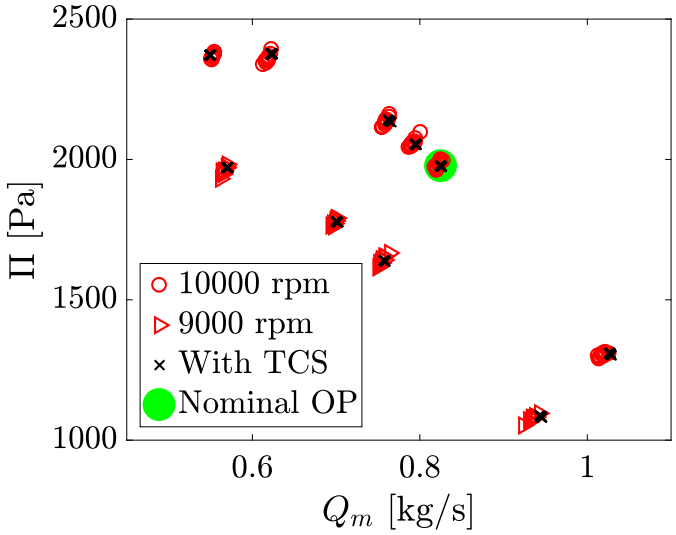

Figure 2.12: Variation of the pressure rise and mass flow rate for 2 different rotational speeds with and without TCS. Operating point recorded every 30 s during the 5 min of recording (cloud of 10 points).

point is shown in Figure 2.13. The Π variations are reduced from around 40 Pa to below 10 Pa. However, it is important to note that initial variations without TCS were already small with a variation amount below the percent. Seemingly, the presence of an inlet vortex also change the barycenter of all variations.

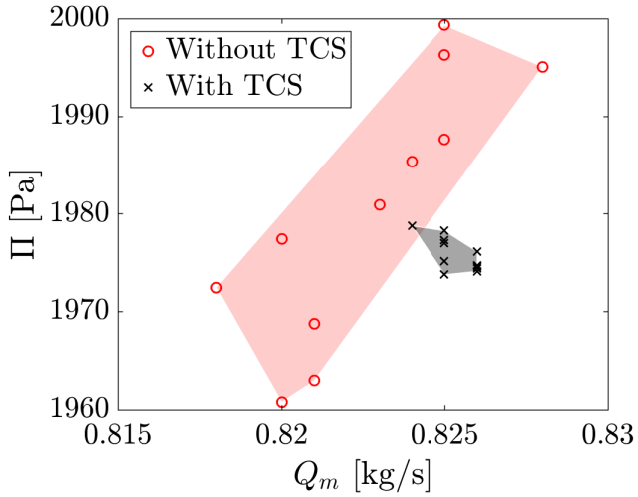

Figure 2.13: Zoom around the nominal operating point that will be investigated at 10,000 rpm. The convex hull of all points is shown with and without TCS.

In addition, one can look at the rotational speed variation recorded from the tachometer signal and shown in Figure 2.14. Variations without TCS can reach 50 rpm and are greatly reduced with the TCS to around 12 rpm. The period of the variations of rotational speed without TCS is observed to be decreased from about 5 rotations to 1 rotation with TCS.

All variations with and without TCS are summarized in Table 3.6. To conclude, the

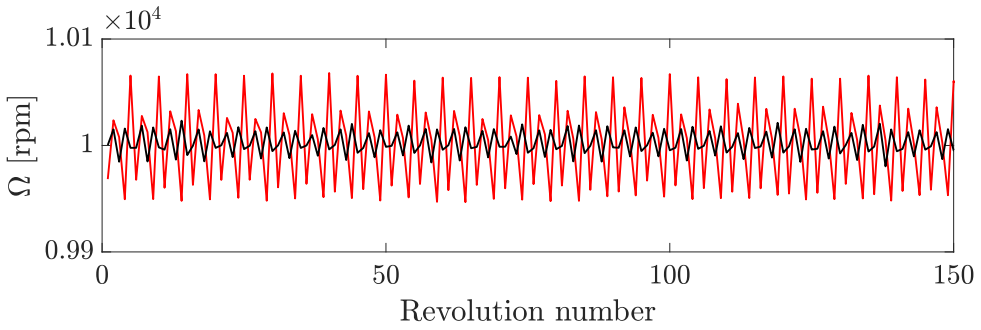

Figure 2.14: Rotational speed time evolution obtained by the tachometer signal. Comparison with TCS ——— and without TCS ——— is shown.

addition of a TCS at the inlet improves the stability of the operating point. Levels of variation are largely below the percent for the mass flow rate, pressure rise and rotational speed.

		With TCS		Without TCS	
		μ	c_v	μ	c_v
Rotational speed	Ω	10002 rpm	0.12%	10003 rpm	0.48%
Mass flow rate	Q_m	0.8254 kg/s	0.08%	0.8227 kg/s	0.34%
Pressure rise	Π	1975.83 Pa	0.08%	1980.63 Pa	0.65%

Table 2.3: Operating point variations at fixed gate valve position. μ is the mean value and c_v the variation coefficient (equal to σ/μ with σ the standard deviation).

The retained nominal operating point that will be simulated afterwards is shown in green in Figure 2.12 and summarized in Table 2.4.

Rotational speed	Ω	10,000 rpm
Mass flow rate	Q_m	0.8254 kg/s
Pressure rise	Π	1975.83 Pa
Atmospheric pressure	p_{atm}	98394 Pa
Turbulence Control Screen		Yes

Table 2.4: Targeted experimental operating point.

2.4.2 Hot-wire anemometry at the inlet

To assess the effectiveness of the Turbulence Control Screen, hot-wire measurements are performed at the inlet as shown in Figure 2.15. Note that the setup has a slightly shorter inlet duct upstream of the rotor compared with the setup used for the acoustic measurements shown in Figure 2.3. This is done for practical reasons regarding the installation of the probe support. Nevertheless, the objective being the characterization of the TCS effectiveness, the duct length difference should not be relevant.

The performed measurement uses a single-sensor miniature wire probe that recovers velocity fluctuations. The hot-wire is positioned in such a way to measure the axial

(a) Hot-wire probe installation at the duct inlet.

(b) Zoom at the hot-wire placed close to the wall.

Figure 2.15: Photos of the hot-wire installation.

velocity component (aligned with the duct direction). However, a small amount of radial flow could be measured because of the inlet geometry which guides the flow inwards the duct. The mesh of measurement positions used is refined close to the duct wall to get acess to the boundary layer and extends from the duct centre to the bottom duct wall.

The mean axial velocity profile is plotted in Figure 2.16 with and without TCS. The mean velocity is nearly constant in the central region and increases towards the tip before the cancellation at the duct wall. The mean profile is not significantly modified with the TCS, with higher variations observed close to the wall.

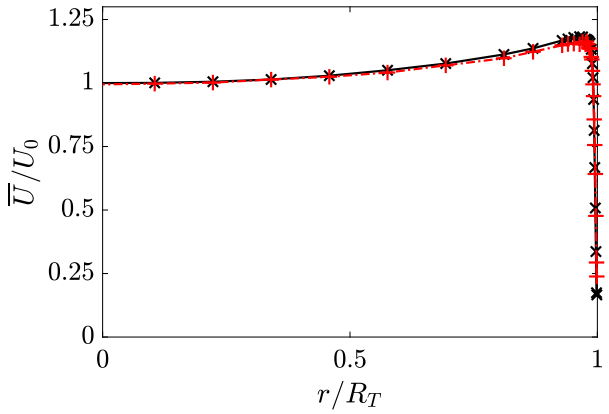

Figure 2.16: Mean velocity profiles $\bar{U}$, measured in the inlet using hot-wire anemometry. R_T denotes the duct radius and U_0 is the velocity at the center of the duct. $\times$: with TCS ; $+$: without TCS

The impact of the TCS on velocity fluctuations is shown in Figure 2.17 where two time signals in the near-wall region are plotted. An important reduction of the fluctuation amplitude is observed with the addition of the TCS. Without TCS, the maximum

fluctuation reaches around 10 m/s, half the mean velocity at that position. The TCS reduces these fluctuations to around 2 m/s.

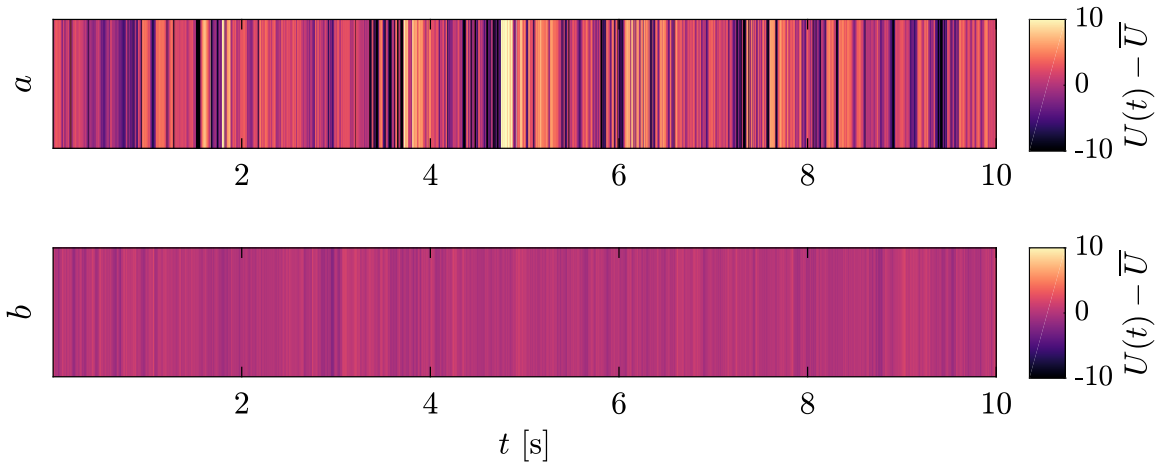

Figure 2.17: Examples of velocity signals $U(t)$ recorded by hot-wire anemometry at the nominal operating point (see Fig. 2.13) at the inlet, at $r/R_T = 0.988$. a) Without TCS ; b) With TCS.

Finally, dimensionless radial profiles of the RMS velocity fluctuation are shown in Figure 2.18. One can see that velocity fluctuations at the centre region are well homogenized with the TCS providing a relatively constant profile of fluctuations below 0.5%. In contrast, the near-wall region corresponds to a higher shear zone due to the friction at the wall. It is where the greatest fluctuation reduction occurs with reductions from 25% to around 2%.

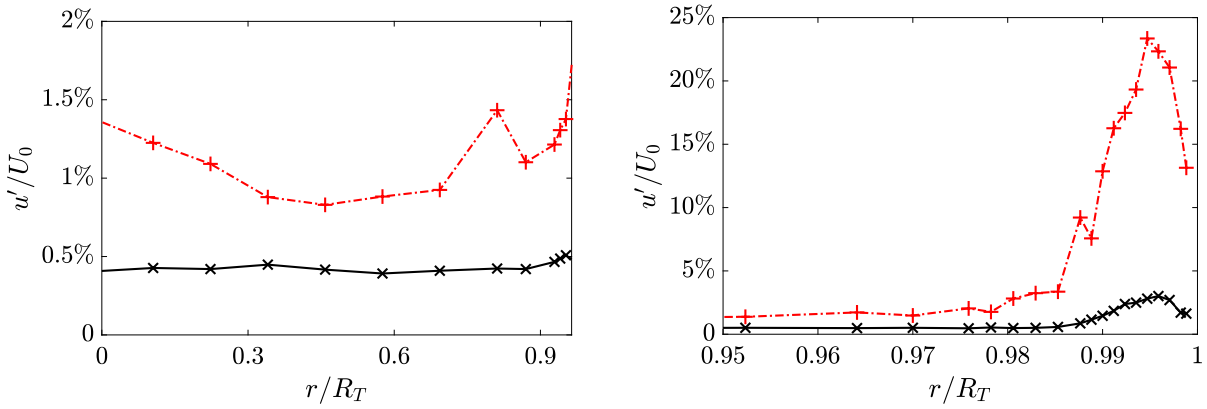

(a) Centre region.

(b) Boundary layer region

Figure 2.18: Root-mean squared velocity fluctuations u' profiles, measured in the inlet using hot-wire anemometry. $U_0 = 28.3$ m.s^{-1} denotes the velocity at the center of the duct, and R_T denotes the radius of the duct. $\times$: with TCS ; $+$: without TCS.

With this analysis, the Turbulence Control Screen effectiveness has been assessed with important reductions of the velocity fluctuations and the homogenization of the velocity profile. As shown in the mean profiles and confirmed in the previous section, the TCS does not change the operating point.

Aerodynamic analysis — Summary

Operating point:

1. Reduction of mass flow rate, pressure rise and rotational speed variations with the Turbulence Control Screen (below 1%)
2. Investigated operating point chosen far from stall and off-design conditions
3. Main investigations at 10,000 rpm

Hot-wire measurements at the inlet:

1. Similar mean velocity profile with and without TCS
2. Homogenisation of the fluctuation velocity profile
3. Reduction of the velocity fluctuation by about 23% near the wall

2.5 Acoustic analysis

In this section, acoustic results will be presented. First, the spectra are calculated from the induct flush-mounted microphones of the upstream and downstream arrays. From these measurements, a more detailed analysis is provided by performing broadband and tonal modal decompositions. According to the Tyler & Sofrin rule, the first two BPFs should be cut-off. Indeed, expected interaction modes should not lie within the cut-on region as shown in Table 2.5. The only cut-on mode should appear at the 3rd BPF with the mode of order $m = 5$. However, in the present case, the heterogeneity is suspected to regenerate cut-on modes at all harmonics.

	p							Cut-on range
	-3	-2	-1	0	1	2	3	
$s = 1$ (BPF 1)	86	63	40	17	-6	-29	-52	$m \in [-3, 3]$
$s = 2$ (BPF 2)	103	80	57	34	11	-12	-35	$m \in [-7, 7]$
$s = 3$ (BPF 3)	120	97	74	51	28	**5**	-18	$m \in [-11, 11]$

Table 2.5: Interaction modes m predicted by the Tyler & Sofrin rule $m = sB - pV$ for the *LP3* case with $B = 17$ and $V = 23$.

2.5.1 Spectral analysis

In Figure 2.19 are shown the averaged spectra of all the microphone signals of the upstream and downstream array with and without TCS. The spectrum is calculated from a 5 min acquisition, over 1 s windows with 66% of overlap using a Hanning window. Spectra of all microphones of the upstream and downstream arrays are then averaged.

In those spectra, tonal and broadband components are observed. On the one hand, the broadband component is here contaminated by turbulent fluctuations (pseudo-sound) since no denoising is performed at this stage. However, all acoustic contributions are also

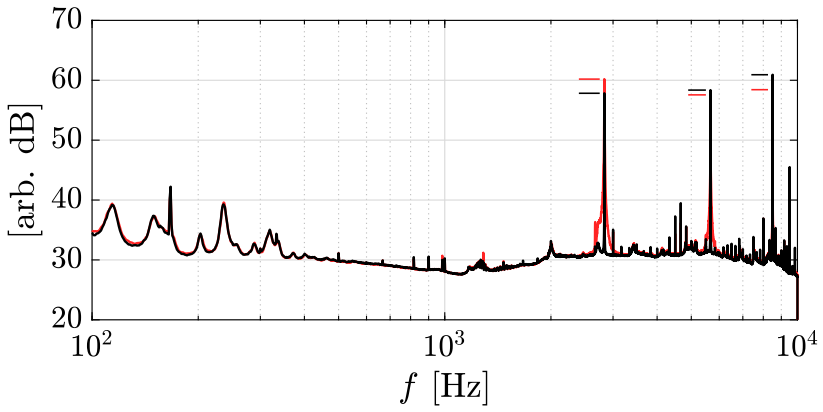

(a) Upstream array

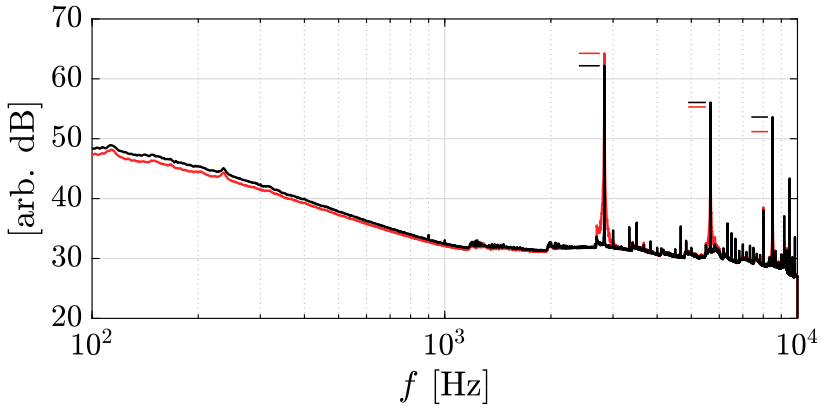

(b) Downstream array

Figure 2.19: Averaged spectra of all microphones of the upstream and downstream arrays. —— with TCS and —— without TCS. $Q_m = 0.8254$ kg.s^{-1}, $\Pi = 1975.83$ Pa and BPF = 2833 Hz. Frequency resolution of 1 Hz

included, such as boundary-layer noise, trailing-edge noise and rotor-stator turbulence impingement noise. In general, the broadband component is seen to be below the tonal noise by 20 to 30 dB. Compared to the upstream array, the downstream array has higher levels at low frequency. This is expected because downstream of the fan, the turbulence rate is higher due to the upstream rotor-stator flow interaction.

On the other hand, clear tones appear at the blade passing frequencies. These tones are generated mainly by rotor-stator interaction mechanisms such as the wake-interaction and potential-interaction. As mentioned previously, the LP3 fan should have the first two BPFs cut-off. However, it can be seen that even with the TCS, they are seen to be radiating at high levels comparable with the 3rd BPF in both arrays. Because inflow distortions have been removed with the TCS, these frequencies are then expected to be caused by the stator heterogeneity. For the upstream array, the BPF level does not decrease for higher BPF harmonics. For the downstream array however, BPF levels are monotonically decreasing with a reduction of more than 10 dB at the 3rd BPF.

Tonal levels are reported in Table 2.6. It can be seen that adding the TCS does not always provide an increase orc a decrease of the BPF level. However, results are similar for both arrays in terms of variation. Levels at the first BPF are decreased by more than 2 dB with TCS, kept almost constant at the second BPF and increased by more than 2 dB at the third BPF.

	Upstream array			Downstream array		
	1 BPF	2 BPF	3 BPF	1 BPF	2 BPF	3 BPF
Without TCS	60.2	57.6	58.4	64.3	55.3	51.2
With TCS	57.8	58.4	60.9	62.2	56.1	53.6
Δ	-2.4	+0.8	+2.5	-2.1	+0.8	+2.4

Table 2.6: Comparison of tone levels (peak levels) in dB with and without TCS.

A zoom on the first 3 BPFs is plotted in Figure 2.20. A clear effect of the TCS is observed with the removal of the broadening around the BPF. This can be partly explained by the removal of an unsteady inflow distortion having a relative motion compared to the rotor rotation as evidenced in section 2.3. Inlet vortices chopped by the rotor will emit sound at frequencies around the BPF and cause a spectral broadening.

Secondly, it was observed that the addition of the TCS also reduced the rotational speed variations. Table 2.7 shows the consequent BPF variations with respect to the rotational speed variations. The addition of the TCS reduces considerably the frequency spreading.

In conclusion, the TCS is very effective in removing the tonal broadening caused by unsteady inlet vortices and by rotational speed variations. Nevertheless, an integrated level around the BPF should be calculated if a more accurate prediction of the tone level variation is wanted. In that case, stronger tone attenuations are expected with the TCS.

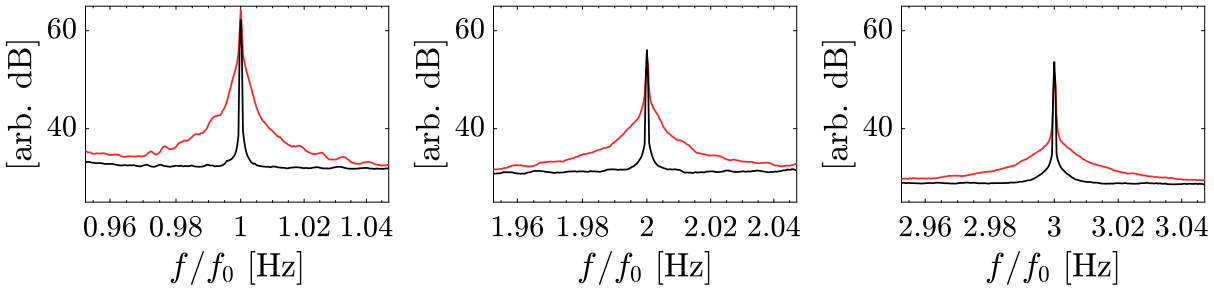

(a) BPF 1 (b) BPF 2 (c) BPF 3

Figure 2.20: Zoomed wall-pressure spectra of the downstream array around the first, second and third blade passing frequencies, the BPF being denoted as f_0. — without TCS and — with TCS. Frequency resolution of 1 Hz.

	cv Ω [%]	Δf BPF 1 [Hz]	Δf BPF 2 [Hz]	Δf BPF 3 [Hz]
without TCS	0.48	$\pm$14	$\pm$27	$\pm$41
with TCS	0.12	$\pm$3	$\pm$7	$\pm$10

Table 2.7: Rotational speed variations and corresponding frequency variations for the nominal operating point at 10,000 rpm with and without TCS. $\Delta f = sB/60 \times \Delta\Omega$.

For the broadband component, levels are identical in both cases.

2.5.2 Engine order analysis

In the previous sections, rotational speed variations were found to lead to a frequency spreading around BPFs. To ensure that the measured level is only related to rotor-stator phenomena occuring at the rotation harmonics, an engine order analysis is performed. The scheme shown in Figure 2.21 explains the procedure. In the previous section, the spectrum was calculated using a fixed time window of 1 s. This should correspond to about 166.67 revolutions contained in 1 s at 10,000 rpm. However, with the rotational speed variations, the number of actually contained revolutions may be increased or decreased.

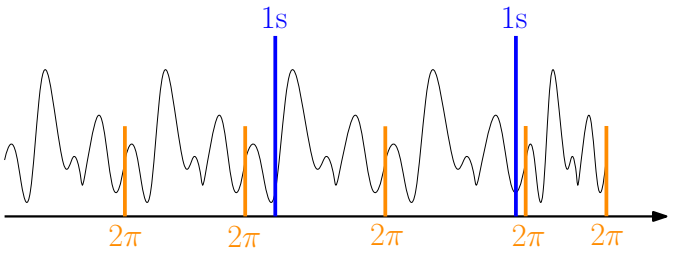

Figure 2.21: Time-signal averaging procedure. Frequency analysis (1 s window) and engine order analysis (1 revolution window).

To overcome this, the signal is resampled so that the new sampling frequency is a multiple of the rotational frequency. With this, it is possible to average the signal over synchronised revolutions. If the number of averages is large enough, the true deterministic part of the signal should be isolated. An engine order is defined as a rotational frequency

harmonic, see Eq. 2.1. For example, the engine order $n = 1$ corresponds to the rotational frequency, $n = B = 17$ to the 1st BPF and so on.

$$\text{EO} = n \quad \text{with} \quad f_n = n\frac{\Omega}{60} \tag{2.1}$$

The resulting spectra are shown in Figure 2.22. The broadband component (read non-deterministic) is greatly reduced by more than 20 dB. However, BPF levels are kept at a similar level with a reduction below 1 dB, see Table 2.8. This means that the measured noise at the BPF is deterministic and due to rotor-stator interactions.

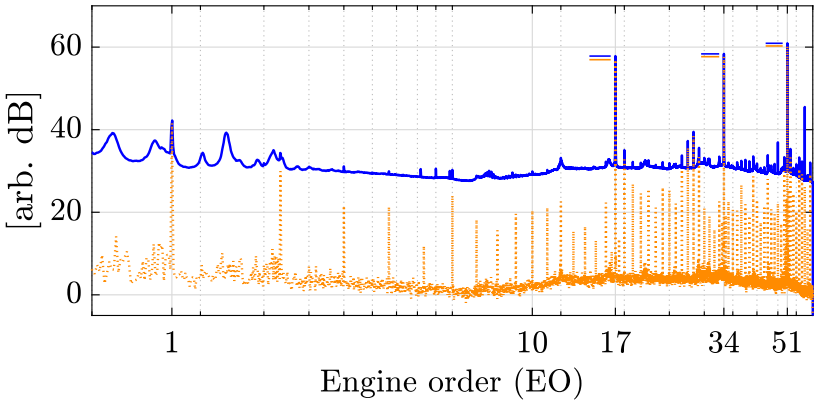

(a) Upstream array

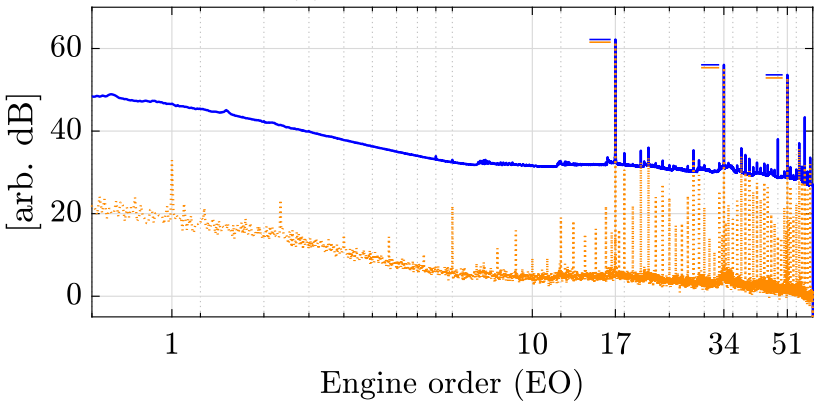

(b) Downstream array

Figure 2.22: —— is the time-average spectrum and —— the rotor-locked averaged spectrum. $Q_m = 0.8254$ kg.s^{-1} and $\Pi = 1975.83$ Pa. Frequency resolution of 1 Hz.

	Upstream array			Downstream array		
	1 BPF	2 BPF	3 BPF	1 BPF	2 BPF	3 BPF
Freq. analysis (1 s window)	57.8	58.4	60.9	62.2	56.1	53.6
EO analysis (1 rev. window)	57.0	57.7	60.3	61.5	55.3	52.9
Δ	-0.9	-0.7	-0.6	-0.7	-0.7	-0.7

Table 2.8: Comparison of tone levels in dB for the frequency and engine order analyses.

The reduction of the broadband component unveils a series of rotational harmonics.

These harmonics should only appear when the rotor geometry in not periodic from blade to blade. An accurate wake measurement would be required in order to conclude. However, some discrepancies from blade to blade may exist from the manufacturing process of the *LP3* stage.

Finally, the cross-spectrum of two neighbouring microphones of the downstream array is shown in Figure 2.23. The selected microphones have the same axial coordinate and are separated by 25° ($\sim$ 40 mm). The cross-spectrum level is about 10 dB below the averaged auto-spectrum. Because the turbulence correlation length is smaller than the distance separating both microphones, calculating the cross-spectrum removes some turbulent fluctuations from the signal. However, at low frequencies and where the correlation length is higher, both auto- and cross-spectra tend to coincide. Finally, it can be observed that the rotor-locked average shown is below the cross-spectrum showing that the non-deterministic part has been correctly removed.

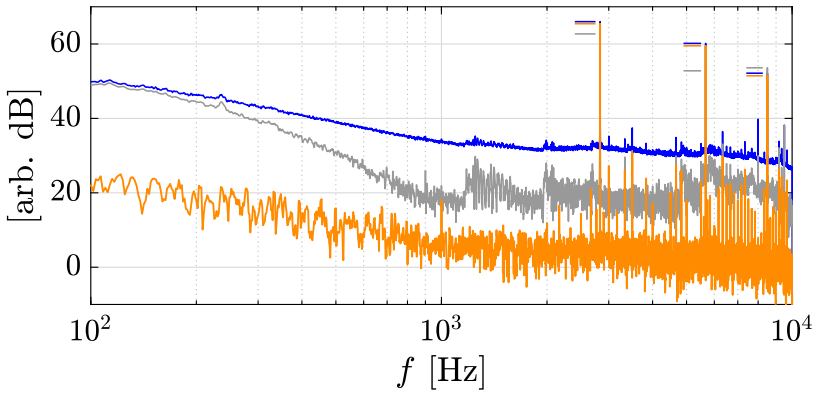

Figure 2.23: Spectra of two closely spaced microphones. In —— is the auto-spectrum of the first microphone, in —— the cross-spectrum of the two microphones and in —— the rotor locked spectrum of the first microphone. $Q_m = 0.8254$ kg.s^{-1} and $\Pi = 1975.83$ Pa. Frequency resolution of 1 Hz.

2.5.3 Modal analysis

In this section, the modal content of the *LP3* stage is computed from the measured pressure fluctuations by the two acoustic arrays. The objective of this decomposition is to provide the modal content of the noise of the turbomachine and to see whether there are or not specific modes possibly generated by the stator heterogeneity. Considering a hard-wall duct with uniform flow, the sound pressure inside the duct can be expressed as a sum of modes as follows:

$$p(x_1, r, \varphi, t) = \sum_{m=-\infty}^{+\infty} \sum_{n=0}^{+\infty} \frac{f_{mn}(r)}{\Gamma_{mn}} \left[A_{mn}^{+} \mathrm{e}^{\mathrm{i}\gamma_{mn}^{+} x_1} + A_{mn}^{-} \mathrm{e}^{\mathrm{i}\gamma_{mn}^{-} x_1} \right] \mathrm{e}^{\mathrm{i}m\varphi} \mathrm{e}^{-\mathrm{i}\omega t}, \qquad (1.1)$$

where the pressure p is measured (known) and $A_{mn}^{\pm}$ are the modal amplitudes (unknowns). More details on the modal basis form are given in Chapter 1 in Section 1.4.2. Far from the

sources and duct discontinuities, the infinite sum may be reduced to a sum over cut-on modes only. This is true when no cut-off modes are measured. As introduced in the previous chapter, the cross-spectral matrix (CSM) is used here and is defined as:

$$\mathbf{S_{pp}} = \mathbb{E}\left\{\mathbf{p}(\omega)\mathbf{p}(\omega)^H\right\}, \tag{1.86}$$

In practice, the expected-value may be well approximated by averaging $\mathbf{p}(\omega)\mathbf{p}(\omega)^H$ over several time-blocks. As also shown, the following equivalent system is solved:

$$\hat{\mathbf{S}}_{\mathbf{cc}} = \mathbf{\Phi}^{\dagger}\hat{\mathbf{S}}_{\mathbf{pp}}{\mathbf{\Phi}^{\dagger}}^{H}, \tag{1.87}$$

The matrix $\mathbf{S_{cc}}$ is called the cross-modal matrix and contains the correlations between the different modes. By taking the diagonal terms, the modal amplitudes defined in the *classical* sense as in Eq. 1.2 can be retrieved:

$$\mathrm{diag}\left\{\hat{\mathbf{S}}_{\mathbf{cc}}\right\} = A^{\pm}_{mn} \times {A^{\pm}_{mn}}^{*} = \left|A^{\pm}_{mn}\right|^2 \tag{2.2}$$

Near the cut-off frequencies or when the number of modes M is larger than the number of microphones N, the matrix $\mathbf{\Phi}$ may be ill-conditioned. In that case, an advanced regularization technique proposed by Pereira et al. [105] can be used.

2.5.3.1 Broadband modal content

In this section, modal decompositions are performed on broadband frequencies. In this case, the difficulty comes from the fact that pressure fluctuations are dominated by turbulent fluctuations (or pseudo sound) generated from the turbulent boundary layer at the wall. Unlike for the tonal noise component which has levels well above the broadband spectrum (more than 20 dB), the hydrodynamic contribution must be removed from measurements to extract the acoustic part. For this, a specific de-noising technique must be performed on the cross-spectral matrix.

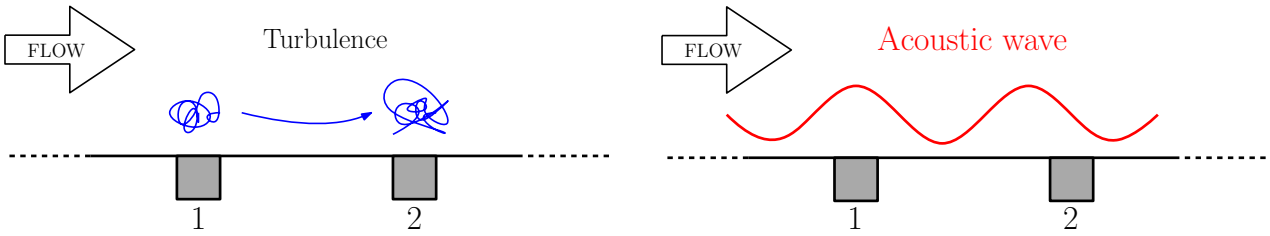

(a) Low correlation between two microphones for hydrodynamic events (turbulence).

(b) High correlation between two microphones for acoustic events.

Figure 2.24: Schematic view of the microphone correlation for hydrodynamic (turbulent) and acoustic events.

The correlation between two microphones for events associated with turbulence and acoustics is sketched in Figure 2.24. At low Mach-number, the evolution time-scales of

turbulence are generally small enough such that if a sufficient distance separates two microphones, what one measures is decorrelated from what the other measures. This implies that the hydrodynamic contributions will be mainly contained in the diagonal of the cross-spectral matrix. On the other hand, the correlation for acoustic events will be higher between the two microphones. This means that acoustic fluctuations will be present not only in the diagonal terms but also in off-diagonal terms of the CSM. The CSM amplitude values are shown for a tonal frequency (the BPF) and a broadband frequency $f = 1000$ Hz in Figure 2.25. On the one hand, the previous hypothesis is validated with a dominant diagonal for the broadband frequency case. On the other hand, at a tonal frequency which is more than 20 dB above the broadband level, the matrix is not dominated by the diagonal.

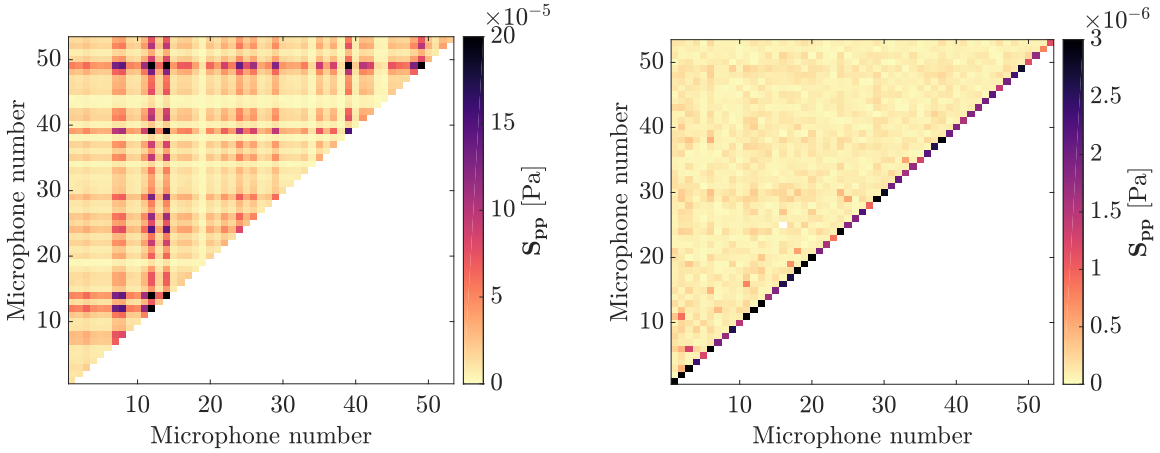

(a) BPF, $f = 2834$ Hz.

(b) Broadband frequency, $f = 1000$ Hz.

Figure 2.25: Cross-Spectral Matrices at tonal and broadband frequencies.

The chosen method for the de-noising is described by Finez et al. [89] and called Sparse & Low-Rank Decomposition (SLRD). The method is also described in chapter 1 in section 1.6.3.

Results for the broadband modal decompositions are shown in Figures 2.27 and 2.26 in the form of diagrams of azimuthal modes order versus frequency. For higher frequencies, the number of cut-on modes increases as evidenced by the results. To highlight the broadband level, the colormap scale has been reduced. Therefore, the tonal component of the noise at the BPF is saturated. In addition, only the radial order $n = 0$ is shown to reduce the number of diagrams and make the interpretation easier. Note that in this configuration the majority of the energy is contained in the radial order $n = 0$.

Results evidence a concentration of the energy close to the cut-off modes [112]. Because the cut-off is a resonant condition, this behaviour is expected. Secondly, one can clearly see that harmonics of BPF at 2.83, 5.67 and 8.5 kHz. The addition of the turbulence control screen is seen again to clearly remove the broadening of the BPFs.

No dominant modes appear at broadband frequencies for the upstream and downstream arrays. However, some spots of higher levels are observed for the downstream

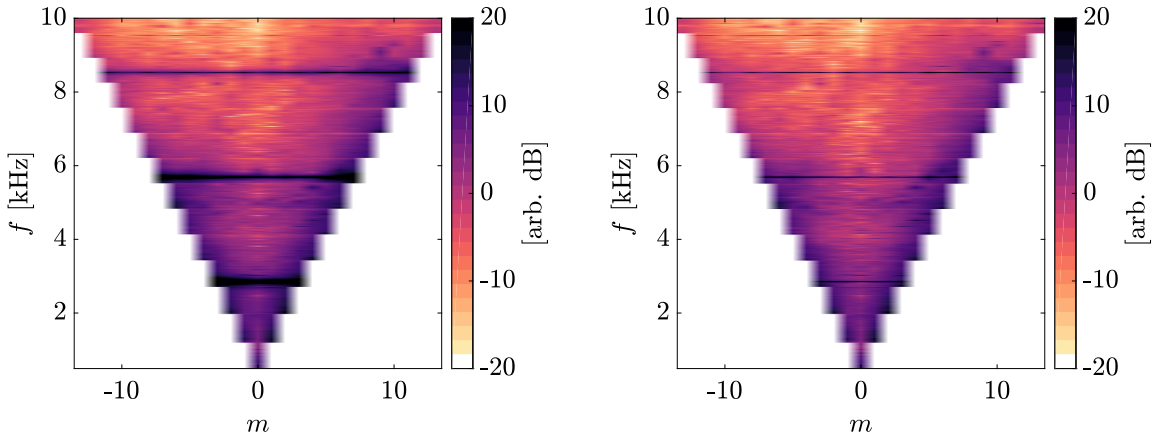

(a) Without TCS. (b) With TCS.

Figure 2.26: Broadband modal content of the upstream array with and without TCS. $Q_m = 0.8254$ kg.s^{-1} and $\Pi = 1975.83$ Pa. Frequency resolution of 8 Hz.

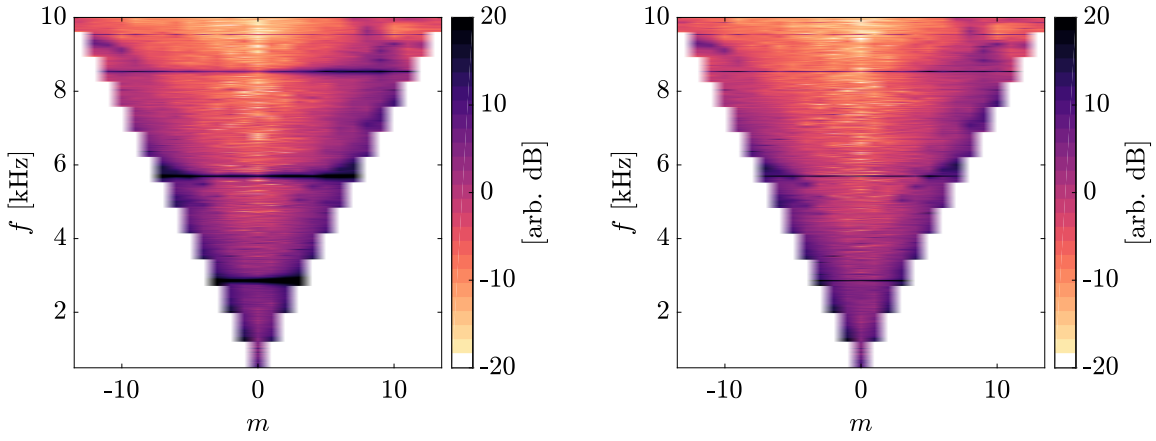

(a) Without TCS. (b) With TCS.

Figure 2.27: Broadband modal content of the downstream array with and without TCS. $Q_m = 0.8254$ kg.s^{-1} and $\Pi = 1975.83$ Pa. Frequency resolution of 8 Hz.

array around the second BPF and above the third BPF close to the cut-off. Because, downstream turbulence levels are higher, these spots could be the noise or turbulent fluctuations associated with strong turbulent structures generated through the rotor-stator interaction. Compared with the downstream array, the upstream array has higher levels in the centre of the area. This increase indicates stronger upstream radiation at those broadband frequencies.

Because the *LP3* stage is a low-speed turbomachine, a strong imbalance between co- and counter- rotating modes is not expected. Nevertheless, a slight predominance of co-rotating modes is observed (see levels between the 1^{st} and 2^{nd} BPFs).

2.5.3.2 Tonal modal content

In this section, we study the tonal component of the noise. For this, we use the previously described modal decomposition at the BPFs. Because the tonal noise emerges from the broadband level by more than 20 dB, no de-noising technique is applied.

In the first place, rotational speed variations are not accounted for. Figures 2.29 and 2.30 show the results for the first 3 BPFs for the upstream and downstream arrays respectively. As a reminder, as part of a perfectly homogeneous theory, the first two FPPs should be cut-off. The generated interaction modes would be of an azimuthal order high enough to be cut-off.

For the first BPF, a dominant mode of order $m = -3$ is clearly observed. This mode has a larger modal amplitude than the other modes and is visible on both upstream and downstream antennas. The amplitude on the downstream antenna is almost 3 times higher compared with the upstream array. At the second BPF, modes $m = 5$ and $m = 7$ for the upstream antenna and the mode $m = 7$ for the downstream antenna are seen to be dominant. Levels are higher for the upstream array. Finally, at the third BPF, two dominant modes of azimuthal order $m = 5$ and $m = 11$ are seen. Amplitudes are higher on the upstream antenna. At this BPF, the mode $m = 5$ is well predicted by the Tyler & Sofrin rule as calculated in equation 2.3. It should also be present for a homogeneous stator.

$$m = sB - pV = 3 \times 17 - 2 \times 23 = 5 \tag{2.3}$$

Globally, levels of the reflected modes are very low. For the upstream array, upstream propagating modes are dominant and for the downstream array, downstream propagating modes are dominant. This means that both duct terminations upstream and downstream are not very reflective, see sketch in Figure 2.28.

Finally, the energy is mostly seen to be contained in the radial order $n = 0$. This is partly explained by the fact that in this configuration, higher radial mode orders are cut-off. The only mode where an important amplitude is measured for the radial order $n = 1$ is the T&S mode found at the third BPF for the upstream array. Table 2.9 summarizes

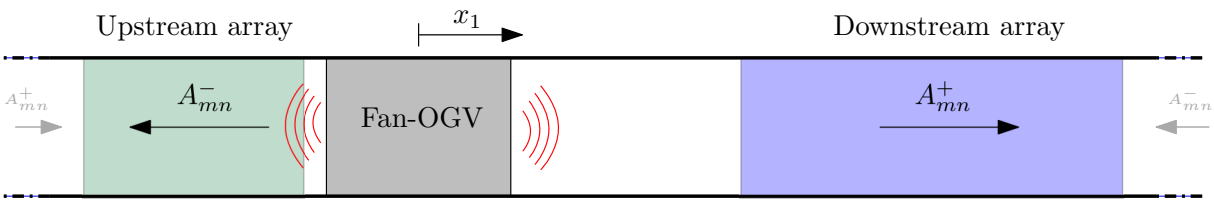

Figure 2.28: Upstream and downstream propagating waves.

the identified dominant modes at the first three BPFs.

	m upstream (A^-_{mn})	m downstream (A^+_{mn})
BPF 1	-3	-3
BPF 2	+5 , +7	+5
BPF 3	+5 , +11	+5

Table 2.9: *LP3* measured dominant modes. Tyler & Sofrin modes in red.

In Figure 2.31, the modal content at the radial order $n = 0$ is shown with and without TCS for the upstream and downstream arrays. Globally, the same dominant modes are identified. However, one particular behaviour is observed at the first BPF of the upstream array, namely the cancellation of the dominant mode from $m = +3$ with TCS. Considering the sensibility of the prediction near the cut-off, this cancellation could be due to the reduction of the unsteadiness observed with the TCS. Globally, the difference in levels observed for the modes agrees with the previous spectral analysis. The addition of the TCS does not reduce the tone levels for all cases. Depending on the frequency, an increase or a decrease can be observed. At the 3$^{\text{rd}}$ BPF, levels increase considerably when adding the TCS as opposed to the 1$^{\text{st}}$ BPF where a reduction is observed.

Finally, engine order modal decompositions are done. They are aimed at verifying that the measured modes are only due to the rotor-stator interaction mechanisms. The rotor-locked time-signals used in the spectral analysis are then used to perform the modal decompositions. Results are shown in Figure 2.32. The engine order analysis gives lower levels for all modes. This is consistent with the spectral analysis where a small reduction of the BPF level has been observed. The same behaviour is observed for the downstream array.

To conclude, the rotational speed variations with the TCS are small enough so that the analyses in frequency and engine order provide similar results. Opposed to that, results without TCS (not shown here) evidence higher discrepancies between both analyses. This is explained by stronger rotational speed variations measured without TCS as shown in section 2.4.1.

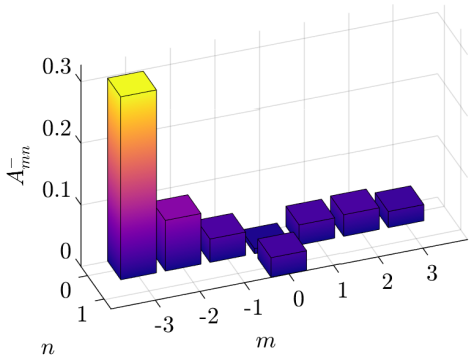

(a) 1st BPF (upstream waves)

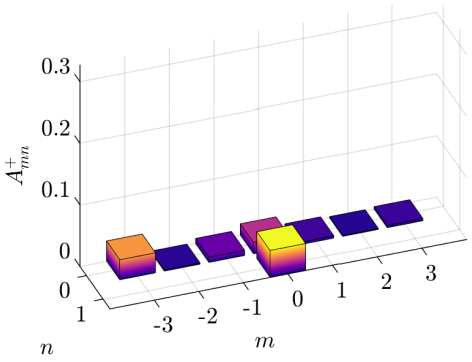

(b) 1st BPF (downstream waves)

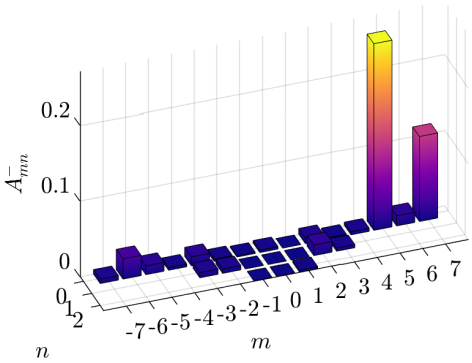

(c) 2nd BPF (upstream waves)

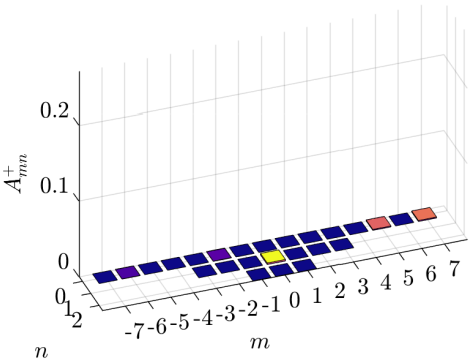

(d) 2nd BPF (downstream waves)

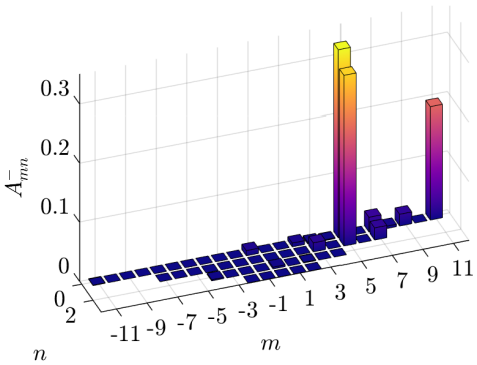

(e) 3rd BPF (upstream waves)

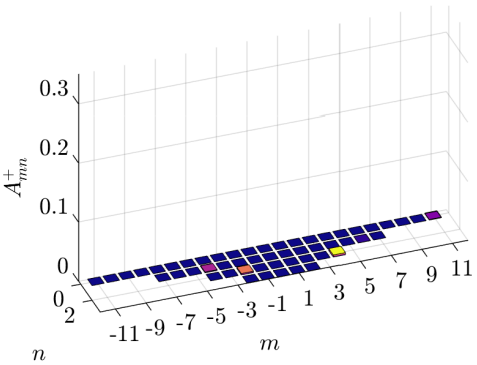

(f) 3rd BPF (downstream waves)

Figure 2.29: Tonal modal content of the upstream array with TCS (frequency analysis). Comparison of upstream and downstream propagating waves. $Q_m = 0.8254$ kg.s^{-1} and $\Pi = 1975.83$ Pa

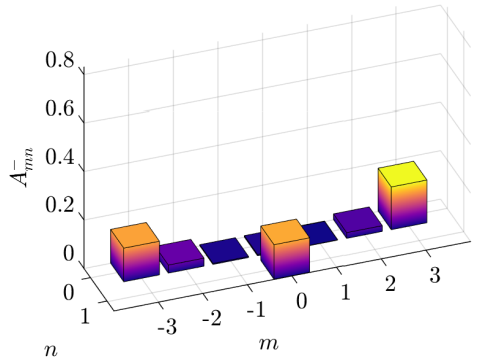

(a) 1st BPF (upstream waves)

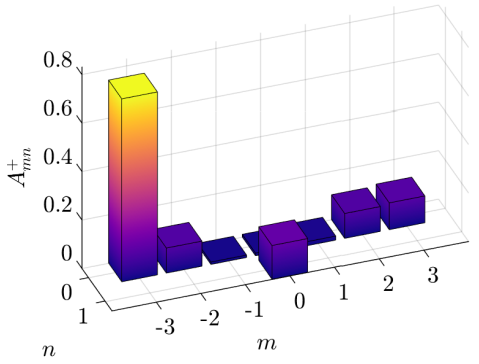

(b) 1st BPF (downstream waves)

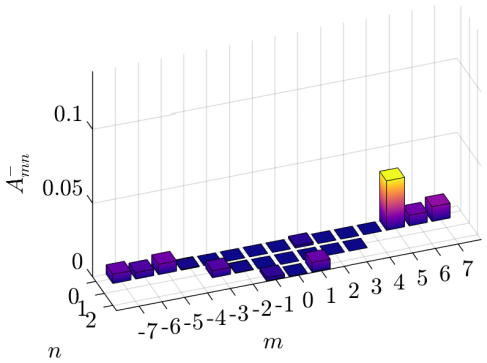

(c) 2nd BPF (upstream waves)

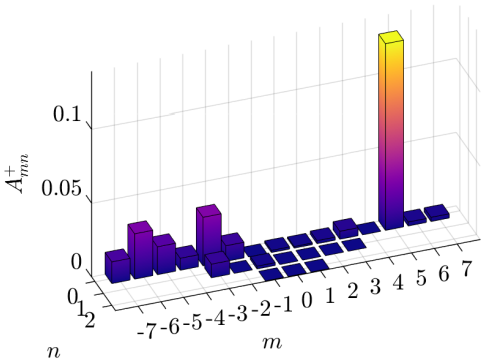

(d) 2nd BPF (downstream waves)

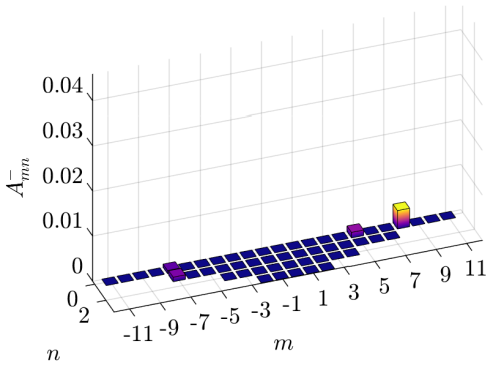

(e) 3rd BPF (upstream waves)

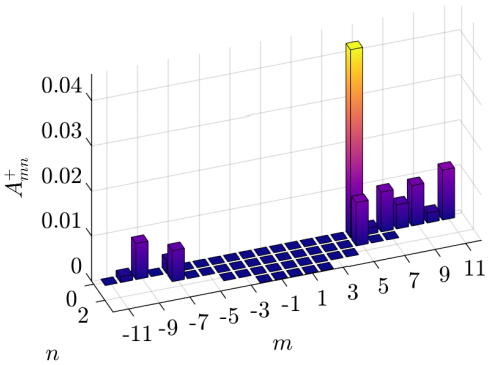

(f) 3rd BPF (downstream waves)

Figure 2.30: Tonal modal content of the downstream array with TCS (frequency analysis). Comparison of upstream and downstream propagating waves. $Q_m = 0.8254$ kg.s^{-1} and $\Pi = 1975.83$ Pa

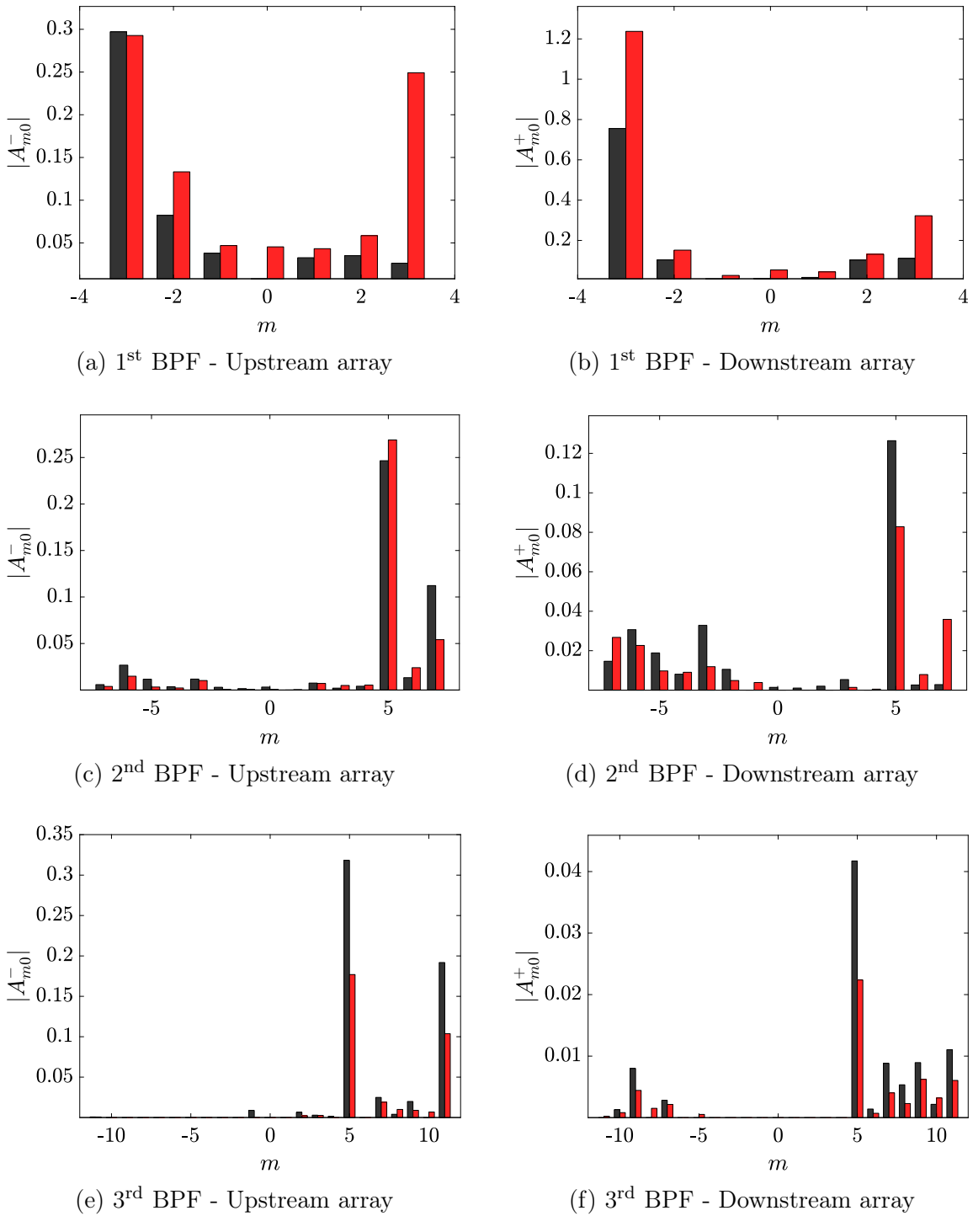

(a) 1st BPF - Upstream array

(b) 1st BPF - Downstream array

(c) 2nd BPF - Upstream array

(d) 2nd BPF - Downstream array

(e) 3rd BPF - Upstream array

(f) 3rd BPF - Downstream array

Figure 2.31: Tonal modal content of the downstream and upstream array (frequency analysis). Comparison with TCS in ■ and without TCS in ■. $Q_m = 0.8254$ kg.s^{-1} and $\Pi = 1975.83$ Pa

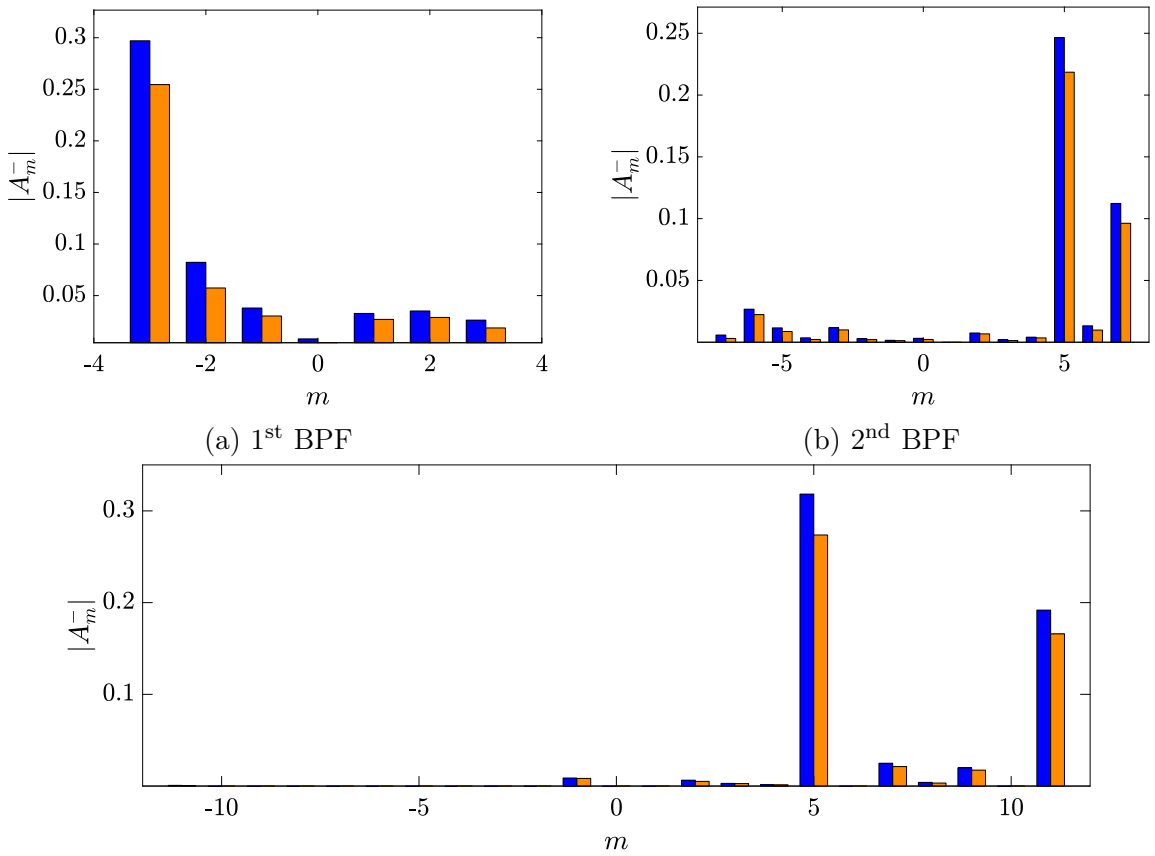

(a) 1st BPF

(b) 2nd BPF

(c) 3rd BPF

Figure 2.32: Tonal modal content of the upstream array with TCS at the radial order $n = 0$. Comparison of the frequency analysis in ■ and the engine order analysis in ■. $Q_m = 0.8254$ kg.s^{-1} and $\Pi = 1975.83$ Pa

Acoustic analysis — Summary

Spectral analysis:

1. Sharpening of BPF tones with the TCS - additional effectiveness validation of the TCS
2. Decrease of the noise level at the 1st BPF with TCS and increase of the noise level for the 2nd and 3rd BPF with TCS
3. Broadband component unchanged
4. Engine order analysis providing similar results as the frequency analysis - low impact of the rotational speed variations with TCS

Broadband modal content:

1. Slight predominance of co-rotating modes
2. Higher mode energy close to the cut-off
3. Similar with and without TCS except for the sharpening of the BPFs

Tonal modal content:

1. Very weak reflections at the duct termination and at duct inlet
2. Dominant modes that should be due to the stator heterogeneity observed at the first 3 BPFs:
   - BPF 1: $m = -3$
   - BPF 2: $m = 5, 7$
   - BPF 3: $m = 11$
3. Mode predicted by the original Tyler & Sofrin's rule found at the expected cut-on frequency (BPF 3, $m = 5$)
4. Change in the mode amplitude with and without TCS in accordance with the spectral analysis
5. Engine order analysis producing slightly decreased mode amplitudes but the same dominant modes

2.6 Conclusion

In this chapter, the experimental characterization of the *LP3* stage has been performed. An identified unsteady inflow distortion was removed with the addition of a Turbulence Control Screen. Hot-wire measurements have shown that no inflow distortion remained in the inlet. This is an essential pre-requisite to isolate the rotor-stator interaction noise.

The spectral analysis evidenced highly emerging first two BPFs upstream and downstream of the fan. As explained before, according to Tyler & Sofrin's rule, the *LP3* should have the first two BPFs cut-off. The heterogeneity is at this point the unique plausible explanation for the re-generation of these frequencies.

The modal decomposition on broadband-noise frequencies was done on a de-noised

Cross Spectral Matrix. No evidence of dominant modes has been found and the impact of the heterogeneity on this component is expected to be negligible.

The tonal modal content evidenced dominant modes at all frequencies. The only expected Tyler & Sofrin mode is found at the 3rd BPF. All the other identified dominant modes are expected to be generated by the stator heterogeneity from the loss of the vane-to-vane periodicity.

To conclude, the question of experimental uncertainties is shortly discussed. In terms of repeatability, it is often complicated to reproduce the exact same operating conditions between two experiments. In fact, a small variation of the operating conditions may induce considerable differences in the level of tones. During the measurements, the operating point was observed to have low variations of about 0.12% for the rotational speed and 0.08% for the mass flow rate with a Turbulence Control Screen. The engine order analysis presented in this chapter is one way to address these uncertainties by accounting for rotational speed variations. However, slight differences in the atmospheric conditions from two different experiments could easily produce gaps up to 1% between both. Weckmüller et al. [113] showed that a difference in the operating condition of about 1.6% induced several decibels of discrepancy on the mode levels. Despite this, the modal content was very similar in both cases. This is to keep in mind when comparing experiments and numerical simulations where fighting for a 1 dB accuracy is certainly too restrictive in this regard.

3 Numerical investigation of the LP3

Contents

In the previous chapter, the *LP3* configuration was experimentally characterized. Unexpectedly, the first two BPFs were observed to radiate at high levels in contradiction with the prediction of the classical theory of rotor-stator noise with homogeneous stages. At these frequencies, some dominant modes were measured by the upstream and downstream acoustic arrays and expected to be caused by the stator inhomogeneity. In this chapter, the objective is to simulate the experimental setup with the LBM and assess if the measured modes are indeed produced by the stator heterogeneity. For that, a homogeneous stator will also be simulated by replacing the thickened vanes by baseline vanes. Secondly, another objective is to estimate the relative weight of the expected two majors tonal noise mechanisms: the potential-interaction noise and the wake-interaction noise.

3.1 Description of the setup and simulated configurations

The used *LP3* geometry corresponds to the original full three-dimensional CAD model where some geometrical simplifications have been introduced. As shown in Figure 3.1a, the rotor blades have been extruded so that no tip gap exists at the duct wall. This simplification has been introduced because of the very small tip gap of about 0.3 mm. In practice, it means that the numerical mesh required to fully resolve this near-wall region is very costly. The finest mesh described in the next section would have four points in this region, which is too low to ensure the good resolution of the tip gap flow.

The second geometrical modification that was introduced is the removal of the rotor and stator hub gap as shown in Figure 3.1b. The secondary flow generated in this region is not expected to have a significant impact on the interstage flow and was thus simplified.

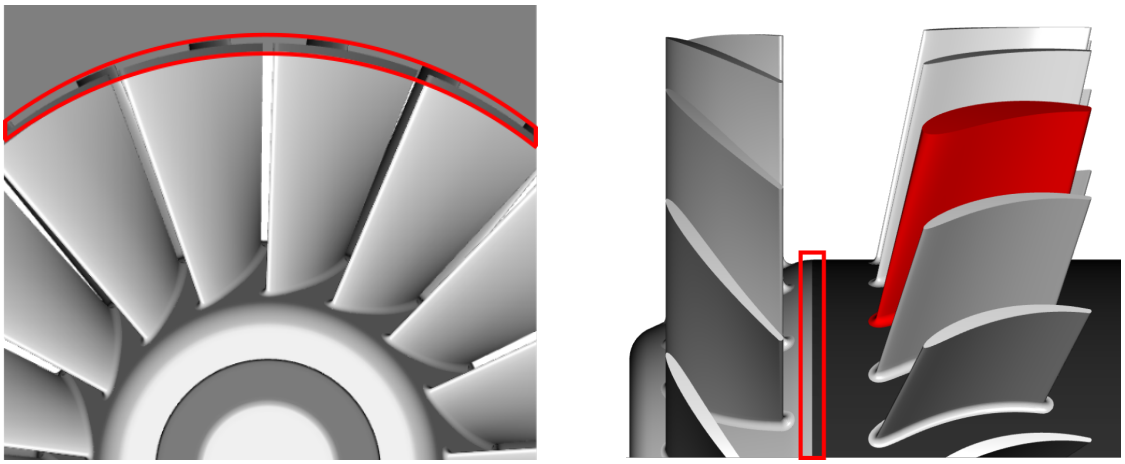

(a) Blade extrusion.

(b) Gap between the rotor and stator hub filled.

Figure 3.1: *LP3* geometrical simplifications.

The *LP3* geometry was then introduced in its experimental environment accounting for the real room dimensions, see Figure 3.2. Note that the fan duct is not centred in the room (see front view in Figure 3.2b) as in the experiments. The consequence of that is the establishment of an inflow inhomogeneity over time [19]. Parameters of the room are summarized in Table 3.1.

l	L	h	H	w	V	Q_v	$t_f = V/Q_v$
6.2 m	8.1 m	3.0 m	3.9 m	4.6 m	139.7 m^3	0.71 m^3/s	$\sim$ 209 s

Table 3.1: Experimental room characteristics and filling time at nominal conditions. V is the fluid volume, Q_v the volumetric flow rate and t_f the filling time.

According to the calculated filling time, one can see that in order to replace the whole fluid volume once, 209 s of simulation time are necessary. Because simulation times are

usually at least two orders of magnitude shorter (below the second), an inflow distortion is not expected in the simulated configurations. With this in mind, there is *a priori* no necessity to model the Turbulence Control Screen (TCS). The assessment of the clean inflow conditions is described in section 3.3.3. Finally, by taking into account the real duct geometry, the same propagating conditions as in experiments are ensured. The real room dimensions have been kept in the following simulations because of the negligible additional computational cost. Indeed, the fan-OGV regions with higher mesh resolutions are the most computationally demanding.

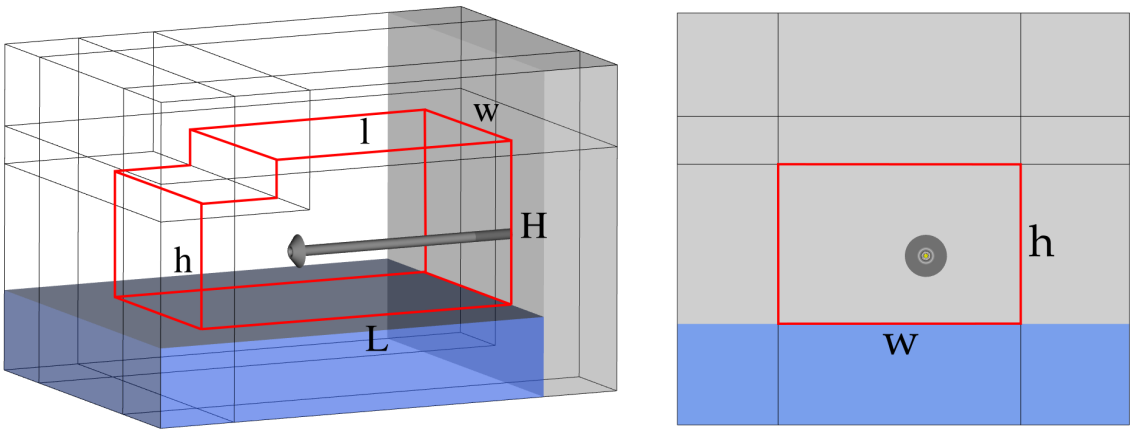

(a) Perspective view. (b) Front view.

Figure 3.2: Simulated domain. Fluid zone highlighted in red.

Compared to the experiments, some simplifications have been introduced in the simulation domain. The anechoic settling chamber has been replaced by sponge zones in the duct far downstream of the fan-OGV. The ejection duct portion used to re-insert the outgoing flow is replaced by a free-velocity inlet back-wall. Details are provided in the meshing section 3.2.

In terms of simulated geometries, three different configurations have been investigated, see Figure 3.3.

The first simulated configuration is the original *LP3*. It has a heterogeneous stator with 3 modified stator vanes and a power-supply cable placed downstream of the stator. The second simulated configuration was obtained by replacing the thickened vanes by baseline vanes. This makes the vane-to-vane periodicity recovered. Finally, in the last configuration, the power-supply cable was removed leading to a homogeneous stator cascade without any downstream azimuthal inhomogeneity. The comparison of the three configurations should allow the quantification of the impact of the stator heterogeneity.

3.1.1 Numerical extractions

In order to have a detailed description of the flow and acoustics in the simulation, several extractions have been placed at regions of interest, see Figures 3.4 and 3.5. The extractions

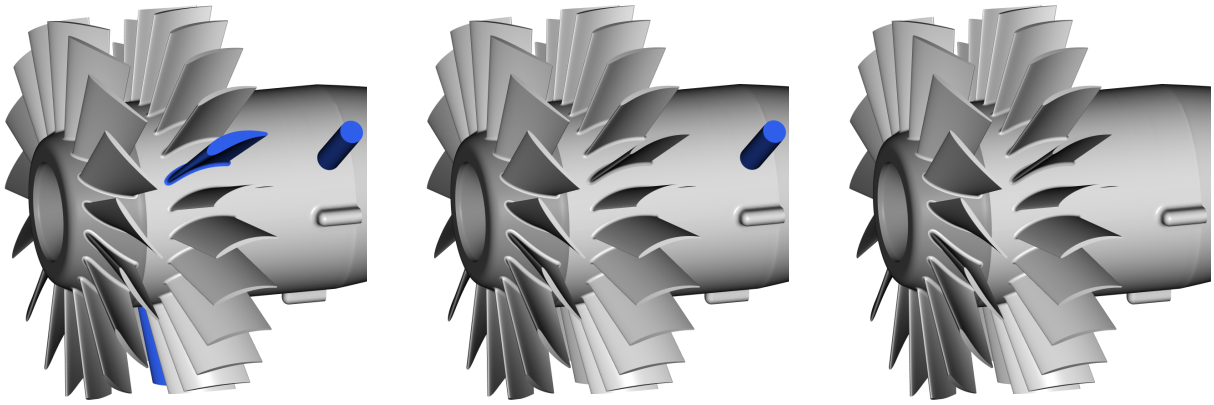

(a) Heterogeneous (experimental configuration).

(b) Homogeneous.

(c) Homogeneous without power-supply cable.

Figure 3.3: Simulated *LP3* configurations.

can be separated in three majors categories: acoustics, low-frequency aerodynamics and high-frequency aerodynamics, as defined in Table 3.2.

Aerodynamic disks	Fig. 3.4 and 3.5a	F_e	1000 Hz
Acoustic disks and probes	Fig. 3.4	F_e	21075 Hz
Fine aerodynamic volume	Fig. 3.5b	F_e	59510 Hz

Table 3.2: Extraction parameters. F_e is the sampling frequency of the extraction.

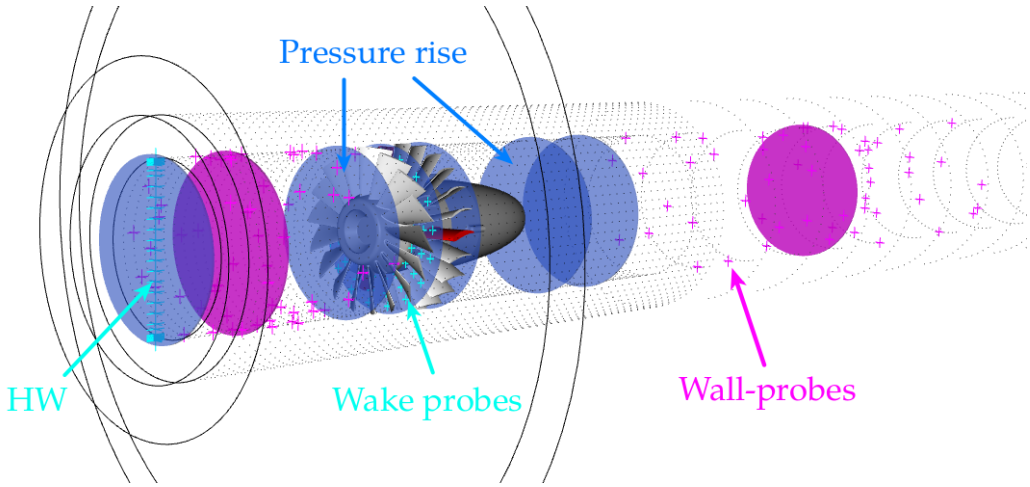

Figure 3.4: Acoustic and aerodynamic numerical extractions.

The low-frequency aerodynamic extractions shown in blue in Figures 3.4 and 3.5a are meant to provide the mean quantities such as the operating conditions and also instantaneous visualizations of the flow field. There are several planes placed at different axial positions and also cylindrical cuts at hub, midspan and tip. Each cut corresponds to a duct height percentage (r/R_T) of 61%, 79% and 95% respectively.

The pressure rise of the *LP3* is computed from two extraction disks placed at the same axial position as in the experiments. The quantity Π is thus calculated from the

disk just upstream of the fan and from the disk just downstream of the hub termination, see Figure 3.4. The pressure is circumferentially averaged at the wall to obtain the mean static pressure.

The acoustic disks and probes shown in magenta ensure a maximal study frequency of 10 kHz, thus around 2 kHz above the third BPF. The relative position of the acoustic probes was taken identical to the experimental antennas to perform the same post-processings and ensure relevant comparisons. Some other probes have been set in the domain. The experimental hot-wire probes have been placed at the inlet and shown in cyan. In addition, some rotor wake probes in the rotating reference frame were also set and are shown in cyan. All these additional probes were set with the same acquisition parameters as of the acoustics probes.

Finally, the volume shown in Figure 3.5b is used to perform fine interstage analysis. The 59,510 kHz sampling frequency is obtained by considering 360 pts/revolution. This fine temporal discretization is necessary in order to perform phase averages to separate contributions from the rotor wakes and the stator potential field. This extraction being expensive in terms of memory, it has only been done in the coarsest mesh and is detailed in section 3.3.6.

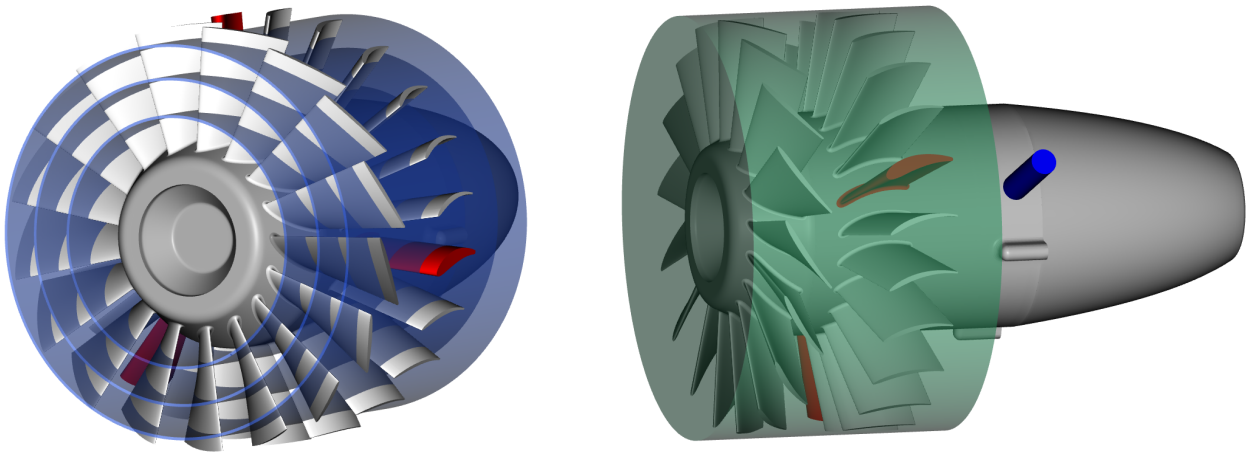

(a) Cylindrical extractions at hub, midspan and tip.

(b) Rotor-stator volume for fine extractions.

Figure 3.5: Rotor-stator extractions.

Description of the setup and simulated configurations ——— Summary

Geometry and simulation domain:

1. Rotor blades extruded up to the duct wall
2. Real room dimensions accounted for
3. 3 stator configurations investigated :
   (a) Heterogeneous (as in experiments)
   (b) Homogeneous (periodic from vane-to-vane)

(c) Homogeneous without the power-supply cable

Numerical extractions:

1. Three categories of extractions: low-, mid- and high-frequency
2. Acoustic probes placed at the same positions as in the experimental antennas

3.2 Meshing strategy and boundary conditions

In this section, the meshing strategy and boundary conditions are detailed. In the LBM, the Cartesian mesh is generated automatically from what are called refinement volumes. A refinement volume (VR) defines a region where the volume cell size (voxel) is constant. Also, the voxel size in the neighbouring coarser VR is decreased by a factor of 2. This is imposed by the mesh refinement method used in PowerFLOW and is discussed in section 1.5.2 of chapter 1.

The first VRs, sponge zones and boundary conditions are shown in Figure 3.6. The outlet boundary condition at the duct termination (shown in red) imposes a uniform axial velocity profile in order to match the desired mass flow rate. The mass flow rate has not been imposed directly because it is a very reflective condition not suited for acoustic studies. The whole back-wall (shown in green) of the domain is used as inlet. The atmospheric pressure is imposed and the velocity set free. This differs from the experimental setup where the air is re-introduced in the room through a duct portion. However, for the considered simulation times and since velocities in this region are very small, this simplification should not impact significantly the way the flow is re-introduced in the room.

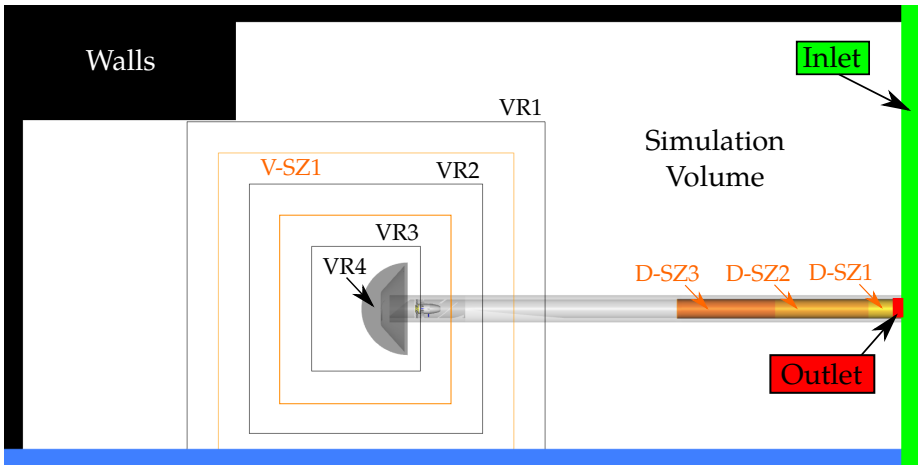

Figure 3.6: Mesh refinement volumes, sponge zones and boundary conditions.

The mesh construction is now described. Starting from the simulation volume with the biggest voxel size, three successive cubic VRs (VR1 to VR3) are added centred on the duct

inlet. An additional semi-spherical refinement volume (VR4) is then added surrounding the inlet.

Regarding the sponge zones, the objective is to absorb acoustic waves and avoid unrealistic hard-wall reflections at the walls or boundary conditions. For this, the viscosity is artificially increased in some areas of interest. Two sponge zones (V-SZ1 and the simulation volume considered as such) have been set in the room and three in the duct far downstream (D-SZ1 to D-SZ3). The sponge zones in the room aim at reproducing some wall treatment actually installed in the experimental room. Those in the duct intend to mimic the anechoic settling chamber that was not modelled in the simulation. For these sponge layers, the viscosity parameter was increased based on past studies using PowerFLOW, see Table 3.3.

Zone	Nu/T
Simulation volume	0.5
V-SZ1	0.05
D-SZ1	0.01
D-SZ2	0.05
D-SZ3	0.5

Table 3.3: Sponge zones parameters.

The next refinements are done inside the duct as shown in Figure 3.7. A particular attention was given to the voxel size in VR5 so that acoustic propagation up to 10 kHz was ensured in the simulation. This is crucial since the acoustic antennas are placed at the duct wall in this VR. A summary of the voxel size and associated maximum resolved propagating frequency is given in Table 3.4 for each VR level.

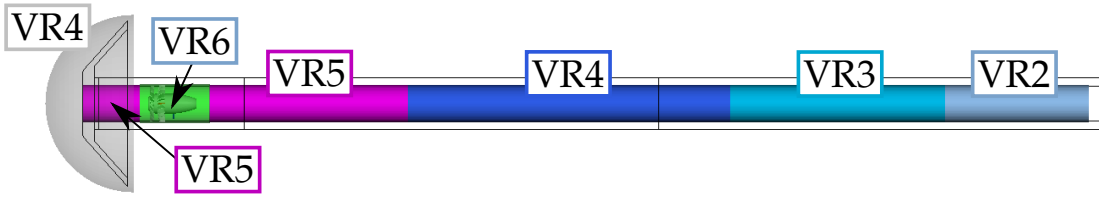

Figure 3.7: Mesh refinement volumes (cylinders) in the duct.

The next VRs are added close to the fan-OGV module as shown in Figure 3.8. A VR7 that incorporates the whole module is set. In addition, two volumes VR6 and VR7 are added at the duct wall upstream of fan. The objective is to ensure a better computation of the boundary layer upstream of the fan and avoid unrealistic thick boundary layers interacting with the fan.

Finally, the last VRs added correspond to an offset of the fan-OGV geometry as shown in detail in Figure 3.9. Different mesh grids have been defined from these offsets. The first mesh named L0 has an offset of 8 voxels at the level VR8. The mesh L1 has an additional

8 voxels at the level VR9 and the mesh L2 another offset of 8 voxels at the level VR10. According to the simulation results, the dimensionless wall coordinate has been computed and is summarized in Table 3.5. The maximum y^+ is found at the rotor and reduced from 70 to 23 at the tip from meshes L0 to L2. In all cases, the flow is not fully resolved at the wall but the influence of the wall-model should be decreased as the y^+ is decreased. Nevertheless, the coarsest mesh L0 provides a reasonable y^+ for a wall-modelled VLES like simulation [114, 115].

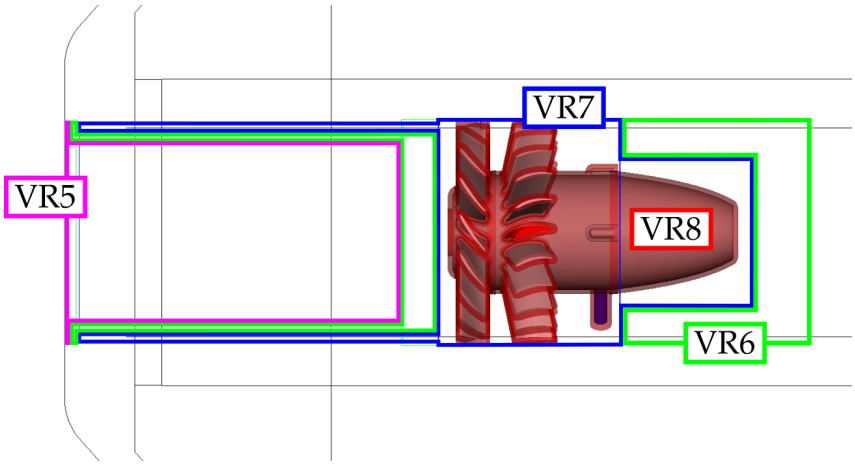

Figure 3.8: Refinement volumes from VR5 to VR7.

Level	Voxel cell size	$f_{\max}$
Sim. Vol.	76.800 mm	494 Hz
VR1	38.400 mm	988 Hz
VR2	19.200 mm	1975 Hz
VR3	9.600 mm	3951 Hz
VR4	4.800 mm	7903 Hz
VR5	2.400 mm	15806 Hz
VR6	1.200 mm	31612 Hz
VR7	0.600 mm	63224 Hz
VR8 (L0,L1,L2)	0.300 mm	126448 Hz
VR9 (L1,L2)	0.150 mm	252896 Hz
VR10 (L2)	0.075 mm	505793 Hz

Table 3.4: Refinement volumes and maximum propagating frequency. The frequency is calculated by considering $N_{\text{ppw}} = 16$ points per wavelength and the local timestep in the VR.

To conclude on the mesh structure, some details are given about the surface mesh of the *LP3* and all the other elements. The meshes of a rotor blade and of a stator vane are shown in Figure 3.10. The objective is to obtain a sufficiently refined mesh without having too many points. Indeed, the solver returns an error if the number of discrete points is too high within a given voxel. As observed, the higher mesh resolution is found at locations with high curvature like the leading and trailing edges or at the hub. In

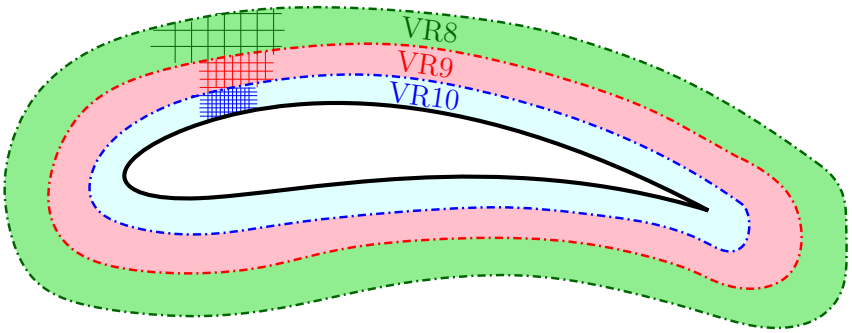

Figure 3.9: Offset refinement volumes.

Mesh level		**L0**	**L1**	**L2**
Offset refinement volumes	VR	8	8-9	8-10
Minimum voxel size [mm]	Δx	0.3	0.15	0.075
Dimensionless wall distance	$y^+_{\max}$ (rotor)	70	39	23
	$y^+_{\max}$ (stator)	45	28	15
Timestep [s]	Δt	4.943×10^{-7}	2.471×10^{-7}	1.236×10^{-7}
Mesh size	N_{voxels}	$\sim 50 \times 10^6$	$\sim 89 \times 10^6$	$\sim 233 \times 10^6$

Reynolds number	Re_D	327795
Tip Mach number	M_{tip}	0.26

Table 3.5: Simulation parameters for all meshes.

terms of parameters, the maximal chordal deviation from the parametric curve is set to 0.375 mm and the maximum turning angle between two successive mesh points is set to 10 degrees. The same meshing strategy is used to obtain the surface meshes of the other parts.

Meshing strategy and boundary conditions — Summary

1. Inlet boundary condition: atmospheric pressure, free-velocity
2. Outlet boundary condition: uniform axial velocity profile
3. 3 meshes defined:
   - Mesh L0, minimum voxel size: 0.3 mm (rotor $y^+_{\max} = 70$)
   - Mesh L1, minimum voxel size: 0.15 mm (rotor $y^+_{\max} = 39$)
   - Mesh L2, minimum voxel size: 0.075 mm (rotor $y^+_{\max} = 23$)
4. Sponge zones added in the room and in the duct to avoid unrealistic hard-wall and boundary condition reflections

3.3 Aerodynamic analysis

In this section, the aerodynamic analysis is provided. Firstly, the performances are discussed and compared with the experiment and RANS simulations. Then, the flow topol-

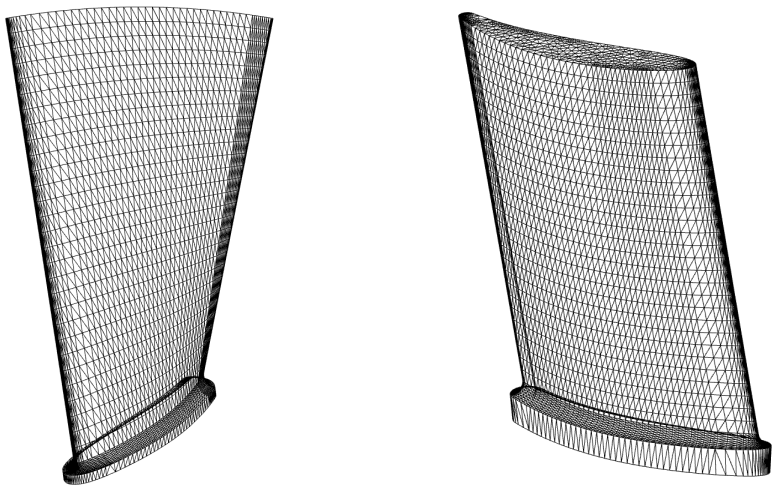

(a) Blade surface mesh. (b) Vane surface mesh.

Figure 3.10: Surface mesh of a blade and a vane done with Pointwise.

ogy for each mesh is analysed. This is followed by an analysis on the inflow to state about the absence of distortions. Next, the steady and unsteady blade and vane loading is provided. Finally, aerodynamic excitations for the wake and potential fields are separated and analysed in detail.

3.3.1 Aerodynamic performances

First of all, the simulation convergence of performances is discussed. For each mesh, the mass flow rate evolution versus time is shown in Figure 3.11. In all cases, the mass flow rate is seen to converge within 0.5% compared with the experiment. When the simulation is started from rest (as for the mesh L0 in Figure 3.11a), a transient regime of about 30 revolutions is observed before convergence. For the finer meshes L1 and L2, the solution is initialized from a converged solution on the previous mesh and shows a faster convergence.

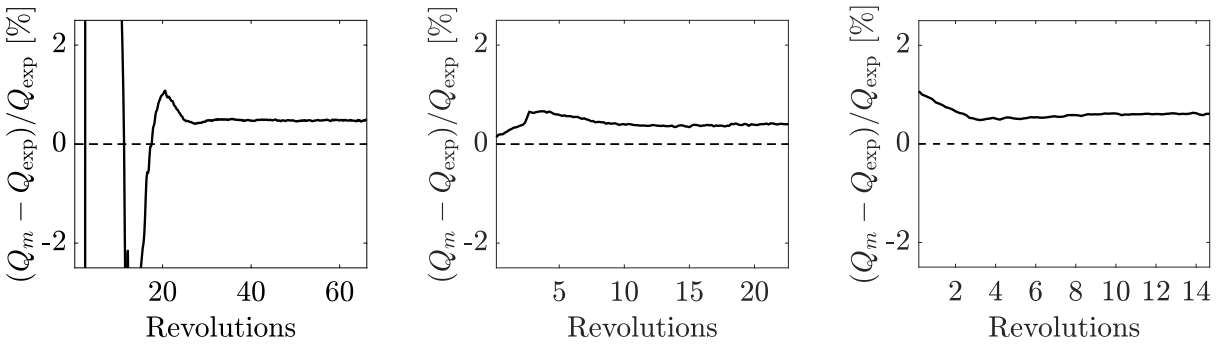

(a) Mesh L0. (b) Mesh L1. (c) Mesh L2.

Figure 3.11: Relative errors related to the mass flow rate convergence for the three different mesh refinements.

For the pressure rise, results are shown in Figure 3.12. The pressure rise is seen to be less sensitive to small mass flow rate variations as evidenced by the results for the

meshes L1 and L2 shown in Figures 3.12b and 3.12c. Convergence is achieved in all cases. Nevertheless, the computed pressure rise underestimates the measured one in all cases.

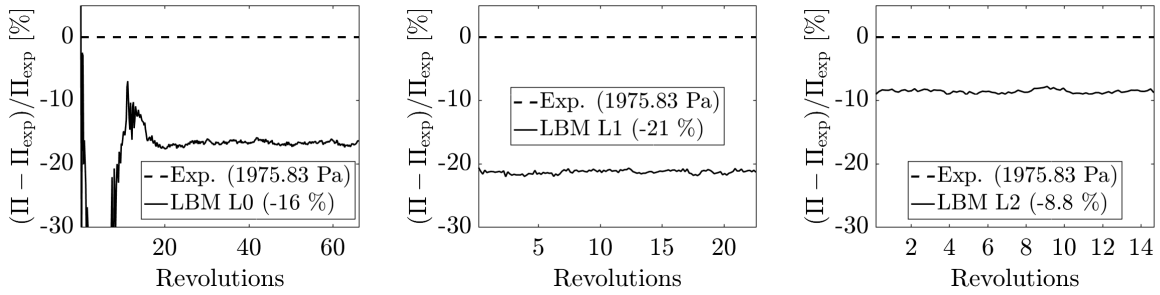

(a) Mesh L0. (b) Mesh L1. (c) Mesh L2.

Figure 3.12: Relative errors related to the pressure rise convergence for the three different mesh refinements.

The compressor map for three different operating conditions on the mesh level L0 is compared with the measurements in Figure 3.13. The nominal operating point is also compared between all meshes and with a wall-resolved RANS simulation.

The RANS simulation was provided by Université de Sherbrooke and has been performed with ANSYS CFX V15.0 using the standard $k-\omega$ SST [116] turbulence model and a second order spatial scheme. The simulation has been performed on a reduced angular sector including 3 rotor blades and 4 baseline stator vanes. Because B and V are prime numbers, the solver uses a scaling technique that allows reducing the angular sector. The boundary conditions involve a no-slip condition at the walls, a specified mass flow rate at the inlet and a constant pressure at the outlet. Lastly, a mixing plane is used at the interface between the rotor and the stator. The mesh consists of 27 millions cells, the boundary layer is fully resolved as the grid resolution achieves a maximum dimensionless wall distance $y^+ = 2$ at the blade/vane walls.

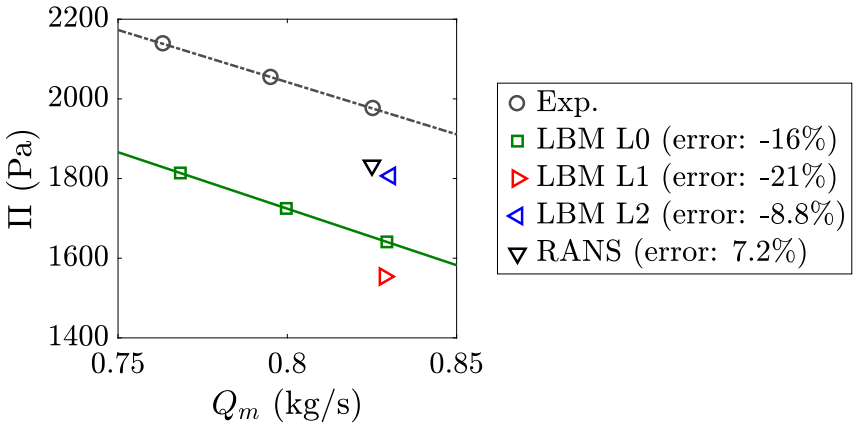

Figure 3.13: Zoom on the compressor map for the different meshes compared to the experiment and to the RANS simulation. Nominal operating point at $Q_m = 0.8254$ kg/s.

The pressure rise is underestimated by 16% for the mesh L0. Nevertheless, the same slope (shown as continuous line between symbols) as in the experiment is retrieved. From

observation of the blade and vane loads presented in section 3.3.4, important flow separations occurring on the stator are the probable cause for the pressure-rise mismatch. The mesh level L1 provides still lower pressure rise with an error of more than 20%. However, in this case, vortex shedding taking place on the rotor blade trailing edges seems to coincide with a loss of performance of the rotor. This point is discussed in section 3.3.2. Regarding the mesh level L2, the pressure rise is better recovered with a reduction of the error from 16% to 8.8%. In this mesh, the vortex shedding is strongly attenuated. At last, the RANS simulation provides a pressure rise 7.2% below the experiment.

Results for all cases are summarized in Table 3.6. The operating conditions are not modified with the different stator configurations in the mesh L0. This is important for the quantification of the stator heterogeneity regarding acoustics. The homogeneous stator configuration gives the same overall performance. When the power-supply cable is removed, a slight increase of 30 Pa is observed. The removal of some pressure losses generated by the power-supply cable may explain this increase of 1.2%. In all cases, variations are below 0.02% for the mass flow rate and below 0.39% for the pressure rise.

		Mass flow rate Q_m		Pressure rise Π	
	Mesh	μ	c_v	μ	c_v
HOM w/o Cable	L0	0.8294 kg/s	0.01%	1671.16 Pa	0.33%
HOM	L0	0.8293 kg/s	0.01%	1651.96 Pa	0.19%
HET	L0	0.8293 kg/s	0.01%	1640.97 Pa	0.31%
HET	L1	0.8287 kg/s	0.01%	1554.41 Pa	0.38%
HET	L2	0.8304 kg/s	0.01%	1806.69 Pa	0.20%
RANS	-	0.8250 kg/s	-	1833.10 Pa	-
Experiments		0.8254 kg/s	0.08%	1975.83 Pa	0.08%

Table 3.6: Mean operating point and fluctuations for the different mesh refinements, the RANS simulation and the experiment. μ is the mean value and c_v the variation coefficient (equal to σ/μ with σ the standard deviation).

For a better insight into the rotor and stator performances, the axial pressure evolution is shown in Figure 3.14. The pressure rise is calculated from the point just upstream of the fan (U-R) and from the last point as in the experiment (D-H). The reference pressure is chosen so that the pressure coincides upstream of the fan (U-R).

For the mesh L0, the pressure rise is only achieved by the rotor. The flow across the stator row is observed to decrease the static pressure levels. As mentioned before, important pressure losses from massive flow separations seem to overwhelm the pressure recovery from the flow straightening in the stator, thus generating an overall static pressure loss. For the mesh L1, the performance deteriorates through the rotor due to this enhanced instability (vortex shedding). Through the stator, the same behaviour as for the mesh L0 is observed leading to a lower pressure. Finally, with the mesh L2, the rotor performance is brought back to the levels obtained on mesh L0. In addition, the stator flow separations are reduced with the mesh refinement. For this reason, no pressure loss is observed through

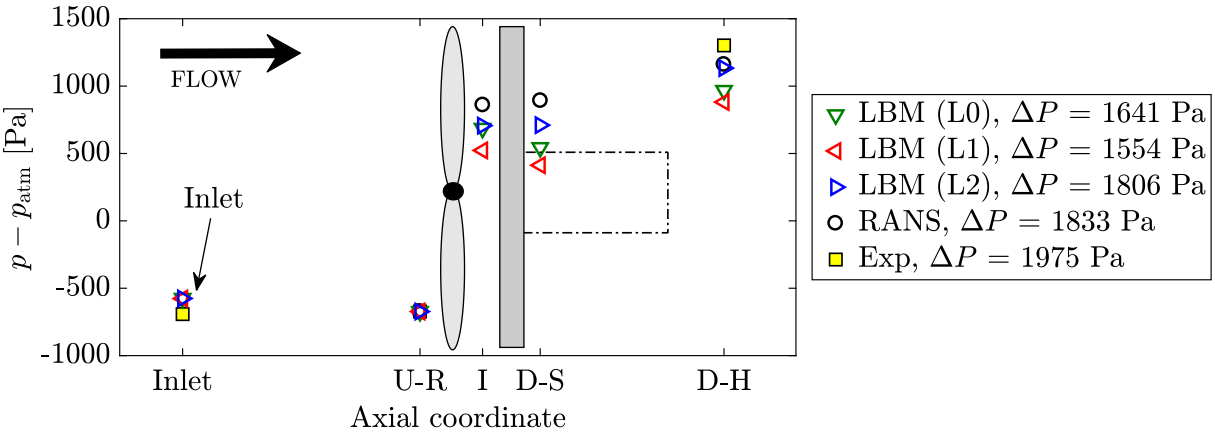

Figure 3.14: Mean static pressure evolution in the duct. U-R stands for upstream rotor, I for interstage, D-S for downstream stator and D-H for downstream hub.

the stator stage even though no significant increase is actually achieved.

Results are also compared with previous resolved RANS simulations of the same configuration. The obtained pressure rise is slightly higher that of the L2 mesh. If attention is paid to the static pressure level just downstream of the rotor (D-R), higher pressure levels are obtained with the RANS. However, some inaccuracy seems to come from the annular to cylindrical duct cross-section change (D-S to D-H) where the LBM is seen to provide a higher pressure increase. As a result, the compensation of both effects yields an outlet static pressure level (D-H) close to the LBM L2. One possibility would be to refine the mesh in the downstream region for the RANS case and investigate if any pressure increase is obtained.

The RANS simulation has put in evidence a lack of rotor performance in the LBM. To conclude on the performance convergence, a refined mesh should then be simulated. In the framework of this study, such a simulation has not been done because of the required computational cost. On the top of that, the pressure rise comparison from static pressure probes at the wall is of increased difficulty for numerical simulations. Indeed, the mesh refinement efforts have been put around the regions of interest, the rotor and the stator. An increased refinement at the duct walls represents a considerable cost for LBM simulations. For that reason, the addition of total pressure profiles upstream and downstream of the fan in the experiments would make the operating point evaluation and comparison easier.

3.3.1.1 Radial profiles

In order to have a more detailed characterization of the operating conditions, the radial velocity profiles are now analysed for all simulations and are shown in Figure 3.15.

Upstream of the rotor (U-R), the results for all meshes are superimposed. This is expected since no mesh refinements have been done in this region and because the mass flow rate is equal in all cases. The RANS is seen to match the LBM simulations. The

axial velocity is lower at the hub because of the flow blockage in front of it, the azimuthal velocity is seen to be zero and some radial flow is observed due to the flow deviation at the hub.

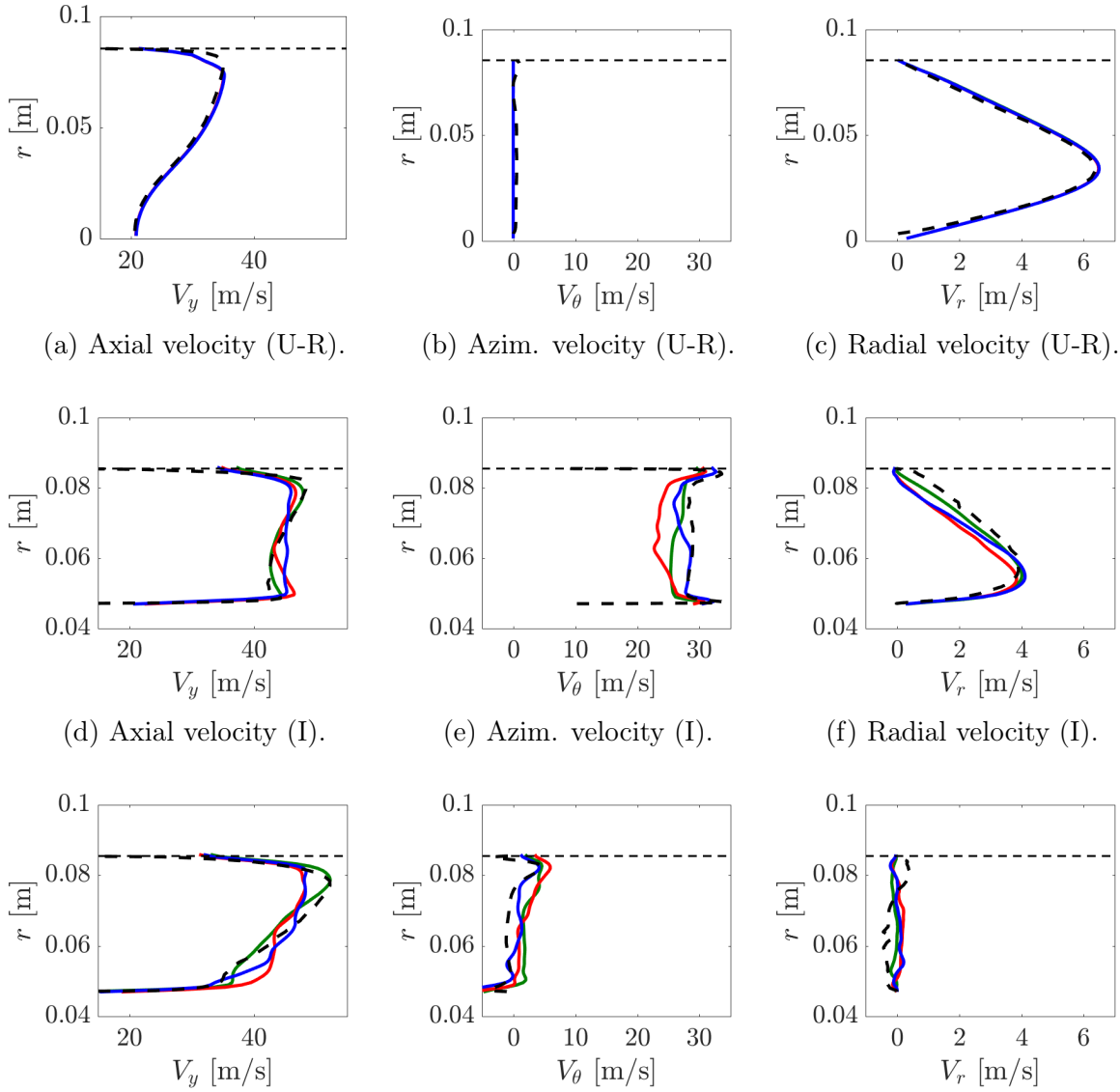

(a) Axial velocity (U-R). (b) Azim. velocity (U-R). (c) Radial velocity (U-R).

(d) Axial velocity (I). (e) Azim. velocity (I). (f) Radial velocity (I).

(g) Axial velocity (D-S). (h) Azim. velocity (D-S). (i) Radial velocity (D-S).

Figure 3.15: Radial velocity profiles for all meshes at the locations: upstream rotor (U-R), interstage (I) and downstream stator (D-S). — is the mesh L0, — the mesh L1, — the mesh L2 and - - - the RANS. Decomposition of the absolute velocity vector. The profiles are time and azimuthally averaged.

In the interstage plane (I), differences appear for all meshes. In terms of axial velocity, the finer mesh allows recovering an almost constant velocity profile over the radius compared to the meshes L0 and L1 for which a deficit is observed at the centre. Unexpectedly, the RANS provides a profile in good agreement with the LBM mesh L0. The azimuthal velocity is increased due to the passage through the rotor. However, some unexpected higher values are seen at the duct walls. These may be generated from corner vortices or

by the rotating rotor hub locally enhancing the azimuthal velocity. The RANS provides a constant radial profile whereas the LBM L2 yields a slight azimuthal velocity deficit from midspan to tip. In addition, the mesh L1 in red evidences lower azimuthal velocities seemingly due to the presence of vortex shedding. In terms of radial velocity, all cases are similar with a peak value at the hub of about 4 m/s.

Downstream the OGV (D-S), the axial velocity profile is seen to have higher values at the tip for the mesh L0 and the RANS. With the LBM mesh refinement, the profile is homogenized but still presents lower values at the hub. In terms of azimuthal velocity, the flow is correctly straightened with velocity magnitudes below 4 m/s. The radial flow is also correctly cancelled with a constant zero velocity profile.

Finally, the static-pressure radial profiles are shown in Figure 3.16. Upstream of the rotor (U-R), the pressure is seen to be higher at the hub in accordance with the lower axial velocity and due to the presence of the hub.

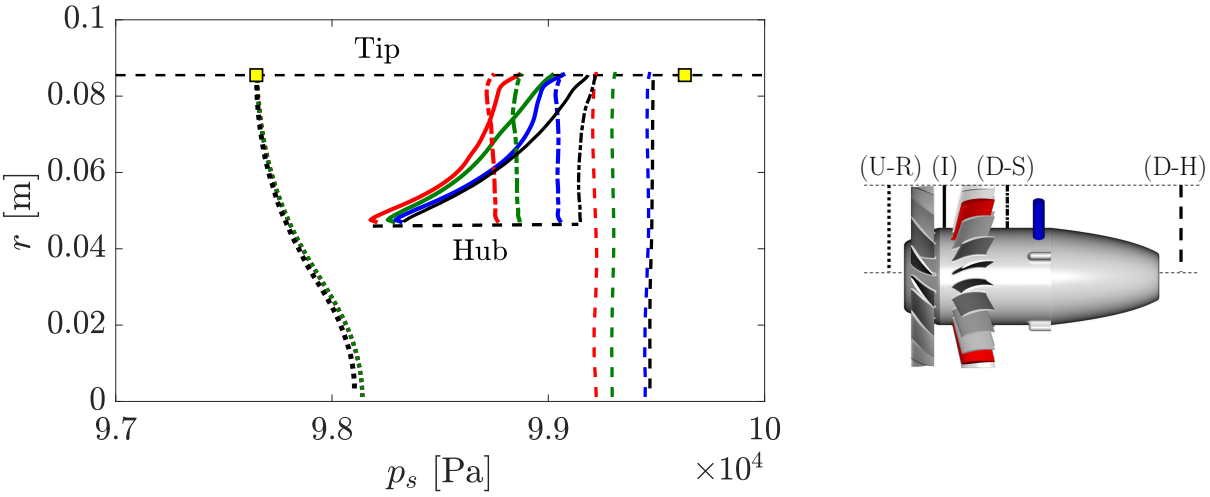

Figure 3.16: Static-pressure radial profiles for all meshes at the locations: upstream rotor (U-R) ·····, interstage (I) ——, downstream stator (D-S) -·-·- and downstream hub (D-H) – – –. The mesh L0 in ■, the mesh L1 in ■, the mesh L2 in ■, the RANS in ■ and the experiment in ■. The pressure rise Π is computed from (U-R) and (D-H). The profiles are time and azimuthally averaged.

In the interstage (I), the pressure increases from hub to tip in all cases. Nevertheless, the pressure increase is lower for the mesh L1 where the vortex shedding has been observed (details are provided in the next section). In the mesh L2, the pressure is higher at all duct heights and reaches a similar value as the mesh L0 at the tip. This is in accordance with what has been observed previously in Figure 3.14 where a similar wall static pressure for the meshes L0 and L2 has been measured in the interstage plane (I). The RANS simulation provides a stronger pressure increase from midspan to tip compared with the LBM mesh L2. Again, this agrees with the better rotor performance shown in Figure 3.14.

Downstream of the OGV (D-S), the pressure is seen to be globally increased to form a constant static-pressure profile. However, in the meshes L0 and L1, a decrease of the

pressure is observed through the stator close to the tip region. This may be explained by the flow separations occuring on the stator yielding pressure losses. In the mesh L2 and the RANS, a higher pressure recovery is obtained at all duct heights. The mesh refinement in the LBM is thus seen to improve the stator efficiency in converting the kinetic energy into pressure. Finally, the annular to cylindrical passage (D-S to D-H) is seen to increase the static pressure levels. Nevertheless, the RANS simulation increases the static pressure by about 260 Pa whereas the LBM provides an increase of about 400 Pa. The experimental static pressure is not reached in all cases as observed previously.

3.3.2 Rotor-stator flow topology

In this section, the simulated flow topology is discussed for the three stator configurations and meshes. Cylindrical cuts of the axial velocity fields are shown in Figure 3.17 at hub, midspan and tip in the mesh L0. Firstly, the flow around the rotor blades is seen to be attached for all duct heights and stator configurations. The rotor wakes are regular and no important wake deviation is observed. Regarding stator vanes, flow separations occur mostly in the hub and midspan regions. The rotor tip-gap not accounted for in the present simulations could have a localized impact on the tip flow topology of the stator vanes. Nevertheless, its influence should be negligible in the hub and midspan regions. In addition, the flow on the thickened stator vanes evidences stronger flow separations seemingly related to their increased thickness. Oscillations in the vane wakes generated from the flow unsteadiness at the wall are less pronounced at the tip. Finally, the flow behind the power-supply cable is seen to be fully detached. When the cable removed, no significant impact on the upstream stator vanes and rotor blades is observed. To conclude, all investigated configurations in the mesh L0 evidence the same flow topology. This is consistent with the same overall operating conditions retrieved for all stator configurations and discussed in the previous section.

In Figure 3.18 are shown vorticity maps for all meshes and for the heterogeneous stator configuration. As expected, the vorticity is seen to be higher in the near-wall regions where the shear stress is stronger but also in the convected wake structures. With all meshes, the unsteadiness in the stator vanes flow is highlighted by spots of higher vorticity convected downstream. A deviation of the rotor wake is also observed in front of the thickened vanes. Since these are instantaneous fields, both wake and potential fields are present and this evidences the impact of the latter. Because the potential field is static, each blade wake will experience the same deviation over a complete revolution.

Surprisingly, clear coherent structures are shed by some of the rotor blades as the mesh is refined (see Figure 3.18e). In fact, the better wall resolution compared with L0 yields the development of a boundary layer instability leading to vortex shedding in the blade wakes. Seemingly, these structures appear with a precise shedding frequency. Their amplitude is stronger at midspan but weaker at the tip. For the finer mesh L2, the vortex shedding amplitude is greatly decreased and its high coherence is lost. In addition, the

near-wall region in the stator vanes evidences weaker vorticity due to the removal of some flow separations. This is in accordance with the pressure evolution shown in the previous section where the pressure loss through the stator stage was not observed anymore in the mesh L2. The better resolution of the small-scale turbulent structures at the vane walls is observed to increase the predicted efficiency of the overall OGV stage.

Regarding the vortex shedding frequency, a quick estimate can be done with the well-known case of the cylinder. The Strouhal number (St) of 0.2 provides a frequency of:

$$f_s = \frac{\mathrm{St}\, U}{D} = 5777\,\mathrm{Hz} \tag{3.1}$$

where $U = 65$ m/s is the relative velocity at midspan and $D = 2.25$ mm is a rough estimate of the characteristic length accounting for the trailing edge and boundary-layer thicknesses (upper and lower).

For a clearer observation, signals from probes in the rotating reference frame and placed in the rotor wakes are shown in Figure 3.19. A periodic phenomenon is clearly seen in some blade wakes with the mesh L1. The appearance of strong vortex shedding only on some blades may be caused by mesh heterogeneities due to the Cartesian discretization approach used in the LBM solver. From these signals, axial velocity spectra are calculated and shown in Figure 3.20 for the meshes L1 and L2. A clear tone appears at a frequency roughly equal to 5200 Hz providing a shedding frequency not far from the previous analytical estimate. However, with the mesh refinement, the peak disappears.

To conclude, the presence of vortex shedding agrees well with the predictions found in the literature for bluff bodies [117, 118, 119] in the considered Reynolds number range. In the present case, the Reynolds number based on the length D is approximately 10^4. For such a turbulent subcritical case, the Strouhal number of 0.2 is usually found in the cited references for cylinders, which makes clear organised vortex shedding also expected here. For these reasons, the observed vortex shedding in this configuration at the mesh L1 could be physical. Yet, the better wall resolution provided by the mesh L2 yields another boundary layer state which does not clearly generates vortex shedding. In fact, the additional resolved small-scale turbulent structures in the mesh L2 do have a relevant impact on the boundary layer development. To sum-up, even if the vortex-shedding observed in the mesh L1 could be physical, it was probably generated from a peculiar boundary layer state only given by the mesh L1.

3.3.3 Inflow distortion

In this section, the inflow conditions are discussed. As previously mentioned, the heterogeneity impact may be correctly evaluated if no inflow distortion exist given that it generates sound at the same frequencies as rotor-stator interaction mechanisms.

First of all, the flow in the room is analysed. From extraction planes shown in Figure 3.21 in red and green, the streamlines can be calculated. They are shown in Fig-

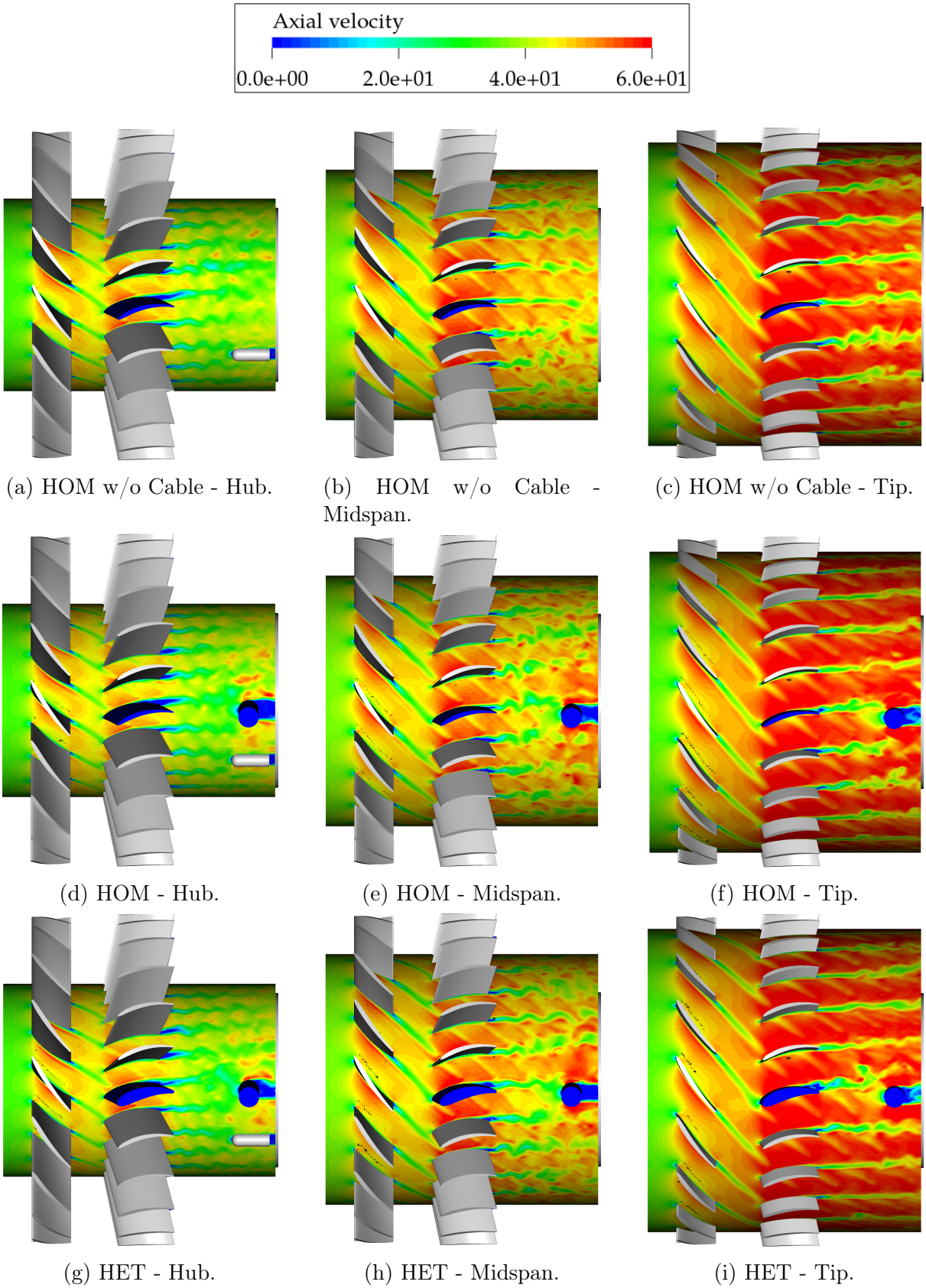

(a) HOM w/o Cable - Hub. (b) HOM w/o Cable - Midspan. (c) HOM w/o Cable - Tip.

(d) HOM - Hub. (e) HOM - Midspan. (f) HOM - Tip.

(g) HET - Hub. (h) HET - Midspan. (i) HET - Tip.

Figure 3.17: Axial-velocity instantaneous fields in m/s for the three stator configurations and at various duct heights in the mesh L0.

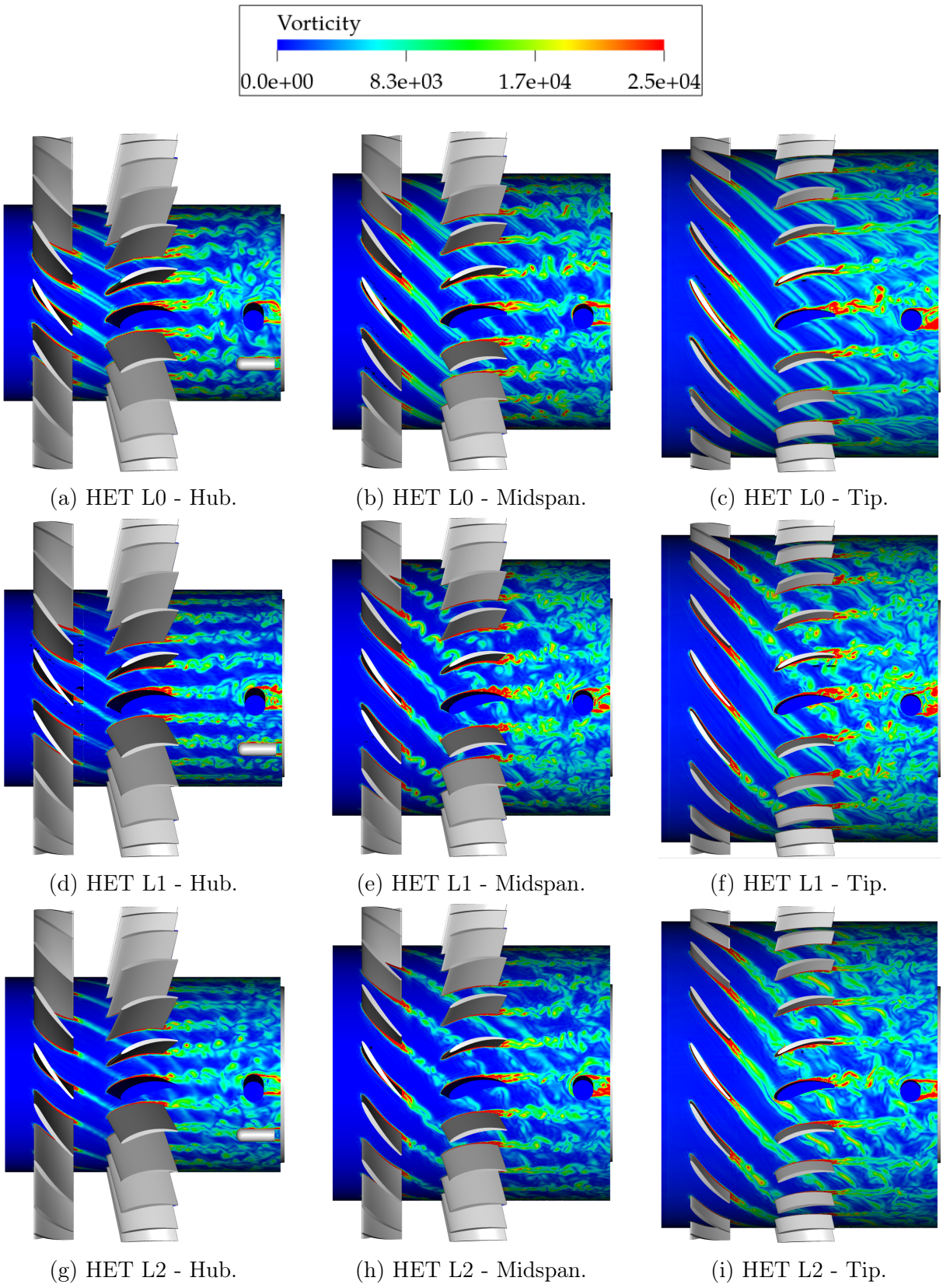

(a) HET L0 - Hub. (b) HET L0 - Midspan. (c) HET L0 - Tip.

(d) HET L1 - Hub. (e) HET L1 - Midspan. (f) HET L1 - Tip.

(g) HET L2 - Hub. (h) HET L2 - Midspan. (i) HET L2 - Tip.

Figure 3.18: Vorticity instantaneous fields in s^{-1} for the heterogeneous stator configuration at various duct heights for all meshes.

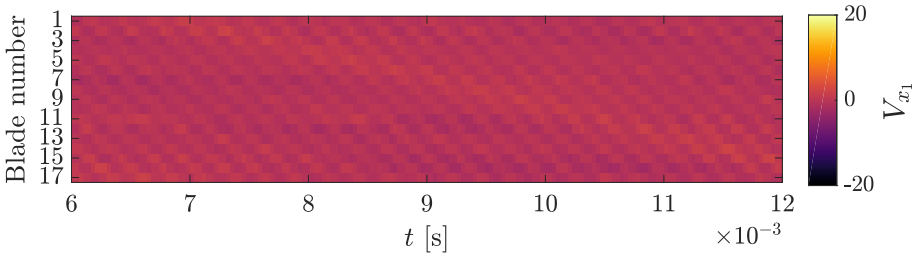

(a) Mesh L0.

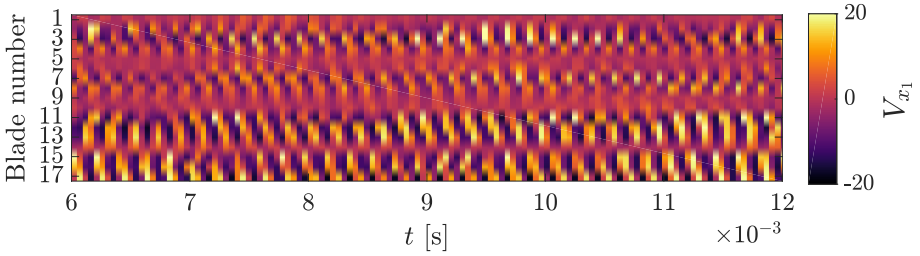

(b) Mesh L1.

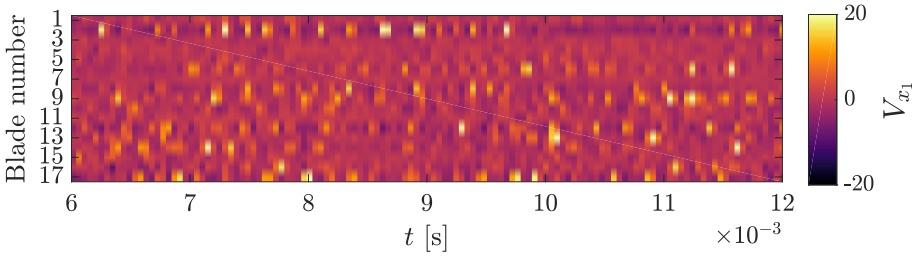

(c) Mesh L2.

Figure 3.19: Time signals of an axial velocity probe placed downstream the rotor blades at midspan and in the rotating frame of reference. Note the periodic patterns observed with mesh L1.

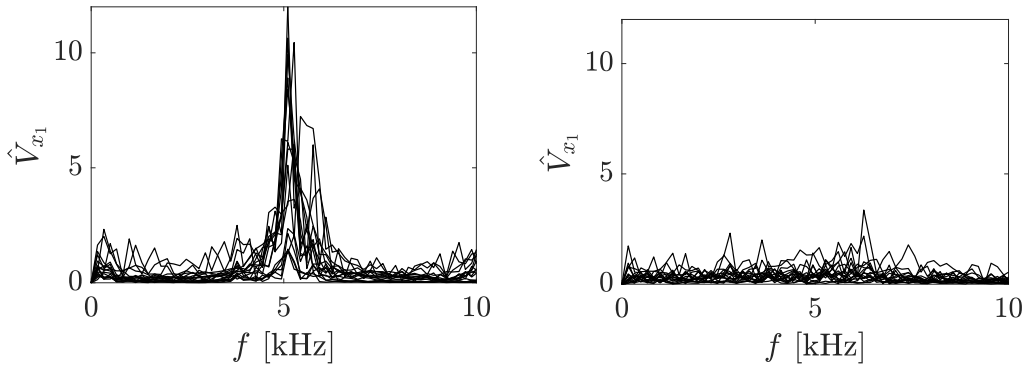

(a) Mesh L1.

(b) Mesh L2.

Figure 3.20: Spectra of the wake axial velocity probes at midspan for the meshes L1 and L2.

ure 3.22. In the x_1x_3-plane, the flow is seen to deviate from the block at the ceiling. Furthermore, the flow deviation at the top and the bottom of the inlet is seen to differ due to the postioning of the duct in the x_3 coordinate (height). The same behaviour is observed in the front view (x_2x_3-plane) because of the positioning of the duct in the x_2 coordinate (not laterally centred).

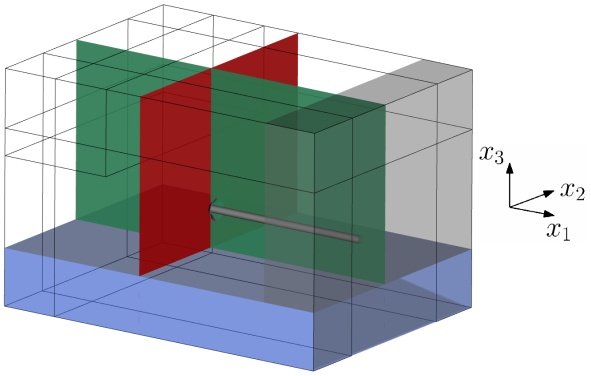

Figure 3.21: Extraction planes in the room. The x_1x_3-plane in green and the x_2x_3-plane in red.

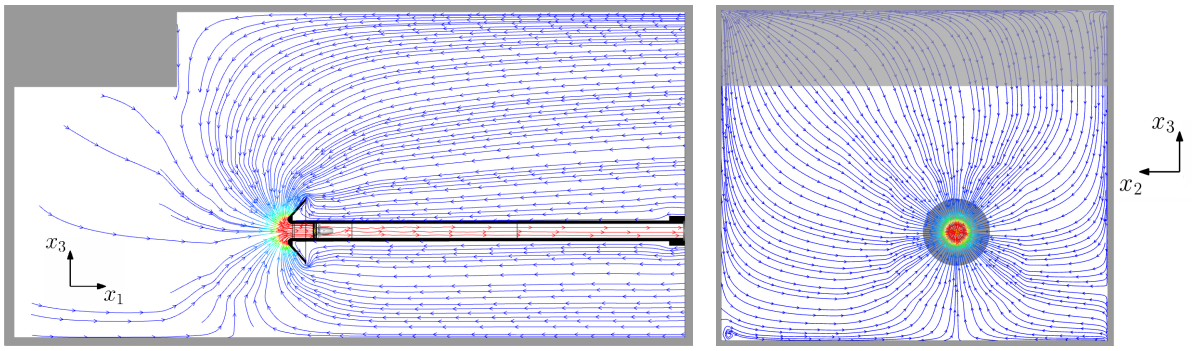

(a) Side view - x_1x_3-plane.

(b) Front view - x_2x_3-plane.

Figure 3.22: Streamlines coloured by the axial velocity in the fluid domain.

Nevertheless, the corresponding velocity amplitudes in the room are in the order of magnitude of 10^{-1} m/s because of the large extent of the domain and the relatively low volume flow rate ($\sim$ 1 m^3/s). For this reason, the establishment of a clear inflow distortion is only expected for long simulation times of the order of the room filling time. Some deviations are also seen at boundaries of the sponge zones where the fluid viscosity is changed but do not impact the clean duct inflow.

For a better quantification of the inflow conditions, maps of the three mean velocity components are shown in Figure 3.23. The axial velocity is seen to be azimuthally homogeneous. In Figure 3.23b are superposed all the radial profiles for all angular positions and the averaged profile is shown in red. Negligible azimuthal variations are observed, within 0.1 m/s.

The radial velocity profile shows decreasing velocities towards the centre. The presence of a radial flow is explained by the inlet geometry which guides the flow into the duct.

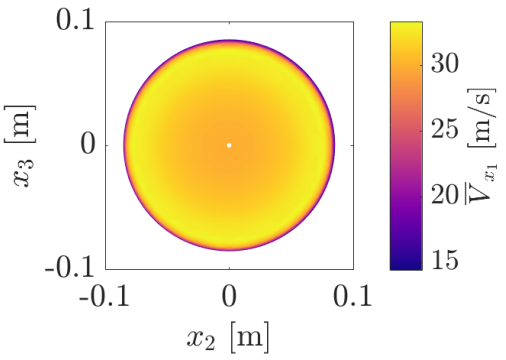

(a) Mean axial velocity.

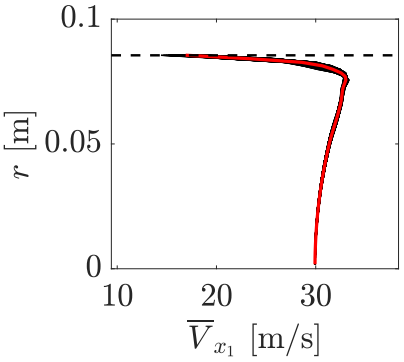

(b) Mean axial velocity plot. The average is in red.

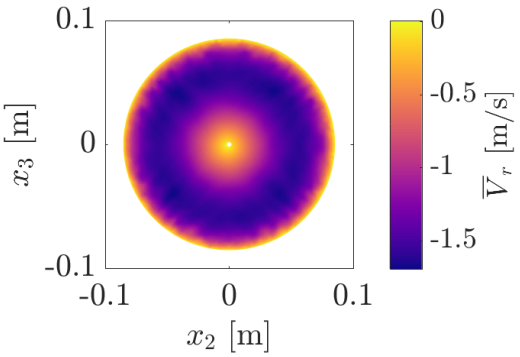

(c) Mean radial velocity.

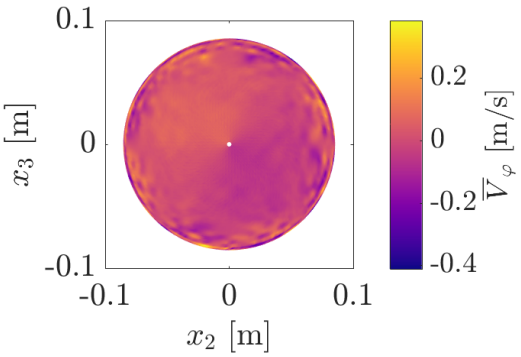

(d) Mean azimuthal velocity.

Figure 3.23: Mean flow field velocities at the inlet for the mesh L0. The time average is performed from when the transient flow establishment is completed and up to the last recorded timestep.

Further downstream inside the duct, this velocity component is negligible. In terms of the azimuthal velocity, inhomogeneities below 0.2 m/s are observed. In comparison with the mean velocity in the duct, these fluctuations can also be considered to be weak.

Velocity fluctuations are shown in Figure 3.24. The numerical simulation evidences very weak fluctuations one order of magnitude lower than in the experiment. As expected, higher fluctuations are observed near the wall where the shear is stronger. The absence of any unsteady distortion is thus verified in agreement with the short simulated physical time. Results have not been directly compared with the experiment because of the duct length difference mentioned in chapter 2.

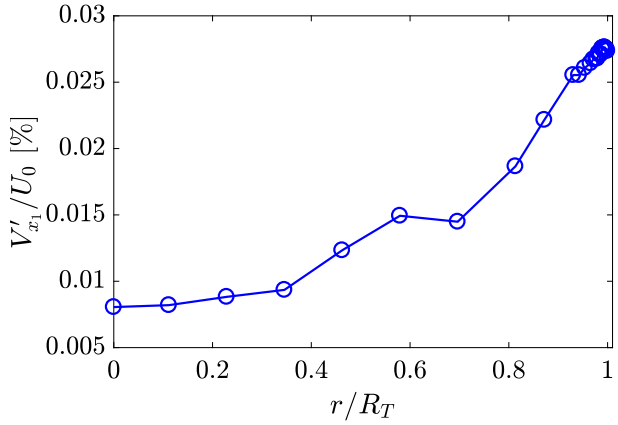

Figure 3.24: RMS velocity fluctuation profile at the inlet.

3.3.4 Mean blade and vane loading

In this section, the mean blade and vane loadings are compared with the RANS simulations. The latter only account for the baseline vanes and for this reason, the comparison is not extended to the thickened vanes. In Figure 3.25 are shown the mean pressure coefficient for the rotor blades and stator vanes in the mesh L0. In general, a good agreement is found for the rotor blades at all duct heights. It is worth noting that some discrepancies are expected near the tip because RANS simulations account for the tip gap flow not included in the present LBM simulations. Nevertheless, the impact is seen to be small because of the small extent of the tip gap in the *LP3*.

For the stator vanes, higher discrepancies are observed especially in the hub and tip regions. The LBM simulation evidences a strong flow separation at the hub whereas the RANS simulation evidences strong flow separation at the tip. In these conditions, higher discrepancies between both methods are expected because of the inaccuracy of RANS predictions of unsteady phenomena and mostly secondary flows such as corner vortices [120].

In Figure 3.26 are shown the vane and blade pressure distributions for the three different meshes at midspan. This extraction has only been done at midspan because of the additional cost required on the finer meshes. For the rotor blades, the vortex shedding

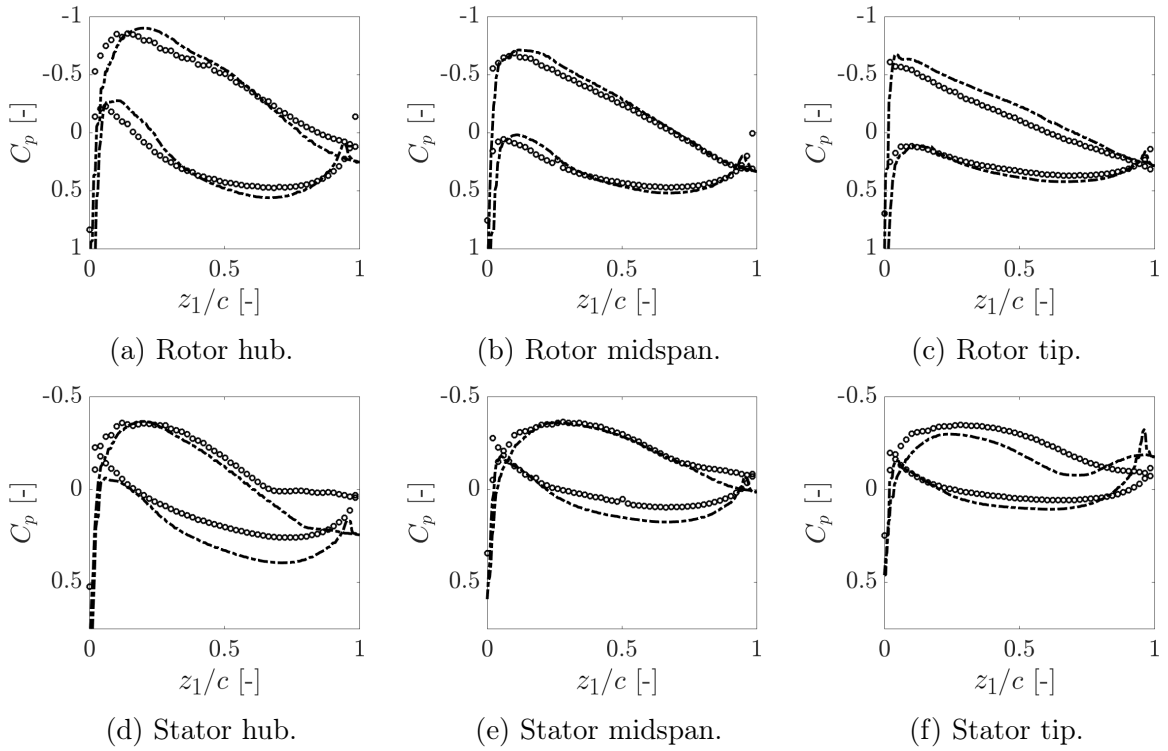

(a) Rotor hub. (b) Rotor midspan. (c) Rotor tip.

(d) Stator hub. (e) Stator midspan. (f) Stator tip.

Figure 3.25: Mean pressure coefficient at hub, midspan and tip. Comparison between the LBM (mesh L0) in ∘ and RANS in - - - . x/c is the dimensionless chordwise coordinate.

previously discussed is clearly seen on the pressure coefficient. Indeed, the pressure on the pressure side is decreased on the aft portion of the airfoil and an important peak is seen at the trailing edge. On the suction side, the pressure is also decreased at the trailing edge. On the mesh L2, the pressure at the pressure side is brought back to the levels of the L0 mesh. However, in the trailing edge region on the suction side, the pressure is lower compared with the L1 mesh.

For the stator vanes, the overall pressure distribution is seen to be improved from mesh L0 to mesh L2. This is in accordance with what is observed in the pressure evolution along the duct sections. The pressure variation through the stator stage was seen to go from a negative value (pressure losses) to a constant pressure for the mesh L2. A flow separation observed for the mesh L0 (plateau at around 65% of the chord) is correctly removed. In addition, the pressure side overpressure is higher and brought closer to the RANS levels. It appears that the overall pressure coefficient is shifted upwards when compared with the RANS. To conclude, the pressure coefficient distribution is seen to be better recovered on the finest mesh and corresponds to the increased pressure rise observed in this mesh.

3.3.5 Unsteady blade and vane loadings

In this section, the unsteady blade and vane loadings are analysed. In the current investigation, it is known that the dominant noise sources are the pressure fluctuations on the blades and vanes. On the one hand, the wake-interaction noise is expected to generate

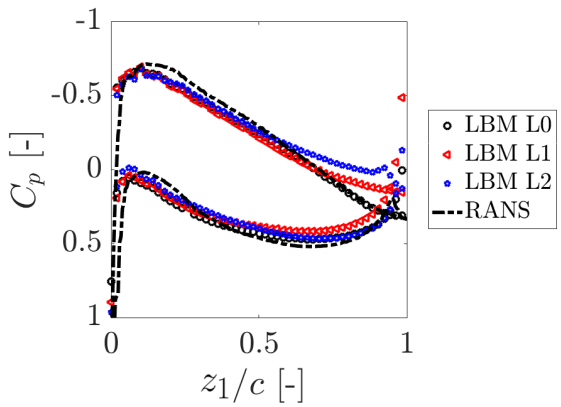

(a) Rotor blades' mean.

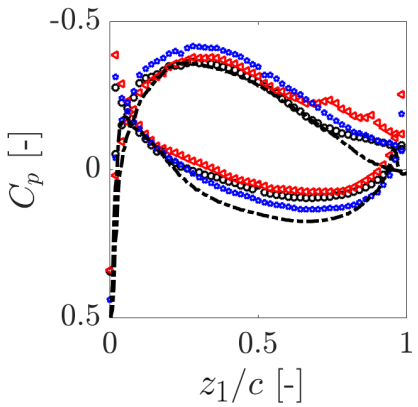

(b) Baseline stator vanes mean.

Figure 3.26: Mean pressure coefficient of stator vanes and rotor blades at midspan. Comparison of all LBM meshes with the RANS simulation. x/c is the dimensionless chordwise coordinate.

higher unsteady loads at the leading edges of the vanes, see Figure 3.27a. Indeed, the wake deficit first impinges on the stator vane. On the other hand, the potential-interaction noise is expected to generate noise mainly at the trailing edges of the rotor blades, see Figure 3.27b. This is because rotor blades firstly interact with the downstream potential field at the trailing edge.

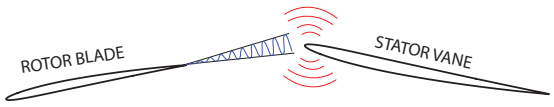

(a) Wake-interaction.

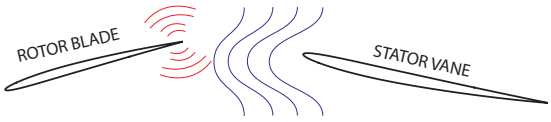

(b) Potential-interaction.

Figure 3.27: Wake-interaction and potential-interaction schemes.

The computation of the pressure jump in the numerical simulations is now detailed. A pressure-jump fluctuation (between the pressure and suction sides) is generated when a blade/vane goes through a velocity disturbance. For the rotor blades, the analysis is performed in the rotating reference frame and for the stator vane it is performed in the stationary reference frame. Firstly, the wall-pressure is Fourier transformed at frequencies $n\Omega$. Secondly, the most distant points in the airfoil are found and set to be the leading and trailing edges. We consider here the geometrical leading and trailing edges. Then, the upper and lower parts of the airfoil are separated and the mean camber line is approximated from the mean vertical coordinate between both. The pressure jump is then calculated as being the difference at the same dimensionless curvilinear abscissa (see Figure 3.28):

$$\Delta P(\omega, s_c) = \hat{P}(\omega, s_e = s_c) - \hat{P}(\omega, s_i = s_c) \tag{3.2}$$

The pressure jump is shown for the stator vanes in Figure 3.29, and for the rotor blades

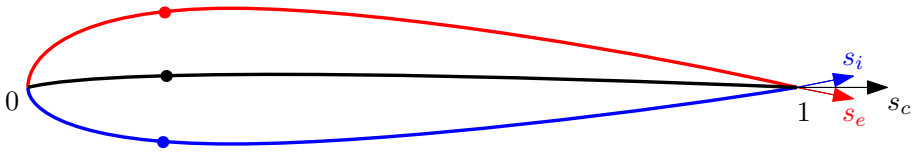

Figure 3.28: Numerical computation of the pressure jump ΔP on an airfoil. It is expressed on the mean camber line and calculated from the pressure and suction sides lines.

in Figure 3.30. Firstly, the maximum stator vane pressure jump can be seen to be about 6.5 times higher than that of the rotor blades. This means that the wake-interaction is the dominant noise source. As expected, the dominant loading harmonics are the multiples of B in the stator vanes and V in the rotor blades.

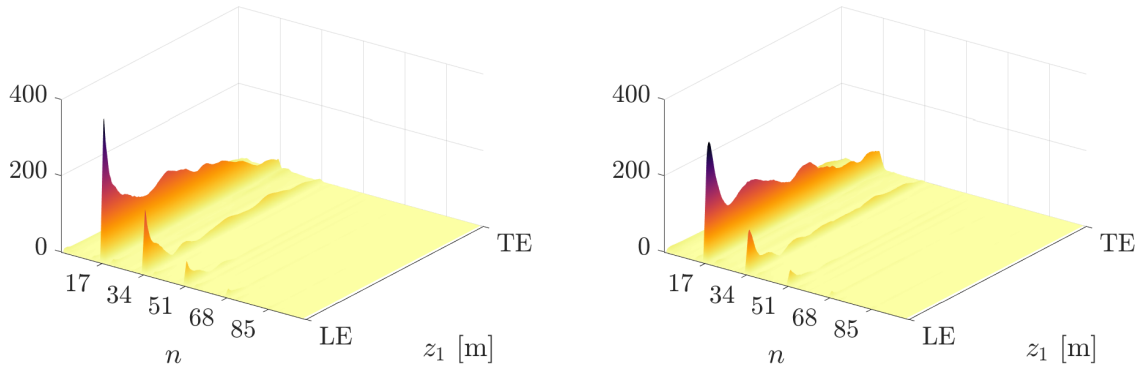

(a) Baseline stator vane mean ΔP.

(b) Thickened stator vane mean ΔP.

Figure 3.29: Fourier analysis of the pressure jump ΔP in Pa on the stator vanes with the mesh L0 at midspan.

The unsteady load is concentrated at the leading edge for the stator vane and rapidly decreases downstream. This agrees with what is obtained with Amiet's model formulated for a leading-edge gust impingement. Secondly, the dominant harmonics are seen to be the blade passing frequencies and their amplitude decreases fast with increasing orders. In fact, the amplitude is seen to decrease by more than one half from the first (17) to the second (34) harmonic. Regarding the thickened vane, it has a lower peak at the leading edge due to its increased thickness. More details on this aspect are given later on.

For the rotor blades, because the problem is treated in the rotating reference frame, the dominant harmonics are seen to be the multiples of the vane count V. As opposed to the stator vanes, the unsteady load has a peak value at around 70% of the chord and is cancelled at the trailing edge in virtue of the Kutta condition. In this case, the pressure jump is not dominated by the leading edge. This is expected because the main contribution here should be the potential interaction. Nevertheless, a small leading edge peak is seen for low orders $n \in [1, 3]$. This could indicate the presence of an upstream distortion interacting with the leading edge of the rotor blades. However, its amplitude is weak and no clear inflow distortion was identified in the previous sections. In addition, because the stator heterogeneity breaks the vane-to-vane periodicity, some other harmonics should

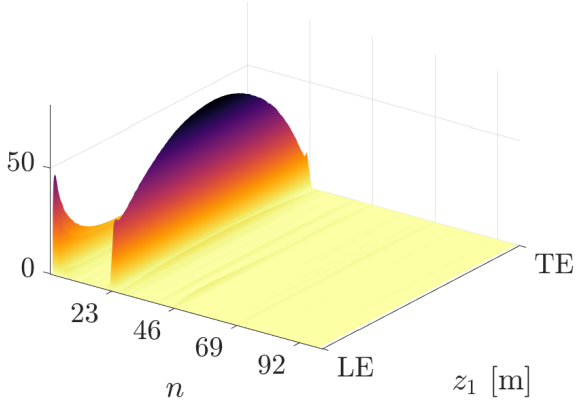

Figure 3.30: Fourier analysis of the pressure jump ΔP in Pa on the rotor blades with the mesh L0 at midspan.

appear. However, in this case, no other dominant harmonics are seen indicating that the stator heterogeneity has a weak impact on the potential-interaction noise. Finally, the harmonic decrease rate is seen to be stronger with the second harmonic being almost cancelled compared with $n = 23$.

The analysis of both stator and rotor unsteady loads shows that the wake-interaction noise is the dominant mechanism despite the short rotor-stator spacing. In fact, this stresses that the stator heterogeneity is not high enough to generate important upstream distortions which would considerably contribute to the potential-interaction noise. To conclude, even if the wake-interaction noise is augmented by the shorter spacing, the impact on the potential-interaction noise remains limited.

More details are now given on the unsteady load differences between a baseline vane and a thickened vane. In Figure 3.31 are shown the averaged loadings for the baseline and the thickened stator vanes at their respective dominant frequency ($B\Omega$) and at three different duct heights.

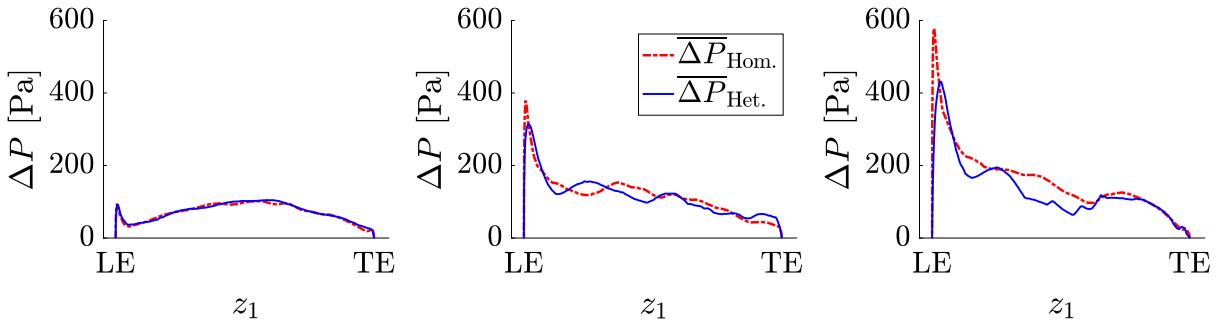

(a) Hub. (b) Midspan. (c) Tip.

Figure 3.31: Averaged stator vanes pressure jump ΔP at the harmonic $n = 17$ for the mesh L0.

In general, an increase of the pressure jump is observed with the radius. In addition, the loading of the thickened vane is seen to be identical at the hub but below the baseline

vane at the other duct heights. This is expected since the thickened vane geometry is identical at the hub whereas its thickness linearly increases towards the tip. This is in accordance with the literature [121, 122] where the unsteady load of thicker airfoils is seen to be reduced. The pressure jump levels from 15% of the chord are seen to be similar between both vane geometries. For a more quantitative analysis, peak levels are noted in Table 3.7 for the baseline and thickened vanes. The peak ratio between both vane geometries is observed to increase towards the tip and is thus highly correlated with the thickened vane geometry variation. A linear regression performed on the ratio provides a coefficient of determination very close to unity ($R^2 = 0.99\%$) indicating a clear linear trend.

Duct height	r/R_T	Hom. peak value [Pa]	Het. peak value [Pa]	Ratio
Hub	61%	94.5	91.4	1.03
Midspan	79%	378.1	314.2	1.20
Tip	95%	577.5	431.4	1.34

Table 3.7: Peak ΔP values at different duct heights for baseline and thickened vanes. The coefficient of determination obtained from a linear regression on the ratio is $R^2 = 0.99\%$.

3.3.6 Inter-stage detailed analysis

In the previous section, the pressure jump responsible for the noise generation was investigated. Here, the focus is put on the aerodynamic excitation responsible for it. As mentioned before, two major excitations are identified: the wake and the potential distortion.

In the instantaneous fields recovered in the simulation, both contributions are included. In order to separate them, an averaging procedure can be applied. The operation consists in time-averaging the fields in the rotating and stationary frames of reference respectively over complete revolutions . When performed in the rotating frame of reference, the average extracts the wakes and thus the aerodynamic excitation responsible for the unsteady loads on the stator vanes. When performed in the stationary reference frame, the averaging suppresses the wakes provided that a sufficient number of timesteps is considered. The average then gives the potential field around the stator vanes responsible for the unsteady loads on rotor blades. The extraction used for this procedure has been described in section 3.1.1. An angular step of 1 degree is used in order to have a fine average that is performed over three complete revolutions.

The obtained rotor wake fields are shown in Figure 3.32. In this case, B regular wakes are observed. Due to the axial wake diffusion, the wake deficit is of about 43 m/s at the rotor trailing edge and about 10 m/s at the stator leading edge. The wake fields are seen to be identical in all stator configurations. This is expected since the stator effect is removed with the average.

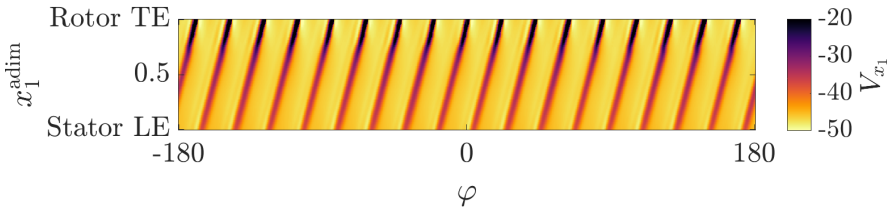

(a) Homogeneous without power-supply cable.

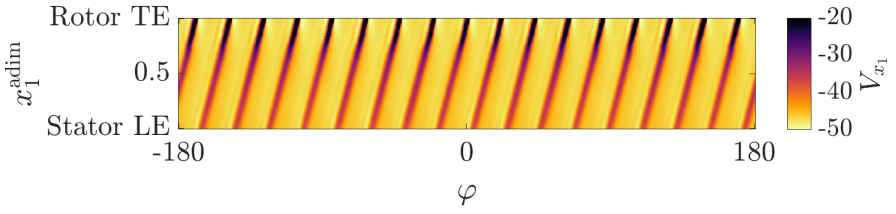

(b) Homogeneous.

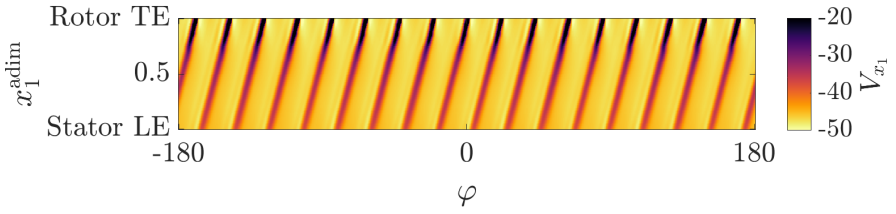

(c) Heterogeneous.

Figure 3.32: Axial velocity field obtained by time-averaging in the rotating reference frame over complete revolutions for the three stator configurations. TE stands for trailing edge and LE for leading edge.

For the potential field, results are shown in Figure 3.33. In this case, clear differences are seen for the three stator configurations. In general, a strong decrease in amplitude is seen towards the rotor blades. This agrees well with the potential theory which predicts an exponential decrease of the potential field. In the heterogeneous configuration (as in experiments), three spots of lower axial velocity are observed in front of the modified vanes. This is due to the larger thickness of those vanes and results from the increased flow blockage. Moreover, the presence of the downstream power-supply cable is also observed. Because the cable is aligned with the second modified vane, the combination of both provides an even lower axial velocity upstream. In this case, the stator can be interpreted as having three modified vanes, one of which having an increased heterogeneity degree. In the homogeneous stator configuration, the identified spots are no longer observed and only the presence of the power-supply cable is observed. Finally, in the homogeneous without power-supply cable, the potential field is seen to be homogeneous and the periodicity from vane-to-vane is recovered.

In order to have a better understanding on these aerodynamic excitations, the fields are azimuthally expanded in Fourier series. This provides the azimuthal modal content and its axial evolution. Results are shown in Figure 3.34 for the wake and potential fields. Firstly, the dominant harmonics for the wake field are seen to be the multiples of the blade count B as expected. Their amplitude is seen to decrease towards the stator vanes.

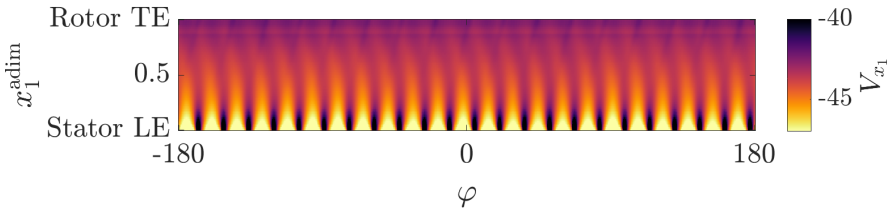

(a) Homogeneous without power-supply cable.

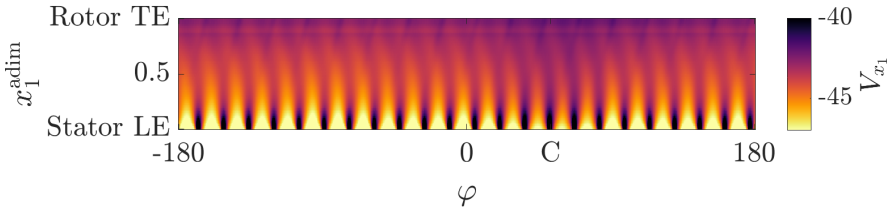

(b) Homogeneous.

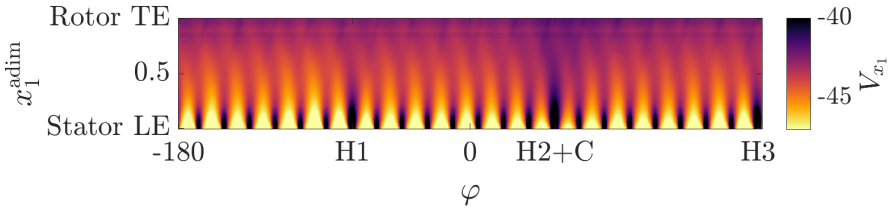

(c) Heterogeneous.

Figure 3.33: Axial velocity field obtained by time-averaging in the stationary reference frame over complete revolutions for the three stator configurations. TE stands for trailing edge and LE for leading edge. H1 to H3 stands for the positions of the three modified vanes and C is the position of the power-supply cable.

On the other hand, the dominant harmonics for the potential field are the multiples of the vane count V. Moreover, because of the stator heterogeneity, low order harmonics are also contributing. Again, the exponential potential decrease is well captured in the simulations. In consequence, levels at the rotor trailing edges are strongly attenuated, reaching a background level at about -15 dB. This is a numerical artefact caused by the interpolations and the time convergence of the average. In addition, the single precision chosen in the LBM solver for the current simulations imposes a background level that could be possibly lowered with a double precision solver at the cost of an increased computational cost. The strong attenuation stresses why the potential-interaction noise is only relevant when the rotor-stator spacing is very small. Nevertheless, in the present configuration, the distance seems to be enough so that the potential field is not important at the rotor trailing edge. In addition, because the stator heterogeneity is here weak, no important potential distortions are observed upstream.

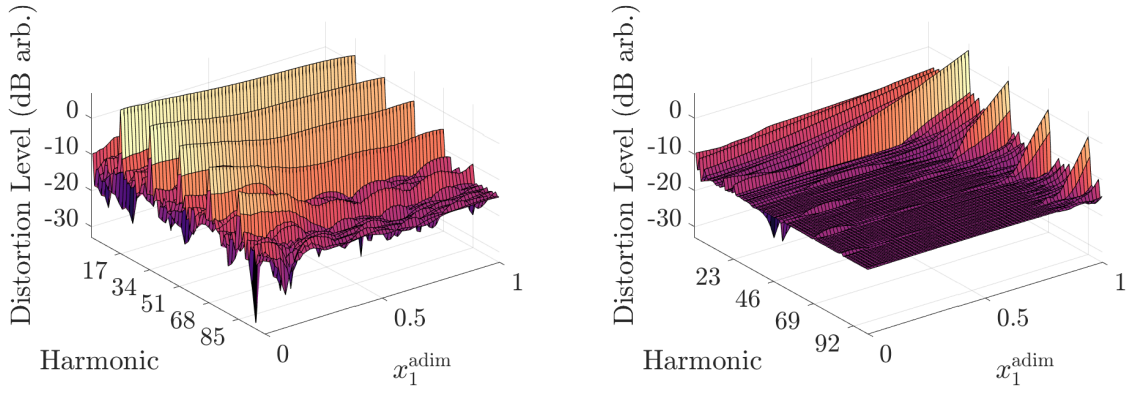

(a) Wake field.

(b) Potential field.

Figure 3.34: Modulus of the azimuthal Fourier coefficients of the axial velocity field in the rotor and stator reference frames for the heterogeneous configuration.

The differences between the different cases are shown in Figure 3.35. For the wake fields, negligible differences are observed in all cases as expected. In the potential field, the difference between the heterogeneous case (1) and homogeneous case with the power-supply cable (2) evidences important variations for the low orders and their harmonics. This is due to the removal of the three modified vanes. When the difference is performed between the homogeneous stator with (2) and without (3) the power-supply cable, the major differences appear at the harmonic orders from one to three. In fact, the cable represents a local azimuthal inhomogeneity that disappears without the cable.

To better visualize the axial evolution, curve plots are shown in Figure 3.36 for the three main wake field harmonics. First of all, all three stator configurations match perfectly indicating no impact of the stator on the wake fields. Note that a linearity assumption is made in order to separate both contributions of the wake and potential fields. This implies that even if a rotor wake is temporarily modified by the stator potential field, the modification should vanish over a complete revolution. In some other architectures,

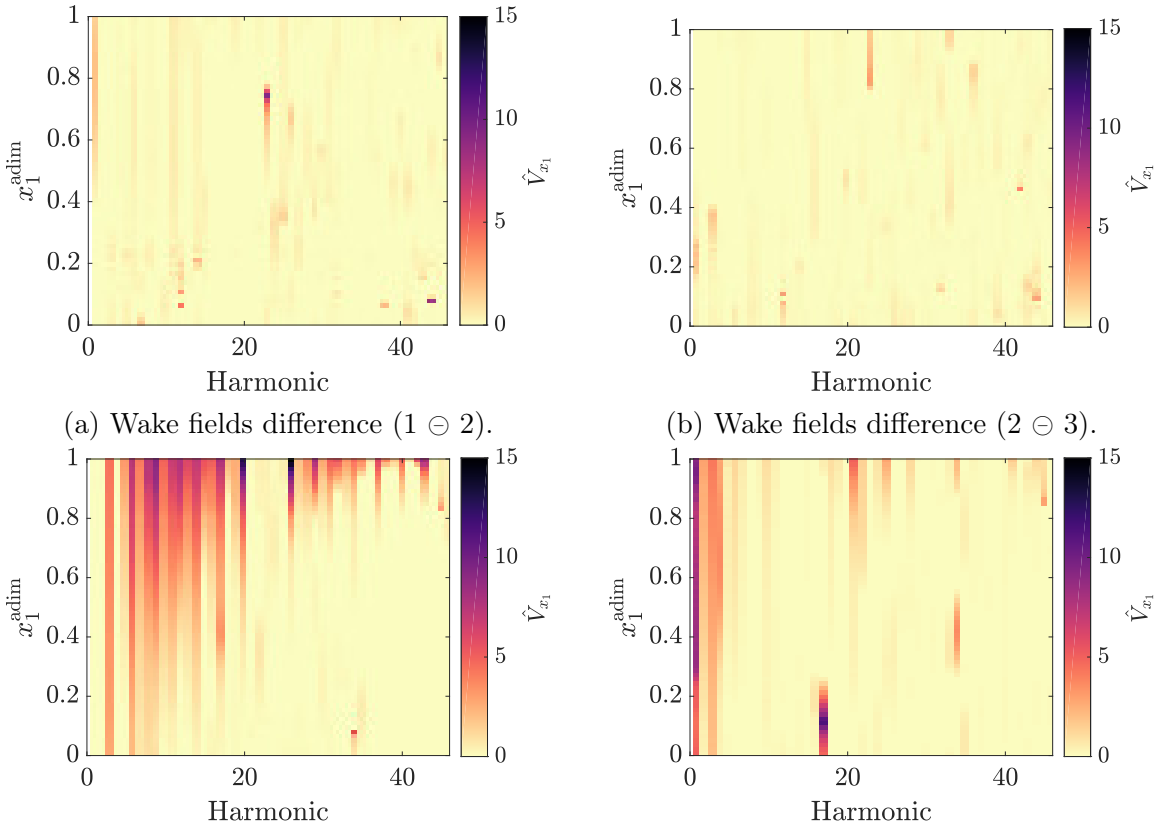

(a) Wake fields difference (1 ⊖ 2).

(b) Wake fields difference (2 ⊖ 3).

(c) Potential field difference (1 ⊖ 2).

(d) Potential field difference (2 ⊖ 3).

Figure 3.35: Difference of the Fourier decomposed axial velocity fields. 1 is the heterogeneous case, 2 the homogeneous case and 3 the homogeneous without power-supply cable.

this might be questioned. A recent study [18] has shown that an interaction of the wake field may appear with strong potential distortions (e.g. turbofan pylon bifurcations). These effects may be attributed to non-linear interactions. In the present investigation, the linearity assumption seems to be validated according to the similarity between all stator configurations. In terms of levels, the dominant harmonic (17) is seen to decrease in amplitude by about 4 dB. The second and third harmonics are seen to decrease faster with the increasing order and their decrease is slower from around 50% of the interstage distance.

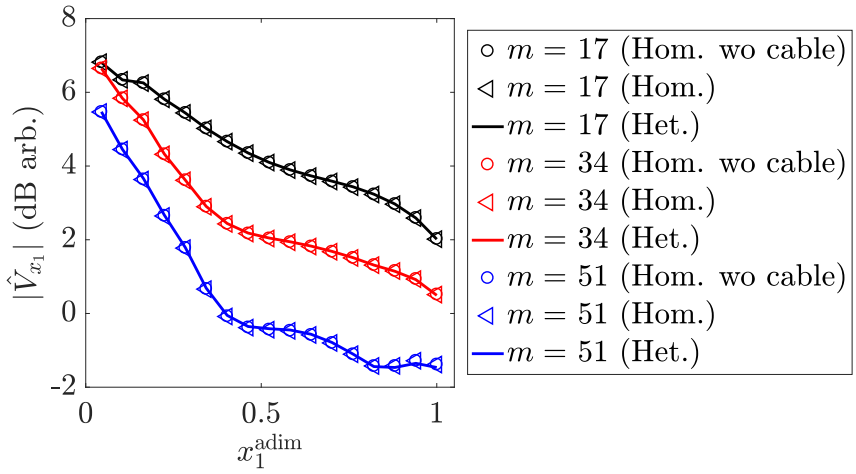

Figure 3.36: Axial evolution in the interstage of the wake field Fourier coefficients.

For the potential distortion, the dominant modes are first analysed at a given axial position (here the stator leading edge) and shown in Figure 3.37. The dominant harmonics are the multiples of the vane count V as discussed previously. Their level is not changed for the three stator configurations. All other harmonics lie in the background level region shown in grey in the figure.

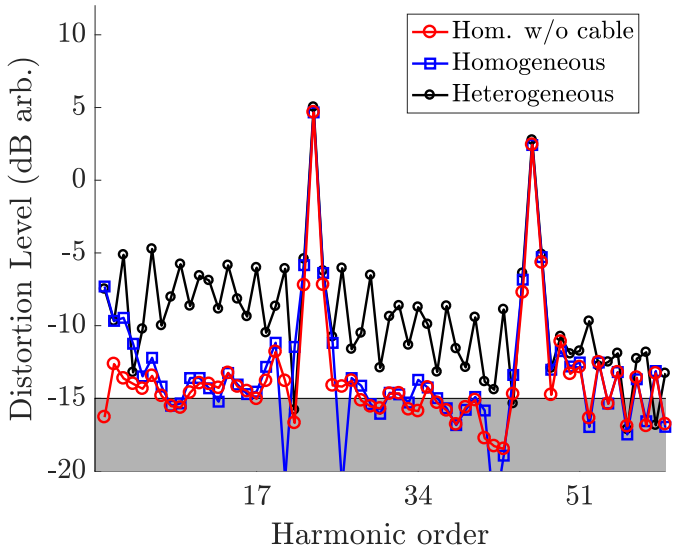

Figure 3.37: Potential field Fourier coefficients at the stator leading edge.

For the homogeneous case with the power-supply cable, the harmonic of order one is increased by more than 8 dB. Most of the other harmonics remain unchanged. Nevertheless, the second, third and fourth harmonics are increased compared with the case without cable. This can be explained by approximating the cable distortion by a Gaussian function as shown in Figure 3.38a and perform a Fourier transform. The Fourier transform of a Gaussian function is also a Gaussian. While a wide Gaussian will provide a fast decrease, a narrow Gaussian will have a slow rate of decrease as shown in Figure 3.38b. In the case of the *LP3* and considering the previous observation, the azimuthal extent of the distortion should be relatively high providing a strong harmonic decrease. To sum-up, having very narrow distortions would be worse in terms of noise levels due to the increased extent of the azimuthal modal content.

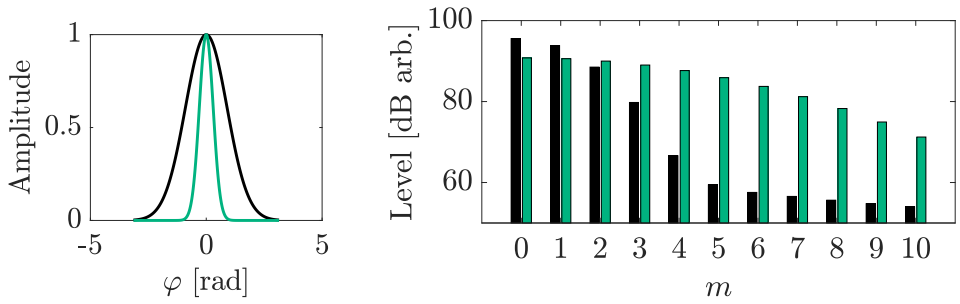

(a) Gaussian function. (b) Fourier transform.

Figure 3.38: Azimuthal Fourier transform of a periodised Gaussian function.

Finally, with the heterogeneous stator, a whole set of harmonics are increased in a sawtooth pattern. The periodicity of these modes is not exact but close to three. Table 3.8 summarizes the dominant modes in the heterogeneous case and the order gap between two consecutive modes. In most of them, a periodicity of three is found. However, at some point only a gap of two is retrieved before recovering again a difference of three. This is due to the fact that the modified stator vanes are not equally spaced which in that case would give a perfect periodicity of three. In fact, the relative positions of the modified vanes are 1, 8 and 16 (with the number of intermediate vanes being 6, 7 and 7 respectively) providing a quasi-periodicity close to three.

								V								$2V$
m	3	6	9	11	14	17	20	**23**	26	29	32	34	37	40	43	**46**
Δm	-	3	3	**2**	3	3	3	3	3	3	3	**2**	3	3	3	3

Table 3.8: Increased modes in the heterogeneous configuration.

From the previous plot, the dominant and some other selected harmonics (namely $n = 1$, 3 and 6) are shown in Figure 3.39. The exponential decrease is well recovered for all harmonics. In addition, one can see that the decay rate of the harmonics is higher with increasing orders. In fact, the harmonic 46 is seen to decrease faster than the 23 reaching thus the background level estimated at -15 dB. In a study performed on the

ANCF configuration and presented in appendix B, the same behaviour was observed. The decay rate evolved linearly with the increasing order. The potential field can be seen as cut-off modes at the frequency zero (steady field). Then, a quick estimation of the exponential decay as a function of the azimuthal order can be obtained. Let us consider a two-dimensional duct in (x_1, x_3) of height D corresponding to the unwrapped cylinder of radius r ($D = 2\pi r$). The dispersion relation of the duct mode of order m gives:

$$k_{x_1} = \pm\sqrt{k^2 - k_{x_3}^2} \quad \text{with} \quad k_{x_3} = \frac{2m\pi}{D} \tag{3.3}$$

if k_{x_1} denoted the axial wavenumber. At the frequency zero ($k = \omega/c_0 = 0$), the axial wave-number writes:

$$k_{x_1} = \pm \mathrm{i}\frac{m}{r} \tag{3.4}$$

so that

$$\exp\left[\mathrm{i}k_{x_1}x_1\right] = \exp\left[\pm\frac{m}{r}x_1\right] \tag{3.5}$$

A linear evolution of exponential decay with respect to the azimuthal mode order m is found. In addition, a higher radius will induce slower exponential decrease. For this reason, the potential field should decrease faster at the hub and slower at the tip.

In accordance with the previous conclusion, the harmonic of order $m = 1$ is seen to have a quasi-steady axial evolution and has higher levels than of the principal harmonics V and $2V$ at the rotor trailing edge. This highlights why having low order spatial modes is prejudicial for the potential-interaction noise. Nevertheless, the weak initial amplitude of this harmonic at the stator leading edge leads to a weak level at the rotor trailing edge. However, in the case of a strong heterogeneity, a high initial amplitude will induce a strong potential-interaction noise. In addition, the interaction of the B blades with the periodicity one will generate all mode orders and thus all cut-on modes. When the power-supply cable is removed, this harmonic is seen to vanish. Regarding the harmonics 3 and 6, even if their initial amplitude is higher compared with harmonic 1, their decay rate is also higher leading to negligible levels at the rotor trailing edge. Note that they are also generated in presence of the power-supply cable as explained previously.

Aerodynamic analysis — Summary

Performances:

1. Pressure rise on the mesh L0 underestimated by 16% compared with the experiments
2. Performance deteriorated for the mesh L1 (coincides with the onset of vortex shedding on the rotor blades)
3. Improvement with the finest mesh L2 (8% of error compared with the exper-

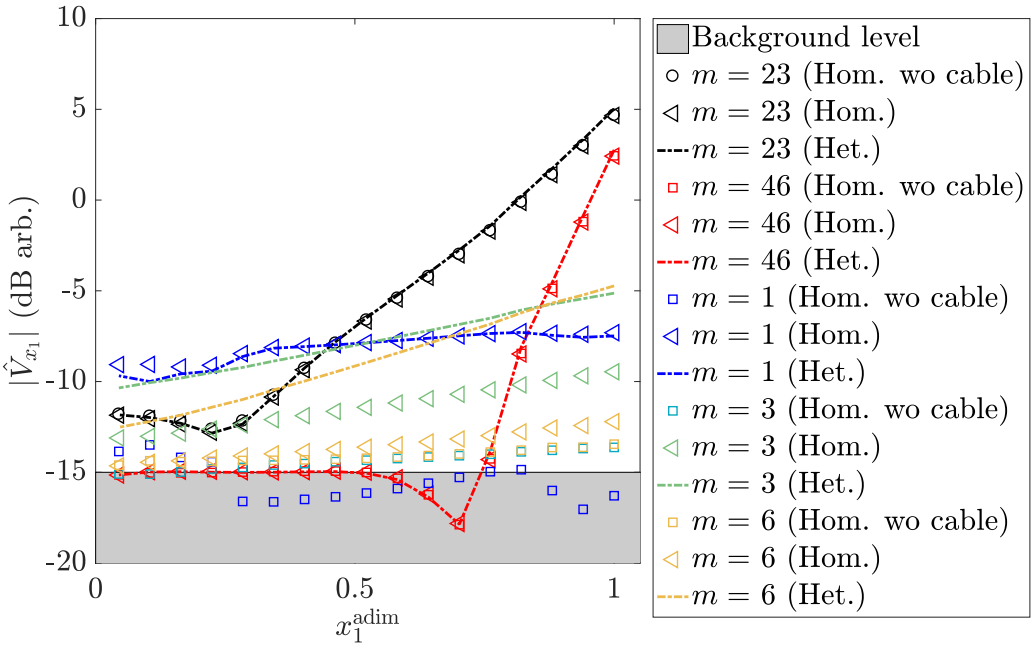

Figure 3.39: Axial evolution in the interstage of the potential field Fourier coefficients.

iment)

4. Better rotor performance with the RANS simulations (increased compression)
5. LBM performance results highly dependent on meshing strategy

Rotor-stator flow topology:

1. No flow topology variation for all stator configurations on the mesh L0
2. Important flow separations on the stator explaining the low performance of the stator
3. Vortex shedding clearly seen in the rotor blade wakes for the mesh L1 but strongly attenuated in the mesh L2

Inflow distortion:

1. No inflow distortion identified in the simulations
2. Velocity fluctuations one order of magnitude below the experimental values

Mean blade and vane loading:

1. Good agreement with the RANS simulation for the rotor
2. Higher discrepancies for the stator due to massive flow separations
3. Reduction of the vane flow separation with the finest mesh

Unsteady blade and vane loading:

1. Stator vane loading dominant compared with the rotor blades
2. Loading higher near the leading edge for the stator vanes as expected for the wake-interaction
3. Lower leading edge peak value for the heterogeneous (thickened) vanes
4. Loading higher at the trailing edge for the rotor blades as expected for the

potential-interaction

Interstage detailed analysis:

1. Wake velocity perturbations higher compared with the potential field in agreement with the previous calculated unsteady loadings
2. Potential field decreasing exponentially upstream
3. Increased axial attenuation of the potential harmonics with the increasing azimuthal order ($f(m) \propto m$ in $\exp[f(m)x]$)
4. Clear impact of the stator heterogeneity and power-supply cable on the potential field
5. Periodicity of three still observed even if the three modified stator vanes are not equally spaced

3.4 Acoustic analysis

In the previous section, the aerodynamic analysis was presented providing information on the aerodynamic excitations that will generate noise. In this section, the acoustic analysis is provided. First a spectral analysis is presented and compared with the experiment. Secondly, the modal content of the noise is retrieved and discussed. According to the experiment presented in the previous chapter, the first two BPFs are expected to be generated by the stator heterogeneity. In addition, some dominant modes identified at these frequencies should be generated by the heterogeneity.

3.4.1 Spectral analysis

In order to compute the wall-pressure spectra, all cases on all mesh levels were run for long simulation times to ensure the acoustic convergence. In Table 3.9 are summarized all the simulated times for each simulation. Because of the increased cost on the finer meshes, the simulated time is considerably reduced for the mesh L1 and L2 even though it is still very high for V-LES like 360° simulations. Note that for each mesh refinement, the solution is initialized from the last timestep of the previous mesh solution.

Geometry	Mesh	Simulation time [rev]
HOM w/o Cable	L0	56.2
HOM	L0	58.5
HET	L0	66.1
HET	L1	22.6
HET	L2	20.9

Table 3.9: Simulated time in revolutions.

The time signals of one probe of the upstream array for the three heterogeneous

simulations are shown in Figure 3.40 ; mean value is removed. In all cases, the fluctuations are well stabilized around zero and are well converged. The length of the time signals has been cropped to the shortest converged simulation (mesh L2). It yields a frequency resolution of 41.2 Hz. In order to compare with the experiment, the same arrays of measuring positions are used.

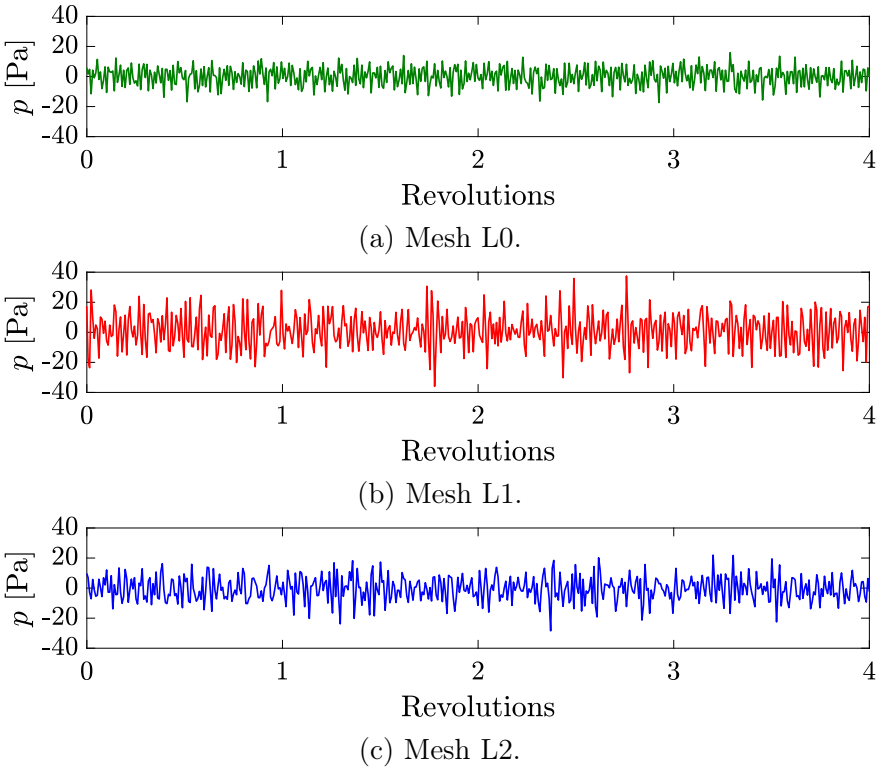

(a) Mesh L0.

(b) Mesh L1.

(c) Mesh L2.

Figure 3.40: Pressure signals of one microphone of the upstream array for the three mesh levels. Last four revolutions plotted.

The various spectra given by the different simulations and the experiment are shown in Figures 3.41 and 3.42 for the upstream and downstream arrays respectively. The first two BPFs that should be cut-off according to Tyler & Sofrin's criterion are observed in both configurations. However, they are clearly increased in the heterogeneous configuration. The first BPF is increased by 10 dB and the second BPF by 13 dB compared to the homogeneous case. The third BPF level is kept almost constant. This is consistent with the clue that heterogeneity modifies more importantly the destructive interferences of cut-off BPFs but has probably a minor effect on cut-on BPFs. These results indicate that sound is not produced by classical rotor-stator interactions of homogeneous stages.

In the homogeneous case, the first two BPFs (black and orange symbols in the figure) are still present but greatly attenuated. Some non-uniformities in the rotor wakes impinging on the stator could also generate rotational shaft harmonics and thus also contribute at the BPFs. Nevertheless, they are hidden by the broadband noise not correctly reproduced for this mesh refinement (L0). The removal of the power-supply cable is seen to have a negligible effect on noise. This agrees with the previous observation where the

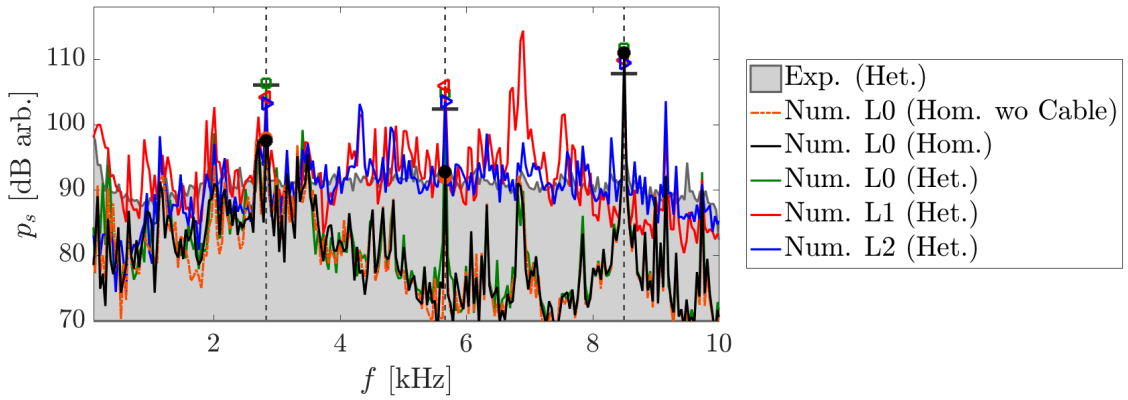

Figure 3.41: Averaged wall-pressure spectra of all microphones of the upstream array.

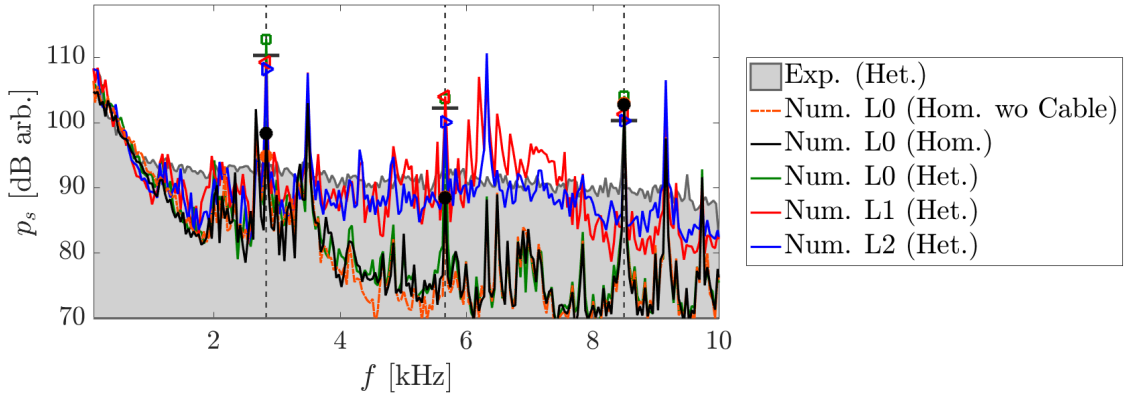

Figure 3.42: Averaged wall-pressure spectra of all microphones of the downstream array.

amplitude of the potential distortion is weak.

The first mesh refinement (L1) is seen to increase the broadband levels, now matching the measurements. However, some important peaks appear around 7 kHz. They are not well understood yet but could be related to the vortex shedding previously discussed. Due to the rotational speed, a modulation of the vortex shedding frequency must result providing a different radiation frequency in the stationary frame of reference. With the mesh level L2, these peaks at 7 kHz are considerably reduced for the upstream array. The broadband level is nevertheless kept at a similar level compared to the mesh L1. For the downstream array, the unexpected peaks remain for the finer mesh L2. They appear to be at a precise frequency of BPF+4Ω. Further investigation is needed before concluding on the precise origin of these peaks.

In order to estimate more precisely the BPF levels, a re-sampling of the time signals is done to perform averages on synchronized revolutions. The result provides a spectrum with only harmonics of the rotational frequency where BPF levels are recovered. Results are shown in Figure 3.43.

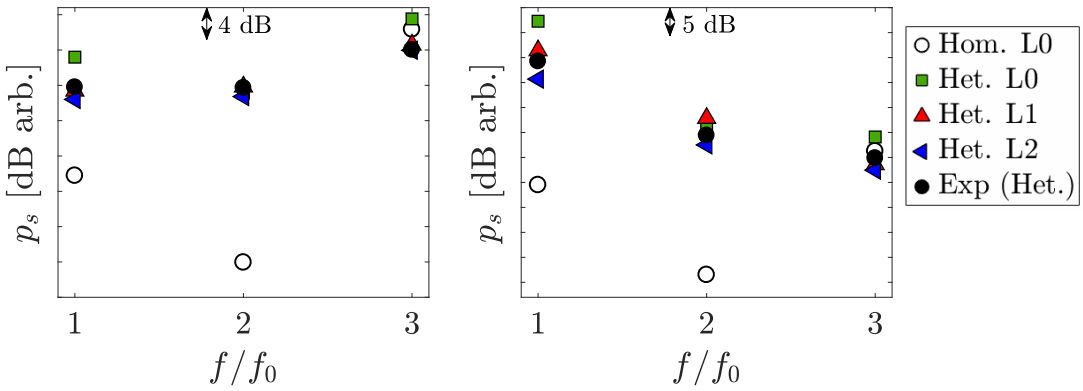

(a) Upstream array. (b) Downstream array.

Figure 3.43: Upstream and downstream BPF level comparison. The evaluation is obtained with synchronized averages (engine order analysis), which provide a better estimation at the BPFs.

The mesh refinement provides a more accurate BPF prediction in all cases. Regarding the BPF 1, the higher mesh resolution reduces the overestimation to about 2 dB in the upstream array. For the second and third BPF, the recovered levels are within 1 dB. In the downstream array, the same overestimation of the BPF 1 is seen to be reduced when refining the mesh. For the mesh L2, results are within 3 dB compared with experiments.

Interestingly, similar BPF variations as in experiments are captured. On the one hand, the first two BPFs have lower levels compared with the third one for the upstream array. On the other hand, levels are monotonically decreasing for the downstream array. The important level differences between the upstream and downstream arrays may be explained by combinations of the modal angle and the equivalent dipole inclination angle of the stator vane. A large efficiency is observed when the modal angle is not far from the dipole angle and a lower efficiency is observed otherwise.

Finally, the tonal noise for the homogeneous case for the first two BPFs is seen to be below that of the heterogeneous case by more than 15 dB. The synchronized average performed on the signals put in evidence a better cancellation of the BPF levels. It can thus be said that the classical cut-off design rule is invalidated by the stator heterogeneity. Taking into account that the stator heterogeneity of the *LP3* is weak, its impact on noise is nevertheless substantial.

3.4.2 Modal analysis

For a more detailed analysis, the azimuthal modal content has been calculated at various radii, leading to the charts shown in Figure 3.44. The post-processing is done on the acoustic extraction plane upstream of the fan shown in Figure 3.4 in order to avoid the hydrodynamic de-noising that would be necessary downstream of the fan-OGV.

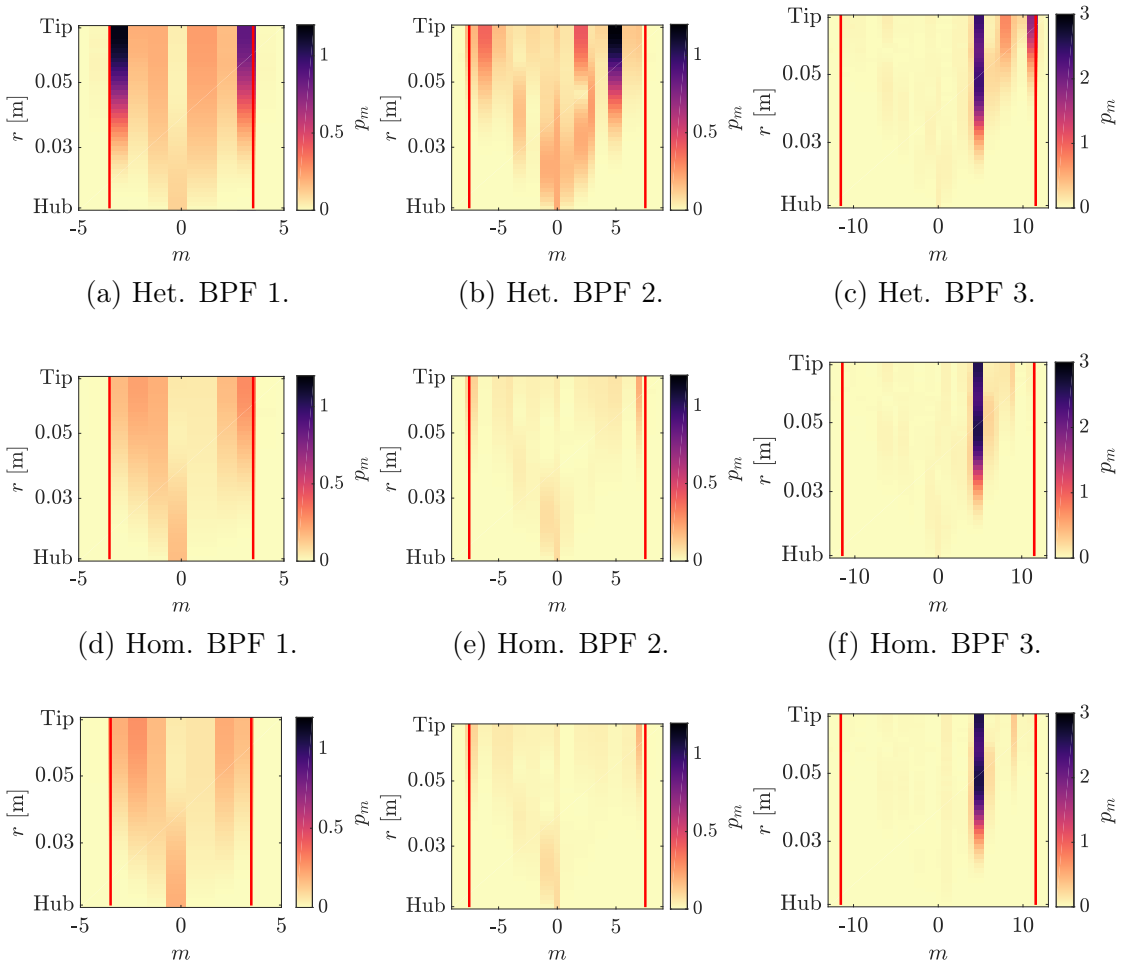

(a) Het. BPF 1. (b) Het. BPF 2. (c) Het. BPF 3.

(d) Hom. BPF 1. (e) Hom. BPF 2. (f) Hom. BPF 3.

(g) Hom. w/o cable. BPF 1. (h) Hom. w/o cable. BPF 2. (i) Hom. w/o cable. BPF 3.

Figure 3.44: Azimuthal modal content upstream of the fan. Vertical red lines define the cut-off limits.

For all BPF tones, the major modal content is concentrated close to the tip. This can be explained by the radial shape functions (Bessel functions) of the dominant modes

observed. At the first BPF in the heterogeneous case, the modes of order $m = -3$ and $m = 3$ are dominant. At the second BPF, the mode $m = 5$ is dominant. Finally, at the third BPF, the Tyler & Sofrin mode $m = 5$ is observed along with another unexpected mode $m = 11$. In the homogeneous case, the first two BPFs have residual levels with no dominant modes. At the third BPF, only the Tyler & Sofrin mode is retrieved. This again highlights the effect of the heterogeneous stator on the first two BPFs. Dominant modes have been generated at all BPFs. The removal of the power-supply cable in the last configuration is seen to have a negligible impact on the mode amplitudes.

Next, full modal decompositions have been also performed according to equation (1.2). These modal decompositions allow to retrieve the radial modal content but also to separate upstream from downstream propagating modes. Results for the upstream/downstream azimuthal modes are shown in Figure 3.45 for the upstream array and in Figure 3.46 for the downstream array. The same modes as those identified from the azimuthal analysis are found.

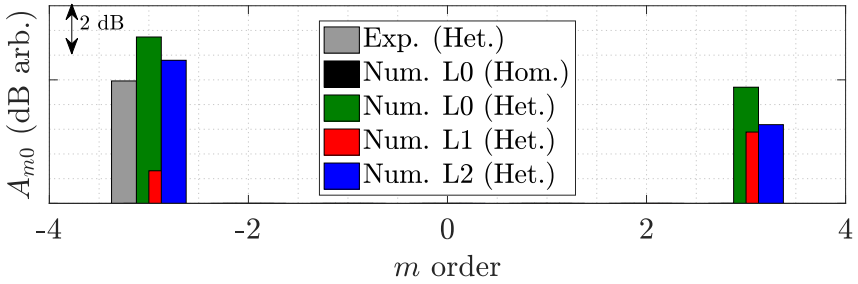

(a) BPF 1.

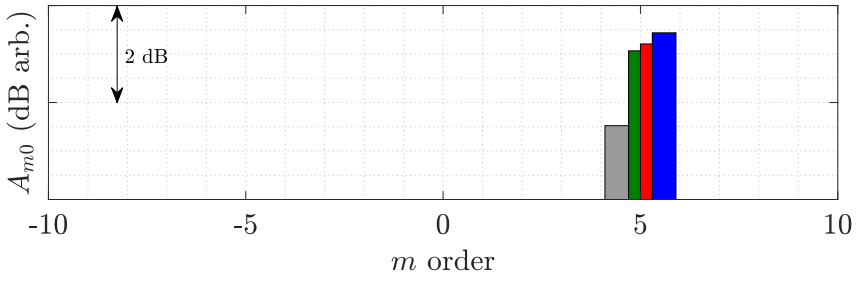

(b) BPF 2.

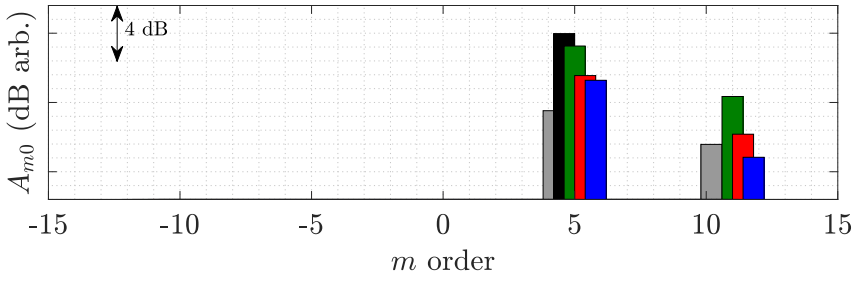

(c) BPF 3.

Figure 3.45: Upstream propagating modes of the upstream array.

First of all, the only radiating mode for the homogeneous configuration is the mode

$m = 5$ observed at the third BPF. It is a Tyler & Sofrin mode given by the simple rule $m = sB - pV$. For the heterogeneous stator, acoustic modes can be identified at the first two BPFs. At the first BPF, the modes $m = -3$ and $m = 3$ are observed in the simulations while in the experiments only the mode $m = -3$ is observed. During the experiment shown in chapter 2, a slight difference in the operating conditions has triggered a switch of dominant mode between the modes -3 and 3. Because in the simulations the operating point was seen to slightly vary, the same phenomenon could be at the origin of this inversion. Moreover, because the mode is close to its cut-off limit, it is very sensitive to small variations of the flow. Nevertheless, the predicted levels are in reasonable agreement with the experiment.

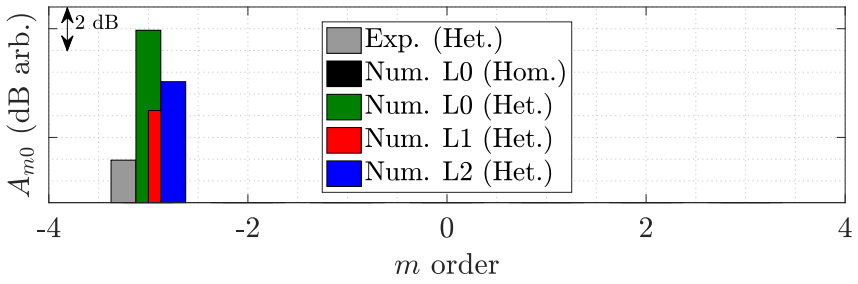

(a) BPF 1.

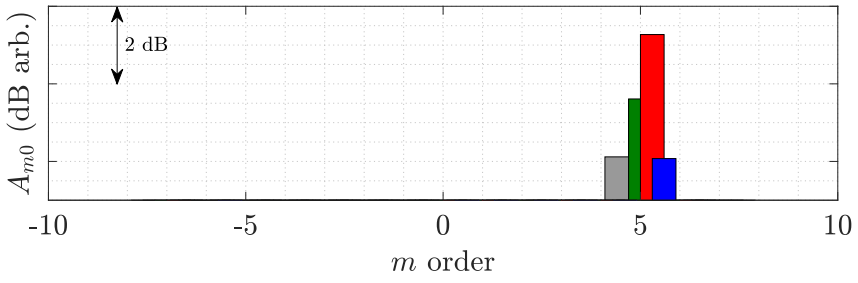

(b) BPF 2.

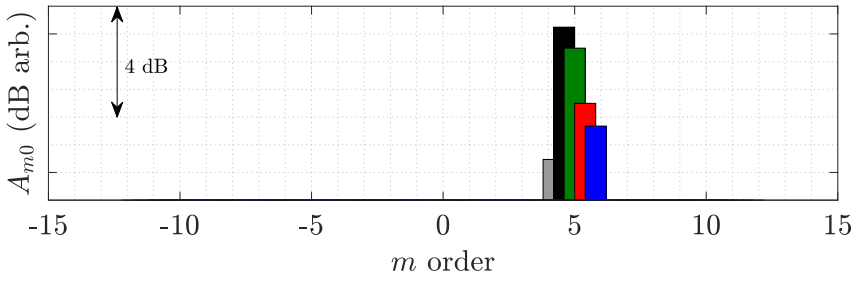

(c) BPF 3.

Figure 3.46: Downstream propagating modes of the downstream array.

At the second BPF, the mode $m = 5$ is dominant. For the downstream array, the mesh refinement is seen to play an important role and considerably reduces the discrepancy with the experiment. Finally, at the third BPF, the mode amplitude is decreased with the mesh refinement, thus decreasing the gap with the experiment. The mode $m = 11$ attributed to the stator heterogeneity is well captured for the upstream array but is not seen as dominant

for the downstream array. This is in good agreement with the experiment where the same behaviour is observed. To conclude, the overall dominant modes are correctly recovered for all meshes. In addition, the refinement of the grid is seen to improve the accuracy of some mode amplitudes.

Regarding the amplitude distribution over radial modes not shown here, the dominant modes are found to be at the order $n = 0$. This is partly due to the fact that higher radial orders are often cut-off for the identified azimuthal modes and at these operating conditions as shown in the experiment in the previous chapter.

The separation of the downstream and upstream propagating modes has also been done. Results have evidenced a very weak amount of reflection at the duct inlet and at the duct termination. The sponge zones are thus seen to be effective for the wave absorption.

Again, it is confirmed that at the first two BPFs of the homogeneous case, no dominant mode can be identified. According to the comparison with the homogeneous and heterogeneous cases, the emergence of these modes at the first two BPFs can now be traced to the heterogeneity of the stator. The analytical prediction of these dominant azimuthal orders will be investigated in the following chapter. Because the modified stator vanes are not equally distributed on azimuth (3 from 23), this prediction exercise is more difficult using simple rules as Tyler & Sofrin's criterion.

Acoustic analysis — Summary

Spectral analysis:

1. Increase of the first two BPFs by more than 15 dB with the heterogeneous stator
2. Vortex shedding observed in the mesh L1 clearly seen in the spectra and greatly attenuated in the mesh L2
3. Unexpected tones at frequencies BPF+4Ω
4. Broadband noise well recovered with the mesh refinement
5. Tone levels in good agreement with the experiment and improved with the mesh refinement
6. Similar BPF variations found for the upstream and downstream arrays

Modal analysis:

1. Both azimuthal and full azimuthal-radial mode analysis providing the same dominant modes as in the experiment except for the mode $m = 3$ not found at these operating conditions
2. Heterogeneity recognized as responsible for the generation of dominant modes at all BPFs:
   - BPF 1: $m = -3, 3$
   - BPF 2: $m = 5$

- BPF 3: $m = 11$

3. Coarse mesh L0 able to correctly reproduce the effect of the heterogeneity (same dominant modes)
4. Mesh refinement seen to increase the prediction accuracy

3.5 Conclusion

In this chapter the *LP3* has been numerically investigated. Results have shown that the pressure rise is underestimated for the mesh L0 but greatly improved for the mesh L2. Nevertheless, comparisons with wall-resolved RANS simulations stress a weaker rotor compression from midspan to tip. A final LBM mesh refinement would allow concluding on the non-monotonic convergence observed from mesh L0 to mesh L2. In future experiments, additional measurements should also be added to improve the operating point characterization such as total pressure surveys upstream and downstream of the fan. This should allow to more convincingly evaluate the discrepancies between the experiment and the numerical simulations (LBM and RANS).

In terms of aerodynamic excitations, the wake interaction is seen to be dominant when compared with the potential interaction. Nevertheless, the impact of the stator heterogeneity is also clearly seen in the potential field. Moreover, the downstream power-supply cable is seen to generate low order azimuthal modes which can be very prejudicial for the noise emissions. Nevertheless, their initial amplitude at the stator leading edge is seen to be weak leading to a negligible impact on noise emissions in this configuration.

Finally, the acoustic analysis evidenced an important impact of the stator heterogeneity on noise. The first two BPFs that are supposed to be cut-off for a homogeneous stator are seen to be increased by more than 15 dB in some cases. It is important to highlight that the present heterogeneity degree is weak and its consequence on noise is nevertheless very high. The stator heterogeneity is seen to invalidate the design criterion that ensures the cut-off of the first two BPFs. The modal analysis has also confirmed the same dominant modes as those found in the experiment. These modes will be analytically investigated in the next chapter. To conclude, the predictive character of the numerical simulations shown in this chapter demonstrates that they are a useful design tool that can be used to optimise the design of heterogeneous OGVs.

4 Analytical modelling and optimisation study

Contents

In the previous chapters, an experimental and numerical characterization of the *LP3* has been established. The numerical simulations on heterogeneous and homogeneous stators have evidenced the effect of the heterogeneity on noise and results agreed well with the experiment. In this chapter, the objective is to analytically investigate the noise of such configurations. Two models for the wake-interaction noise and the potential-interaction noise are presented. Finally, an optimisation study on the *LP3* configuration and some general conclusions on the stator heterogeneity are given.

4.1 Potential-interaction noise

The potential-interaction noise is generated from the interaction of the rotor blades with the downstream stator potential field. As shown in the previous chapter, the loading generated from this kind of interaction is expected to be dominated by the trailing edge area. Moreover, the potential field decreases exponentially. For this reason, this noise source should only be relevant for short rotor-stator distances. According to the numerical simulation results, this source is nevertheless negligible compared to the wake interaction

in this configuration. However, the heterogeneity is seen to play a role on the azimuthal content of the potential field that will be analytically investigated.

As a reminder, a sketch of the potential-interaction noise is shown in Figure 4.1b. In this case, the sources (rotor blades) are homogeneous and thus periodic from blade to blade. However, the perturbation field is heterogeneous in the presence of a modified vane geometry. This means that the potential field loses its periodicity from vane to vane and has an increased spatial modal content which is not anymore only composed of multiples of the vane count V. Yet, this noise source can still be modelled by the classical Goldstein's analogy which considers equally spaced sources. The heterogeneity is here introduced through an heterogeneous disturbance field (the potential field).

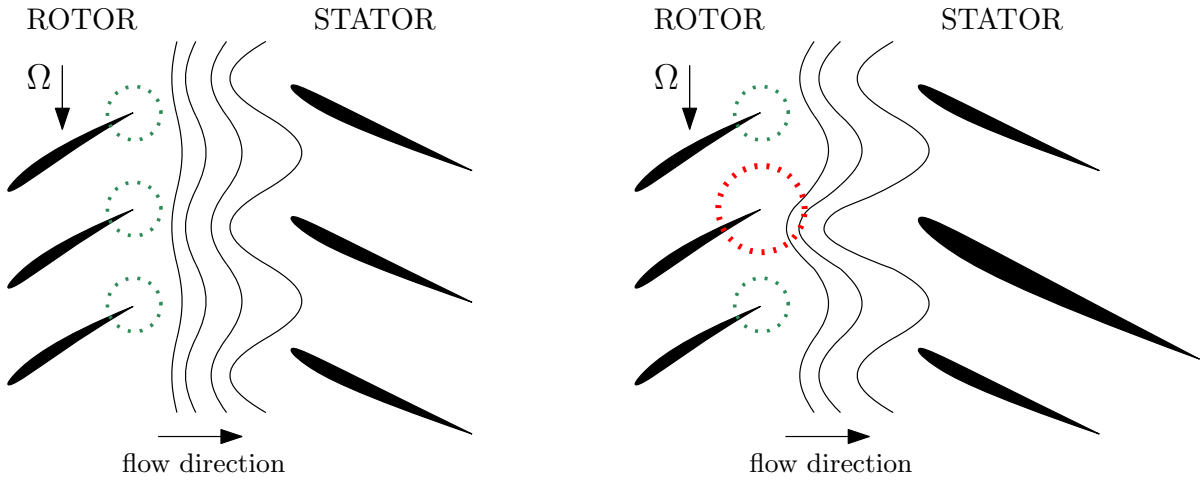

(a) Homogeneous (b) Heterogeneous

Figure 4.1: Representation of the potential interaction noise mechanism for a homogeneous and heterogeneous stators.

4.1.1 Modelling

The model of this noise source relies on Goldstein's analogy for duct flows as described in chapter 1. It does not account for cascade effects and has the rotor blade pressure jump as input. The acoustic power for sources located on the rotor is given by:

$$\mathcal{P}_{sB}^{\pm} = \frac{B^2\beta^4}{2\rho c_0}\left(\frac{sB\Omega}{c_0}\right)\sum_{m=-\infty}^{+\infty}\sum_{n=1}^{+\infty}\frac{|mD_{mn}^{\pm(p)} - \gamma_{mn}^{\pm}T_{mn}^{\pm(p)}|^2}{\Gamma_{mn}k_{mn}\left[\frac{sB\Omega}{c_0} \pm Mk_{mn}\right]^2} \tag{1.37}$$

where T_{mn} and D_{mn} are functions of the chordwise pressure jump ΔP on a rotor blade. The pressure jump is then function of the velocity perturbation field, that is to say, the stator potential field. More details on Goldstein's analogy are given in chapter 1.

4.1.1.1 Parry's versus Reversed Sears' airfoil response models

The focus is now given on the pressure jump modelling for the potential interaction. Because we are dealing with downstream interactions, the classical Amiet's model (presented in chapter 1) for a leading edge gust impingement is not suited. It would be only for small blade angles ensuring that the potential distortion is entered by the leading edge first. In addition, in the case of wake gusts, the perturbation is considered to be frozen and solely convected downstream. For the potential field case, the disturbance decreases exponentially upstream in the opposite direction of the mean flow as shown in the previous chapter. The velocity perturbation is defined as a gust as follows:

$$u = u_a \exp\left[\mathrm{i}K_1 z_1 + \mathrm{i}K_2 z_2 - \mathrm{i}\omega t\right] \tag{4.1}$$

This velocity perturbation will generate an unsteady load on the rotor blades. But unlike constant-amplitude frozen gusts where $K_1 \in \mathbb{R}$ and for which $|v| = |u_a|$, the axial wave-number K_1 is in this case complex-valued:

$$K_1 = \frac{\omega}{U_0} + \mathrm{i}k_a \tag{4.2}$$

$$= M_0^{-1}k + \mathrm{i}k_a \tag{4.3}$$

where the real part $M_0^{-1}k$ corresponds to the classical hydrodynamic wave-number and the imaginary part k_a to a damping or amplification coefficient of the perturbation. The origin of the reference frame $\mathbf{z}$ is set at the trailing edge of the plate, see Figure 4.2. z_1 points downstream and z_3 is the vertical coordinate with respect to the airfoil.

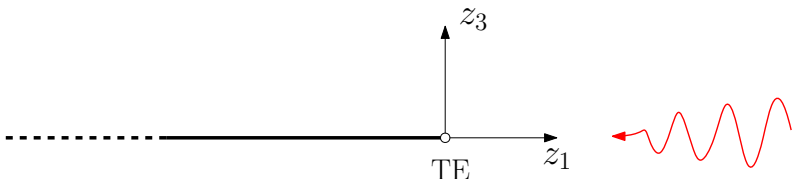

Figure 4.2: Chosen reference frame. TE stands for trailing edge.

In order for the disturbance to be attenuated towards the rotor blades ($-\mathbf{e}_{z_1}$), the imaginary part of the axial wave number must be negative ($k_a < 0$):

$$\exp\left[\mathrm{i}K_1 z_1\right] = \exp\left[\mathrm{i}M_0^{-1}k\, z_1 - k_a\, z_1\right] \tag{4.4}$$

The description of the amplitude u_a and the damping factor k_a are given by the analytical or numerical description of the potential distortion which is expressed as a sum of elementary gusts where we can identify the two previous parameters.

Once the disturbance is described, let us focus on the modelling of the airfoil response. A first model accounting for a reversed gust was proposed by Roger & Moreau [17],

referred to as the Reversed Sears model. This model was then applied with a complex hydrodynamic wave-number by Conte et al. [51]. The model considers a reversed Amiet's problem for trailing edge interactions in which the Kutta condition is not applied. The following system of equations is solved:

$$\begin{cases} \nabla^2\phi - \dfrac{1}{c_0^2}\dfrac{D^2\phi}{Dt^2} = 0 & \\ \dfrac{\partial\phi}{\partial z_3} + u_a \exp\left[\mathrm{i}K_1 z_1 + \mathrm{i}K_2 z_2 - \mathrm{i}\omega t\right] = 0 & \text{for} \quad z_1 < 0 \\ \phi = 0 & \text{for} \quad z_1 \geq 0 \end{cases} \tag{4.5}$$

The rigidity condition is imposed on the flat plate and the potential is cancelled downstream of it. The main differences with the classical Amiet's approach for the leading-edge gust impingement are:

- frame of reference placed at the trailing edge first ;
- complexed-valued gust chordwise wavenumber ;
- no Kutta condition imposed at the trailing edge ;
- first iteration performed in the opposite direction of the flow.

An improved model accounting for the Kutta condition can be found in the thesis of Parry [16]. The model is stated in a similar way as the previous problem but imposes the cancellation of the pressure difference at the trailing edge instead of the potential. The following system is thus solved:

$$\begin{cases} \nabla^2\phi - \dfrac{1}{c_0^2}\dfrac{D^2\phi}{Dt^2} = 0 & \\ \dfrac{\partial\phi}{\partial z_3} + u_a \exp\left[\mathrm{i}K_1 z_1 + \mathrm{i}K_2 z_2 - \mathrm{i}\omega t\right] = 0 & \text{for} \quad z_1 < 0 \\ \Delta P = 0 & \text{for} \quad z_1 \geq 0 \end{cases} \tag{4.6}$$

Compared with the Reversed Sears' model, the improvement is achieved by applying the Kutta condition at the trailing edge. In Parry's thesis, the problem is solved using the Wiener-Hopf technique. It is proposed here to solve the same boundary-value problem using the Amiet-Schwarzschild formalism. Solutions of both models will then be compared.

The first boundary condition is a rigidity condition of the airfoil according to which the normal velocity of the response $\partial\phi/\partial z_3$ cancels that of the velocity perturbation at the wall. The second condition corresponds to the Kutta condition which introduces a viscosity effect and ensures the continuity of the pressure at the trailing edge. It is convenient to formulate this problem in the form of a canonical Helmholtz equation. For this, we perform the following change of variables:

$$\phi(z_1, z_2, z_3) = \Psi(z_1, z_3)\mathrm{e}^{\mathrm{i}(K_2 z_2 - \omega t)} \tag{4.7}$$

We introduce the change of variables in equation 4.6 and we obtain:

$$\beta^2 \frac{\partial^2 \Psi}{\partial z_1^2} + \frac{\partial^2 \Psi}{\partial z_3^2} + 2\mathrm{i} M_0 k \frac{\partial \Psi}{\partial z_1} + (k^2 - K_2^2)\Psi = 0 \tag{4.8}$$

where $M_0 = U_0/c_0$, $k = \omega/c_0$ et $\beta = \sqrt{1 - M_0^2}$. The rigidity condition becomes:

$$\frac{\partial \Psi}{\partial z_3} + u_a \, \exp\left[\mathrm{i} K_1 \, z_1\right] = 0 \tag{4.9}$$

We now perform a second change of variables, the Reissner transform [123]:

$$\Psi(z_1, z_3) = \psi(z_1, z_3) \mathrm{e}^{-\mathrm{i}\frac{M_0 k}{\beta^2} z_1} \tag{4.10}$$

$$z_1 = \bar{z}_1 \qquad z_2 = \bar{z}_2 \qquad \beta z_3 = \bar{z}_3 \tag{4.11}$$

After some calculus, the new Helmholtz equation writes:

$$\frac{\partial^2 \psi}{\partial \bar{z}_1^2} + \frac{\partial^2 \psi}{\partial \bar{z}_3^2} + \left(\frac{k}{\beta^2}\right)^2 \left[1 - \left(\frac{K_2 \beta}{k}\right)^2\right] \psi = 0 \tag{4.12}$$

Setting $\Theta = k/K_2\beta$ and $\mu = k/\beta^2$ leads to a canonical Helmholtz equation:

$$\boxed{\frac{\partial^2 \psi}{\partial \bar{z}_1^2} + \frac{\partial^2 \psi}{\partial \bar{z}_3^2} + \mu^2 \left[1 - \frac{1}{\Theta^2}\right] \psi = 0} \tag{4.13}$$

Only parallel gusts are considered in the following, so $K_2 = 0$ and $\Theta = +\infty$ (i.e. supercritical gusts). After the change of variables, the boundary condition becomes:

$$\boxed{\frac{\partial \psi}{\partial \bar{z}_3} = -\frac{u_a}{\beta} \mathrm{e}^{\mathrm{i}\mathcal{K}\bar{z}_1}} \tag{4.14}$$

where $\mathcal{K} = K_1 + M_0 k/\beta^2$. The first resolution step consists in finding a solution to the Helmholtz equation that fullfills the rigidity condition. We are therefore looking for a solution of the following system:

$$\begin{cases} \nabla^2 \psi_0 + \mu^2 \psi_0 = 0 \\ \dfrac{\partial \psi_0}{\partial \bar{z}_3} = -\dfrac{u_a}{\beta} \mathrm{e}^{\mathrm{i}\mathcal{K}\bar{z}_1} \qquad \forall \, \bar{z}_1 \end{cases} \tag{4.15}$$

This solution can be written as:

$$\psi_0 = A \mathrm{e}^{B\bar{z}_1 - \mathrm{i}\sqrt{\mu^2 + B^2}\bar{z}_3} \tag{4.16}$$

The normal derivative at $\bar{z}_3 = 0$ writes

$$\frac{\partial \psi_0}{\partial \bar{z}_3} = -\mathrm{i}\sqrt{\mu^2 + B^2} A \mathrm{e}^{B\bar{z}_1} = -\frac{u_a}{\beta}\,\mathrm{e}^{\mathrm{i}\mathcal{K}\bar{z}_1} \tag{4.17}$$

We thus have the constants by identification:

$$A = -\frac{u_a}{\beta}\frac{\mathrm{i}}{\sqrt{\mu^2 - \mathcal{K}^2}} \tag{4.18}$$

$$B = \mathrm{i}\mathcal{K} \tag{4.19}$$

and the potential ψ_0 at $\bar{z}_3 = 0$ writes

$$\psi_0 = -\frac{u_a}{\beta}\frac{\mathrm{i}}{\sqrt{\mu^2 - \mathcal{K}^2}}\,\mathrm{e}^{\mathrm{i}\mathcal{K}\bar{z}_1} \tag{4.20}$$

In order to impose the Kutta condition, the potential is expressed in terms of pressure. The potential-pressure link is given by the following relation:

$$P = -\rho_0 \left(\frac{\partial \phi}{\partial t} + U_0 \frac{\partial \phi}{\partial z_1}\right) \tag{4.21}$$

$$= -\rho_0 U_0 \left(\frac{\partial \psi}{\partial \bar{z}_1} - \mathrm{i}\left[\frac{\omega}{U_0} + \frac{M_0 k}{\beta^2}\right]\psi\right)\,\mathrm{e}^{-\mathrm{i}\frac{M_0 k}{\beta^2}\bar{z}_1 - \mathrm{i}\omega t} \tag{4.22}$$

$$\tag{4.23}$$

We set $k^* = \omega/U_0 + M_0 k/\beta^2 = k/M_0\beta^2$ so that:

$$P = -\rho_0 U_0 \left(\frac{\partial \psi}{\partial \bar{z}_1} - \mathrm{i}k^*\psi\right)\,\mathrm{e}^{-\mathrm{i}\frac{M_0 k}{\beta^2}\bar{z}_1 - \mathrm{i}\omega t} \tag{4.24}$$

We also set

$$P = -\rho_0 U_0 \mathrm{e}^{-\mathrm{i}\frac{M_0 k}{\beta^2}\bar{z}_1 - \mathrm{i}\omega t}\,P^* \tag{4.25}$$

From this, we can now relate the potential to the pressure:

$$\boxed{P_0 = -\rho_0 U_0 \frac{u_a(\mathcal{K} - k^*)}{\beta\sqrt{\mu^2 - \mathcal{K}^2}}\mathrm{e}^{\mathrm{i}K_1\bar{z}_1 - \mathrm{i}\omega t}} \tag{4.26}$$

In a similar way to what is done in Amiet's problem for the potential cancellation upstream, a new boundary value problem is stated in order to cancel the pressure at the

trailing edge and impose the Kutta condition. The new boundary-value problem writes:

$$\begin{cases} \nabla^2 P_1^* + \mu^2 P_1^* = 0 & \\ \dfrac{\partial P_1^*}{\partial \bar{z}_3} = 0 & \text{for} \quad \bar{z}_1 < 0 \\ P_1^* = -P_0^* & \text{for} \quad \bar{z}_1 \geq 0 \end{cases} \tag{4.27}$$

where P_1 is a new solution defined so that $P_1 + P_0$ is cancelled at the trailing edge. The solution to this problem is given by the Amiet-Schwarzschild procedure described in chapter 1. After some calculus, the pressure writes:

$$P_1^*(\bar{z}_1, 0) = \frac{\mathrm{i} u_a \left(\mathrm{i}\mathcal{K} - \mathrm{i}k^*\right)}{\beta\sqrt{\mu^2 - \mathcal{K}^2}} \times \mathrm{e}^{\mathrm{i}\mathcal{K}\bar{z}_1} \left[1 - (1+\mathrm{i})\mathrm{E}^\star[(\mu + \mathcal{K})\bar{z}_1]\right] \tag{4.28}$$

where

$$\mathrm{E}^\star[x] = \int_0^x \frac{\mathrm{e}^{-\mathrm{i}t}}{\sqrt{2\pi t}} \mathrm{d}t \tag{4.29}$$

is a combination of Fresnel integrals. The argument of the integral being complex, we then have branch cuts (positive imaginary axis for a zero real part). In order to manage these branch-cut, the complex error function with complex arguments is used instead. Both are related by:

$$\Phi(\sqrt{\mathrm{i}x}) = (1+\mathrm{i})\mathrm{E}^\star[x] \tag{4.30}$$

Finally:

$$\boxed{P_1(\bar{z}_1, 0) = \rho_0 U_0 \frac{u_a \left(\mathcal{K} - k^*\right)}{\beta\sqrt{\mu^2 - \mathcal{K}^2}} \mathrm{e}^{\mathrm{i}K_1\bar{z}_1} \left[1 - \Phi\left[\sqrt{\mathrm{i}(\mu + \mathcal{K})\bar{z}_1}\right]\right] \mathrm{e}^{-\mathrm{i}\omega t}} \tag{4.31}$$

The complete wall-pressure field accounting for the Kutta condition writes:

$$P^* = P_0^* + P_1^* \tag{4.32}$$

Considering that pressure oscillations at the trailing edge are in phase opposition between the upper and lower sides (dipolar character of the sources), the pressure-jump is written as:

$$\Delta P = P^{\text{upper}} - P^{\text{lower}} \tag{4.33}$$

$$= P^{\text{upper}} - (-P^{\text{lower}}) \tag{4.34}$$

$$= 2\, P(\bar{z}_1, 0) \tag{4.35}$$

Finally, the pressure jump writes:

$$\Delta P = 2p(\bar{z}_1, 0) = -2\rho_0 U_0 \frac{u_a}{\beta} \frac{\mathrm{i}k_a}{\sqrt{\mu^2 - \mathcal{K}^2}} \mathrm{e}^{\mathrm{i}K_1 \bar{z}_1} \Phi\left[\sqrt{\mathrm{i}(\mu + \mathcal{K})\bar{z}_1}\right] \mathrm{e}^{-\mathrm{i}\omega t} \tag{4.36}$$

The same result as in Parry's thesis is found assessing that both resolution methods are equivalent. When the same methodology is applied to the Reversed Sears problem stated in equation (4.5), the solution writes:

$$\Delta P = -2\rho_0 U_0 \frac{u_a}{\beta} \frac{\mathrm{i}k_a}{\sqrt{\mu^2 - \mathcal{K}^2}} \mathrm{e}^{\mathrm{i}K_1 \bar{z}_1} \Phi\left[\sqrt{\mathrm{i}(\mu + \mathcal{K})\bar{z}_1}\right] \mathrm{e}^{-\mathrm{i}\omega t} + \frac{\mathrm{e}^{\mathbf{i}\mu(M_0+1)\bar{z}_1 + \mathbf{i}\pi/4}}{\sqrt{\pi(\mu + \mathcal{K})\bar{z}_1}} \mathrm{e}^{-\mathrm{i}\omega t} \tag{4.37}$$

The only difference is the presence of an additional singular term at the trailing edge. This is the consequence of ignoring the Kutta condition. Interestingly, the same expression can be found in Parry's developments before the application of the Kutta condition. Parry applies the condition by cancelling the square root singularity at the trailing edge. It is shown that this is equivalent to introducing a vortex sheet extending to downstream infinity. Quoting Parry: *If the strength of the vortex sheet is fixed in order to cancel exactly the trailing edge singularity, then a Kutta condition is said to be satisfied.* The Reversed Sears approach is then equivalent to the resolution proposed by Parry before the application of the Kutta condition. The comparison of both approaches is shown in the AIAA journal paper reproduced in Appendix B.

In the present resolution, the Kutta condition was applied by directly solving the stated boundary-value problem. In the Wiener-Hopf resolution done by Parry, the condition is not intrinsic to the resolution but set through an additional term added to cancel the singularity. In this regard, the Amiet-Schwarzschild procedure looks like a more straightforward physical resolution allowing the direct application of the Kutta condition.

The first iteration performed does not account for finite-chord effects since a semi-infinite flat plate was considered. This is equivalent as saying that the source is not compact and that the solution is valid for high-frequency applications. For low-frequency applications where the chord is comparable with the wavelength, a second iteration should be performed. It corresponds to a second iteration of the Amiet-Schwarzschild procedure where the problem is now solved for an airfoil extending to downstream infinity and where the potential is cancelled upstream of the airfoil leading edge. This iteration has not been performed in the framework of this study but constitutes an improvement of the airfoil response for low-frequency applications. Similarly to what has been done for the first step, the solution is given by Parry using the Wiener-Hopf technique.

Finally, it is observed that the damping coefficient k_a appears as a factor in the airfoil

response. This suggests that the no-damping case with $k_a = 0$ would give a null airfoil response. This is one limitation of the model meaning that it cannot be used for constant chordwise perturbations. Nevertheless, to ensure that the reduction of the damping increases the unsteady loading on the airfoil aside from the critical case of $k_a = 0$, a parametric study was performed, shown in Figure 4.3.

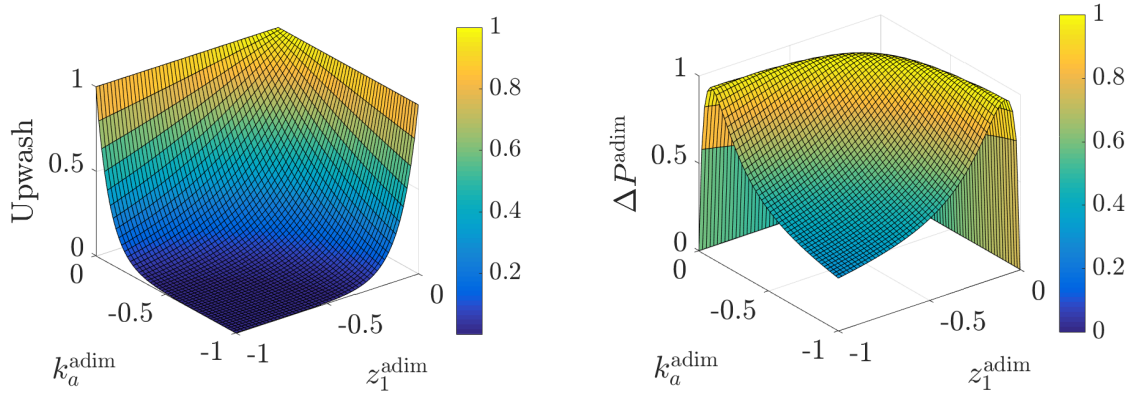

(a) Upwash disturbance.

(b) Pressure jump.

Figure 4.3: Damping coefficient variation using Parry's model on a generic case.

Lower damping values can be seen to increase the chordwise pressure jump up to a limit beyond which the pressure jump is strongly reduced and then cancelled. This results show that the model is behaving correctly for reasonably weak potential attenuations.

An improvement of the model could also be tested in order to avoid the critical point at zero damping. Instead of considering velocity gusts, the problem could be then formulated considering pressure gusts. This is similar to what has been done by Rozenberg [50] to deal with growing pressure fluctuations from a boundary layer transition. It is an equivalent problem as the one of the potential field that has a growing intensity towards the stator vanes. The solution of this problem is not anymore critical in the limit of zero damping.

The analytical pressure jump at midspan is shown in Figure 4.4. It was computed from the numerical potential field amplitude at the rotor trailing edge and from the analytical decay rate given by m/r. The correct harmonics are generated but important discrepancies are observed in terms of amplitude. The loading provided by Parry's model is seen to be concentrated at the trailing edge region as expected. Nevertheless, it has a peak value around 10 Pa compared with more than 50 Pa for the numerically predicted pressure jump. In addition, the low order harmonics are seen to have comparable amplitudes with the main harmonic V. This is expected because of the similar upwash levels at the rotor trailing edge seen in the numerical potential field. Nevertheless, this is not observed in the numerical pressure jump. In this case, the time-harmonic $n = V$ is underestimated but the low-order harmonics are comparable with the numerical pressure jump. The airfoil response is physically consistent with higher amplitudes at the trailing edge but fails to accurately relate the velocity perturbations to the airfoil unsteady pressure. In the next section, the analytical and numerical potential fields are compared.

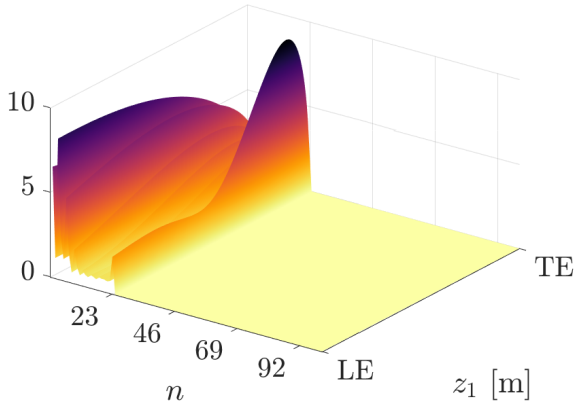

Figure 4.4: Rotor blade loading calculated with Parry's airfoil response model using the numerical potential field as input.

4.1.1.2 Potential field modelling

The analytical modelling of the potential field is now described. As discussed in chapter 1, the potential field over a set of geometries is calculated using conformal mappings. The flow past a cylinder is a known analytical solution which can then be transformed to the potential field around several different shapes by using different transformation parameters. In this investigation, the cascade of airfoils is obtained by performing a sum of phase-lagged solutions where a Hanning filter is applied to ensure the potential field continuity of the individual solutions at 0 and 2π. This sum assumes the linearity of the potential field.

For the ANCF configuration presented in appendix B, the flat plate geometry was chosen because the stator heterogeneity was characterized by an increased chord with almost no thickness variation. In the present cooling-fan case, the heterogeneity is characterized by a constant chord but increased thickness over the radius. For this reason, the ellipse is chosen for the predictions. The potential field is shown in Figure 4.5 for the baseline and thickened vanes.

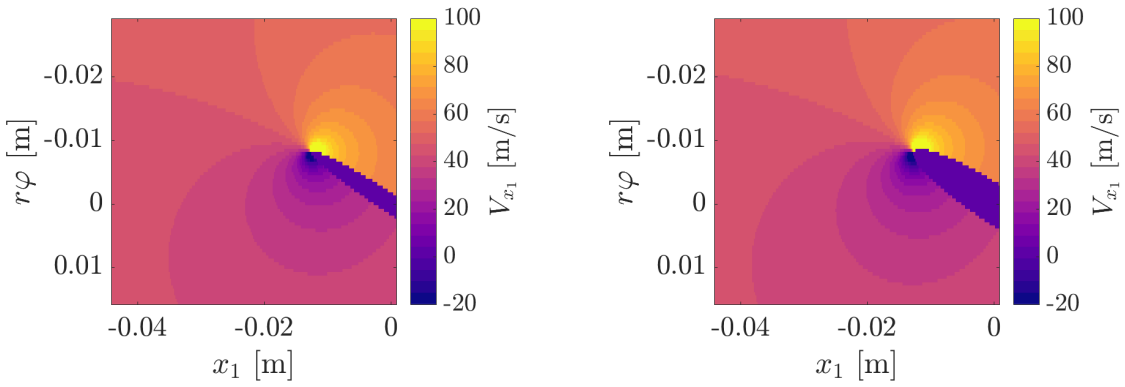

(a) Baseline ellipse.

(b) Thickened ellipse.

Figure 4.5: Analytical potential field around a single ellipse. Axial velocity component.

The thickened vane is observed to slightly modify the upstream potential field as expected. Parameters of the ellipse have been chosen according to the real *LP3* stator geometry (maximum thickness and chord). From this potential field around an ellipse, a cascade of ellipses was then generated and the thickened ellipses were set at the positions of the thickened vanes. The potential field is then Fourier decomposed as done in the previous chapter for the numerical solution. Results are shown in Figure 4.6 and in Figure 4.7 for the heterogeneous and homogeneous cases respectively.

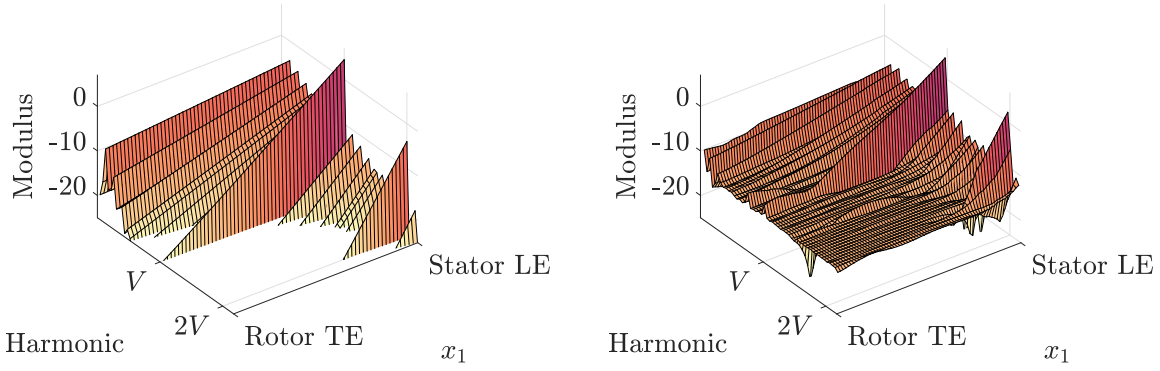

(a) Analytical. (b) Numerical simulation.

Figure 4.6: Modulus of the azimuthal Fourier coefficients of the potential field for the heterogeneous configuration. TE stands for trailing edge and LE for leading edge.

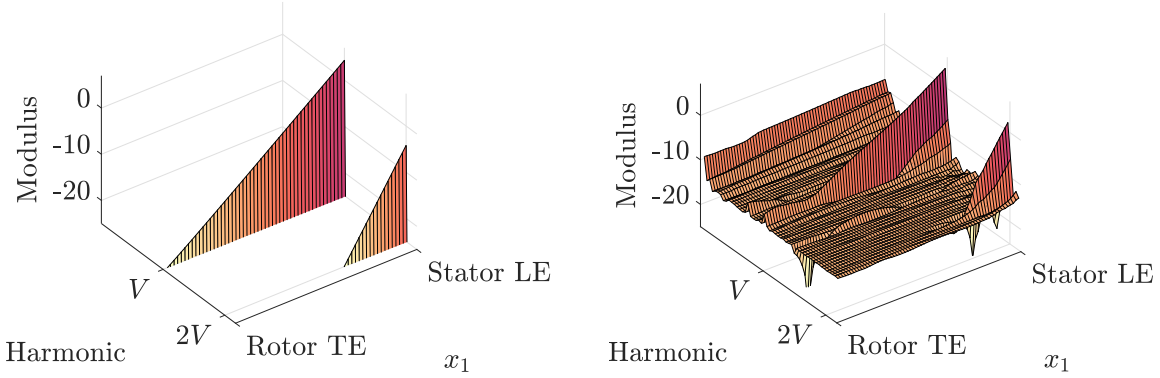

(a) Analytical. (b) Numerical simulation.

Figure 4.7: Modulus of the azimuthal Fourier coefficients of the potential field for the homogeneous configuration. TE stands for trailing edge and LE for leading edge.

For the heterogeneous case, similar results are obtained between the numerical and analytical potential fields. The dominant harmonics are those multiple of the vane count V. Because of the stator heterogeneity, other harmonics are also generated and are well recovered by the analytical model. Nevertheless, the numerical saturation phenomenon observed in the simulation is not observed in the analytical predictions. For this same reason, the dominant harmonic of order V is seen to monotonically decrease towards the rotor trailing edge. In the numerical field, the decrease of this harmonic is seen to

saturate at around 25% of the interstage coordinate reaching thus a plateau slightly above the background level.

For the homogeneous stator configuration, the analytical model predicts only harmonics of the vane count V as expected. In the numerical simulation, the level of the other harmonics is seen to be significantly reduced reaching the background level. Results are thus in good agreement with the analytical prediction.

For a better visualization, the potential field at the stator leading edge and at the rotor trailing edge is shown in Figure 4.8a for both the analytical prediction and numerical simulation. Interestingly, the same sawtooth pattern is observed with the quasi-three periodicity behaviour discussed in the previous chapter. Nevertheless, higher discrepancies are observed with the increasing harmonic order. This is strictly related to the distortion shape and the analytical case seemingly has a wider distortion profile leading to an increased decay rate over harmonics. The first and second orders are not seen in the analytical field because they are generated by the power-supply cable not accounted for in the analytical model.

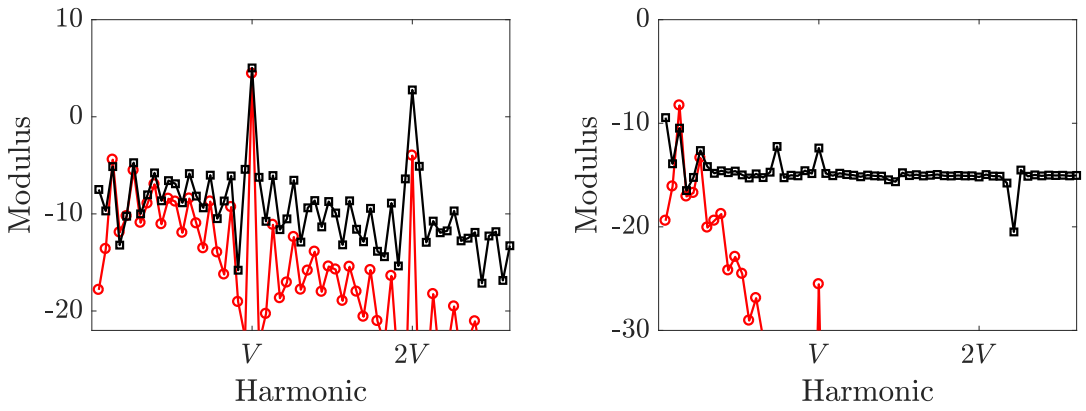

(a) Stator leading edge.

(b) Rotor trailing edge.

Figure 4.8: Modulus of the azimuthal Fourier coefficients at the stator leading edge and rotor trailing edge. The analytical model is in ━ and the numerical simulation in ━ (probable numerical background noise around -15 dB). Levels in arbitrary decibels.

At the rotor trailing edge, high discrepancies appear between both cases. Two causes may be cited. First, the increased error in amplitude for the high orders is emphasized with the axial decay. Secondly, the background level observed in the numerical simulation is observed to block the potential decay. Nevertheless, low-order harmonics that did not reach the background level are seen to be close the analytical harmonics.

Finally, the analytical potential field was interpolated by an exponential function as shown in Figure 4.9. The decay of the harmonic $m = V$ shown in Figure 4.9a is seen to perfectly fit the exponential function confirming that the analytical potential field is exponentially decreasing. The same behaviour is observed for all harmonics. This analysis has not been performed on the numerical potential field because of the previously observed threshold. Such a plateau would lead to failed interpolations. However, the numerical

potential field is observed to decrease exponentially above the threshold and is thus in good agreement with the analytical estimate.

The exponential decay rate b_m obtained with the interpolation is then compared with the analytical function m/r discussed in the previous chapter in section 3.3.6. The exponential fit is seen to match the analytical function in most cases but high order harmonics. The discrepancy observed at these orders is due to the numerical error generated from very low potential values. Nevertheless, the analytical decay rate b_m is then assessed and can be simply computed from the analytical function m/r.

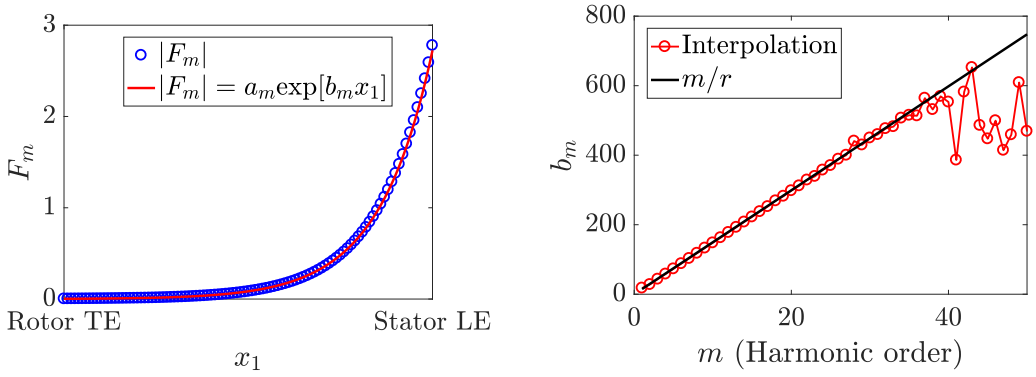

(a) Interpolation of order $m = V$.

(b) Decay rate b_m obtained by the interpolation and by the analytical equation m/r.

Figure 4.9: Interpolation of the decay of the analytical potential field by an exponential function $F_m = a_m \exp[b_m x_1]$.

According to this decay rate function, the potential velocity perturbation should decrease slowly at the tip because of the increased radial coordinate ($b_m(R_H) < b_m(R_T)$). To conclude, the analytical model is observed to correctly reproduce the potential field modification with a heterogeneous stator. Nevertheless, the harmonic decay rate is higher for both the homogeneous and heterogeneous cases when compared with the numerical results.

4.1.2 *LP3* potential-interaction noise predictions

In this section, the objective is to analytically estimate the potential-interaction noise contribution. For that, Parry's airfoil response and the analytical potential fields presented in the previous sections have been implemented in the OPTIBRUI analytical prediction tool. It is a software developed at Université de Sherbrooke[(a)] that considers several analytical models for the prediction of tonal and broadband noise of rotating machines. Parameters of the calculation are summarized in Table 4.1.

Total acoustic power results are shown in Figure 4.10. First of all, the effect of the heterogeneity is clearly seen on the first two BPFs which are not cut-off in the hetero-

[(a)] within the frame of an industrial chair with Valeo, Airbus and Safran

Modelling step	Model
Aerodynamic excitation	Potential theory (cascade of ellipses)
Airfoil response	Parry (first iteration)
Acoustic propagation	Goldstein's analogy

Table 4.1: Chosen models for the analytical prediction.

geneous case. The impact on cut-on BPFs is minor and is in accordance with what has been observed in the numerical simulation. Levels of sound propagating downstream are also seen to be slightly higher.

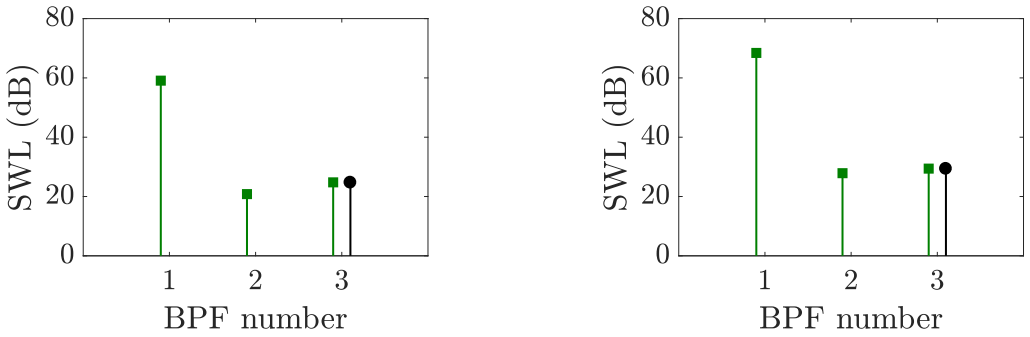

(a) Upstream. (b) Downstream.

Figure 4.10: Upstream and downstream power levels at the BPFs for the potential-interaction noise. The homogeneous stator is in ——— and the heterogeneous stator in ——— .

Interestingly, the first BPF dominates upstream and downstream with levels above 40 dB compared with the following BPF harmonics. This behaviour agrees well with the potential and blade pressure jump predictions discussed in the previous section. For the potential field, higher harmonic orders have been observed to have stronger axial attenuations. In terms of noise, this translates into high levels at the first BPF but strongly attenuated levels at the following BPFs. According to this, the potential interaction noise is expected to contribute mainly at the first BPF.

For a better physical insight, the upstream and downstream modal contents for the heterogeneous case are shown in Figure 4.11. Dominant modes are observed at all BPFs. At the third BPF, the Tyler & Sofrin mode is correctly found. At the second BPF, the mode $m = 5$ is dominant and caused by the heterogeneity. At the first BPF, the mode $m = 3$ is found to be dominant downstream but not upstream where the mode $m = 0$ is dominant. Nevertheless, the plane wave mode amplitude is one order of magnitude below the downstream propagating mode $m = 3$ evidencing why the total upstream level is about 10 dB below. Aside from this plane-wave mode upstream, the identified modes correspond to those measured in the experiment but also found in the numerical simulation. As expected, the heterogeneity is seen to generate dominant modes at the first and second BPF. These results show the ability of the analytical model to account for the stator heterogeneity here introduced through an heterogeneous potential field.

This potential-interaction noise source will then be compared with the wake-interaction predictions in the next section.

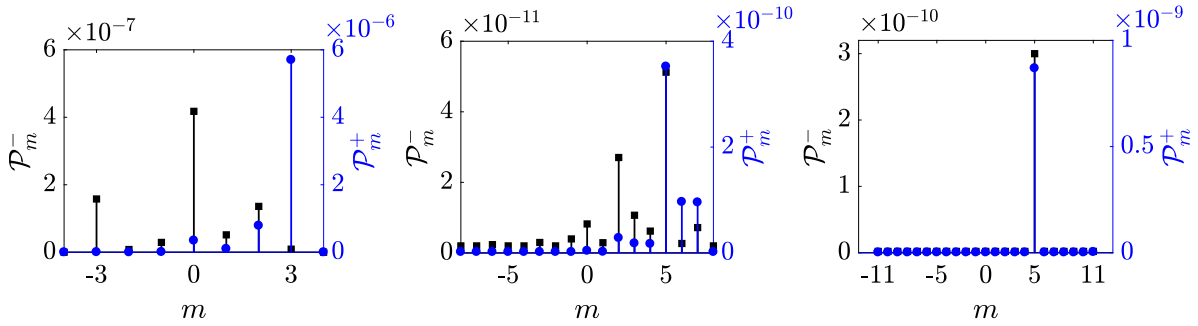

(a) BPF 1. (b) BPF 2. (c) BPF 3.

Figure 4.11: Acoustic power modes for the potential-interaction noise in the heterogeneous stator configuration. Downstream propagating modes $\mathcal{P}^+$ are in ——— and upstream propagating modes $\mathcal{P}^-$ in ——— . A sum is performed on the radial modes.

Potential-interaction noise — Summary

Modelling:

1. Parry's model derived using the Amiet-Schwarzschild formalism - same solution retrieved
2. Straightforward application of the Kutta condition compared with the Wiener-Hopf technique
3. Damping coefficient as factor of the airfoil response - good physical behaviour far from the no-damping limit
4. Pressure jump prediction:
   - Loads concentrating at the trailing edge area
   - Underestimation of the principal harmonic $n = V$ by the analytical model compared with the numerical simulation
5. Potential field:
   - Good agreement between the numerical simulation and the analytical model (ellipses) in terms of spatial modal structure for the heterogeneous configuration
   - Stronger harmonic attenuation at higher orders for the analytical model

***LP3* potential-interaction noise predictions:**

1. Low noise levels for this source in accordance with the highly attenuated potential field
2. First BPF dominating with levels 40 dB above those of the second and third BPFs
3. Unexpected plane-wave mode $m = 0$ upstream
4. Analytical model predicting similar dominant modes compared to the exper-

iment and the numerical simulation

4.2 Wake-interaction noise

In this section, the objective is to estimate the contribution of the wake-interaction noise. This source is expected to be dominant according to the numerical results shown in the previous chapter. To recall, the wake-interaction noise is generated from the wake impingement on the stator vanes. A scheme of this noise source is shown in Figure 4.12.

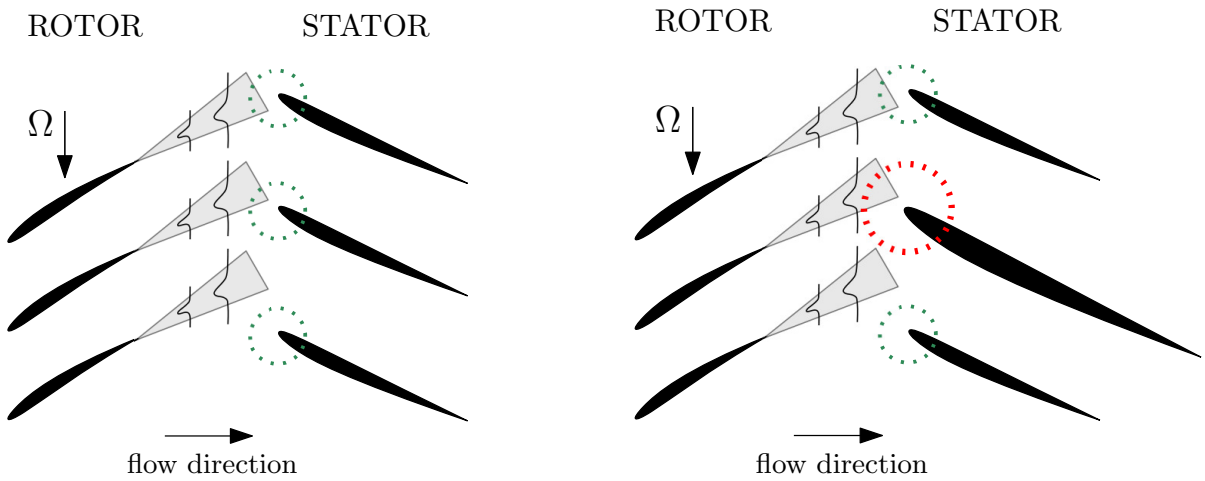

(a) Homogeneous (b) Heterogeneous

Figure 4.12: Representation of the wake interaction noise mechanism for homogeneous and heterogeneous stators.

Contrarily to what occurs with the potential interaction, the aerodynamic excitation is here homogeneous. In this case, sources are heterogeneous meaning that some of the stator vanes respond differently to a same excitation. In the following section, the modelling of the aerodynamic perturbation and of the airfoil response is not discussed. A simple Gaussian wake model and well-known Amiet's model for leading edge gust impingement are used. The focus is put on the modelling of the acoustic propagation from heterogeneous sources.

4.2.1 Modelling

In this case, the modelling of the stator heterogeneity has to be done in Goldstein's analogy. The strategy proposed by Roger et al. [6] is used. In order to account for the stator heterogeneity, an interference sum is introduced. This sum allows writing a more general form of Goldstein's analogy in which individual vane characteristics can be

introduced. The acoustic power writes at the BPF harmonic of order s:

$$\mathcal{P}_{sB}^{\pm} = \frac{V\beta^4}{2\rho_0 c_0}\left(\frac{sB\Omega}{c_0}\right)\sum_{m=-\infty}^{+\infty}\sum_{n=1}^{+\infty}\sum_{k=0}^{V-1} \mathrm{e}^{\mathbf{i}k(sB-m)\frac{2\pi}{V}} \frac{|mD_{mn,k}^{\pm(sB)} - \gamma_{mn}^{\pm} T_{mn,k}^{\pm(sB)}|^2}{\Gamma_{mn} k_{mn}\left[\frac{sB\Omega}{c_0} \pm M k_{mn}\right]^2} \tag{4.38}$$

This expression can be re-written in terms of pressure in the form:

$$p_{sB}(\vec{x}) = \sum_{m=-\infty}^{+\infty}\sum_{n=1}^{+\infty}\frac{f_{mn}(r)}{\Gamma_{mn}}\mathrm{e}^{\mathbf{i}(m\varphi - \gamma_{mn}^{\pm} x_1)} \times \frac{1}{2k_{mn}}\sum_{k=0}^{V-1}\mathrm{e}^{\mathbf{i}k(sB-m)\frac{2\pi}{V}}\left(mD_{mn,k}^{\pm} - \gamma_{mn}^{\pm} T_{mn,k}^{\pm}\right) \tag{4.39}$$

When all stator vanes are identical, the classical Goldstein's formulation is recovered. Let us look in more detail how the interference sum works. We define the following interference function:

$$\mathrm{IS}_m = \sum_{k=0}^{V-1} A_k \mathrm{e}^{\mathbf{i}k(sB-m)\frac{2\pi}{V}} \tag{4.40}$$

where A_k is the coefficient representative of the k^{th} vane response. The interference sum allows introducing the individual contribution of each vane by adding a phase shift. When $A_k = a$ is a constant, then the interference function simply writes:

$$\mathrm{IS}_m = aV \tag{4.41}$$

with $m = sB - pV$. The destructive interferences that appear with the vane to vane periodicity simplify the expression and only generate Tyler & Sofrin modes. On the other hand, if vane to vane loading changes, the energy is spread onto a new set of modes.

An example is shown in Figure 4.13. The homogeneous case considers $A_k = 1$ for all vanes and the heterogeneous case $A_k = 0.5$ for the modified vanes.

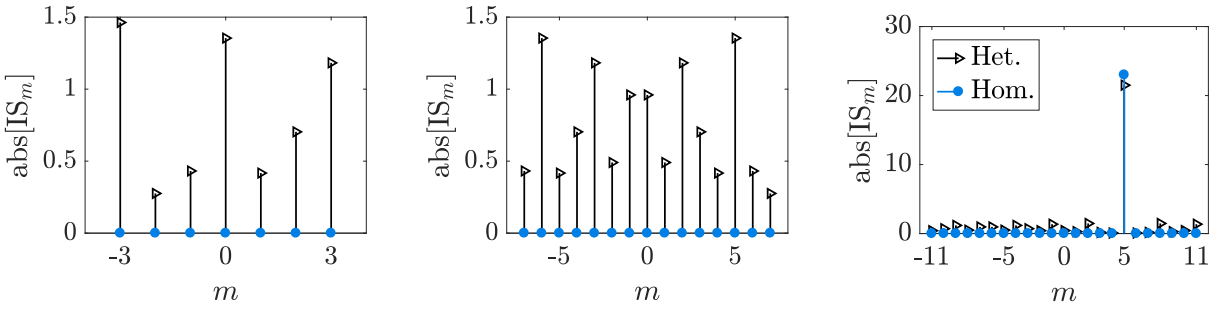

(a) BPF 1. (b) BPF 2. (c) BPF 3.

Figure 4.13: Interference function IS_m from equation (4.40) calculated for homogeneous and heterogeneous stators. $A_k = 1$ for a baseline vane and $A_k = 0.5$ for a modified vane.

In the homogeneous case the sum does not generate any mode in the cut-on range at the first two BPFs. The only generated mode is the Tyler & Sofrin mode $m = 3B - 2V$ where the sum equals $V = 23$.

In the heterogeneous case, several additional modes are generated at all frequencies. It can be seen that not all mode orders are re-generated. However, even if the dominant modes predicted in the previous chapters are observed among them, some additional modes also are present. In order to improve this simple prediction, a new interference function is defined based on the previous pressure expression of equation (4.39). The new function writes:

$$\mathrm{IS}_m^{(2)} = \sum_{k=0}^{V-1} A_k \mathrm{e}^{\mathbf{i}k(sB-m)\frac{2\pi}{V}} \qquad \text{with} \quad A_k = \frac{1}{k_{mn}}(mD - \gamma_{mn}^{\pm} T) \tag{4.42}$$

Because T and D are parameters related to the unsteady force projections in the axial and azimuthal directions, different values have been chosen for both. For a low staggered stator vane, the projection of the unsteady loading should be dominant on the azimuthal component (read drag component D) and minor on the axial component (read thrust T) as shown in Figure 4.14.

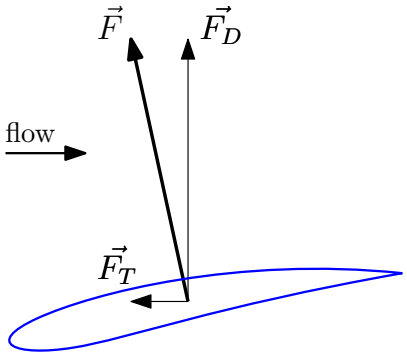

Figure 4.14: Unsteady force projections for a low-stagger stator vane.

For this reason, the drag component was set higher than the thrust component. For the modified vanes, because thickened vanes have lower response, the default value was arbitrarily divided by two. Test parameters are summarized in Table 4.2.

Parameters	Homogeneous vane	Heterogeneous vane ($k = 1, 9, 16$)
D (azimuth)	10.0	5.0
T (axis)	1.0	0.5

Table 4.2: Parameters of the interference sum.

The objective is to see whether it is possible or not to recover the same dominant modes without a precise description of the stator geometry and/or the vane pressure jump. Results are shown in Figure 4.15 for all BPFs. In this case, we can see that only some modes are selected in the heterogeneous case. The first BPF has the dominant mode $m = 3$, the second BPF the mode $m = 5$ and the third BPF the Tyler & Sofrin mode $m = 5$. These modes are identical to the previous numerical and experimental modal expansions.

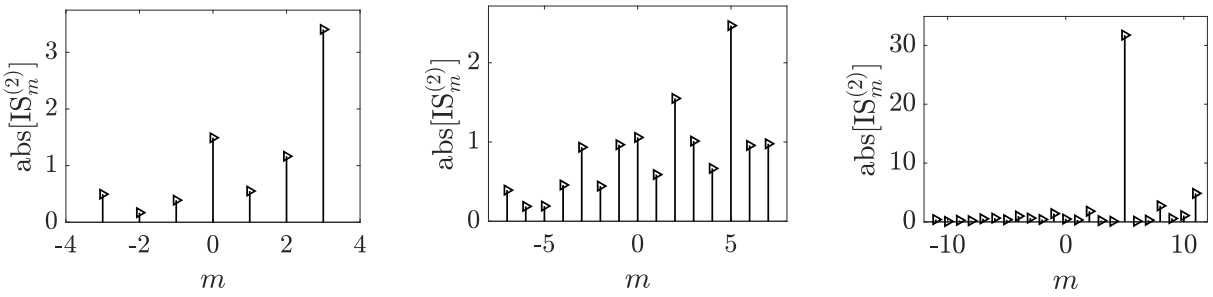

(a) BPF 1. (b) BPF 2. (c) BPF 3.

Figure 4.15: Interference function $\mathrm{IS}_m^{(2)}$ from equation (4.42) calculated for homogeneous and heterogeneous stators.

This simple study on the interference sum allowed identifying the dominant modes generated by the *LP3* heterogeneity. We can see that in this case, no simple rule can be deduced as for the Tyler & Sofrin modes. For heterogeneous stages, a non-trivial expression like the definition of A_k in equation (4.42) is necessary and plays an important role on the attenuation or amplification of certain modes.

For the final heterogeneous predictions using the heterogeneous Goldstein's analogy, a new parameter was set to introduce the heterogeneity. In the considered configuration, the chord is constant but the thickness varies from hub to tip. Because Amiet's model does not account for thickness effects (since it considers a flat plate), a tuning factor was applied to the pressure jump of thickened vanes as:

$$\Delta P_k(z_1, r) = A_k(r)\Delta P(z_1) \qquad A_k(r) = -6.5r + 1.3 \tag{4.43}$$

where z_1 is the chordwise coordinate. The function $A_k(r)$ was set according to the peak value attenuation of the numerical vane pressure jump shown in chapter 3. The evolution of this parameter is linearly decreasing from hub to tip. It constitutes an approximation and does not reproduce exactly the impact of the heterogeneity. In fact, multiplying the response by a constant attenuates the whole chord loading. However, because the peak value is seen to dominate the pressure jump, it is expected to be representative of the unsteady loading attenuation. In the case of a baseline vane, $A_k = 1$.

4.2.2 *LP3* wake-interaction noise predictions

The wake-interaction noise is analytically estimated using again OPTIBRUI. Similarly to what has been done for the potential-interaction noise, the heterogeneous Goldstein's analogy was implemented in OPTIBRUI. Parameters of the study are summarized in Table 4.3 and the BPF levels are shown in Figure 4.16 for the wake-interaction noise and the potential-interaction noise.

First of all, the wake-interaction noise can be seen to be the dominant contribution with levels above 20 dB compared with the potential-interaction noise. Interestingly, similar

Modelling step	Model
Aerodynamic excitation	Symmetric Gaussian wake
Airfoil response	Amiet (with back-scattering)
Acoustic propagation	Goldstein's analogy (heterogeneous version of equation (4.38))

Table 4.3: Chosen models for the analytical prediction (wake-interaction noise).

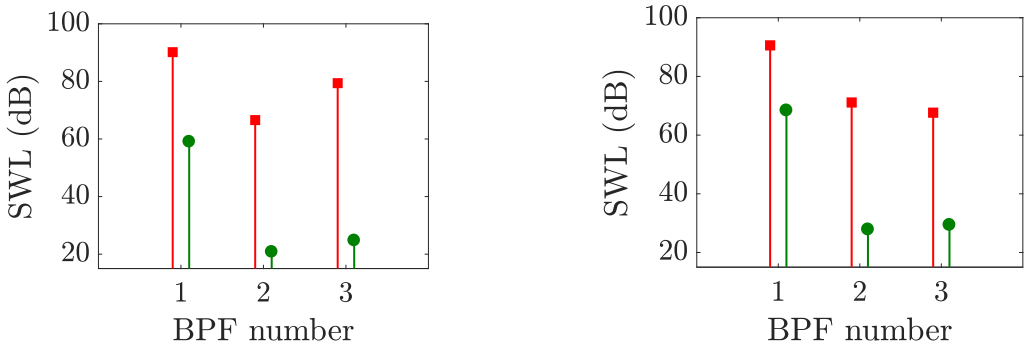

(a) Upstream. (b) Downstream.

Figure 4.16: Upstream and downstream power levels for the wake-interaction noise in ——— and for the potential-interaction noise in ——— .

relative levels of BPF harmonics are recovered with the analytical model. The levels are monotonically decreasing for the downstream array as observed in the simulation and experiment. For the upstream propagating waves, the level is not monotonically decreasing and increases for the third BPF similarly to what has been observed in the simulation. Nevertheless, levels of the first BPF are seen to be stronger than of the second BPF, contrary to what has been predicted in the simulation.

The upstream and downstream modal contents are now investigated and plotted in Figure 4.17. Surprisingly, the upstream and downstream propagating modes at the first BPF have opposed signs ($m = 3, -3$). In the numerical simulation both modes have been found upstream but only the mode $m = -3$ has been observed downstream. The analytical model seemingly captures this behaviour correctly. Nevertheless, only the mode $m = -3$ is measured in the experiment. Again, the prediction of these modes is particularly complicated because they are at the cut-off limit which corresponds to a resonant condition.

At the second BPF, the mode $m = 5$ is observed upstream but the unexpected mode $m = -6$ is predicted downstream. It is not clear why this mode appears and it has not been observed in the numerical simulations or in the experiment. The fact that the mode appears only in one propagation direction may indicate that it is related to the dipole orientation. In the analytical modelling, a flat plate without camber is considered. However, the real stator geometry is cambered and has a considerable thickness for the modified vanes. In practice, this means that the leading-edge and trailing-edge orientations are not equal modifying thus the chordwise orientation of the distributed dipoles. And last but not least, cascade effects which are not accounted for in the current modelling are

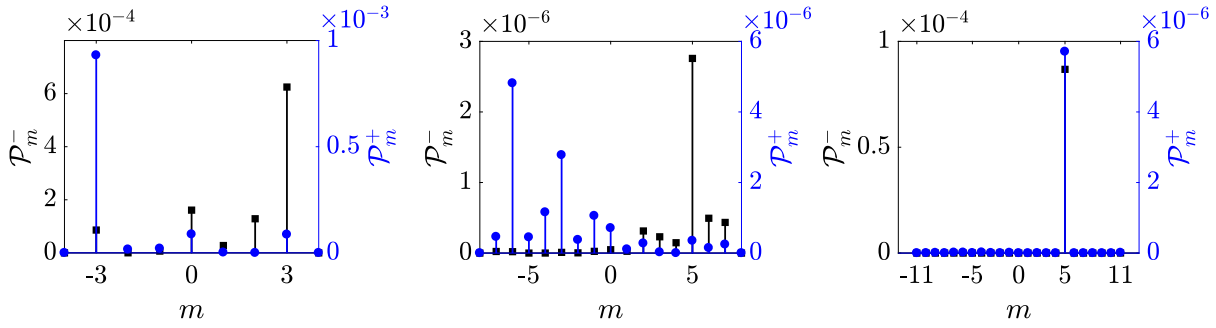

(a) BPF 1. (b) BPF 2. (c) BPF 3.

Figure 4.17: Acoustic power modes for the wake-interaction noise on the heterogeneous stator. Downstream propagating modes $\mathcal{P}^+$ are in ——— and upstream propagating modes $\mathcal{P}^-$ in ——— . A sum is performed on the radial modes.

expected to impact both the unsteady load but also the acoustic propagation. In fact, the cambered stator acts as an acoustic guide for modes and could modify their propagation. These are some elements that may explain the inability of the analytical model to recover some modes.

Finally, at the third BPF, the Tyler & Sofrin mode is correctly predicted both upstream and downstream. To conclude, the analytical model predicts most of the modes related to the heterogeneity apart from the extra mode $m = -6$. The section 4.3 will use the present model in order to perform an optimisation study.

The precise comparison of the predicted levels with the experiment and the numerical simulation has not been done because of the simplistic inputs used to feed the analytical models. Because of their modelling simplicity (no cascade effects, simple Gaussian model for the wake velocity deficit), an accurate level prediction was not expected. However, the objective of this study was to assess the capability of analytical models to retrieve the major features of an heterogeneous stator. As a perspective, numerical inputs such as the wake and potential aerodynamic excitations could be used in order to improve the analytical modelling accuracy. To conclude, the fast analytical model recovered most of the features of the *LP3* configuration. For this reason, an optimisation of the stator geometry will be presented in the next section, based on its use.

Wake-interaction noise — Summary

Modelling:

1. Heterogeneous modal content retrieved with a study on the interference sum
2. Pressure jump attenuation due to the increased thickness accounted for by a multiplying constant tuned on the numerical simulation results

***LP3* wake-interaction noise predictions:**

1. Wake-interaction noise found to be the dominant contribution with levels at least 20 dB above the potential-interaction noise

2. Similar relative sound levels of the BPF as in the experiment and numerical simulation: monotonically decreasing BPFs downstream and non-monotonic evolution upstream
3. Inversion of the modes $m = -3$ and $m = 3$ upstream and downstream at the first BPF
4. Unexpected mode $m = -6$ upstream but correct mode $m = 5$ downstream at the second BPF
5. Analytical model able to reproduce the major features of an heterogeneous stage and predicting most of the dominant modes compared with the experiment and numerical simulation

4.3 Optimisation study and conclusions on the stator heterogeneity

In this final section, the objective is to perform an optimisation study and draw some conclusions on the stator heterogeneity. A similar study has been performed by Roger [124] to reduce the rotor-stator noise using the so-called blade modulation technique. An irregular spacing of the rotor blades has been imposed to decrease the BPFs level.

In the present case, the optimisation study aims at optimising the angular positions of the modified stator vanes which are schematically shown for the *LP3* in Figure 4.18.

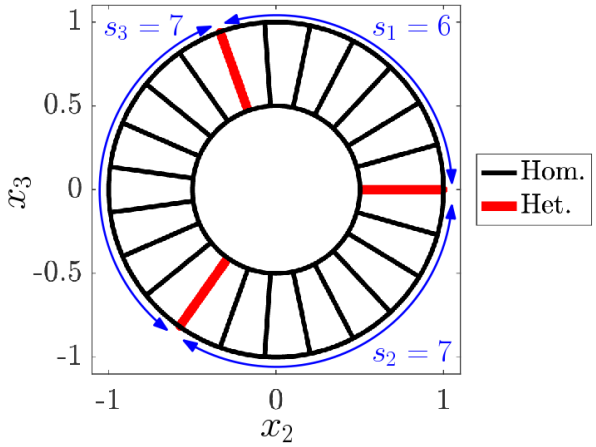

Figure 4.18: *LP3* stator scheme. The modified vanes are shown in red at the relative angular positions: 1, 9 and 16. The number of baseline vanes between two modified ones s_i is shown in blue.

The present vane disposition is the one that maximizes the spacing s_i between the thickened vanes. In fact, this is the configuration with the best structural interest to hold the fan-OGV module. Nevertheless, this disposition has been shown to be very prejudicial in terms of noise emissions. More generally, the same strategy could be applied using the

models on similar configurations of interest.

From a simplified point of view, the design objective of a low-noise OGV grid is to change the modal content such that only cut-off modes are generated. This was the case with the classical Tyler & Sofrin's rule for which the number of stator vanes and rotor blades could be carefully chosen in order to avoid cut-on modes at the BPF. For heterogeneous stator rows, it has been seen that all modes could *a priori* be re-generated. With the current analytical models accounting for the heterogeneous stages, it is now possible to minimize the amplitude of these cut-on modes. With this, a more suitable azimuthal distribution of the stator vanes can be found in order to take benefit of the destructive interferences such that it attenuates some of the dominant modes.

The objective here is to analytically investigate all non-redundant combinations of angular positions of the modified vanes and then verify if there is an optimal disposition in terms of acoustics. An example of two redundant configurations are the modified vanes positions $(1, 2, 3)$ and $(2, 3, 4)$. In fact, when dealing with azimuthal interferences, the absolute angular position is not relevant.

We define the total of number of stator vanes $V = 23$, the number of modified vanes $V^{(h)} = 3$ and the total spacing $M = \sum_{i=1}^{3} s_i = V - V^{(h)}$. The spacing s_i is here defined as the number of baseline vanes between two consecutive modified vanes. The total spacing should always equal M (number of baseline vanes). The total number of combinations without repetition of spacings are given by:

$$N = \frac{V!}{V^{(h)}!\, M!} = 1771 \tag{4.44}$$

The function `nmultichoosek` from matlab allows recovering all N combinations. Nevertheless, not all combinations satisfy the condition $M = 20$. By selecting those respecting the condition, only 44 non-redundant combinations are found and all of them are shown in Figure 4.19 and some schematically in Figure 4.20. For instance, the combination 1 has the three stator vanes together with no spacing. The last combination number 44 corresponds to the *LP3* original positioning shown in Figure 4.18.

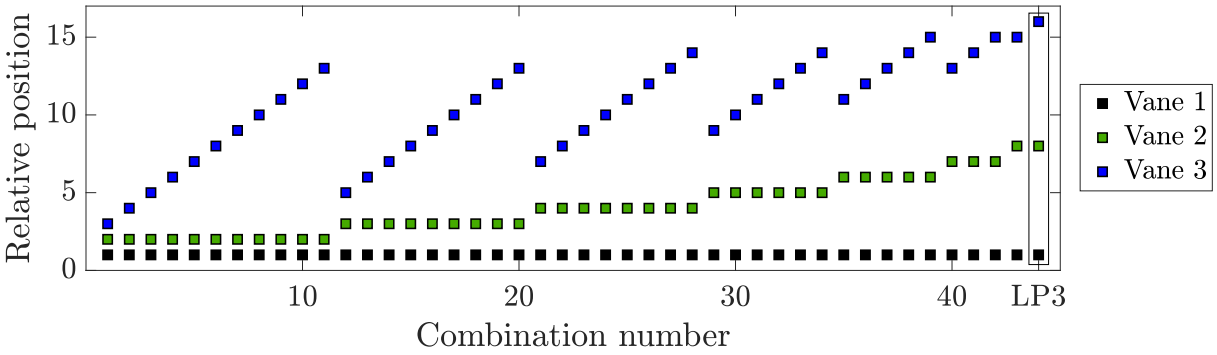

Figure 4.19: All non-redundant combinations of modified stator vane positions.

The optimisation is performed on the dominant noise-source, the wake-interaction noise by computing that noise for all stator combinations using the OPTIBRUI analytical

tool. The chosen models are given in the previous section in Table 4.3 and are kept identical for the current analysis. Results for the BPF level variations upstream and downstream of the OGV are shown in Figure 4.21.

The third BPF variations have not been plotted because they were found negligible. In fact, because of the presence of a Tyler & Sofrin mode $m = 5$, the variation of the other adjacent modes from the heterogeneity did not modify consequently the level at this frequency.

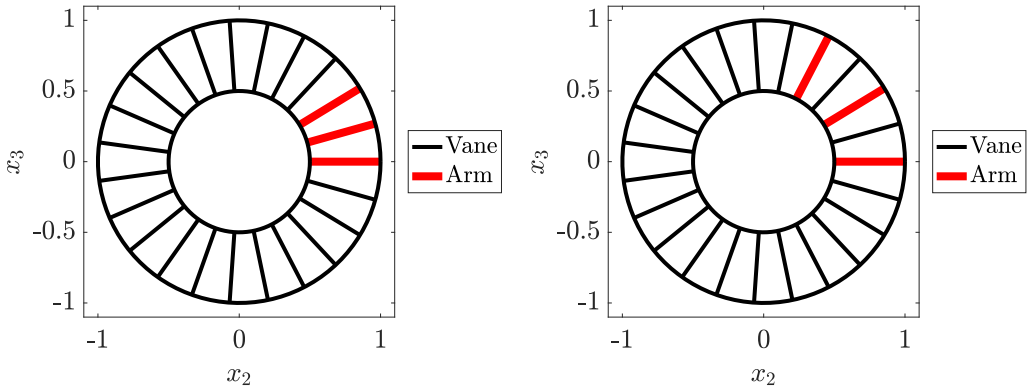

(a) Combination 1. (b) Combination 12.

Figure 4.20: Two different heterogeneous stators from Figure 4.19.

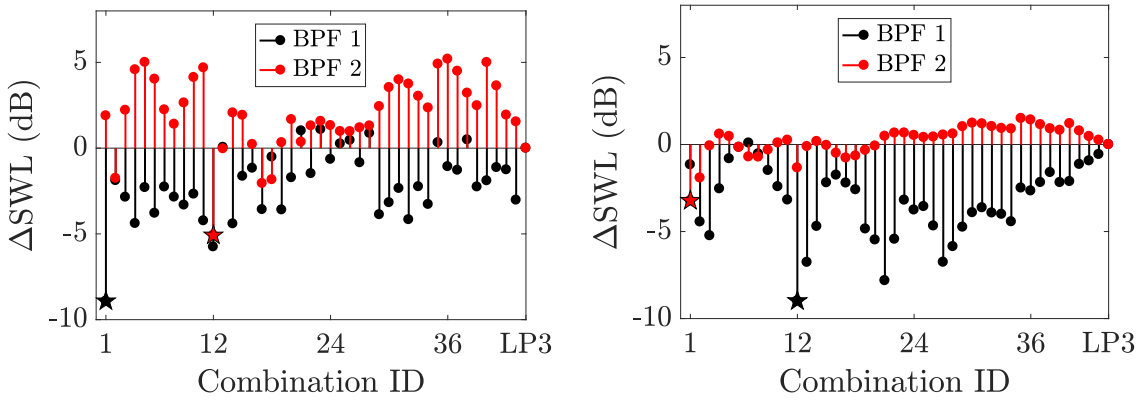

(a) Upstream. (b) Downstream.

Figure 4.21: BPF level variation compared with the reference configuration 44 (the *LP3*). The optimum solution is shown with a star symbol.

Strong variations appear upstream and downstream for the various stators. Among all configurations, two stators appear as optimal: the combinations 1 and 12 shown in Figure 4.20. The stator 1 is the most silent upstream at first BPF and downstream at the second BPF. The stator 12 is the most silent upstream at the second BPF and downstream at the first BPF. Although structural analysis of the modified stator cascades are not performed in this thesis, a compromise would need to be found to allow for a realistic configuration to be designed.

From this results, it can be seen that the rearrangement of the angular position of a constant number of modified vanes itself is enough to impact the noise levels at expectedly cut-off BPFs. At the first BPF, the *LP3* configuration is one of the noisiest according to the analytical predictions. In fact, the quasi-three periodicity given when the thickened stator vanes are spaced to their maximum seemingly increases the noise levels. In addition, it can be seen that the second BPF has very few combinations with a noise reduction compared to a lot more for the first BPF. For this reason, the potential of efficient attenuation is expected for the first BPF in the *LP3*.

For a better insight into the reasons why the sound levels were reduced for the optimal configurations, the upstream and downstream modal contents are also compared and shown in Figures 4.22 and 4.23 respectively. Upstream of the fan, the configuration 12 is seen to attenuate the dominant mode $m = 3$ at the first BPF and the mode $m = 5$ at the second BPF. The configuration 1 is more efficient at the first BPF but levels are increased at the second BPF. In fact, the mode $m = 5$ is attenuated but the mode $m = 7$ is strongly increased.

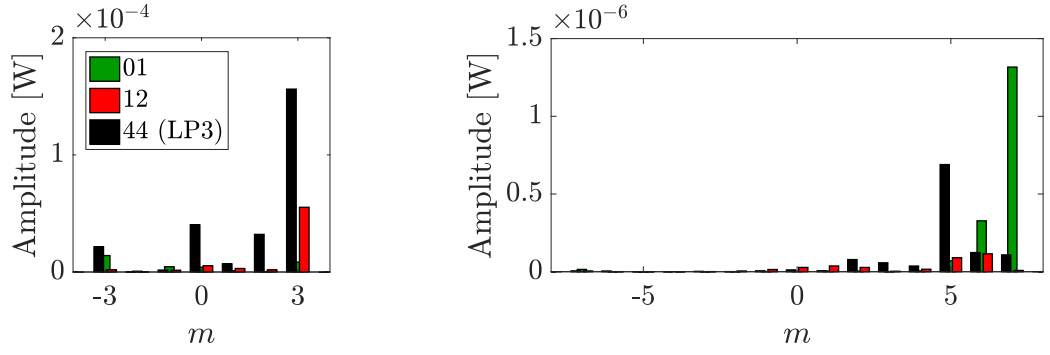

(a) BPF 1. (b) BPF 2.

Figure 4.22: Upstream modal content for three stator configurations.

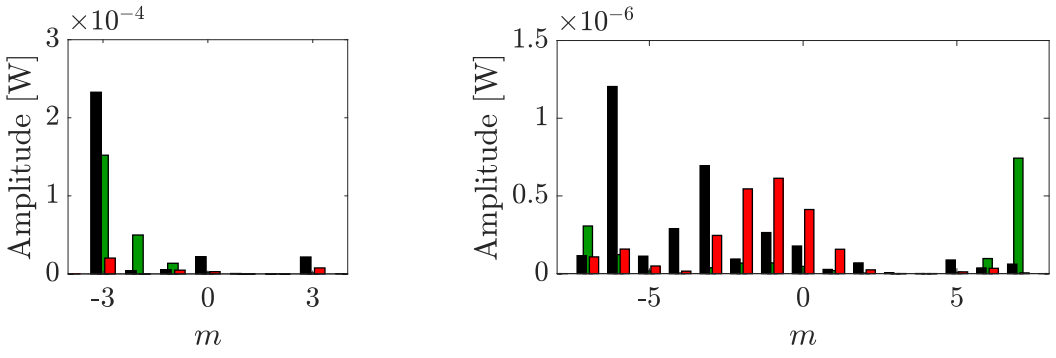

(a) BPF 1. (b) BPF 2.

Figure 4.23: Downstream modal content for three stator configurations.

Downstream of the fan, the stator combination 12 is seen to strongly attenuate the mode $m = 3$. The configuration 1 is less effective at this frequency. At the second BPF, both configurations cancel the mode $m = -6$. Nevertheless, the configuration 12

re-generates some low-order modes and the stator 1 has the mode $m = 7$ as dominant, close to the cut-off limit.

In order to assess the noise reduction of one configuration, a LBM simulation has been performed on the combination 12 interesting both at the first and second BPF. The simulation has been run on the mesh L0 where the tonal noise levels have been reproduced accurately and where the correct dominant modes have also been retrieved for the original *LP3*. Only the angular positioning of the modified stator vanes has been modified. They have been placed at the relative positions 1, 3 and 5.

The simulation times and converged performances are shown in Table 4.4 and in Table 4.5. As expected, it can be seen that the stator modification has a minor impact on performances. Compared with the original stator, the mass flow rate is 0.3% lower and the pressure jump 1.1% higher. The operating conditions with the acoustically optimised stator are thus not modified.

Geometry	Mesh	Simulation time [rev]
■ HOM	L0	58.5
■ HET	L0	66.1
■ HET (Stator 12)	L0	22.1*

* initialized from the ■ HET L0 simulation.

Table 4.4: Simulated time in revolutions.

		Mass flow rate Q_m		Pressure jump ΔP	
	Mesh	μ	c_v	μ	c_v
HOM	L0	0.8293 kg/s	0.01%	1651.96 Pa	0.19%
HET	L0	0.8293 kg/s	0.01%	1640.97 Pa	0.31%
HET (Stator 12)	L0	0.8265 kg/s	0.01%	1660.00 Pa	0.35%

Table 4.5: Mean operating point and fluctuations for both stator geometries. μ is the mean value and c_v the variation coefficient (equal to σ/μ with σ the standard deviation).

The upstream and downstream wall-pressure spectra are shown in Figures 4.24 and 4.25 respectively. The optimised configuration is seen to greatly impact the noise levels at the first two BPFs with minor modifications on the third. On the other hand, the broadband levels are seen to be kept the same. These results put in evidence that the azimuthal positioning of the modified vanes has only a significant impact on the interference phenomena which determine the tonal noise.

According to the analytical results, this stator configuration should decrease the noise levels at the first two BPFs. This is clearly observed in the numerical results with the best cancellation occurring at the first BPF downstream. For a better estimation of the tonal noise levels, synchronised averages are performed and the results are shown in Figure 4.26.

The first BPF is attenuated by 12 dB upstream and by 25 dB downstream of the fan. The second BPF is attenuated by 12 dB upstream and by 8 dB downstream of the

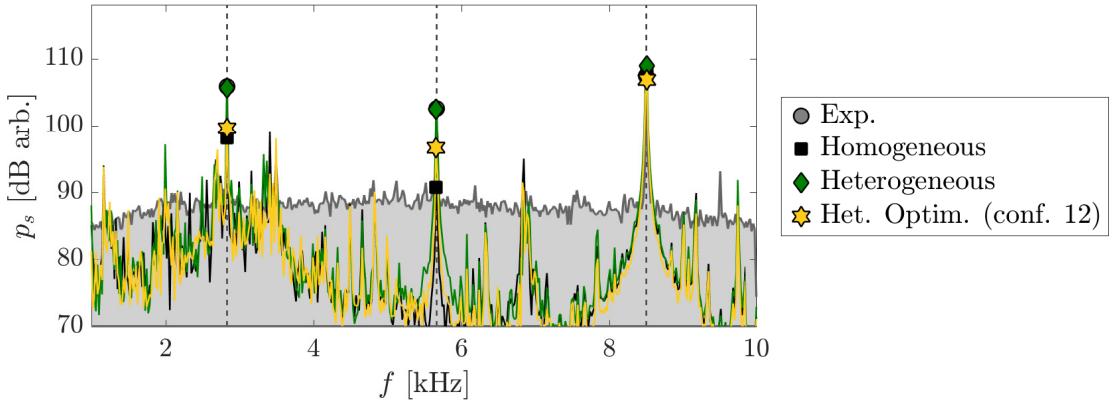

Figure 4.24: Upstream mean wall-pressure spectra for different stator configurations. The optimised stator arrangement number 12 is shown with a star symbol.

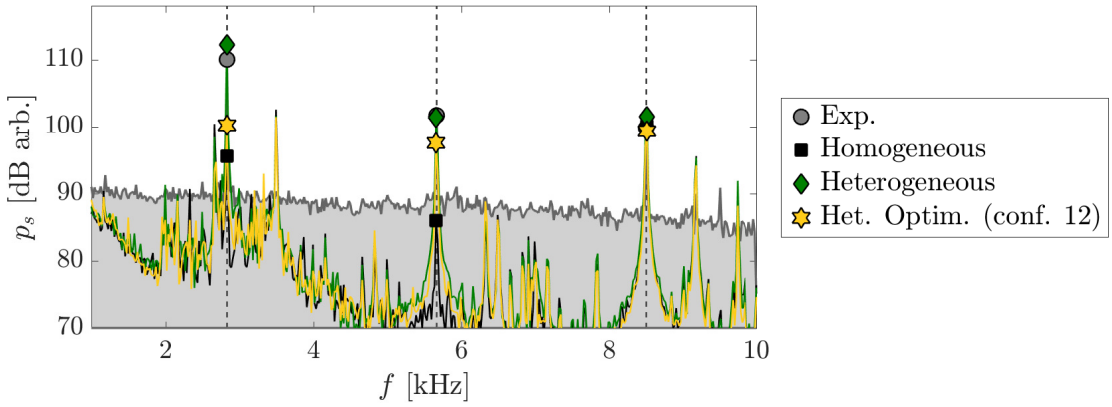

Figure 4.25: Downstream mean wall-pressure spectra for different stator configurations. The optimised stator arrangement number 12 is shown with a star symbol.

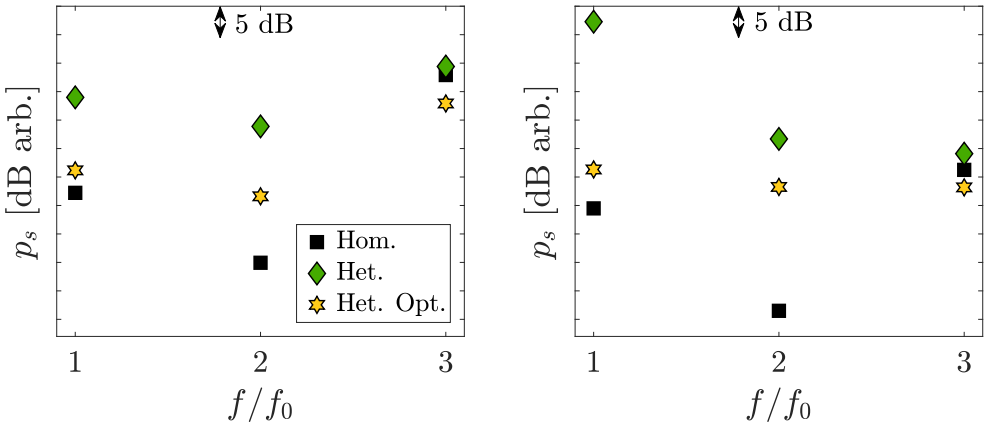

(a) Upstream array. (b) Downstream array.

Figure 4.26: Upstream and downstream BPF level comparison. The evaluation is obtained with synchronised averages (engine order analysis) which provide a better estimation at the BPFs.

fan. Finally, the third BPF is attenuated by 6 dB in both acoustic arrays. This was not predicted by the analytical model which provided constant levels at the third BPF.

The optimised stator configuration is seen to be very efficient at reducing the first BPF level with the levels being brought close to the homogeneous stator residual levels. In general, the BPF attenuation is higher for the numerical simulation compared with the analytical estimation. Nevertheless, the analytical optimisation provided an optimal configuration that agrees well with the relative attenuation between BPFs. Upstream of the fan, the first and second BPF have identical attenuations and downstream of the fan the first BPF is more attenuated compared with the second.

To complement the analysis, modal decompositions are shown in Figures 4.27 and 4.28 for the upstream and downstream arrays.

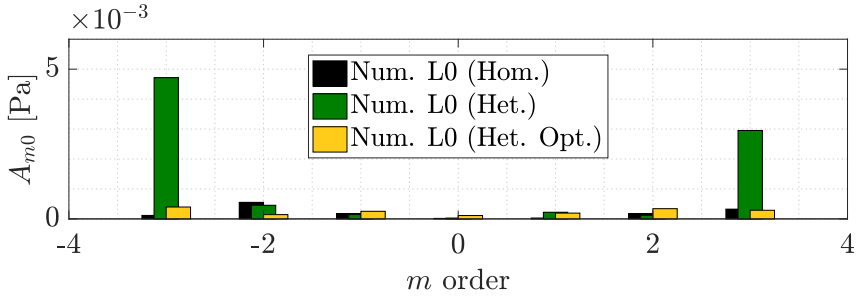

(a) BPF 1.

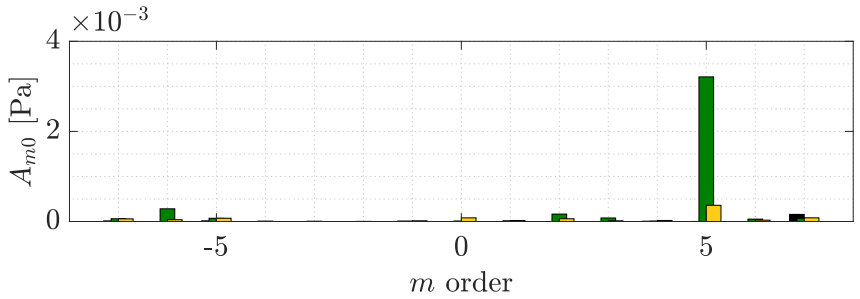

(b) BPF 2.

Figure 4.27: Upstream propagating modes of the upstream array at the first two BPFs.

Upstream of the fan, the optimised configuration is seen to attenuate both dominant modes $m = 3$ and $m = -3$ at the first BPF and the mode $m = 5$ at the second BPF. The optimised configuration is not seen to generate other dominant modes.

Downstream, the mode $m = -3$ is effectively attenuated reaching a level not far from the homogeneous case. At the second BPF, the mode $m = -5$ is attenuated but residual modes from $m = -5$ to $m = -1$ remain. Seemingly, this is why the reduction at the second BPF is not as efficient. With respect to the analytical results shown in Figures 4.22 and 4.23, the same mode attenuation is observed aside for the mode $m = -6$ not observed in the numerical simulation downstream. At the third BPF (not shown here), some noise reduction is achieved by a slight attenuation of the Tyler & Sofrin mode $m = 5$. Such

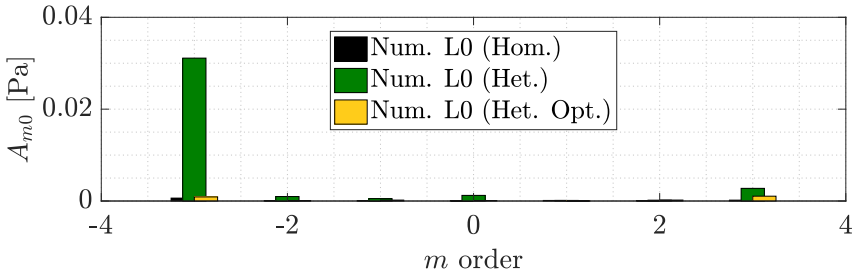

(a) BPF 1.

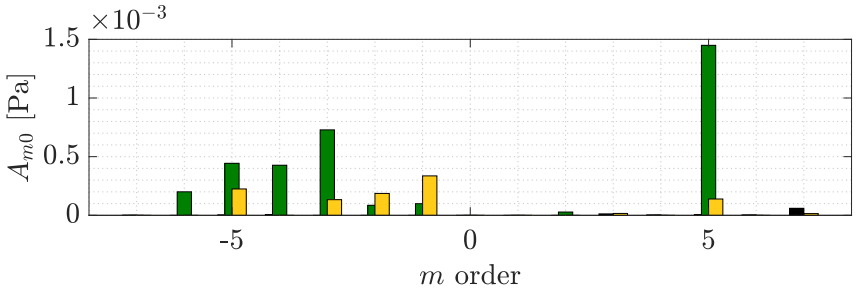

(b) BPF 2.

Figure 4.28: Downstream propagating modes of the upstream array at the first two BPFs.

attenuation is not predicted by the analytical model.

To sum-up, the angular re-arrangement of the modified vanes allowed reducing the BPF level. Despite the low interest of the optimum solution (shown in Figure 4.20b) regarding its structural role, this application has the interest of illustrating the methodology. The current exercise kept the number of modified vanes constant. However, some other configurations could be tested with a lower number of modified vanes (thicker) or an increased number of baseline vanes. Additional interesting configurations having a good compromise in terms of noise reduction and structural role could be found.

Optimisation study and conclusions on the stator heterogeneity — Summary

1. 44 non-redundant stator combinations investigated analytically
   - Same number of total vanes (23)
   - Same number of modified vanes (3)
   - Different azimuthal positioning of the modified vanes
2. Two optimal configurations at the first and second BPFs
3. Combination 12 (interesting both upstream and downstream) simulated with the LBM
4. Significant attenuation of the BPFs and dominant modes
5. Slight attenuation at the third BPF opposed to a constant level predicted by the analytical model

6. Strong effect of the arrangement of baseline and modified vanes on the regeneration of cut-off tones

4.3.1 Conclusions on the stator heterogeneity

In this final section, some conclusions on the stator heterogeneity are presented. The degree of heterogeneity of an OGV cascade can be characterized by the geometrical differences between the vanes. In the investigated case (*LP3*), the heterogeneity is characterized by three equal thickened vanes of constant chord. It is known that in recent turbofan configurations this is not the case. Such configurations possess several vane geometries with massive bifurcations included in the stator row.

In both cases, the lack of vane to vane periodicity modifies the destructive interferences that take place in homogeneous stages. The interest of these destructive interferences lies in the selection of precise azimuthal orders predicted by the Tyler & Sofrin criterion. According to this criterion, the number of blades and vanes can be carefully chosen such that some BPFs are cut-off by the duct. In a heterogeneous stator, this rule is invalidated because all azimuthal mode orders are *a priori* regenerated. An OGV row that regenerates low azimuthal mode orders may be considered as more heterogeneous than an OGV row generating higher azimuthal orders. Indeed, the low mode orders are more likely to be cut-on and are more effective in their acoustic radiation. For the *LP3* case investigated in this study, the stator heterogeneity has been shown to increase the BPF levels by more than 10 dB compared with a homogeneous stage in the numerical simulations. The simulated homogeneous stator still evidenced residual levels from the mesh inhomogeneities. In the analytical predictions, the homogeneous stator configuration evidenced cut-off as expected while the heterogeneous stator configuration predicted strong radiation at the first two BPFs. This drastic increase is seen to invalidate the cut-off design. In addition, the modal decompositions evidenced that the acoustic energy was found to be concentrated in a few dominant modes.

A stator row with an increased number of modified vanes is not necessarily noisier compared to a stator with less modified vanes. A quick calculation by considering two different heterogeneous stators with a constant number of vanes can highlight this point. Let us consider a rotor having $B = 16$ blades and $V = 24$ stator vanes. We will consider two different configurations. In case 1, $V_1 = 12$ of the 24 blades are modified and evenly distributed. In case 2, $V_2 = 6$ of the 24 blades are modified and evenly distributed. The considered rotational speed as well as the duct dimensions make that only the azimuthal modes $m \in [-3, 3]$ are cut-on at the first BPF. Within the linearised theory, the heterogeneous stator can be assimilated to the sum of two homogeneous stators with different vane geometries, see Figure 4.29. For this reason, the B wakes will interact with the periodicity V but also V_i.

Results are shown in Table 4.6. It can be seen that the stator with a higher number of

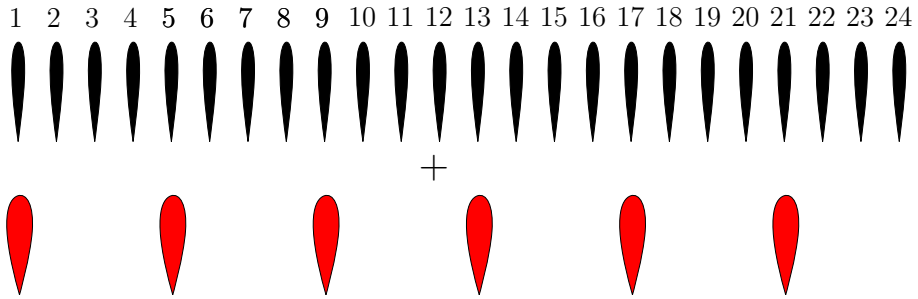

Figure 4.29: Decomposition of the heterogeneous stator as being the sum of a homogeneous stator with modified vanes. Illustration of the case 2.

modified vanes will not generate cut-on modes, unlike case 2. The first BPF will therefore remain cut-off despite the increased number of modified vanes. This example puts in evidence that an increased number of modified vanes is not necessarily worse.

p	-2	-1	0	1	2	3	4	
$m = sB - pV$	64	40	16	-8	-32	-56	-80	Homogeneous stator (24 vanes)
$m = sB - pV_1$	40	28	16	4	-8	-20	-32	Case 1 (12 het. vanes)
$m = sB - pV_2$	28	22	16	10	4	**-2**	-8	Case 2 (6 het. vanes)

Table 4.6: Interaction modes predicted by the Tyler & Sofrin's criterion for $B = 16$ rotor blades and $V = 24$ stator vanes at the first BPF ($s = 1$). Case 1: $V_1 = 12$ evenly spaced modified vanes. Case 2: $V_2 = 6$ evenly spaced modified vanes.

The case for which vanes are unevenly distributed (as the *LP3*) makes simple estimations more difficult. In that case, analytical predictions using the Goldstein's analogy can be used to deduce its modal content. In the *LP3* case, results have shown that even if the modified vanes are not equally spaced, the mode energy is not spread over a set of modes but is concentrated in some precise dominant modes. With a simple re-arrangement of the angular positions of the structural vanes, noise levels can be drastically reduced.

From the previous example, we can deduce that a single bifurcation could be very harmful in terms of interaction noise. On the one hand, its thickness compared to a stator vane could generate strong upstream disturbances. Secondly, having a distortion with simple 2π periodicity will regenerate all possible modes, which is undesirable, equation. 4.45.

$$m = sB - p\cancel{V} \qquad \rightarrow \qquad m \in \mathbb{Z} \tag{4.45}$$

In this case, we cannot take advantage of some vane to vane periodicity between the structural arms which would allow the cancellation of some modes. This was the case considered for the ANCF configuration shown in appendix B where the heterogeneous stator had only one modified stator vane.

In the present investigation, it has been shown that the decay rate of the potential field is proportional to the harmonic order m. For this reason, low harmonic distortions

will be more prejudicial because of their slow decay. It has also been shown in chapter 3 that if the distortion is assimilated to a Gaussian function, the sharper it is, the richer the modal content (increased number of contributing harmonics). In this regard, a wider distortion of smaller amplitude is preferable to have less contributing harmonics.

The degree of heterogeneity can also be characterized by the obstruction that the modified vanes generate in the flow. It is therefore expected that a profiled body will generate weaker upstream disturbances compared to a non-profiled body. The radius of curvature at the leading edge can then be considered as a key parameter. For example, three different geometries are illustrated in Figure 4.30.

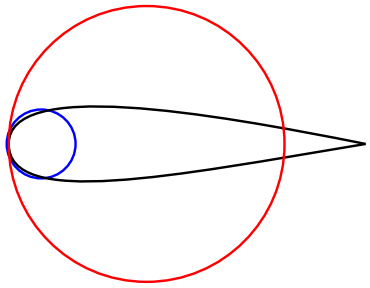

Figure 4.30: Illustration of three different vane geometries.

The leading edge radius has *a priori* a stronger impact than the chord in terms of upstream distortions. Thus, the blue cylinder and the black profile would have a similar degree of heterogeneity. Nevertheless, the stationary loading could have also an impact on the upstream distortion. At zero angle of attack, it is probable that both geometries are identical in terms of distortion but not with an oblique flow. In this regard, upstream distortion variations between a zero-circulation cylinder and a non-symmetrical profile would be likely to appear. In the case of the red cylinder, the distortion is expected to be stronger because of its larger obstruction.

Finally, profiling may not be sufficient in itself to reduce strong upstream disturbances. Indeed, we can see in Figure 4.31 the potential effect generated by bifurcations in a turbofan configuration. Despite their profiling, their thickening downstream generates a significant blockage and we can see strong inhomogeneities upstream of the stator.

To conclude, some general guidelines have been summarized to minimize the contribution of the wake-interaction and potential-interaction noise.

For the potential-interaction noise:

1. Maximize the rotor-stator distance - benefit from the exponential decay ;
2. Avoid generating low azimuthal mode orders of the distortion - slower axial decay ;
3. Avoid sharp (very localized) distortions - lower harmonic decay (more contributing harmonics) ;
4. Profile the structural stator vanes so that they minimize the upstream distortion amplitude.

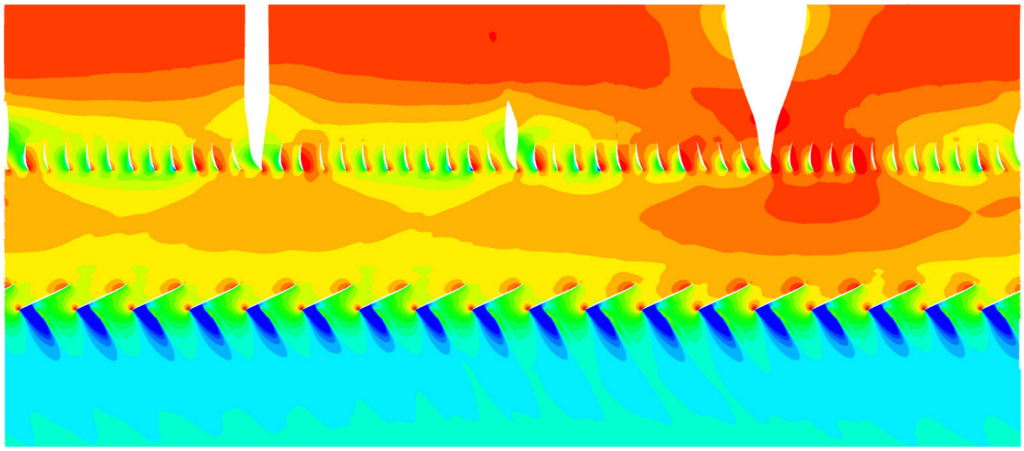

Figure 4.31: Static-pressure contours from URANS simulations, Daroukh *et al.* [18].

For the wake-interaction noise:

1. Avoid deviations from the Tyler & Sofrin's rule because they generate dominant modes that should not be excited ;
2. In addition, benefit from a periodicity of the modified vanes or optimise their angular position in such a way to attenuate the new generated cut-on modes.

General conclusions and perspectives

General conclusions

The objective of this PhD thesis was to investigate the impact of heterogeneous stators on the noise emissions of rotor-stator stages. A heterogeneous stator is defined as a stator in which the vane-to-vane periodicity is not conserved. Such heterogeneity can be observed in modern turbofans which include structural arms in the stator row to obtain a more compact engine architecture. In the presented investigation, the chosen configuration was a low-speed fan, the *LP3* stage. This fan has two major characteristics of modern and future turbofan configurations: a heterogeneous stator and a short rotor-stator spacing. The considered stator has three thickened stator vanes yielding a relatively weak heterogeneity degree. In addition, the rotor-stator spacing at midspan is less than one rotor chord (short distance). In this configuration, previous measurements evidenced the radiation of the first two BPFs expected to be cut-off according to the Tyler & Sofrin's rule. Therefore, the main goal of this research study was to investigate if the heterogeneity is the cause for this unexpected radiation and to explain how classical rotor-stator interaction mechanisms are modified accordingly.

The first step consisted in investigating experimentally the *LP3* stage. Experiments were conducted in a fan test-rig at École Centrale de Lyon allowing a detailed characterization of the noise sources (spectral and modal contents). These experiments used a Turbulence Control Screen to remove a previously identified inflow distortion. This was a crucial point because the inlet distortion noise contributes at the same frequencies as those of rotor-stator interaction mechanisms. Results evidenced a strong radiation of the first two BPFs with the TCS. With the addition of the screen, BPFs were found sharper but still radiating at high levels seemingly due to the stator heterogeneity. At these frequencies, dominant acoustic modes were identified. These modes were not predicted by the classical Tyler & Sofrin rule and for this reason were suspected to be caused by the stator heterogeneity. The only predicted mode by the rule is found at the third BPF and was correctly measured in the experiment.

Secondly, the experiment was numerically simulated using the Lattice-Boltzmann Method. The simulation accounted for the whole experimental setup with some simplifications. In fact, accounting for the whole experimental setup allowed placing the same acoustic antennas in the simulation to use the same post-processing methods as in the experiment. In addition, the uneven azimuthal positioning of the three modified stator vanes (3 over 23) required the simulation of a 360° geometry. Three main *LP3* configurations were simulated: the original heterogeneous stator (experimental configuration), a homogeneous stator and a final configuration where the downstream power-supply cable was removed. The TCS was not modelled but no distortion was identified at the inlet. In fact, the short simulated time compared to the room filling time did not allow the development of any distortion. In terms of aerodynamic performance, the simulations showed a good physical consistency but evidenced a lower pressure-rise compared with the experiment. The gap was considerably reduced with the last mesh refinement. Nevertheless, RANS simulations predicted a better rotor performance from midspan to tip. A last LBM mesh refinement could not be done but should be considered as a perspective to conclude on the performance convergence. Note that the mesh refinements on both simulations (LBM and RANS) were put on the blades and vanes and not at the duct walls where the static pressure rise measurement was performed. The refinement at the duct walls constitutes one possible improvement for future simulations along with an additional global mesh refinement. Regarding the experiment, other aerodynamic measurements could be added in order to better characterize the operating point like total pressure surveys upstream and downstream of the fan.

The acoustic analysis of the simulations led to one of the principal results of the thesis. The heterogeneity was responsible for an increase in the tonal level of more than 10 dB at the first two BPFs. At the third BPF, the level remained mostly unchanged because of the presence of a dominant Tyler & Sofrin mode generated in all stator configurations. The homogeneous stator still provided residual levels at the BPF seemingly due to mesh heterogeneities related to the Cartesian mesh used by the solver. Finally, removing the power-supply cable had a negligible impact on the noise emissions. The drastic increase in the levels observed for the first two BPFs in the heterogeneous configuration can be explained by the modification of the destructive interferences that only allow the generation of Tyler & Sofrin modes (cut-off at the first two BPFs). For this reason, the Tyler & Sofrin rule is invalidated in such stator configurations. Surprisingly, the energy is not spread over all azimuthal mode orders despite the lack of periodicity of the three stator vanes (uneven spacing between the three). On the contrary, the energy is concentrated on a couple of dominant modes that have been explained with the analytical models. Both measured and simulated modal contents are in good agreement and attest that the stator heterogeneity is the real cause for the radiation of the first two BPFs. Despite the weak heterogeneity of the *LP3* stage, the impact on cut-off BPFs is drastic revealing important modifications of rotor-stator interaction phenomena. This highlights the importance of

optimising future heterogeneous stators to avoid important tonal noise penalties. The simulations did not evidence any impact on the broadband noise component, identical in all cases. This was expected since the broadband noise is generated by phenomena that are uncorrelated with the vane-to-vane periodicity broken in the case of heterogeneous stators.

Simulations have also provided an insight into the aerodynamic excitations responsible for the noise generation. Phase averages made it possible to separate the wake-field of the rotor from the potential field of the stator. On the one hand, the analysis of the wake field showed regular wake profiles decreasing downstream and identical in all stator configurations. On the other hand, the potential field evidenced a clear impact of the stator heterogeneity. The periodic pattern observed for the homogeneous case was clearly perturbed with the heterogeneity. Spots of lower velocity were observed in front of the thickened vanes because of the stronger flow blockage. Nevertheless, the potential field was greatly attenuated at the location of the rotor trailing edge because of its exponential decay. The presence of the power-supply cable was also clearly seen evidencing a wide distortion of weak amplitude in front the cable position. From these results, the wake-interaction was seen to remain the dominant noise source despite the reduced rotor-stator distance. However, results on the aerodynamic potential field put in evidence some general conclusions about this noise source. The axial decay rate increases with the increasing azimuthal mode order meaning that even a low order disturbance with a small amplitude could be dominant at the rotor trailing edge (because of its slow decay). For this reason, generating very localized potential distortions (that have a rich azimuthal modal content) will contribute significantly more to this noise source. The analysis of cut-off modes at the frequency zero (seen as the potential field) gave an analytical estimate of the decay rate as a function of the mode order.

Lastly, analytical models were investigated. The focus was first put on the modelling of the airfoil response to the potential field (downstream perturbation decreasing upstream). The model presented in Parry's thesis [16] and based on the Wiener-Hopf technique was re-derived from another point of view, resorting to Amiet-Schwarzschild's technique. This model improves the Reversed Sears' model [17] by accounting for the Kutta condition. The same result as Parry was found proving the equivalence between both mathematical methods. As expected, the analytical model predicted a concentration of the unsteady loading at the trailing edges of the blades. Nevertheless, the amplitude was approximately five times below the numerical estimate. Then, heterogeneous potential fields were modelled based on the analytical potential theory. The heterogeneous stator was simulated by summing phase-lagged elementary sources. The obtained field showed a good agreement with the numerical heterogeneous potential field in terms of modal structure. Nevertheless, the harmonic decay was stronger in the analytical model. According to these results, the ellipse geometry used to model the stator vanes generated wider distortion profiles that led to a stronger harmonic decrease. The final noise predictions using Gold-

stein's analogy have shown low acoustic levels with a dominant first BPF as shown by Fournier [125]. This was expected from the weak potential field at the rotor blade trailing edge. In terms of modal content, the measured modes were recovered meaning that the analytical heterogeneous potential field successfully reproduced the major features of the heterogeneity.

The wake-interaction noise mechanism was then analytically investigated. The heterogeneity was introduced in Goldstein's analogy as proposed by Roger et al. [6]. An interference sum allowed introducing each vane loading individually and thus vane-to-vane variations. Because Amiet's model was considered for the airfoil response, thickness effects could not be accounted for directly. These effects were introduced by analysing the numerical results and by introducing a damping factor on the response of the thickened vanes. The analytical predictions have evidenced higher levels compared with the potential-interaction noise as expected. In terms of modal content, the predicted dominant modes were found to agree well with the experiment for the downstream propagating modes. Surprisingly, an inversion of the modes is observed for the upstream propagating modes. This inversion does not appear in the experiment nor in the numerical simulation and is yet to be explained. Combinations of the dipole radiation angle and the mode angle could be at the origin of interferences that are too cruedly accounted for in the present analytical modelling. The results stressed that no simple rule can be deduced for the prediction of the dominant modes like the Tyler & Sofrin's rule for homogeneous stages.

To conclude the investigation, an optimisation of the heterogeneous stator was performed. It has been observed that the modal content was dependent on the azimuthal distribution of the modified vanes. For this reason, the positioning of the three modified stator vanes was optimised. According to the analytical model, the optimum combination had the thickened vanes placed at the relative positions 1, 3 and 5. Even if this positioning was not interesting from the structural standpoint, it was simulated using the LBM to assess its noise reduction potential. Results evidenced an important attenuation of the BPF levels with the first BPF being attenuated by 25 dB downstream. The optimal solution simulated with the LBM was then in good agreement with the analytical prediction. The modal content of this stator evidenced an important attenuation of the dominant modes generated in the original stator. With this simple study, it was shown that the angular positioning of the modified vanes played an important role in the tonal levels because of the modal content modification. Other stator configurations could be tested with fewer or more structural vanes. A compromise could then be found in order to satisfy the structural needs but also reduce the acoustic levels.

To sum-up, this PhD project aimed at investigating the impact of heterogeneous stators in terms of acoustic emissions. A combined experimental, numerical and analytical investigation was carried out on a low-speed ducted fan allowing this quantification. The heterogeneity had a drastic impact on tonal noise but was negligible in terms of broadband noise. In fact, interference phenomena were greatly modified with the loss of the vane-to-

vane periodicity in heterogeneous stages. For this reason, important modifications were observed on the classical rotor-stator interaction phenomena.

Original contributions of the thesis

In this PhD, the first quantification of the impact of a heterogeneous stator on noise has been achieved. The analytical, numerical and experimental study provided the first comprehensive analysis of a realistic fan-OGV stage. This has been achieved by coherent cross-analyses between all of them that have allowed improving the understanding of the underlying physics in presence of heterogeneous stators.

The experiments performed on an available test-rig at Ecole Centrale de Lyon have allowed assessing several new features developed by the experimental team. A new calibration method applied on the *LP3* stage has been validated and the absence of any inflow distortion has been achieved with a Turbulence Control Screen.

The numerical study simulated the complete geometry (360°) of the *LP3* in its experimental environment. The comparison between homogeneous and heterogeneous stators has shown the impact of the stator heterogeneity for the first time. With specific analyses, simulations have also allowed separating contributions of the wake and potential interaction noise components and drawing general conclusions on both of them.

In terms of analytical modelling, the model of Parry [16] has been shown to be equivalent to the Reversed Sears' model [17] with the application of the Kutta condition. The analytical modelling has been able to reproduce most of the features of the heterogeneity (same dominant modes) and evidenced a weak contribution of the potential-interaction noise. Finally, the thesis has shown the ability of analytical models to perform optimisation studies of heterogeneous stators that would be useful in the acoustic design of low-speed fan stages.

Perspectives

This work opens the path to new opportunities and improvements in the study of heterogeneous stators. First of all, experiments could be completed. Additional probes could be added in the setup in order to better characterize the operating conditions of the *LP3* stage. In the current experiments, the operating point was characterized by the mass flow rate and the static pressure rise using probes at the duct walls. In future experiments, some additional measurements should be added in addition to the wall pressure measurements. Total pressure at different sections of the duct (upstream, in the interstage and downstream) would provide additional data in the flow that would allow better comparisons with the numerical simulations. This would allow to point out regions with higher discrepancies in the simulation that would need further refinements for instance. In addition, a characterization of the wake profiles would give more information on possible

blade-to-blade geometry discrepancies. This could explain the emergence of unexpected rotational harmonics observed in the measurements. In order to improve the experimental characterization, the vanes could also be instrumented and would allow identifying flow separated areas that would be compared with the available numerical database. Finally, other stator configurations and rotor-stator spacings could be investigated. In the current investigations, only the heterogeneous stator was investigated. First, the simulated homogeneous configuration could be tested to experimentally assess the impact of the heterogeneity. This step is an objective of the laboratory; indeed a version of the fan with a homogeneous stator has been recently delivered by Safran Ventilation Systems for future investigations. Some optimised heterogeneous stators could also be tested to assess their potential in the noise reduction. Secondly, various rotor-stator spacings would provide additional information on the rotor-stator interaction mechanisms, especially on the potential-interaction contribution.

Regarding the numerical simulations, different simulation methodologies could be tested. The range of Mach and Reynolds numbers of the fan is particularly adapted to LBM and LES methods: a moderate tip Mach number and relatively low Reynolds number. LES simulations on this configuration would provide additional information that could be compared to the present LBM simulations. The comparison of both would confirm their reliability, or on the contrary, highlight critical regions necessitating further investigations. For the LBM, the ignored tip gap in the current simulations could be accounted for to quantify its impact on aerodynamic performances and noise. In addition, further mesh refinements could be investigated to conclude on the aerodynamic convergence.

In terms of analytical modelling, models with increased complexity could be tested. The mode-matching method [49] is a good example where cascade effects are accounted for and where the extension to heterogeneous stators could be done (with the so-called equivalent edge-dipole approach). In fact, cascade effects are expected to be higher for the wake-interaction noise because sources are located on the stator where the overlapping of adjacent vanes is pronounced. Finally, the airfoil response to downstream perturbations could be improved. In the current study, the model was based on velocity perturbations. The problem could be approached considering pressure gusts which is similar to what has been investigated by Rozenberg [50] to treat boundary layer growing perturbations.

Finally, a different heterogeneous configuration with a higher tip Mach number could be investigated. This has been partly done in the literature [10] but the comparison with an equivalent homogeneous stator to precisely quantify the heterogeneity impact is still lacking. More realistic heterogeneous stators, not far from actual turbofans, could also be further investigated. Additional analyses on the potential-interaction noise with a stronger heterogeneity degree would be interesting to conclude on the behaviour and contribution of this noise source.

Conclusions générales et perspectives

Conclusions générales

L'objectif de cette thèse était d'étudier l'impact de stators hétérogènes sur les émissions sonores d'étages rotor-stator. Un stator hétérogène est défini comme un stator dans lequel la périodicité d'aube à aube n'est pas conservée. Une telle hétérogénéité peut être observée dans les configurations de turboréacteur double flux modernes incorporant des bras structuraux dans le stator dans le but d'obtenir une architecture de moteur plus compacte. Dans la présente étude, la configuration choisie fut un ventilateur à basse vitesse, l'étage *LP3*. Ce ventilateur présente deux caractéristiques principales des configurations de turbomachines modernes et futures: un stator hétérogène et un espacement rotor-stator court. Le stator considéré a trois aubes de stator épaissies et donc un degré d'hétérogénéité relativement faible. De plus, l'espacement rotor-stator à mi-envergure est inférieur à une corde de rotor (courte distance). Dans cette configuration, des mesures précédentes ont montré des forts niveaux pour les des deux premières fréquences de passage de pales (FPP) qui devaient être coupées conformément à la règle de Tyler & Sofrin. Par conséquent, l'objectif principal de cette étude était de déterminer si l'hétérogénéité était la cause de ce rayonnement inattendu et d'expliquer comment les mécanismes classiques d'interaction rotor-stator étaient modifiés en conséquence.

La première étape a consisté à étudier expérimentalement l'étage *LP3*. Les essais ont été menés sur un banc basse vitesse à l'École Centrale de Lyon permettant une caractérisation détaillée des sources de bruit (contenus spectral et modal). Afin d'éliminer une distorsion d'entrée d'air précédemment identifiée, un écran pour le contrôle de la turbulence (TCS) a été utilisé. Ce point était crucial car le bruit de distorsion d'entrée d'air contribue aux mêmes fréquences que celles des mécanismes d'interaction rotor-stator. Les résultats ont alors mis en évidence un fort rayonnement des deux premières FPP. Avec l'ajout de l'écran, les FPP étaient plus fines mais émettaient toujours à des niveaux élevés. À ce stade, on pouvait suspecter que ces raies étaient générées par l'hétérogénéité du stator. A ces fréquences, des modes acoustiques dominants ont été mesurés. Aucun de

ces modes était prédit par la règle classique de Tyler & Sofrin et furent alors attribués à l'hétérogénéité du stator. Le seul mode prédit par la règle se trouvait à la troisième FPP et a été correctement mesuré durant l'essai.

Deuxièmement, les essais ont été simulés numériquement à l'aide de la méthode de Boltzmann sur réseau (LBM). Les simulations ont pris en compte l'ensemble de la configuration expérimentale (dimensions réelles de la pièce) avec quelques simplifications. Cela a alors permis de placer les mêmes antennes acoustiques dans le domaine de calcul afin d'utiliser les mêmes méthodes de post-traitement que dans les essais. En outre, le positionnement azimutal non-équiréparti des trois aubes de stator structurelles (3 sur 23) a nécessité la simulation de la géométrie complète du LP3 sur 360°. Trois configurations de l'étage *LP3* ont été simulées : le stator hétérogène d'origine (configuration expérimentale), un stator homogène et une configuration finale dans laquelle le câble d'alimentation en aval a été retiré. Le TCS n'a pas été modélisé mais aucune distorsion n'a été identifiée à l'entrée. En effet, le court temps physique simulé comparé au temps de remplissage de la pièce n'a pas permis le développement d'une distorsion. En termes de performances aérodynamiques, les simulations ont montré un bon comportement physique de la turbomachine, mais ont montré un taux de compression inférieur à celui de l'expérience. L'écart a été considérablement réduit avec le dernier raffinement du maillage. Néanmoins, les simulations RANS ont prédit une meilleure performance du rotor de mi-envergure jusqu'au carter. Un dernier raffinement du maillage LBM n'a pas pu être fait mais doit être considéré comme une perspective pour conclure sur la convergence des performances. Notez que les raffinements de maillage des deux simulations (LBM et RANS) ont été appliqués sur les pales et les aubes et non sur les parois du conduit où la mesure de l'augmentation de pression statique a été effectuée. Un raffinement ciblé sur les parois du conduit constitue une amélioration possible pour les simulations futures ainsi qu'un raffinement global supplémentaire du maillage. En ce qui concerne l'essai, d'autres mesures aérodynamiques pourraient être ajoutées afin de mieux caractériser le point de fonctionnement, telles que des relevés de pression totale en amont et en aval du ventilateur.

L'analyse acoustique des simulations a conduit à l'un des principaux résultats de la thèse. L'hétérogénéité est responsable d'une augmentation du niveau tonal de plus de 10 dB aux deux premières FPP. À la troisième FPP, le niveau est resté sensiblement inchangé en raison de la présence d'un mode Tyler & Sofrin dominant généré dans toutes les configurations de stator. Le stator homogène a néanmoins fourni des niveaux résiduels des deux premières FPP, certainement dus à des hétérogénéités de maillage liées à l'approche cartésienne utilisée par le solveur. Enfin, le retrait du câble d'alimentation a eu un impact négligeable sur les émissions sonores. L'augmentation drastique des niveaux observés pour les deux premières FPP dans la configuration hétérogène peut être expliquée par la modification des interférences destructives qui permettent uniquement la génération des modes de Tyler & Sofrin (coupés aux deux premières FPP). Pour cette raison, la règle de Tyler & Sofrin habituelle n'est plus vérifiée dans de telles configurations de stator. Étonnam-

ment, l'énergie n'est répartie sur tous les ordres de modes azimutaux malgré le manque de périodicité des trois aubes du stator (espacement non uniforme entre les trois). Au contraire, l'énergie est concentrée sur quelques modes dominants expliqués plus tard avec les modèles analytiques. Le contenu modal mesuré et simulé est en bon accord et atteste que l'hétérogénéité du stator est la cause réelle du rayonnement des deux premières FPP. Malgré la faible hétérogénéité de l'étage *LP3*, l'impact sur des FPP qui devraient être coupées est radical, révélant des modifications importantes des phénomènes d'interaction rotor-stator. Cela souligne l'importance d'optimiser les futurs stators hétérogènes afin d'éviter d'importantes pénalités sur le bruit tonal. Les simulations n'ont mis en évidence aucun impact sur la composante du bruit à large bande, identique dans tous les cas. Cela était attendu dans la mesure où le bruit à large bande est généré par des phénomènes non corrélés avec la périodicité d'aube à aube qui est brisée dans le cas de stators hétérogènes.

Les simulations ont également permis de mieux comprendre les excitations aérodynamiques responsables de la génération de bruit. Des moyennes de phase dans le repère relatif et absolu ont permis de séparer les sillages du rotor du champ potentiel du stator. D'une part, l'analyse du champ de sillage montre des profils réguliers décroissant en aval et identiques dans toutes les configurations de stator. D'autre part, le champ potentiel a mis en évidence un impact important de l'hétérogénéité du stator. Le schéma périodique observé pour le cas homogène était clairement perturbé par l'hétérogénéité. En effet, des taches de faible vitesse ont été observées devant les aubes épaissies en raison du blocage plus important de l'écoulement. Néanmoins, le champ potentiel était fortement atténué au bord de fuite du rotor en raison de sa décroissance exponentielle. La présence du câble d'alimentation a également été clairement mise en évidence, montrant une distorsion importante de faible amplitude devant la position du câble. À partir de ces résultats, l'interaction de sillage s'est avérée être la source de bruit dominante malgré la distance rotor-stator réduite. Cependant, les résultats sur le champ de potentiel aérodynamique ont mis en évidence certaines conclusions générales sur cette source de bruit. Le taux de décroissance axiale augmente avec un ordre azimutal du mode croissant, ce qui signifie que même une perturbation de faible amplitude mais d'ordre faible peut être dominante au bord de fuite du rotor (en raison de sa décroissance lente). Pour cette raison, la génération de distorsions potentielles très localisées (ayant un contenu modal azimutal riche) contribuera d'avantage à cette source de bruit. L'analyse des modes coupés à la fréquence zéro (ce qui peut être vu comme le champ potentiel) a donné une estimation analytique du taux de décroissance en fonction de l'ordre du mode.

Enfin, des modèles analytiques ont été étudiés. L'accent a d'abord été mis sur la modélisation de la réponse du profil au champ potentiel (perturbation en aval décroissante en amont). Le modèle présenté dans la thèse de Parry [16] basé sur la technique de Wiener-Hopf a été re-dérivé d'une autre façon en utilisant la technique d'Amiet-Schwarzschild. Ce modèle améliore le modèle de Sears inversé [17] en prenant en compte la condition de Kutta. Le même résultat que Parry a été trouvé prouvant l'équivalence entre les deux

méthodes mathématiques. Comme attendu, le modèle analytique a mis en évidence une concentration du chargement instationnaire aux bords de fuite des pales du rotor. Néanmoins, l'amplitude était environ cinq fois inférieure à l'estimation numérique. Ensuite, le champ potentiel modifié par la présence d'un stator hétérogène a été modélisé sur la base de la théorie potentielle analytique. Le stator hétérogène a été créé en sommant des sources élémentaires déphasées. Le champ obtenu montre un bon accord avec le champ potentiel numérique hétérogène en termes de structure modale. Néanmoins, la décroissance en harmonique était plus forte dans le modèle analytique. Selon ces résultats, la géométrie d'ellipse utilisée pour modéliser les aubes de stator génère des profils de distorsion plus larges, ce qui entraîne une décroissance plus forte des harmoniques d'ordre supérieur. Les prédictions finales de bruit utilisant l'analogie de Goldstein ont montré de faibles niveaux acoustiques avec une première FPP dominante, comme le montre Fournier [125]. Cela était attendu par la faible amplitude du champ potentiel au bord de fuite des pales du rotor. En termes de contenu modal, les modes mesurés ont bien été prédits, ce qui signifie que le champ de potentiel analytique hétérogène a reproduit avec succès les principales caractéristiques de l'hétérogénéité.

Le mécanisme de bruit d'interaction de sillage a ensuite été étudié analytiquement. L'hétérogénéité du stator a été introduite dans l'analogie de Goldstein par l'approche proposée par Roger et al. [6]. Une somme d'interférence permet alors d'introduire le chargement de chaque pale et ainsi des variations de pale à pale. Étant donné que le modèle d'Amiet a été choisi pour la réponse des pales, les effets d'épaisseur ne peuvent pas être directement pris en compte. Ces effets ont alors été introduits en analysant les résultats numériques et en ajoutant un facteur d'atténuation sur la réponse des aubes épaissies. Comme prévu, les prédictions analytiques ont mis en évidence des niveaux supérieurs par rapport au bruit d'interaction potentielle. En termes de contenu modal, les modes dominants prédits s'accordent bien avec l'expérience pour les modes se propageant vers l'aval. De manière surprenante, une inversion des modes est observée pour les modes se propageant vers l'amont. Cette inversion n'apparaît ni dans l'expérience ni dans la simulation numérique et reste à expliquer. Des combinaisons de l'angle de rayonnement dipolaire et de l'angle d'émission du mode pourraient être à l'origine d'interférences non prises en compte dans la modélisation analytique actuelle. Les résultats ont souligné qu'aucune règle simple ne peut être déduite pour la prédiction des modes dominants comme la règle de Tyler & Sofrin pour le cas des stators homogènes.

Pour conclure l'étude, une optimisation du stator hétérogène a été réalisée. Il a été observé que le contenu modal dépendait considérablement de la distribution azimutale des aubes structurelles. Pour cette raison, le positionnement des trois aubes de stator épaissies a été optimisé. Selon le modèle analytique, la combinaison optimale avait les aubes structurelles placées aux positions azimutales relatives 1,3 et 5. Même si ce positionnement n'était pas intéressant du point de vue structurel, il a été simulé à l'aide de la LBM pour évaluer son potentiel de réduction du bruit. Les résultats ont mis en

évidence une importante atténuation des niveaux des FPP, la première ayant été atténué de 25 dB en aval. La solution optimale simulée avec le LBM était alors en bon accord avec la prédiction analytique. Le contenu modal de ce stator témoigne d'une importante atténuation des modes dominants générés avec le stator d'origine. Avec cette simple étude, il a été montré que le positionnement angulaire des aubes épaissies jouait un rôle important au regard des niveaux de bruit tonal en raison de la modification du contenu modal. Dans le futur, d'autres configurations de stator pourraient être testées avec plus ou moins d'aubes structurelles. Un compromis pourrait alors être trouvé afin de satisfaire les besoins structurels tout en réduisant les niveaux acoustiques.

En résumé, ce projet de thèse avait pour objectif d'étudier l'impact de stators hétérogènes sur les émissions sonores. Une analyse expérimentale, numérique et analytique a été réalisée sur un ventilateur à basse vitesse permettant cette quantification. L'hétérogénéité a eu un impact considérable sur le bruit tonal mais était négligeable en termes de bruit à large bande. En effet, les phénomènes interférentiels se sont considérablement modifiés avec la perte de la périodicité de pale à pale sur un stator hétérogène. Pour cette raison, des modifications importantes ont été observées sur les phénomènes classiques d'interaction rotor-stator.

Contributions originales de la thèse

Dans cette thèse, la première quantification de l'impact d'un stator hétérogène sur le bruit a été réalisée. L'étude analytique, numérique et expérimentale a fourni la première analyse complète d'un étage rotor-stator réaliste et hétérogène. Cet objectif a été atteint grâce à des analyses croisées entre les différentes facettes de l'étude qui ont permis d'améliorer la compréhension de la physique sous-jacente en présence de stators hétérogènes.

Les essais réalisés sur un banc d'essai disponible à l'Ecole Centrale de Lyon ont permis d'évaluer plusieurs nouveaux développements de l'équipe expérimentale. Une nouvelle méthode d'étalonnage appliquée sur l'étage *LP3* a été validée et l'absence de toute distorsion d'entrée d'air a été obtenue avec un écran pour le contrôle de la turbulence.

L'étude numérique a simulé la géométrie complète (360°) du *LP3* dans son environnement expérimental. La comparaison entre des stators homogène et hétérogène a mis en évidence l'impact de l'hétérogénéité du stator pour la première fois. Avec des analyses spécifiques, les simulations ont également permis de séparer les contributions du bruit d'interaction potentielle et du bruit d'interaction de sillages et de tirer des conclusions générales sur les deux.

En termes de modélisation analytique, on a montré que le modèle de Parry [16] est équivalent au modèle de Sears inversé [17] avec l'application de la condition Kutta. La modélisation analytique a pu reproduire la plupart des caractéristiques de l'hétérogénéité (mêmes modes dominants) et a mis en évidence une faible contribution du bruit d'interaction potentielle. Enfin, la thèse a montré la capacité des modèles analytiques à réaliser des études d'optimisation des stators hétérogènes qui seraient utiles dans la conception acous-

tique des étages de ventilateurs à basse vitesse.

Perspectives

Ce travail ouvre la voie à de nouvelles opportunités et améliorations dans l'étude des stators hétérogènes. Tout d'abord, les essais sont passés en revue. Des sondes supplémentaires pourraient être ajoutées dans la configuration afin de mieux caractériser les conditions de fonctionnement de l'étage *LP3*. Dans les essais réalisés, le point de fonctionnement était caractérisé par le débit masse et l'augmentation de la pression statique mesurée par des sondes aux parois du conduit. Dans des expériences futures, des mesures supplémentaires devront être ajoutées aux mesures de pression pariétale. La pression totale dans différentes sections du conduit (en amont, entre les étages et en aval) fournirait des données supplémentaires dans l'écoulement qui permettrait une meilleure comparaison avec les simulations numériques. Cela permettrait de mettre en évidence les régions présentant des écarts plus importants dans la simulation qui nécessiteraient par exemple de raffinements ou études supplémentaires. De plus, une caractérisation des profils de sillage donnerait plus d'informations sur des possibles différences géométriques de pale á pale. Cela pourrait expliquer l'émergence inattendue d'harmoniques de la fréquence de rotation observées dans les mesures. Afin d'améliorer la caractérisation expérimentale, les aubes pourraient également être instrumentées et permettraient d'identifier les zones de décollement qui seraient comparées à la base de données numérique disponible. Enfin, d'autres configurations de stator et des espacements rotor-stator différents pourraient être étudiés. Dans l'étude présentée, seul le stator hétérogène a été mesuré expérimentalement. Premièrement, la configuration homogène simulée pourrait donc être testée pour évaluer de manière expérimentale l'impact de l'hétérogénéité. Cette étape est un objectif du laboratoire. En effet, Safran Ventilation Systems a récemment livré une version du ventilateur avec un stator homogène pour des études futures. Certains stators hétérogènes optimisés pourraient également être testés afin d'évaluer leur potentiel de réduction du bruit. Deuxièmement, différents espacements rotor-stator fourniraient des informations supplémentaires sur les mécanismes d'interaction rotor-stator, en particulier sur la contribution du bruit d'interaction potentielle.

En ce qui concerne les simulations numériques, différentes méthodologies de simulation pourraient être testées. La gamme de nombres de Mach et de Reynolds du *LP3* est particulièrement adaptée aux méthodes LBM et LES: un nombre de Mach en bout de pale relativement faible et un nombre de Reynolds relativement bas. Des simulations LES sur cette configuration fourniraient des informations supplémentaires pouvant être comparées aux simulations actuelles LBM. La comparaison des deux confirmerait leur fiabilité ou, au contraire, mettrait en évidence des régions critiques nécessitant des investigations supplémentaires. Pour ce qui concerne les simulations LBM, il serait possible de prendre en compte le jeu du rotor non résolu dans les simulations actuelles et ce afin de quantifier son

impact sur les performances aérodynamiques et le bruit. En outre, d'autres améliorations du maillage pourraient être étudiées pour conclure sur la convergence des performances aérodynamiques.

En termes de modélisation analytique, des modèles de complexité accrue pourraient être testés. La méthode de raccordement modal [49] est un bon exemple prenant en compte des effets de cascade et permettant l'extension pour des stators hétérogènes (appelée approche du dipôle de bord équivalent). En effet, les effets de cascade devraient être plus importants pour le bruit d'interaction de sillage car les sources sont situées sur le stator, où le recouvrement par les aubes adjacentes est plus élevé. Enfin, le modèle de réponse de profil aux perturbations avales pourrait être améliorée. Dans la présente étude, le modèle était basé sur des perturbations de vitesse. Le problème pourrait être abordé en considérant des rafales de pression, ce qui est similaire à ce qui a été étudié par Rozenberg [50] pour traiter des perturbations croissantes de la couche limite.

Enfin, une configuration hétérogène différente avec un nombre de Mach plus élevé pourrait être étudiée. Ceci a été fait en partie dans la littérature [10], mais il lui manque encore la comparaison avec un stator homogène équivalent pour quantifier avec précision l'impact de l'hétérogénéité. Des stators hétérogènes plus réalistes, non loin des turboréacteurs double flux réels, pourraient également être approfondis. Finalement, des analyses supplémentaires sur le bruit d'interaction potentielle avec un degré d'hétérogénéité plus élevé seraient intéressantes pour conclure sur le comportement et la contribution de cette source de bruit.

List of Figures

Bibliography

[1] ACARE, "Strategic research & innovation agenda: Flightpath 2050 goals," (2017). (Cited on page 1.)

[2] M. J. Lighthill, "On sound generated aerodynamically. I. General theory," in "Proceedings of the Royal Society of London A: Mathematical, Physical and Engineering Sciences," , vol. 211 (The Royal Society, 1952), vol. 211, pp. 564–587. (Cited on page 1.)

[3] M. J. Lighthill, "On sound generated aerodynamically. II. Turbulence as a source of sound," in "Proceedings of the Royal Society of London A: Mathematical, Physical and Engineering Sciences," , vol. 222 (The Royal Society, 1954), vol. 222, pp. 1–32. (Cited on page 1.)

[4] M. J. Smith, *Aircraft noise. Cambridge aerospace series* (Cambridge University Press, 1989). (Cited on pages 3 and 193.)

[5] ENOVAL, "Ultra high bypass ratio aero engines," (2017). (Cited on page 3.)

[6] M. Roger and P. Caule, "Assessement of the effect of stator inhomogeneity on rotor-stator tonal noise," in "ISROMAC-15," (2014). (Cited on pages 5, 9, 10, 62, 160, 182, 188, and 193.)

[7] S. L. Dixon and C. Hall, *Fluid mechanics and thermodynamics of turbomachinery* (Butterworth-Heinemann, 2013). (Cited on page 8.)

[8] S. Rienstra and A. Hirschberg, *An Introduction to Acoustics* (Eindhoven University of Technology, 2004). (Cited on pages 9, 19, and 193.)

[9] M. J. Crocker, *Handbook of noise and vibration control* (John Wiley & Sons, 2007). (Cited on page 9.)

[10] V. Bonneau, C. Polacsek, R. Barrier, S. Lewy, J.-M. Roux, and Y. Gervais, "Tonal noise prediction of a turbofan with heterogeneous stator and bifurcations," AIAA Journal (2015). (Cited on pages 10, 11, 184, 191, and 193.)

[11] A. Holewa, C. Weckmüller, and S. Guérin, "Impact of bypass-duct bifurcations on fan noise," in "18th AIAA/CEAS Aeroacoustics Conference," (Colorado Springs, CO, 2012), AIAA-2012-2129. (Cited on page 10.)

[12] A. V. Kozlov, H. M. Atassi, A. A. Ali, and D. Topol, "Modelling fan noise produced by downstream mounting structural blockage," in "23rd AIAA/CEAS Aeroacoustics Conference," (2017), p. 3871. (Cited on pages 10 and 11.)

[13] J. Thisse, "Prévision du bruit d'onde de choc d'un turboréacteur en régime transsonique par des méthodes analytiques et numériques," Ph.D. thesis (2015). Thèse de doctorat dirigée par Khelladi, Mohamed Sofiane et Gloerfelt, Xavier Acoustique Paris, ENSAM 2015. (Cited on page 12.)

[14] N. Peake and A. B. Parry, "Modern challenges facing turbomachinery aeroacoustics," Annual Review of Fluid Mechanics **44**, 227–248 (2012). (Cited on page 13.)

[15] R. Parker, "Paper 1: relation between blade row spacing and potential flow interaction effects in turbomachines," in "Proceedings of the Institution of Mechanical Engineers, Conference Proceedings," , vol. 184 (Sage Publications Sage UK: London, England, 1969), vol. 184, pp. 1–8. (Cited on page 14.)

[16] A. B. Parry, "Theoretical prediction of counter-rotating propeller noise," Ph.D. thesis, University of Leeds (1988). (Cited on pages 14, 35, 38, 148, 181, 183, 187, and 189.)

[17] M. Roger, S. Moreau, and A. Guédel, "Vortex-shedding noise and potential-interaction noise modeling by a reversed Sears' problem," in "Proceedings of the 12th AIAA/CEAS Aeroacoustics Conference and Exhibit," (2006), pp. 8–10. (Cited on pages 14, 16, 33, 147, 181, 183, 187, and 189.)

[18] M. Daroukh, S. Moreau, N. Gourdain, J.-F. Boussuge, and C. Sensiau, "Effect of distortion on turbofan tonal noise at cutback with hybrid methods," International Journal of Turbomachinery, Propulsion and Power **2**, 16 (2017). (Cited on pages 15, 131, 177, and 200.)

[19] M. Sturm and T. Carolus, "Tonal fan noise of an isolated axial fan rotor due to inhomogeneous coherent structures at the intake," Noise Control Engineering Journal **60**, 699–706 (2012). (Cited on pages 15, 100, and 193.)

[20] S. Caro, "Contribution à la prévision du bruit d'origine aérodynamique d'un ventilateur de refroidissement," Ph.D. thesis, Ecully, Ecole centrale de Lyon (2003). (Cited on page 15.)

[21] R. K. Amiet, "Noise due to turbulent flow past a trailing edge," Journal of sound and vibration **47**, 387–393 (1976). (Cited on pages 15 and 28.)

[22] M. Roger and S. Moreau, "Back-scattering correction and further extensions of Amiet's trailing-edge noise model. Part 1: theory," Journal of Sound and Vibration **286**, 477–506 (2005). (Cited on pages 15, 28, and 32.)

[23] S. Moreau and M. Roger, "Back-scattering correction and further extensions of Amiet's trailing-edge noise model. Part II: Application," Journal of Sound and Vibration **323**, 397–425 (2009). (Cited on pages 15, 28, and 29.)

[24] M. Roger and S. Moreau, "Extensions and limitations of analytical airfoil broadband noise models," International Journal of Aeroacoustics **9**, 273–305 (2010). (Cited on page 15.)

[25] T. Zhu, D. Lallier-Daniels, M. Sanjosé, S. Moreau, and T. H. Carolus, "Rotating coherent flow structures as a source for narrowband tip clearance noise from axial fan," AIAA Paper 2016 **2822** (2016). (Cited on page 16.)

[26] S. Magne, S. Moreau, and A. Berry, "Subharmonic tonal noise from backflow vortices radiated by a low-speed ring fan in uniform inlet flow," The Journal of the Acoustical Society of America **137**, 228–237 (2015). (Cited on pages 16 and 48.)

[27] S. Moreau and M. Sanjose, "Sub-harmonic broadband humps and tip noise in low-speed ring fans," The Journal of the Acoustical Society of America **139**, 118–127 (2016). (Cited on pages 16, 48, and 49.)

[28] D. Lallier-Daniels, M. Piellard, B. Coutty, and S. Moreau, "Aeroacoustic study of an axial engine cooling module using lattice-Boltzmann simulations and the Ffowcs Williams and Hawkings' analogy," European Journal of Mechanics-B/Fluids **61**, 244–254 (2017). (Cited on pages 16, 48, 49, 50, and 194.)

[29] D. B. Hanson, "Spectrum of rotor noise caused by atmospheric turbulence," The Journal of the Acoustical Society of America **56**, 110–126 (1974). (Cited on pages 17 and 69.)

[30] H. H. Hubbard, *Aeroacoustics of Flight Vehicles: Noise sources*, vol. 1 (NASA Office of Management, Scientific and Technical Information Program, 1991). (Cited on page 18.)

[31] M. E. Goldstein, *Aeroacoustics*, vol. 1 (1976). (Cited on pages 18, 22, 23, 25, and 194.)

[32] D. Casalino, S. Moreau, and M. Roger, "One, no one and one hundred thousand methods for low-speed fan noise prediction," International Journal of aeroacoustics **9**, 307–327 (2010). (Cited on page 18.)

[33] C. P. Arroyo, T. Leonard, M. Sanjosé, S. Moreau, and F. Duchaine, "Large Eddy Simulation of a scale-model turbofan for fan noise source diagnostic," Journal of Sound and Vibration **445**, 64–76 (2019). (Cited on page 18.)

[34] M. L. Munjal, *Acoustics of ducts and mufflers with application to exhaust and ventilation system design* (John Wiley & Sons, 1987). (Cited on page 19.)

[35] J. M. Tyler and T. G. Sofrin, "Axial flow compressor noise studies," Tech. rep., SAE Technical Paper (1962). (Cited on pages 19, 25, 26, and 194.)

[36] J. F. Williams and D. L. Hawkings, "Sound generation by turbulence and surfaces in arbitrary motion," Philosophical Transactions of the Royal Society of London A: Mathematical, Physical and Engineering Sciences **264**, 321–342 (1969). (Cited on pages 21 and 22.)

[37] T. Wright, *Fluid machinery: performance, analysis, and design* (CRC press, 1999). (Cited on page 21.)

[38] W. Neise, "Review of fan noise generation mechanisms and control methods," (1992). (Cited on page 22.)

[39] C. Morfey, "Tone radiation from an isolated subsonic rotor," The Journal of the Acoustical Society of America **49**, 1690–1692 (1971). (Cited on page 22.)

[40] R. Camussi, *Noise sources in turbulent shear flows: fundamentals and applications*, vol. 545 (Springer Science & Business Media, 2013). (Cited on page 24.)

[41] W. R. Sears, "Some aspects of non-stationary airfoil theory and its practical application," Journal of the Aeronautical Sciences **8** (1941). (Cited on page 28.)

[42] R. K. Amiet, "Acoustic radiation from an airfoil in a turbulent stream," Journal of Sound and vibration **41**, 407–420 (1975). (Cited on pages 28, 29, and 31.)

[43] R. K. Amiet, "High frequency thin-airfoil theory for subsonic flow," AIAA journal **14**, 1076–1082 (1976). (Cited on pages 28, 29, 31, and 33.)

[44] C. Ventres, M. Theobald, and W. Mark, "Turbofan noise generation. volume 1: Analysis," (1982). (Cited on page 28.)

[45] D. B. Hanson and K. P. Horan, "Turbulence/cascade interaction: spectra of inflow, cascade response, and noise," AIAA Paper **2319** (1998). (Cited on page 28.)

[46] S. A. Glegg, "The response of a swept blade row to a three-dimensional gust," Journal of sound and vibration **227**, 29–64 (1999). (Cited on page 28.)

[47] H. Posson, S. Moreau, and M. Roger, "On the use of a uniformly valid analytical cascade response function for fan broadband noise predictions," Journal of sound and vibration **329**, 3721–3743 (2010). (Cited on page 28.)

[48] H. Posson, S. Moreau, and M. Roger, "Broadband noise prediction of fan outlet guide vane using a cascade response function," Journal of Sound and Vibration **330**, 6153–6183 (2011). (Cited on page 28.)

[49] S. Bouley, B. François, M. Roger, H. Posson, and S. Moreau, "On a two-dimensional mode-matching technique for sound generation and transmission in axial-flow outlet guide vanes," Journal of Sound and Vibration **403**, 190–213 (2017). (Cited on pages 28, 184, and 191.)

[50] Y. Rozenberg, "Modélisation analytique du bruit aérodynamique à large bande des machines tournantes : utilisation de calculs moyennés de mécanique des fluides," Theses, Ecole Centrale de Lyon (2007). (Cited on pages 32, 153, 184, and 191.)

[51] F. Conte, M. Roger, S. Moreau, and P. Caule, "Modeling of installation effects on the noise from subsonic axial fans," in "17th AIAA/CEAS Aeroacoustics Conference (32nd AIAA Aeroacoustics Conference)," (2011), p. 2948. (Cited on pages 33 and 148.)

[52] D. Philbrick and D. Topol, "Development of a fan noise design system, Part 1: system design and source modeling," in "15th AIAA Aeroacoustics Conf," (1993). (Cited on page 36.)

[53] I. S. Gradshteyn and I. M. Ryzhik, *Table of integrals, series, and products* (Academic press, 2014). (Cited on page 36.)

[54] B. Thwaites and R. Street, "Incompressible aerodynamics," Physics Today **13**, 60 (1960). (Cited on page 37.)

[55] R. L. Panton, *Incompressible Flow* (John Wiley & Sons, 2013). (Cited on pages 37 and 38.)

[56] P. Sagaut, S. Deck, and M. Terracol, *Multiscale and multiresolution approaches in turbulence: LES, DES and hybrid RANS/LES methods: applications and guidelines* (World Scientific, 2013). (Cited on pages 40 and 194.)

[57] P. R. Spalart, S. R. Allmaras *et al.*, "A one equation turbulence model for aerodynamic flows," La Recherche Aerospatiale (1994). (Cited on page 41.)

[58] B. Mohammadi and O. Pironneau, "Analysis of the k-epsilon turbulence model," (1993). (Cited on page 41.)

[59] F. R. Menter, "Improved two-equation $k-\omega$ turbulence models for aerodynamic flows," (1992). (Cited on page 41.)

[60] K. Hanjalic and B. Launder, "A Reynolds stress model of turbulence and its application to thin shear flows," J. Fluid Mech **52**, 609–638 (1972). (Cited on page 41.)

[61] J. Smagorinsky, "General circulation experiments with the primitive equations: I. The basic experiment," Monthly weather review **91**, 99–164 (1963). (Cited on page 41.)

[62] F. Nicoud and F. Ducros, "Subgrid-scale stress modelling based on the square of the velocity gradient tensor," Flow, turbulence and Combustion **62**, 183–200 (1999). (Cited on page 41.)

[63] D. R. Chapman, "Computational aerodynamics development and outlook," AIAA J **17**, 1293–1313 (1979). (Cited on page 41.)

[64] H. Choi and P. Moin, "Grid-point requirements for Large Eddy Simulation: Chapman's estimates revisited," Physics of fluids **24**, 011702 (2012). (Cited on page 41.)

[65] S. Moreau, "Numerical simulation of low-speed fan aeroacoustics," in "Progress in simulation, control and reduction of ventilation noise," (Von Karman Institute, 2015). (Cited on page 42.)

[66] S. Moreau, "Direct noise computation of low-speed ring fans," Acta Acustica united with Acustica **105**, 30–42 (2019). (Cited on page 42.)

[67] S. Succi, *The lattice Boltzmann equation: for fluid dynamics and beyond* (Oxford university press, 2001). (Cited on page 43.)

[68] P. L. Bhatnagar, E. P. Gross, and M. Krook, "A model for collision processes in gases. I. small amplitude processes in charged and neutral one-component systems," Physical review **94**, 511 (1954). (Cited on page 43.)

[69] S. Marié, "Etude de la méthode Boltzmann sur réseau pour les simulations en aéroacoustique." Ph.D. thesis (2008). (Cited on page 44.)

[70] X. He and L.-S. Luo, "Theory of the lattice Boltzmann method: From the Boltzmann equation to the lattice Boltzmann equation," Physical Review E **56**, 6811 (1997). (Cited on page 45.)

[71] Z. Guo, C. Zheng, and B. Shi, "Discrete lattice effects on the forcing term in the lattice Boltzmann method," Physical Review E **65**, 046308 (2002). (Cited on page 45.)

[72] V. Yakhot and S. A. Orszag, "Renormalization group analysis of turbulence. I. Basic theory," Journal of scientific computing **1**, 3–51 (1986). (Cited on page 45.)

[73] J. Latt, "Hydrodynamic limit of lattice Boltzmann equations," Ph.D. thesis, University of Geneva (2007). (Cited on page 45.)

[74] O. Filippova and D. Hänel, "Grid refinement for lattice-BGK models," Journal of Computational Physics **147**, 219–228 (1998). (Cited on page 46.)

[75] H. Chen, O. Filippova, J. Hoch, K. Molvig, R. Shock, C. Teixeira, and R. Zhang, "Grid refinement in lattice Boltzmann methods based on volumetric formulation," Physica A: Statistical Mechanics and its Applications **362**, 158–167 (2006). (Cited on page 46.)

[76] Y. Li, R. Shock, R. Zhang, and H. Chen, "Numerical study of flow past an impulsively started cylinder by the lattice-Boltzmann method," Journal of Fluid Mechanics **519**, 273–300 (2004). (Cited on page 47.)

[77] S. Marié, D. Ricot, and P. Sagaut, "Comparison between lattice Boltzmann method and Navier–Stokes high order schemes for computational aeroacoustics," Journal of Computational Physics **228**, 1056–1070 (2009). (Cited on page 47.)

[78] S. Marié, D. Ricot, and P. Sagaut, "Accuracy of lattice Boltzmann method for aeroacoustics simulations," AIAA-paper **3515**, 2007 (2007). (Cited on page 47.)

[79] G. A. Bres, F. Pérot, and D. Freed, "Properties of the lattice-Boltzmann method for acoustics," AIAA Paper **3395**, 2009 (2009). (Cited on pages 47, 48, and 194.)

[80] F. Pérot, A. Mann, M.-S. Kim, D. Casalino, and E. Fares, "Investigation of inflow condition effects on the ANCF aeroacoustics radiation using LBM," in "INTER-NOISE and NOISE-CON Congress and Conference Proceedings," , vol. 2012 (Institute of Noise Control Engineering, 2012), vol. 2012, pp. 4267–4280. (Cited on pages 48, 50, and 194.)

[81] A. Mann, F. Pérot, M.-S. Kim, D. Casalino, and E. Fares, "Advanced Noise Control Fan direct aeroacoustics predictions using a lattice-Boltzmann method," AIAA paper **2287**, 2012 (2012). (Cited on page 48.)

[82] F. Pérot, M.-S. Kim, S. Moreau, and M. Henner, "Axial fan noise aeroacoustics predictions and inflow effect on tonal noise using LBM," in "CFD Canada 2013 Conference, Canada," (2013). (Cited on page 48.)

[83] M. Sturm, M. Sanjosé, S. Moreau, and T. Carolus, "Aeroacoustic simulation of an axial fan including the full test rig by using the Lattice Boltzmann Method," (2015). (Cited on pages 48, 49, and 194.)

[84] M. Sanjosé, M. Daroukh, W. Magnet, D. L. Jérôme, S. Moreau, and A. Mann, "Tonal fan noise prediction and validation on the ANCF configuration," in "Proceedings of the Fan 2015 Conference," (2015). (Cited on pages 48, 50, and 51.)

[85] D. Casalino, A. Hazir, and A. Mann, "Turbofan broadband noise prediction using the lattice Boltzmann method," AIAA Journal pp. 1–20 (2017). (Cited on page 48.)

[86] I. Gonzalez-Martino and D. Casalino, "Fan tonal and broadband noise simulations at transonic operating conditions using lattice-Boltzmann methods," in "2018 AIAA/CEAS Aeroacoustics Conference," (2018), p. 3919. (Cited on page 48.)

[87] U. Tapken, T. Raitor, and L. Enghardt, "Tonal noise radiation from an UHBR fan-optimized in-duct radial mode analysis," in "Proceedings of the 15th AIAA/CEAS Aeroacoustics Conference, Miami, FL, May," (2009), pp. 11–13. (Cited on pages 54, 61, and 195.)

[88] A. Pereira, A. Finez, Q. Leclere, E. Salze, and P. Souchotte, "Modal identification of a small-scale ducted fan," in "22nd AIAA/CEAS Aeroacoustics Conference," (2016), p. 3063. (Cited on pages 54, 57, 70, and 195.)

[89] A. Finez, A. Pereira, and Q. Leclere, "Broadband mode decomposition of ducted fan noise using cross-spectral matrix denoising," in "Fan Noise 2015," (2015). (Cited on pages 54, 59, 70, and 88.)

[90] M. Sturm and T. Carolus, "Large scale inflow distortions as a source mechanism for discrete frequency sound from isolated axial fans," AIAA **2105**, 27–19 (2013). (Cited on pages 54, 55, 56, and 195.)

[91] U. Tapken, B. Pardowitz, and M. Behn, "Radial mode analysis of fan broadband noise," in "23rd AIAA/CEAS Aeroacoustics Conference," (2017), p. 3715. (Cited on pages 54, 55, and 195.)

[92] É. Salze, C. Bailly, O. Marsden, E. Jondeau, and D. Juvé, "An experimental characterization of wall pressure wavevector-frequency spectra in the presence of pressure gradients," in "20th AIAA/CEAS Aeroacoustics Conference," (2014), 2014-2909. (Cited on pages 57 and 59.)

[93] U. Tapken and L. Enghardt, "Optimisation of sensor arrays for radial mode analysis in flow ducts," AIAA paper (2006). (Cited on page 57.)

[94] Q. Leclère, A. Pereira, A. Finez, and P. Souchotte, "Indirect calibration of a large microphone array for in-duct acoustic measurements," Journal of Sound and Vibration **376**, 48–59 (2016). (Cited on pages 58 and 72.)

[95] F. Farassat, D. M. Nark, and R. H. Thomas, "The detection of radiated modes from ducted fan engines," in "7th AIAA/CEAS Aeroacoustics Conference, Maastricht, The Netherlands, 2001," (2001), 2138. (Cited on page 58.)

[96] E. Rademaker, P. Sijtsma, and B. Tester, "Mode detection with an optimised array in a model turbofan engine intake at varying shaft speeds," in "7th AIAA/CEAS Aeroacoustics Conference and Exhibit," (2001), p. 2181. (Cited on page 58.)

[97] L. Enghardt, L. Neuhaus, and C. Lowis, "Broadband sound power determination in flow ducts," in "10th AIAA/CEAS Aeroacoustics Conference," (American Institute of Aeronautics and Astronautics, 2004). AIAA 2004-2940. (Cited on page 58.)

[98] S. Lewy, "Inverse method predicting spinning modes radiated by a ducted fan from free-field measurements," The Journal of the Acoustical Society of America **117**, 744–750 (2005). (Cited on page 58.)

[99] F. O. Castres and P. F. Joseph, "Experimental investigation of an inversion technique for the determination of broadband duct mode amplitudes by the use of near-field sensor arrays," The Journal of the Acoustical Society of America **122**, 848–859 (2007). (Cited on page 58.)

[100] F. O. Castres and P. F. Joseph, "Mode detection in turbofan inlets from near field sensor arrays," The Journal of the Acoustical Society of America **121**, 796–807 (2007). (Cited on page 58.)

[101] G. J. Bennett, C. O'Reilly, U. Tapken, and J. Fitzpatrick, "Noise source location in turbomachinery using coherence based modal decomposition," in "Proceedings of the 15th AIAA/CEAS Aeroacoustics Conference, Miami, FL, USA," (2009), 3367. (Cited on page 58.)

[102] U. Tapken, T. Raitor, and L. Enghardt, "Tonal noise radiation from an UHBR fan - Optimized in-duct radial mode analysis," in "Proceedings of the 15th AIAA/CEAS Aeroacoustics Conference, Miami, FL, USA," (2009), 3288. (Cited on page 58.)

[103] F. O. Castres and P. F. Joseph, "Mode detection in turbofan inlets from near field sensor arrays," The Journal of the Acoustical Society of America **121**, 796–807 (2007). (Cited on page 58.)

[104] W. Schuster and T. R. Marotta, "Comparison of in-duct phased array measurements," in "25th AIAA/CEAS Aeroacoustics Conference," (2019), p. 2652. (Cited on page 58.)

[105] A. Pereira, J. Antoni, and Q. Leclere, "Empirical Bayesian regularization of the inverse acoustic problem," Applied Acoustics **97**, 11–29 (2015). (Cited on pages 59 and 87.)

[106] J. Y. Chung, "Rejection of flow noise using a coherence function method," The Journal of the Acoustical Society of America **62**, 388–395 (1977). (Cited on page 59.)

[107] J. Bultè, "Acoustic array measurements in aerodynamic wind tunnels: A subspace approach for noise suppression," in "13th AIAA/CEAS Aeroacoustics Conference, Rome, Italy," (2007). (Cited on page 59.)

[108] P. Druault, A. Hekmati, and D. Ricot, "Discrimination of acoustic and turbulent components from aeroacoustic wall pressure field," Journal of Sound and Vibration **332**, 7257 – 7278 (2013). (Cited on page 59.)

[109] E. Envia, "Fan noise reduction: an overview," International Journal of Aeroacoustics **1**, 43–64 (2002). (Cited on pages 60 and 195.)

[110] L. Enghardt, U. Tapken, W. Neise, P. Schimming, R. Maier, and J. Zillmann, "Active control of fan noise from high-bypass ratio aeroengines: Experimental results," The Aeronautical Journal **106**, 501–506 (2002). (Cited on pages 61 and 195.)

[111] B. Brouard, B. Castagnede, M. Henry, D. Lafarge, and S. Sahraoui, "Mesure des propriétés acoustiques des matériaux poreux," Techniques de l'ingénieur. Mesures et contrôle pp. R6120–1 (2003). (Cited on page 74.)

[112] U. W. Ganz, P. D. Joppa, T. J. Patten, and D. F. Scharpf, "Boeing 18-inch fan rig broadband noise test," (1998). (Cited on page 88.)

[113] C. Weckmüller, S. Guérin, and G. Ashcroft, "CFD/CAA coupling applied to DLR UHBR-fan: Comparison to experimantal data," in "15th AIAA/CEAS Aeroacoustics Conference (30th AIAA Aeroacoustics Conference)," (2009), p. 3342. (Cited on page 97.)

[114] C. Wagner, T. Hüttl, and P. Sagaut, *Large-Eddy Simulation for acoustics*, vol. 20 (Cambridge University Press, 2007). (Cited on page 106.)

[115] P. Sagaut, *Large Eddy Simulation for incompressible flows: an introduction* (Springer Science & Business Media, 2006). (Cited on page 106.)

[116] F. Menter, M. Kuntz, and R. Langtry, "Ten years of industrial experience with the SST turbulence model," Turbulence, heat and mass transfer **4**, 625–632 (2003). (Cited on page 109.)

[117] B. Etkin and H. S. Ribner, "Canadian research in aerodynamic noise," Tech. rep., University of Toronto (1958). (Cited on page 115.)

[118] P. Bearman, "On vortex shedding from a circular cylinder in the critical Reynolds number regime," Journal of Fluid Mechanics **37**, 577–585 (1969). (Cited on page 115.)

[119] E. Achenbach and E. Heinecke, "On vortex shedding from smooth and rough cylinders in the range of Reynolds numbers 6×10^3 to 5×10^6," Journal of fluid mechanics **109**, 239–251 (1981). (Cited on page 115.)

[120] G. Zambonini, "Unsteady dynamics of corner separation in a linear compressor cascade," Ph.D. thesis, Lyon (2016). (Cited on page 121.)

[121] W. Olsen and J. Wagner, "Effect of thickness on airfoil surface noise," AIAA Journal **20**, 437–439 (1982). (Cited on page 126.)

[122] S. A. Glegg and W. Devenport, "Unsteady loading on an airfoil of arbitrary thickness," Journal of Sound and Vibration **319**, 1252–1270 (2009). (Cited on page 126.)

[123] E. Reissner, "On the application of Mathieu functions in the theory of subsonic compressible flow past oscillating airfoils," (1951). (Cited on page 149.)

[124] M. Roger, "Contrôle du bruit aérodynamique des machines tournantes axiales par modulation de pales," Acta Acustica united with Acustica **80**, 247–259 (1994). (Cited on page 166.)

[125] F. Fournier, "Mise au point d'une méthode de calcul adaptée au bruit de fenestron d'hélicoptères," Ph.D. thesis, Ecully, Ecole centrale de Lyon (1988). (Cited on pages 182 and 188.)

A

List of publications

The list of written publications is provided in this appendix.

2017

- Sanjosé Marlène, **Pestana Miguel**, Moreau Stéphane & Roger Michel, Effect of Weak Outlet-Guide-Vane Heterogeneity on Rotor-Stator Tonal Noise, Journal: AIAA Journal Vol. 55, No. 10, pp. 3440-3457, 2017.
- **Pestana Miguel**, Pereira Antonio, Salze Edouard, Thisse Johan, Sanjosé Marlène, Jondeau Emmanuel, Souchotte Pascal, Roger Michel, Moreau Stéphane, Regnard Josselin & Gruber Mathieu, Aeroacoustics of an axial ducted low Mach-number stage: numerical and experimental investigation, 23rd AIAA/CEAS Aeroacoustics Conference, paper 2017-3215, Denver, USA.

2018

- **Pestana Miguel**, Sanjosé Marlène, Moreau Stéphane, Roger Michel & Gruber Mathieu, Investigation on the noise of an axial low Mach-number fan stage with a heterogeneous stator, Fan Noise 2018, paper 105, Darmstadt, DE.

2019

- **Pestana Miguel**, Sanjosé Marlène, Moreau Stéphane, Roger Michel & Gruber Mathieu, Assessment of the Impact of a Heterogeneous Stator on the Noise of an Axial-Flow Low Mach-Number Stage, 25th AIAA/CEAS Aeroacoustics Conference, paper 2019-2589, Delft, NL.

Active Noise Control Fan (ANCF) configuration

In this appendix, a supplementary investigation on the heterogeneity impact is shown on the Active Noise Control Fan (ANCF) from NASA. A numerical and analytical investigation is performed. The study is based on simulation done with the LBM solver PowerFLOW and from analytical developments implemented in the analytical prediction tool OPTIBRUI.

The article has been published in the AIAA journal in 2017.

AIAA Journal
Vol. 55, No. 10, October 2017

Effect of Weak Outlet-Guide-Vane Heterogeneity on Rotor–Stator Tonal Noise

Marlène Sanjosé* and Stéphane Moreau†
Université de Sherbrooke, Sherbrooke, Quebec J1K 2R1, Canada
and
Miguel Pestana‡ and Michel Roger§
École Centrale de Lyon, 69134 Écully, France

DOI: 10.2514/1.J055525

Four numerical simulations of the NASA Active Noise Control Fan rig with some modifications have been performed to investigate the influence of the heterogeneity of the stator row on the tonal noise radiation for a realistic turbofan with a high hub-to-tip ratio. These simulations achieved with the Powerflow solver based on the lattice Boltzmann method provide a direct acoustic prediction for both tonal and broadband noise. The numerical simulations are used to evaluate the noise contributions of the rotor-wake interaction with the stator vanes, and the rotor interaction with both the inlet distortion and the potential field generated by the stator row. Analytical models are evaluated on this configuration using the flow description provided by the simulations. Rotor-wake and inlet-distortion interaction noise generation with in-duct propagation uses the classical Amiet's response, whereas Parry's model is used for the rotor response to the potential field. The simulation is used to evaluate simple excitation models for the potential field and the rotor-wake evolutions. The analytical results for homogeneous and heterogeneous configurations compare well with the detailed acoustic modal powers extracted from the direct acoustic field simulated with Powerflow. The wake interaction remains the dominant source in the present heterogeneous configurations.

Nomenclature

$\mathcal{A}$	=	amplitude of g [see Eq. (9)]
a, b	=	ellipse parameters
a_m, b_m	=	interpolation parameters
B	=	number of rotor blades
$\mathcal{B}$	=	phase angle from duct to profile coordinates
b	=	blade/vane half-chord
C_R, C_S, C_{MS}	=	blade, vane, and modified vane chord, respectively
c_0	=	speed of sound
$d_{R/S}$	=	rotor–stator distance
E	=	Fresnel integral
E_{nj}	=	duct radial function
ES, Es	=	modified Fresnel functions
$\boldsymbol{e}_r$, $\boldsymbol{e}_\theta$, $\boldsymbol{e}_x$	=	cylindrical unit vectors
F_m	=	Fourier coefficient of the upwash velocity
F_T, F_D	=	axial and tangential lift components, respectively
$\boldsymbol{f}$	=	force exerted by the blade/vane surface S on the fluid
$f(M)$	=	function to account for the compressibility effects at high frequency in the Sear's response
G	=	annular duct Green's function
g	=	normalized pressure jump
J_n	=	Bessel function of the first kind of order n
j	=	radial order of the duct mode (n, j)
K	=	conformal mapping parameter
$\mathcal{K}$	=	convective wave number [see Eq. (9)]
k	=	vane summation index
k_c	=	complex aerodynamic wave number
k_d	=	damping coefficient
k_m	=	gust acoustic wave number
k_x, k_y	=	streamwise and normal aerodynamic wave number, respectively
k_0	=	acoustic wave number
l	=	unsteady lift function
M_a	=	mean duct axial Mach number
M	=	local Mach number
m	=	loading harmonic index
N_{nj}	=	coefficient of duct radial function
N_{nj}	=	amplitude in duct mode shape function
n	=	azimuthal order of the duct mode (n, j)
P	=	aerodynamic unsteady pressure
p	=	acoustic pressure
q	=	parameter of the conforming mapping
$\mathcal{R}_d(r, \theta, x)$	=	cylindrical reference frame (fixed to the duct)
R_H, R_T	=	hub and tip duct radius, respectively
S	=	radial cut perimeter
$\mathcal{S}$	=	Sears's function
$\mathcal{S}$	=	blade surface
s	=	blade-passing frequency index
T	=	time period
T_{bpp}	=	blade-passing period
T_q	=	conformal mapping
T_{nj}, D_{nj}	=	modal coefficients of loading components (axial and tangential, respectively)
t, τ	=	observer and emission time, respectively
U, U_c	=	freestream and convection speed, respectively
u_{pot}	=	upwash velocity
$\hat{u}_{\text{abs}}$	=	Fourier coefficient of absolute velocity
V	=	number of stator vanes
w_0	=	gust amplitude
w_m	=	aerodynamic gust of loading harmonic m
$\boldsymbol{x}$	=	(r, θ, x) observer position in $\mathcal{R}_d$ reference frame
$\boldsymbol{x}'$	=	(r', θ', x') source position in $\mathcal{R}_d$ reference frame
x_0	=	source plane localization
(x_c, y_c)	=	blade/vane Cartesian coordinate system
Y_n	=	Bessel function of the second kind of order n
z	=	complex number

Received 19 July 2016; revision received 14 March 2017; accepted for publication 4 April 2017; published online 27 June 2017.

*Researcher, Mechanical Engineering Department; marlene.sanjose@usherbrooke.ca.
†Professor, Mechanical Engineering Department. Lifetime Member AIAA.
‡Ph.D. Student, LMFA.
§Professor, LMFA.

β	=	compressibility parameter
β, β_a	=	compressibility parameters based on M and M_a, respectively
Γ_{nj}	=	duct radial function normalization factor
θ_i $(i = 1, 4)$	=	constants in radiation integrals
γ_{nj}	=	axial wave number
κ_{nj}	=	cutoff criterion
λ	=	wavelength
μ	=	frequency parameter
τ_{nj}	=	phase angle in duct mode shape function definition
ρ_0	=	fluid density
$\Phi[z]$	=	complex error function of argument z
φ_0	=	modified acoustic potential solution to the Helmholtz equation
χ_{nj}	=	duct eigenvalues
$\chi_R, \chi_S, \chi_{MS}$	=	blade, vane, and modified vane stagger angle
Ω	=	engine rotational speed, rad/s
ω	=	acoustic angular frequency
ω_m	=	gust angular frequency

Subscripts

n	=	azimuthal mode order
j	=	radial mode order

Superscripts

$\pm$	=	downstream and upstream propagation
$-$	=	made nondimensional by b
$\star$	=	Fourier conjugate
δ	=	relative to potential effect

I. Introduction

TO REDUCE pollutant emissions and fuel consumption, future turbofan architectures will have increased bypass ratio and reduced size of the nacelle. The advantage of such engines is to reach the necessary thrust at takeoff with a smaller fan rotational speed. In terms of acoustic emission, it is changing the relative contribution of noise sources; in particular, the interaction of the rotor wakes with the outlet guiding vanes (OGVs) becomes dominant especially because the fan OGV distance is reduced. Furthermore, structural components are included in the stator row, yielding a heterogeneity that generates stronger upstream distortions and induce additional noise sources on the fan itself. Noise prediction tools based on analytical models must be improved to account for these new challenges.

The present work addresses a simplified but representative configuration to isolate the effect of the heterogeneity of the OGV on tonal noise sources. It mostly focuses on the potential field distortion interacting with the rotor and compares it with the rotor–stator wake interaction that has been more intensively studied by de Laborderie et al. [1–3], Holewa et al. [4], and more recently Bonneau et al. [5] and Daroukh et al. [6], for instance. Compared with the last three studies, the present heterogeneity does not involve massive bifurcations that create strong flow modifications in the blades passages so that the various noise sources could be more easily separated. The baseline configuration of the NASA Active Noise Control Fan (ANCF) test rig is used as a reference case typical of a low-speed high-bypass-ratio turbofan. The ANCF has been intensively studied at the Aeroacoustic Propulsion Laboratory facility at NASA Glenn Research Center. Measurements have been performed on various stage configurations and flow conditions, yielding a large aerodynamic and acoustic database [7–9]. Therefore, this low hub-to-tip ratio axial fan stage provides an excellent test bed for aeroacoustic code validation of ducted turbomachines with significant modal content. Moreover, the relatively low Mach number of the ANCF allows comparing various numerical approaches, solving either the Navier–Stokes equations [10] or the Boltzmann equations for the gas dynamics. Detailed three-dimensional (3-D) turbulent compressible unsteady simulations have been recently performed on two configurations of this fan stage using a lattice Boltzmann method (LBM) particularly adapted to low Mach numbers [11–13]. These simulations including the full geometry of the installation were shown to accurately reproduce the acoustic measurements made in the anechoic facility. They complement the experimental database by possibly providing a direct insight into the aerodynamic sources (mainly the rotor wakes impinging on the stator) in addition to the in-duct and far-field direct acoustic propagation.

From the baseline LBM simulation with a homogeneous stator row, a heterogeneous configuration is built by enlarging a single stator vane, keeping the profile definition and blade stacking identical. For the same operating condition, the heterogeneous configuration allows isolating the influence of the potential effect of the stator row limiting the strong modification of flow structure in the machine. This case is intensively used to calibrate and validate analytical methods used for the noise predictions of realistic turbofans.

The numerical setups of the homogeneous and heterogeneous configurations are described in Sec. II. The aeroacoustic models for tonal noise are described in Sec. III. The analytical and numerical excitation models as well as the unsteady blade loading are studied in Sec. IV, and the acoustic predictions based on analytical and numerical approaches are compared in Sec. V.

II. Numerical Simulation of a Simplified Heterogeneous Configuration

The present simulations use the Powerflow solver 5.0a based on the lattice Boltzmann method (LBM). The approach is naturally transient and compressible, providing a direct insight into hydrodynamic mechanisms responsible for the acoustic emission but also into acoustic propagation in the nacelle and outside in the free field.

Instead of studying macroscopic fluid quantities, the LBM tracks the time and space evolution on a lattice grid of a truncated particle distribution function. The particle distribution evolution is driven to the equilibrium by the so-called collision operator, approximated by the Bhatnagar–Gross–Krook model. The discrete lattice Boltzmann equations need to be solved for a finite number of particle velocities. The discretization retained in Powerflow involves 19 discrete velocities for the third-order truncation of the particle distribution function, which has been shown sufficient to recover the Navier–Stokes equations for a perfect gas at low Mach number in isothermal conditions [14–16]. In Powerflow, a single relaxation time is used, which is related to the dimensionless laminar kinematic viscosity [17]. This relaxation time is replaced by an effective turbulent relaxation time that is derived from a systematic renormalization group procedure detailed in Chen et al. [18]. It captures the large structures in the anechoic room (included in the computational domain) but also the small turbulent scales that develop along the blade and duct surfaces where wall-law boundary conditions accounting for pressure gradients are applied using specular reflections [19]. The particular extension of the method developed for rotating machines can be found in Zhang et al. [20].

With this method, the flowfield is computed on the full test rig of the Aero-Acoustic Propulsion Laboratory at NASA Glenn Research Center [7–9]. Only the rotor driving system and the measurement system are not considered in the setup. A detail of the ducted fan is shown in Fig. 1. The actual laboratory is also replaced by a very large anechoic room of dimensions $132 \times 113 \times 113$ m to mimic the actual experimental setup and to include damping zones around it. The present full setup is similar to the one used in previous studies [11,12]. The configuration includes the 1.22-m-diam duct with the precise geometry for the bell mouth and the hub. The study focuses on the nominal fan conditions; the fan has $B = 16$ blades and is rotating at 1800 rpm. The tip clearance of 0.05% fan diameter is ignored by extruding the blades to the duct. The finest grid resolution around the rotor and stator is 0.1% fan diameter and 0.2% fan diameter in the interstage space. The refinement is not sufficient to capture all turbulent scales, as shown in a previous study [13], but it is sufficient

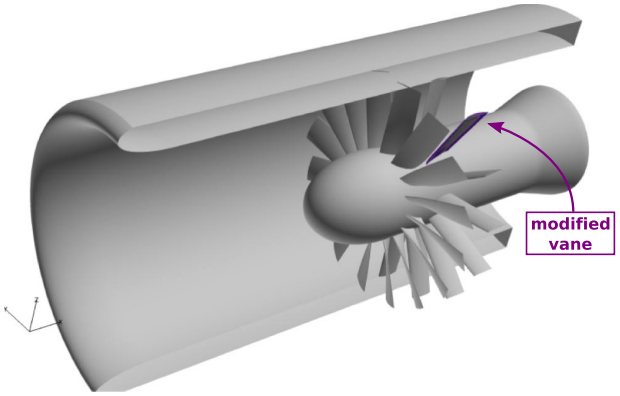

Fig. 1 Simulated geometry with half the nacelle hidden for visualization purpose. The modified vane is highlighted in purple.

to capture the deterministic interactions between the rotor and the stator and to propagate acoustic waves within the nacelle up to the third blade-passing frequency (BPF) harmonic thanks to the very low-dissipation properties of the LBM numerical method. With this model, converged results are obtained within three weeks using 288 processors allowing some parametric studies at a reasonable cost. In the present work, two stator configurations have been investigated to isolate the effect of the stator heterogeneity. The rotor–stator distance $d_{R/S} = 0.5C_R$ is measured at the hub and given in terms of rotor chord C_R. Two OGV configurations are investigated with a vane count of $V = 14$ or 26 respectively. The comparison of the two setups allows investigating the heterogeneity impact on the first blade-passing frequency, which is cut on in the homogeneous configuration with $V = 14$ vanes and cut off in the homogeneous configuration with $V = 26$ vanes. In the homogeneous configuration, all vanes are identical, whereas in the heterogeneous configuration, one single vane is scaled up by a factor 1.5, keeping the leading-edge aligned with all other vanes. For the four simulations, the same mesh refinement zones are used based on the work of Mann et al. [11]. The simulation time step is 2.44×10^{-6} s. A transient time of 10 fan rotations is observed for all configurations; then, volume measurements are recorded in a volume around the rotor–stator stage 26 times per blade-passing period $T_{\text{bpp}} = 2\pi/B\Omega$, yielding a sampling frequency of 12,480 Hz. Additional axial extraction planes are recorded upstream of the rotor row, in the middle of the rotor–stator interstage, and downstream of the OGV with a smaller sampling period of $T_{\text{bpp}}/123$ corresponding to a sampling frequency of 59,040 Hz to extract the upstream distortion, the velocity deficit in the rotor wakes, and the acoustic power in the duct.

III. Aeroacoustic Analytical Models

The rotor/stator is mounted in an infinite annular duct of constant section. The cylindrical reference frame $\mathcal{R}_d(r, \theta, x)$ is fixed to the duct with its axial direction corresponding to the machine axis oriented toward the exhaust of the duct.

For the implementation of analytical models, the true blades and vanes are simplified to flat plates extruded over the radial direction. The blades and vanes are divided into 19 strip elements on which neither sweep nor lean are considered, and the chord C and stagger angle χ defined from the machine axis are assumed constant over the strip heights. This so-called strip theory allows to capture the main variations of geometry and flow parameters over the duct section. The parameters extracted from the ANCF geometry at midspan are given in Table 1.

For the acoustic propagation, with the rotational speed of the machine being low, the swirl effects are ignored [21]. Only an inviscid mean axial flow of Mach number M_a is considered. Within these assumptions, Goldstein's analogy [22] provides the acoustic pressure in the duct resulting from the force $\boldsymbol{f}$ exerted by the blade surface S on the fluid using the annular duct Green's function G, the expression of which is provided in the frequency domain in Appendix A:

$$p(\boldsymbol{x}, t) = \int_{-T}^{T} \iint_{S(\tau)} \frac{\partial G(\boldsymbol{x}, t|\boldsymbol{x}', \tau)}{\partial x_i'} f_i(\boldsymbol{x}', \tau)\, \mathrm{d}S(\boldsymbol{x}')\, \mathrm{d}\tau \qquad (1)$$

where T is a large but finite time period sufficient to capture all the aerodynamic effects on the sound; τ and t are the emission and reception times; and $\boldsymbol{x}'$ and $\boldsymbol{x}$ are the source and observer positions, respectively, in the duct coordinate system.

Neglecting the radial component of the force, the latter can be decomposed as a thrust (axial) component and a drag (tangential) component, $\boldsymbol{f} = F_D \boldsymbol{e}_\theta + F_T \boldsymbol{e}_x$, that are related to the unsteady lift l: $F_D = \text{sign}(\chi) l(x_c) \cos(\chi)$ and $F_T = \text{sign}(\chi) l(x_c) \sin(\chi)$, with the force on the blade pointing toward the suction side. Because of the low counts of rotor blades and stator vanes, an isolated airfoil response model is used to compute the pressure jump.

A. Homogeneous Rotor Row

For the rotor with B identical blades experiencing a periodic excitation over a revolution, the acoustic pressure due to the potential distortion can be expressed at a given harmonic of the blade-passing frequency ($\omega = sB\Omega$) as

$$p_{sB}(\boldsymbol{x}) = \frac{B}{2} \sum_{n=-\infty}^{+\infty} \sum_{j=1}^{+\infty} \frac{E_{nj}(r)}{\Gamma_{nj}\kappa_{nj}} \mathrm{e}^{i(n\theta - \gamma_{nj}^{\pm} x)} \times (nD_{nj}^{\pm} - \gamma_{nj}^{\pm} T_{nj}^{\pm}) \qquad (2)$$

with the modal coefficients $D_{nj}^{\pm}$ and $T_{nj}^{\pm}$ defined as the integration of the lift weighted by a noncompactness phase shift over the blade surface. After a change of variable to make the abscissa dimensionless with the half-chord $\bar{x}_c = x_c/b$ and neglecting phase angles (that do not contribute to the acoustic power in the present single-strip approximation), $D_{nj}^{\pm}$ and $T_{nj}^{\pm}$ can be written as

$$\begin{aligned} D_{nj}^{\pm} &= (R_T - R_H) E_{nj}(r') \frac{b}{r} \int_{-1}^{1} \mathrm{e}^{-i\mathcal{B}\bar{x}_c} l(\bar{x}_c) \sin(\chi)\, \mathrm{d}\bar{x}_c \\ T_{nj}^{\pm} &= (R_T - R_H) E_{nj}(r') \frac{b}{r} \int_{-1}^{1} \mathrm{e}^{-i\mathcal{B}\bar{x}_c} l(\bar{x}_c) \cos(\chi)\, \mathrm{d}\bar{x}_c \end{aligned} \qquad (3)$$

where the phase angle $\mathcal{B} = b(\gamma_{nj}^{\pm} \cos\chi - (n/r') \sin\chi)$ comes from the wave number expressed in the blade Cartesian coordinates.

By integrating the expression of the acoustic intensity originally proposed by Cantrell and Hart over the duct section, the upstream and downstream acoustic powers are written as

$$\Pi^{\pm} = \frac{\pi \rho_a^4 B^2}{2\Gamma_{nj}\rho_0 c_0} \sum_{s=1}^{\infty} \sum_{n=-\infty}^{+\infty} \sum_{j=0}^{\infty} \frac{sB\Omega |nD_{nj}^{\pm} - \gamma_{nj}^{\pm} T_{nj}^{\pm}|^2}{\kappa_{nj}(sB\Omega/c_0 \pm \kappa_{nj} M_a)^2} \qquad (4)$$

with $\beta_a = \sqrt{1 - M_a^2}$ [22–24].

Table 1 Geometrical parameters of the rotor–stator stage

Row	Blade/vane number	Chord, cm	Stagger angle, deg	Solidity (chord/blade gap)
Rotor	$B = 16$	$C_R = 13.4$	$\chi_R = -53.7$	0.86
Stator	$V = 14$ or 26	$C_S = 11.5$	$\chi_R = 9.9$	0.65 or 1.20
Modified vane	— —	$C_{\text{MS}} = 17.3$	$\chi_{\text{MS}} = 9.6$	— —

B. Heterogeneous Stator Row

For the stator, each vane is submitted to a periodic excitation from the rotor wakes. The pressure from the rotor–stator interaction can be expressed at the harmonic of the blade-passing frequency $sB\Omega$ as a sum over all stator vanes:

$$p_{sB}(\boldsymbol{x}) = \frac{1}{2}\sum_{n=-\infty}^{+\infty}\sum_{j=1}^{+\infty}\frac{E_{nj}(r)}{\Gamma_{nj}\kappa_{nj}}\mathrm{e}^{i(n\theta-\gamma_{nj}^{\pm}x)} \times \sum_{k=0}^{V-1}\mathrm{e}^{ik(sB-n)(2\pi/V)}(nD_{nj,k}^{\pm}-\gamma_{nj}^{\pm}T_{nj,k}^{\pm}) \tag{5}$$

where the double sum is limited to the acoustic duct modes (n, j) excited by the rotor–stator interaction following the extended Tyler and Sofrin's rule [5,25,26]:

$$\mathrm{sign}(\Omega)sB - n = m \quad \text{with: } m \in \mathbb{Z} \tag{6}$$

with the same expression for $D_{nj,k}^{\pm}$ and $T_{nj,k}^{\pm}$ as in Eq. (3), accounting for the specific half-chord b_k and stagger angle χ_k of each vane.

In the previous expressions, the remaining terms to be calculated are the loadings of the blades/vanes, detailed in the next sections.

C. Amiet's Blade/Vane Response

The lift response function for an airfoil in rectilinear motion to a harmonic gust at the angular frequency $\omega_m = m\Omega$, with m the loading harmonic index defined by

$$w_m = w_0\mathrm{e}^{i(k_x x_c + k_y y_c - \omega_m t)} \tag{7}$$

is given as the conjugate of the expression provided by Amiet [27], accounting only for gusts parallel to the leading edge:

$$l(\overline{x}_c) = 2\pi\rho_0 U w_0 g^{\star}(\overline{x}_c, \overline{k}_x, 0, M) \tag{8}$$

where $g^{\star}$ is the normalized pressure jump given in Appendix B ($\star$ denotes the conjugate required because of a different convention in the Fourier transform). U_c is the convection velocity of the gust assumed to be equal to the freestream velocity U in the reference frame of the blade; $\overline{k}_x = \omega_m b/U$ the dimensionless axial wave number; $\overline{\mu} = bk_m/\beta^2$, where $k_m = \omega_m/c_0$ is the acoustic wave number of the gust; and M is the local Mach number seen by the airfoil. The overbar defines a variable made dimensionless by the half-chord.

This model is applied for rotor-wake interaction on the homogeneous and heterogeneous stator rows under the assumption that the cascade effect is negligible.

D. Parry's Blade Response

The response of a blade due to a potential perturbation from downstream is modeled in this section. In the case of small enough rotor–stator spacings, the potential field in the upstream vicinity of stator vanes is seen as a downstream distortion by the rotor blades. This interaction cannot be modeled by the classical Amiet's theory because it represents a contamination at the trailing edge instead of at the leading edge. Moreover, the amplitude of the velocity perturbation decreases going upstream, as opposed to a classical unsteady-aerodynamics approach, where a frozen disturbance is convected downstream by the flow. Previous studies [28] have modeled this interaction noise by a reversed Amiet's resolution formulated on the potential ignoring the Kutta condition. The modeling is readdressed here with the approach presented in Parry's dissertation [29]. A boundary-value problem is formulated on the pressure imposing the Kutta condition and considering a complex hydrodynamic wave number to reproduce the potential decrease. The Kutta condition imposes a zero pressure jump at the trailing edge. The velocity upwash seen by the rotor blades is described using the same convention as previously defined in Eq. (7).

The axial wave number is now defined as $k_c = k_x + ik_d$. k_x is the classic hydrodynamic wave number of the gust, and k_d corresponds to a damping factor. The velocity potential associated with the blade response satisfies a convected wave equation that is solved analytically on an infinite flat plate on which the rigidity condition is imposed. Parry [29] uses a Wiener–Hopf technique to solve the convected Helmholtz equation with boundary conditions. When the Kutta condition is not imposed, the pressure jump is singular at the trailing edge. Parry removes the singularity by means of a vortex sheet. Here, the Kutta condition is intrinsic to the formulated problem. An equivalent approach is adopted by solving the previous system with Schwarzschild's technique [30,31]. When applied to finite-chord airfoils, this method is based on the iterative solving of half-plane problems, considering alternatively semi-infinite flat plates extending upstream or downstream from the trailing edge or the leading edge.

The first approximation is solved in two subiterations with subscripts 0 and 1. The first one consists of applying the rigidity condition to an artificial infinite flat plate. The solution $\varphi_0(\overline{x}_c, 0)$ of this first subiteration can then be related to the pressure by

$$P_0 = -\rho_0 U w_0 \mathcal{A}\mathrm{e}^{i\overline{k}_c(\overline{x}_c-1)} \quad \text{with } \mathcal{A} = \frac{i\overline{k}_d}{\beta\sqrt{\overline{\mu}^2-\overline{\mathcal{K}}^2}} \tag{9}$$

where $\overline{\mathcal{K}} = \overline{k}_c + M\overline{k}_m/\beta^2$.

Then, a new Amiet–Schwarzschild boundary-value problem is formulated on the additional pressure P_1 that is needed to satisfy the Kutta condition for the total pressure written $P = P_0 + P_1$. The solution for the additional pressure is then given by

$$P_1(x,0) = \rho_0 U w_0 \mathcal{A}\mathrm{e}^{i\overline{k}_c(\overline{x}_c-1)}\left[1-\Phi\left[\sqrt{i(\overline{\mu}+\overline{\mathcal{K}})(\overline{x}_c-1)}\right]\right] \tag{10}$$

where Φ is the complex error function for complex arguments [32].

For the case of a flat plate, oscillations at the trailing-edge are considered to be in phase opposition, which allows to express the unsteady lift as two times the pressure $l = 2P$. This leads to the final unsteady load expressed in terms of the dimensionless coordinate $\overline{x}_c$:

$$\begin{aligned} l^{\Delta}(\overline{x}_c, 0) &= 2P(\overline{x}_c, 0) = 2[P_0(\overline{x}_c, 0) + P_1(\overline{x}_c, 0)] \\ &= 2\rho_0 U w_0 g^{\Delta}(\overline{x}_c, \overline{k}_c, 0, M) \end{aligned} \tag{11}$$

with

$$g^{\Delta}(\overline{x}_c, \overline{k}_c, 0, M) = -\mathcal{A}\mathrm{e}^{i\overline{k}_c(\overline{x}_c-1)}\Phi\left[\sqrt{i(\overline{\mu}+\overline{\mathcal{K}})(\overline{x}_c-1)}\right] \tag{12}$$

In Fig. 2, the pressure jump according to the reversed Sears's theory [28] is compared with the present formulation that accounts for the Kutta condition. The additional singular term present when the Kutta condition is not applied is responsible for an increase in the pressure jump over the whole chord length and for the singularity at the trailing edge. Otherwise, when the Kutta condition is applied, the pressure jump is correctly canceled at the trailing edge, and the present formulation exactly fits with Parry's Wiener–Hopf derivation. In both models, as expected for this kind of interaction,

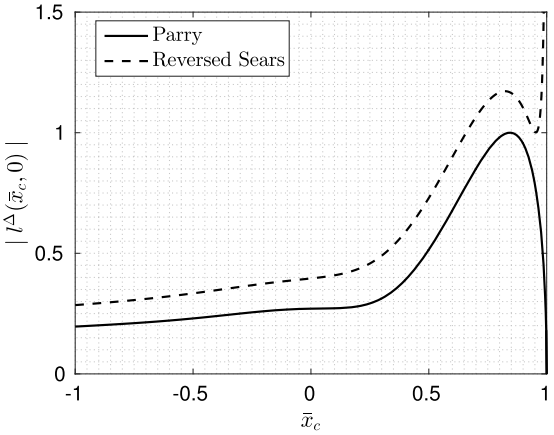

Fig. 2 Typical chordwise distribution of the unsteady pressure jump amplitude according to analytical models.

the unsteady loading concentrates in the trailing-edge region and strongly decreases in the upstream direction.

This iteration is a good approximation at high frequencies for which the source is not compact, $2b \gg \lambda$ (where λ is the wavelength). To extend the model, a further leading-edge correction (second Amiet–Schwarzschild iteration) should be carried out. This is not addressed in the present work.

The pressure jump is finally introduced in the radiation integral in Eq. (3). After some derivations, the chordwise integral is found as

$$\begin{aligned}\mathcal{L}^{\Delta} \equiv &= \int_{-1}^{1} \mathrm{e}^{-i\mathcal{B}\overline{x}_c} l^{\Delta}(\overline{x}_c)\,\mathrm{d}\overline{x}_c \\ &= -2\rho_0 U w_0 \mathcal{A} \frac{(1+i)\mathrm{e}^{-i\mathcal{B}}}{\Theta_3}\left\{ i\mathrm{e}^{-2i\Theta_3} E^{\star}[-2i\Theta_4] \right. \\ &\left. - i\sqrt{\frac{\Theta_4}{\Theta_4-\Theta_3}} E^{\star}[-2(\Theta_4-\Theta_3)] \right\} \end{aligned} \tag{13}$$

where $\Theta_3 = \overline{k}_c - \mathcal{B}$, and $\Theta_4 = (\overline{\mu} + \overline{\mathcal{K}})$. The parameters w_0 and k_d of the gust are investigated in the next section.

This model adapted for trailing-edge interactions is formulated in a way similar to Amiet's airfoil response and under the assumption of a negligible cascade effect. This effect could be added in a future work following the methodology developed for the trailing-edge noise [33]. In the case of rotor excitation by nonidentical stator vanes, the heterogeneity is introduced in the expression of the gust through the value of w_0.

All the models presented in this section are available in the analytical noise prediction code OPTIBRUI developed in the framework of an industrial consortium.

IV. Excitation Models

A. Analytical Models for the Potential Field

The modeling of the potential field can be achieved with the classical potential theory or by extracting computational fluid dynamics (CFD) data.

Potential inviscid theories for two-dimensional flows are investigated here. Using a conformal mapping, the uniform flow around a cylinder in rotation can be transformed into the flow around an isolated airfoil. The mapping reads

$$T_q : z \mapsto z + \frac{q^2}{z} \tag{14}$$

In the present section, three conformal mappings T_q are investigated that transform the cylinder into a flat plate, an ellipse, and a thin Joukowski profile. The parameter q of the conformal mapping and the origin of the complex plane are related to the vane chord, thickness, and camber at each radius [29,34]. The uniform velocity and angle of attack of the flow on the vane are extracted from the numerical simulations in the rotor–stator interstage at each radius. The Kutta condition is ensured by the value of the circulation around the cylinder.

The velocity field for an isolated profile is then duplicated for each vane with a spacing $s = 2\pi r/V$, interpolated on the same grid, and then summed. Compared with the proposed transformation in Appendix 6 of Parry's thesis [29], the present potential field does not include compressibility effects that are presumably negligible in the present configuration.

The velocity of the duplicated potential field is projected along the rotor normal direction $\overline{y}_c$, shown in Fig. 3. (x, y) is a fixed frame of reference with the axial origin placed at the rotor trailing edge and where the origin in y is arbitrary. $(\overline{x}_c, \overline{y}_c)$ is a frame of reference attached to the blade. This upwash velocity u_{pot} is then Fourier transformed in the azimuthal direction $y = r\theta$ in Fig. 3, yielding the excitation seen by the rotor blades at multiples of the rotational frequency:

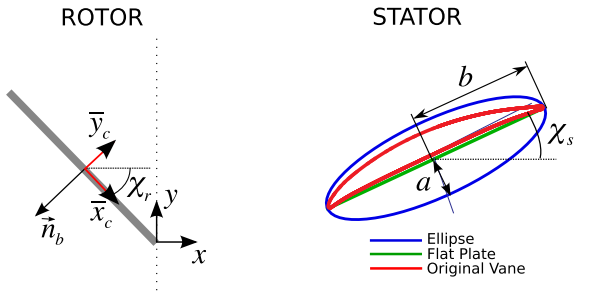

Fig. 3 Geometrical parameters for the computation of the potential effect of the stator.

$$\begin{aligned} w(x,y) &= \sum_{m=-\infty}^{+\infty} F_m(x)\mathrm{e}^{imy(2\pi/S)} \\ \text{with } F_m(x) &= \frac{1}{S}\int_0^S u_{\mathrm{pot}}(x,y)\mathrm{e}^{-imy(2\pi/S)}\,\mathrm{d}y \end{aligned} \tag{15}$$

where $S = 2\pi r$. In general, the Fourier coefficients do not have closed-form expressions and cannot be analytically integrated. For that goal, their decay in the upstream direction is fitted with an exponential axial evolution:

$$w(x,y) = \sum_{m=-\infty}^{+\infty} a_m \mathrm{e}^{b_m x}\mathrm{e}^{imy(2\pi/S)} \tag{16}$$

where a_m and b_m are computed by interpolation for each harmonic order m. This is consistent with the model for potential flow disturbance proposed by Parker [35,36]. Further on, the CFD database will allow analyzing the evolution of the potential upwash velocity and verifying the amplitude and exponential evolution of the coefficients from the three potential theories. Finally, the upwash expression is expressed in a reference frame attached to the rotor blade of coordinates

$$\begin{cases} x = b(\overline{x}_c - 1)\cos\chi_R - \overline{y}_c \sin\chi_R \\ y = b(\overline{x}_c - 1)\sin\chi_R + \overline{y}_c \cos\chi_R \end{cases} \tag{17}$$

A single Fourier component of the upwash gust at $(\overline{x}_c, \overline{y}_c = 0)$ is written

$$\begin{aligned} w_m(\overline{x}_c, 0) &= a_m \mathrm{e}^{i(my(2\pi/S)\sin\chi_R - ib_m\cos\chi_R)b(\overline{x}_c-1)} \\ &= a_m \mathrm{e}^{i(k_x - ib_m\cos\chi_R)b(\overline{x}_c-1)} \\ &= w_0 \mathrm{e}^{i\overline{k}_c(\overline{x}_c-1)} \end{aligned} \tag{18}$$

The parameters of the gust are found by identification: $w_0 = a_m$ and $\overline{k}_c = \overline{k}_x - ib_m\cos\chi_R b$, which leads to a damping factor $\overline{k}_d = -b_m\cos\chi_R b$. Those parameters define the velocity disturbance introduced in Parry's airfoil response model. The Fourier decomposition of the upwash done in this section will be also used with potential fields extracted from CFD simulations in Sec. IV.C for comparison.

B. Identification of the Excitations in the Numerical Simulations

The flow rates for the four simulated configurations are given in Table 2. The difference between the two stator vane numbers is lower than 1%, and the difference between the homogeneous and heterogeneous configurations is almost not noticeable.

This means that the modification of a single vane does not really affect the flow globally. The instantaneous static pressure and axial velocity flowfields on two unwrapped cuts of constant radius are shown in Figs. 4 and 5 for the four simulations. In Fig. 4, the velocity distributions around the rotor blades and the wake deficits at 50% of duct height are not noticeably modified. For the configuration with $V = 14$ vanes, a flow separation is seen at 80% of duct height on the stator suction sides in Fig. 5a. This flow separation is suppressed in the modified vane passage and the preceding one in Fig. 5b. With the solidity being higher in the $V = 26$ configuration, the cascade effect reduces the corner recirculation that cannot be seen anymore at 80% of duct height in Figs. 5c and 5d. Still, the pressure fields shown on the upper part of each field map are noticeably affected by the thickened vane mainly around the stator rows. In the homogeneous

Table 2 Flow rates in the rotor–stator interstage as deduced from the four Powerflow calculations

Configuration	$V = 14$, homogeneous	$V = 14$, heterogeneous	$V = 26$, homogeneous	$V = 26$, heterogeneous
Flow rate, kg/s	54.27	54.27	54.19	54.17

configuration with 14 stator vanes, the pressure patterns around the stator vanes are quite regular at midsection in Fig. 4a. In its heterogeneous version, the pressure patterns from the thickened vane contaminate the neighboring vanes, as shown in Fig. 4b. This is less clear at 80% of duct height because the unsteady detachment on the suction sides modifies the pressure distribution (Figs. 5a and 5b).

In the configuration with 26 stator vanes, the pressure patterns around the stator vanes are also quite regular, but they are affecting each other. A similar pattern with wider spreading is also clearly visible in the heterogeneous configuration in Fig. 4d. Concerning the pressure contours around the rotor blades, no obvious modification by the heterogeneity or the cascade effect could be identified by inspection of Figs. 4 and 5. The setup is thus a relevant test case to isolate the heterogeneity effect on the deterministic rotor–stator interactions at identical flow parameters.

From the result files saved periodically on a volume including the rotor and the stator, the pressure and the absolute velocity are interpolated on a cylindrical regular mesh at several radial locations using the postprocessing python API Antares [37]. The interpolated fields can then be averaged in the rotor or stator reference frame to identify the deterministic excitation of a row by the other one. The phase-locked averages in the rotor and stator reference frames over two full rotor revolutions for the heterogeneous configuration with $V = 14$ are shown in Figs. 6a and 6b, respectively. The cut is performed at midsection of the duct to avoid the contamination by the secondary flows; corner vortices are indeed formed at both vane hub and tip, as already shown by Sanjose et al. [13] (Fig. 4) and Guedeney and Moreau [38] (Figs. 5–8). The analysis is then reduced to two dimensions by unwrapping the cut and neglecting the radial velocity component that is less than 5% of the absolute velocity. Finally, the velocity field is projected on the normal direction to the considered blade and expanded in a Fourier series as explained in Sec. IV.A.

C. Potential Interaction

A comparison between the potential distortion fields predicted by the analytical models and the numerical results is presented in Figs. 7 and 8 for the two heterogeneous stator configurations. Arbitrary levels of the Fourier coefficients F_m are plotted for different harmonic orders m and axial positions between the rotor trailing edge and the stator leading edge.

The first two multiples of the number of vanes V dominate the spectra by 20 dB. However, all orders will contribute to the rotor unsteady lift as shown in Sec. III.A. This results from the modification of one vane, thus breaking the periodicity on the number of stator vanes V. The global surface shape of these excitation spectra is similar in the analytical models and the numerical extraction. For the homogeneous case, not plotted here, the analytical models would only predict tones at the multiples of the number of vanes. For all cases, the 3-D surface

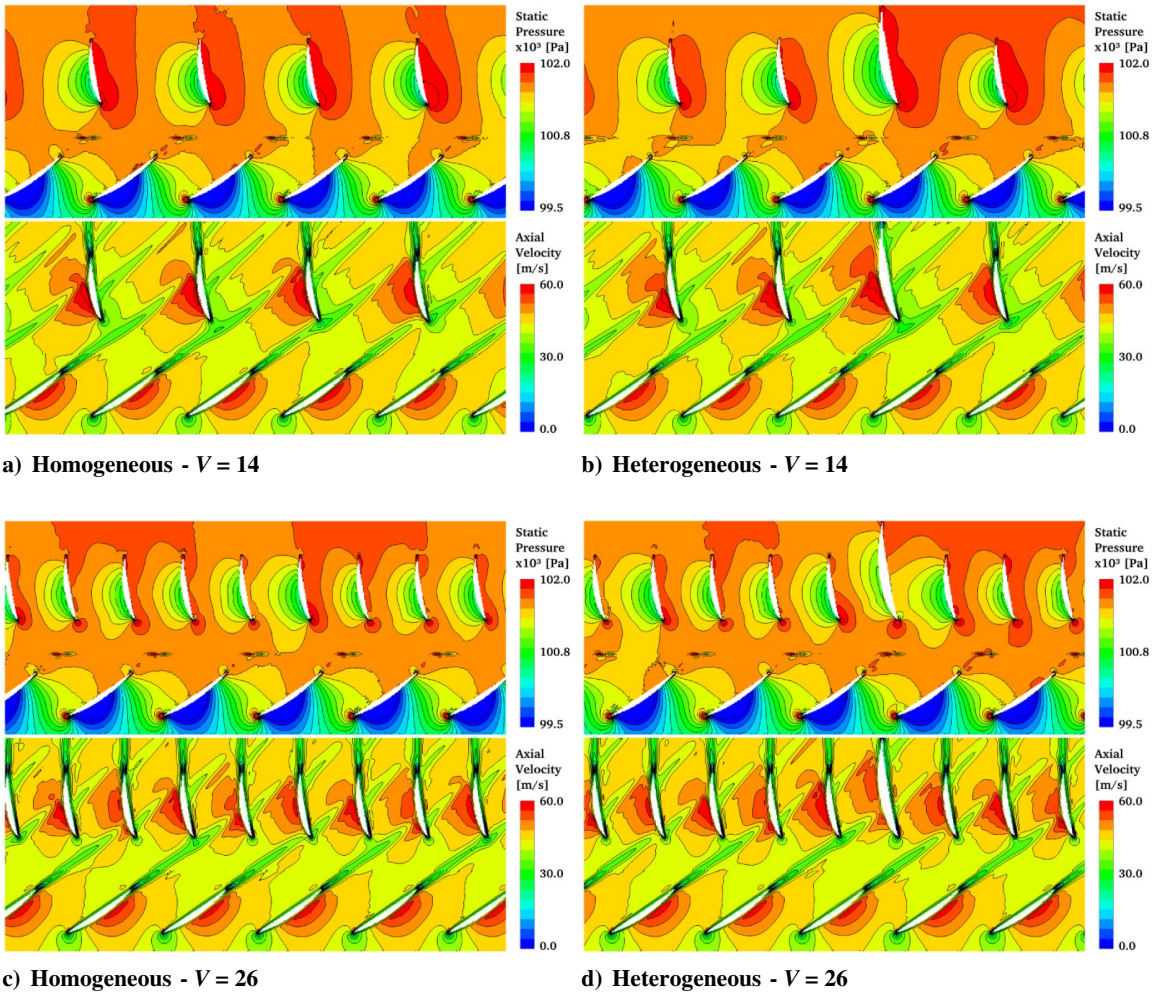

a) Homogeneous - $V = 14$ b) Heterogeneous - $V = 14$

c) Homogeneous - $V = 26$ d) Heterogeneous - $V = 26$

Fig. 4 Instantaneous flowfield in the rotor–stator interstage at 50% of the section height. Static pressure in the upper maps and axial velocity in the lower maps.

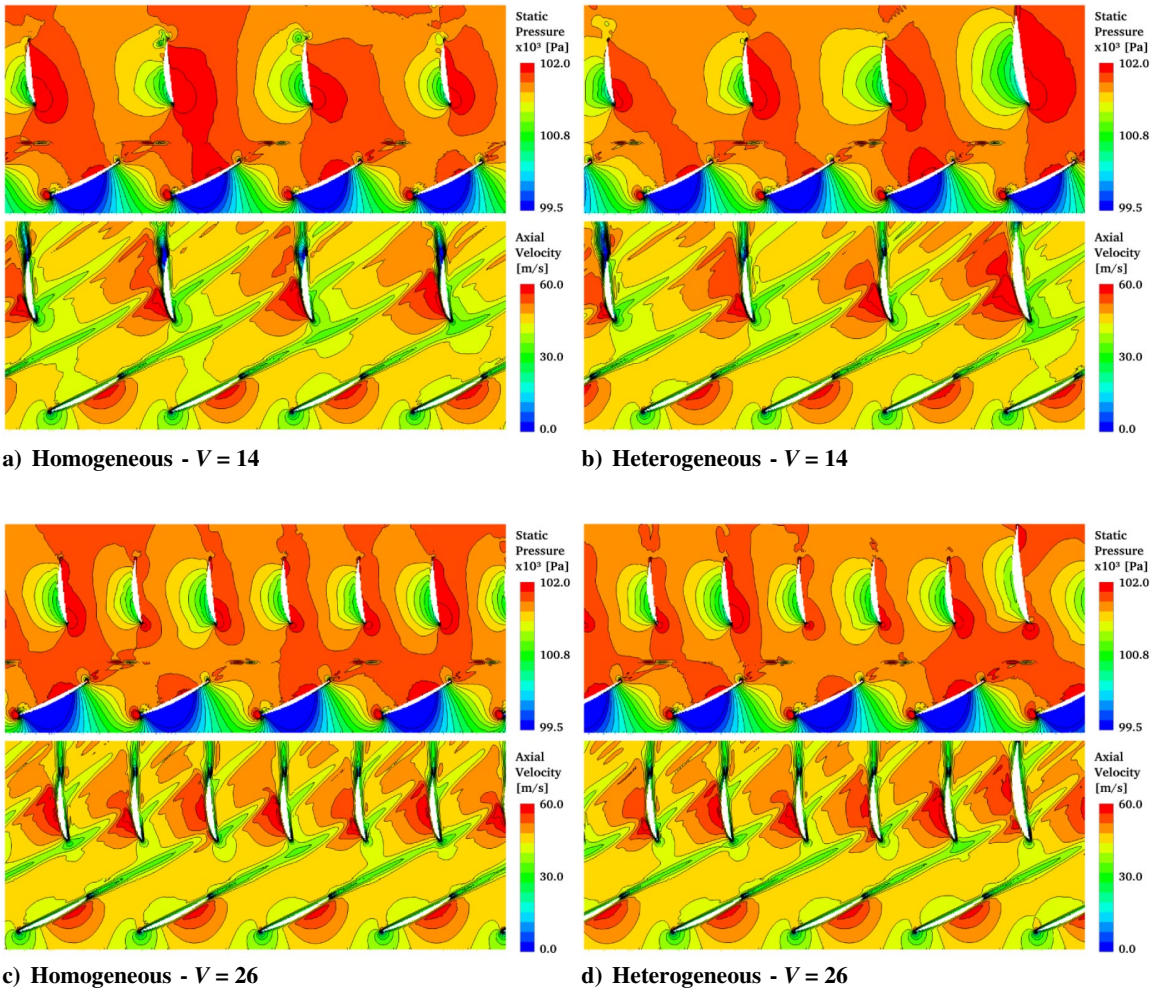

a) Homogeneous - $V = 14$ b) Heterogeneous - $V = 14$

c) Homogeneous - $V = 26$ d) Heterogeneous - $V = 26$

Fig. 5 Instantaneous flowfield in the rotor–stator interstage at 80% of the section height. Static pressure in the upper maps and axial velocity in the lower maps.

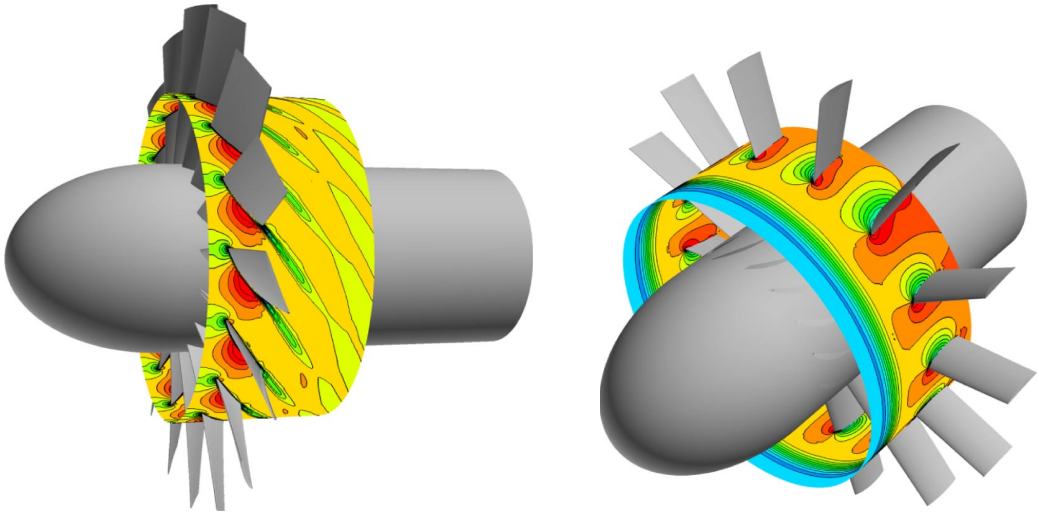

a) Absolute axial velocity field in the rotor reference frame b) Pressure field in the stator reference frame

Fig. 6 Phase-locked averages at midsection of the duct for the heterogeneous configuration with $V = 14$.

suggests a nearly exponential decrease with the upstream distance from the stator leading edge. In the numerical extraction, the levels always exceed a background level around −35 dB. This is a numerical artifact from the interpolations and the time convergence of the average. The same behavior is observed in the two stator configurations, with the main harmonic order changing from 14 to 26 due to the different number of vanes. However, Fig. 8c features an additional peak at the harmonic order 38 when approaching the rotor trailing edge

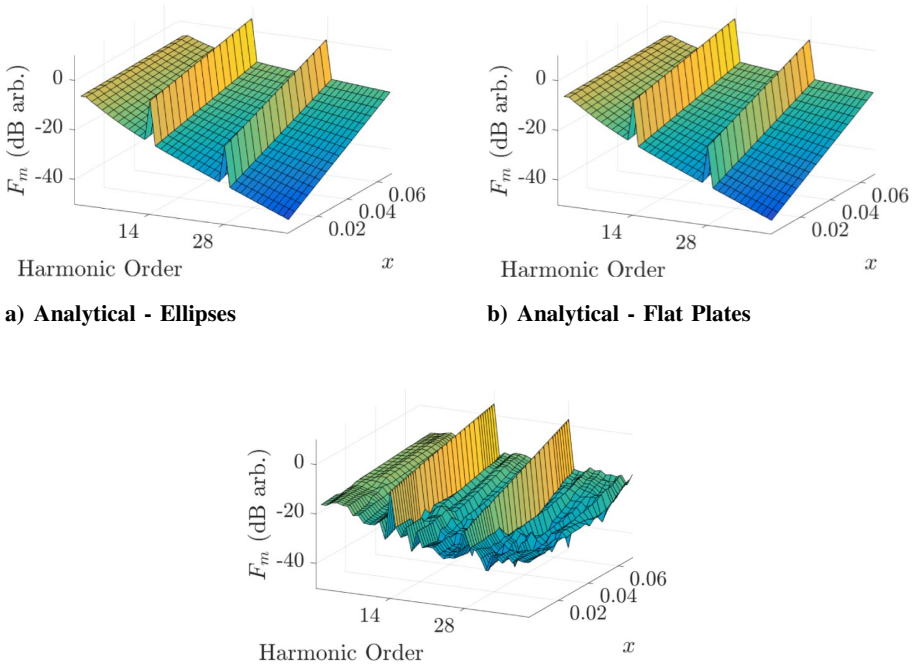

a) Analytical - Ellipses b) Analytical - Flat Plates

c) Numerical LBM Simulation

Fig. 7 Fourier decomposition of the upwash velocity of the potential distortion for the analytical models and the numerical results in the heterogeneous configuration ($V = 14$).

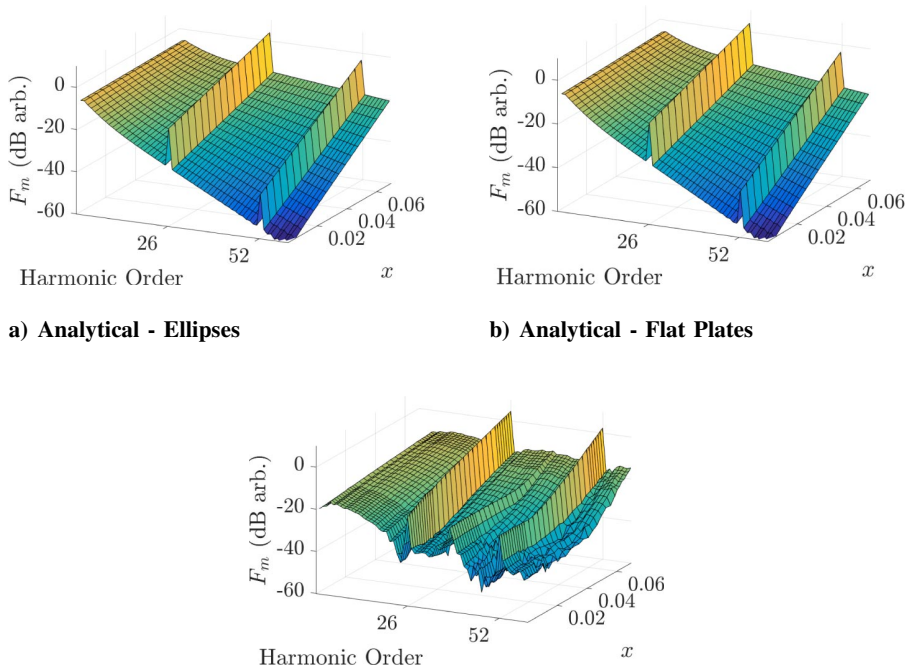

a) Analytical - Ellipses b) Analytical - Flat Plates

c) Numerical LBM Simulation

Fig. 8 Fourier decomposition of the upwash velocity of the potential distortion for the analytical models and the numerical results in the heterogeneous configuration ($V = 26$).

(smaller axial coordinate x). To better visualize its axial evolution, two-dimensional plots are given for some selected harmonic orders in Fig. 9a. This harmonic 38 is seen to reach a plateau at approximately ∼0.7 of the dimensionless interstage coordinate. With the continuous decrease of the main harmonic 26, at the rotor leading edge, the levels of the two harmonics become comparable. Another minor harmonic of order $m = 30$ has also been plotted to illustrate that not all harmonics reach a saturation in the heterogeneous case of the high-solidity stator and to ensure that it is not a numerical artifact.

The origin of such a saturation phenomenon can be traced to a nonlinear interaction between the stator potential field and the rotor wake. A first indication is shown in Fig. 9b, where the space Fourier harmonics 38 of both the wake (rotating pattern) and the potential stator field (stationary pattern) are seen to merge at about ∼0.7 of the dimensionless interstage coordinate. The order 38 is unexpected for the rotor wakes according to analytical linear theories. The latter predict the nearly exponential decrease for the potential field. In contrast, nonlinear interactions yielding saturation could be

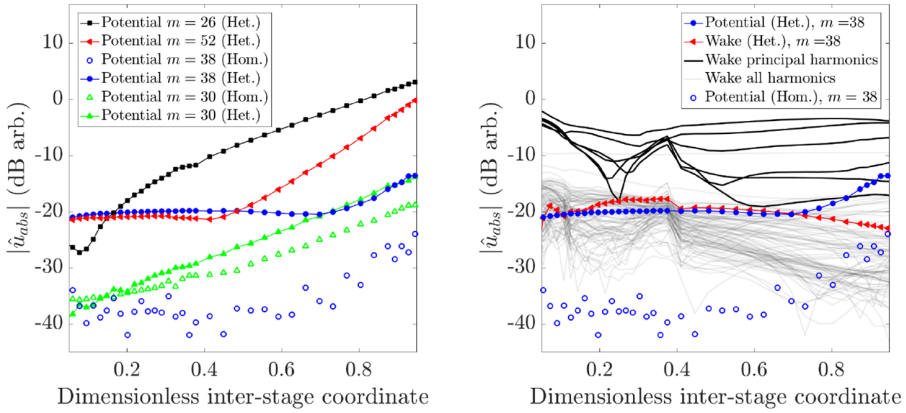

a) Potential harmonics **b) Combined wake harmonics and potential harmonic**

Fig. 9 Axial evolution of wake and potential harmonics for the vane count $V = 26$.

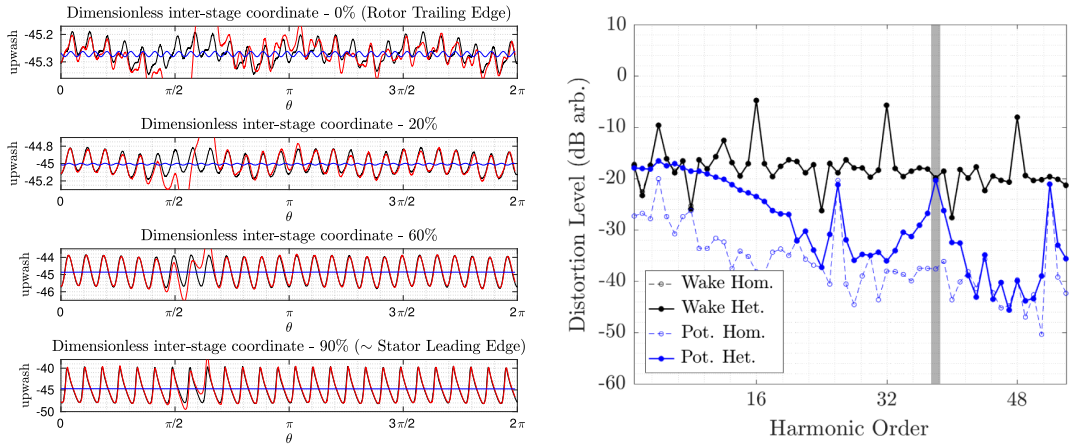

a) Upwash velocity along circumferential coordinate at several locations in the interstage

b) Wake and potential velocity harmonics at 15% of the rotor-stator distance

Fig. 10 Wake and potential fields for the vane count $V = 26$.

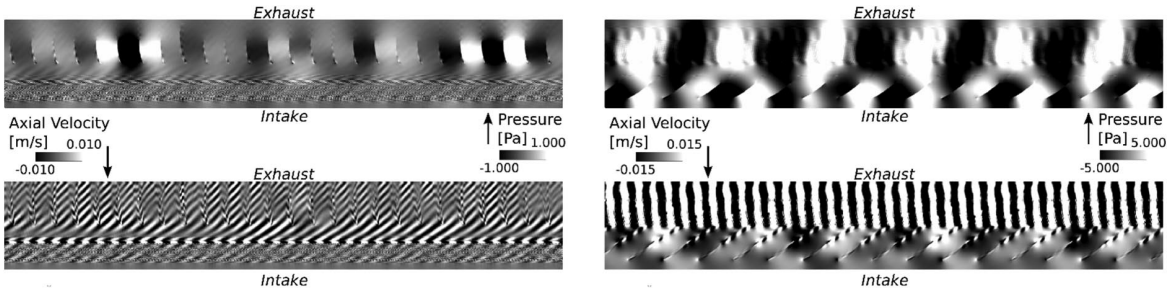

a) In the stator reference frame **b) In the rotor reference frame**

Fig. 11 Pressure and axial velocity instantaneous fields of time harmonic 38.

expected in the numerical potential field at high solidity as was found both experimentally and numerically by Parker [39]. Moreover, by looking at the axial evolution of the potential upwash velocity profiles in Fig. 10a, the modification of one vane is seen to perturb the regular profile with V lobes, to progressively interfere with the B rotor wakes, and with the decrease of the potential getting closer to the rotor, a periodic structure with 38 lobes is observed. This is further confirmed by looking at the harmonics of the wake and potential absolute velocity fields at various dimensionless interstage coordinates (at 15% of the rotor–stator distance in Fig. 10b).

The presence of the harmonic 38 is observed again in the rotor-blade unsteady loadings in Sec. IV.D, where it is also seen dominant. This particular mode structure has further been investigated by decomposing the axial-velocity and pressure fields in both the stator and rotor reference frames as Fourier time series. The time harmonic of order 38 can then be reconstructed in the two reference frames, as shown in Fig. 11. According to linear principles, the time harmonic 38 would only make sense in the rotor reference frame, and the space harmonic 38 would only be present in the stator reference frame. Yet, in the present case, both the time and space harmonics are obviously seen in both reference frames, which confirms the aforementioned coupling. In the stator reference frame, the mode is trapped in the interstage, and some acoustic resonance involving three successive vane passages can be observed in the pressure field, which can be referred to Parker's β mode (pressure peak centered at the vane midchord) weighted by some stationary-wave envelope [35]. In the rotor reference frame, a particular structure on the pressure field involving three successive blade passages can be identified, and a clear

interaction with the stator vane passage can be seen. In the velocity field, lobes in the wake following the orientation of the blade are also found and are especially intense in front of locations in the stator reference frame, where the saturation of pressure was identified in Fig. 11a (top). They correspond to large coherent structures, again supporting Parker's observations that such nonlinear developing modes in rotor–stator configurations are forced by the rotor vortex-shedding structures [40].

For a more quantitative comparison of the analytical and numerical potential fields, the interpolated exponential coefficients from Eq. (16) are shown in Figs. 12 and 13 and compared with the extraction for the homogeneous case. The a_m coefficient directly determines the distortion amplitude of the gust and b_m the rate of axial decay. The numerical extraction for $V = 14$ shows identical distortion levels at the vane-number harmonics. The analytical models overestimate the numerical extractions for a_m by 5 to 15 dB at low orders. Yet the overall trend of the rate of decrease (b_m) is well captured by the two models. The analytical models predict a linear growth of the coefficient b_m with the order, which means that the distortion with higher harmonic orders will decrease faster axially. This is also consistent with Parker's findings [36]. Numerical results seem to reproduce that feature, even though errors become larger for higher orders. The broad bell-shaped hump that can be observed at low orders for the numerical results of the heterogeneous configuration is not reproduced by the analytical models. For this reason, an additional analytical model was investigated based on a Joukowski airfoil accounting for both camber and thickness effects. Higher distortion levels were observed; however, the hump at low orders was still not observed.

Finally, results are plotted for a stator of 26 vanes in Fig. 13. As previously mentioned, the harmonic $m = 38$ is found in the heterogeneous numerical case. The second harmonic order $m = 2$ V is underpredicted by the analytical models, but numerical results for a_m get closer to the analytical predictions at the lowest orders.

In all the investigated cases, the flat-plate potential theory reproduced the major characteristics of the numerical potential field accurately. This model is therefore chosen for its simplicity and its low number of parameters (stagger and chord). It is worth noting that, even in the homogeneous numerical case, because of flow distortion in the simulation induced by the filling of the laboratory and the transition from a square room to a circular bell mouth [41], all orders are generated, unlike in the ideally periodic analytical models. However, their level is lower than in the heterogeneous case and often lay close to the numerical background errors.

Finally, the surface of Fourier coefficients reconstructed from the interpolations performed for each order using the exponential fit mentioned in Sec. IV is shown in Fig. 14. The surface is quite similar to the one shown in Fig. 7c. The exponential fit is then a satisfactory approximation. It is worth noting that, for the case of harmonic saturation, the exponential rate of decrease is not captured because analytical models do not account for this nonlinear phenomenon.

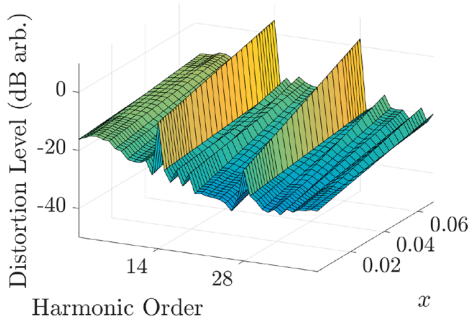

Fig. 14 Interpolated Fourier coefficients of the potential upwash velocity. Same parameters as in Fig. 7c.

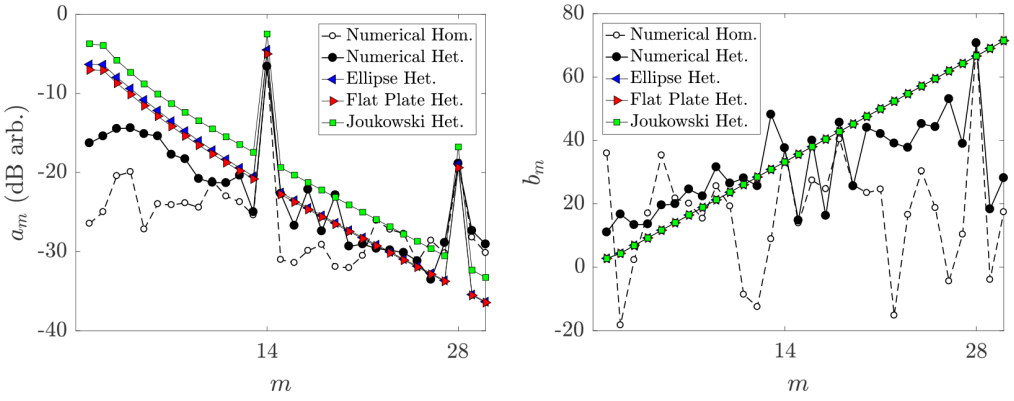

a) a_m coefficients as a function of the order **b) b_m coefficients as a function of the order**

Fig. 12 Exponential-fit parameters of the interpolated Fourier coefficients of the potential upwash velocity for $B = 16$ and $V = 14$.

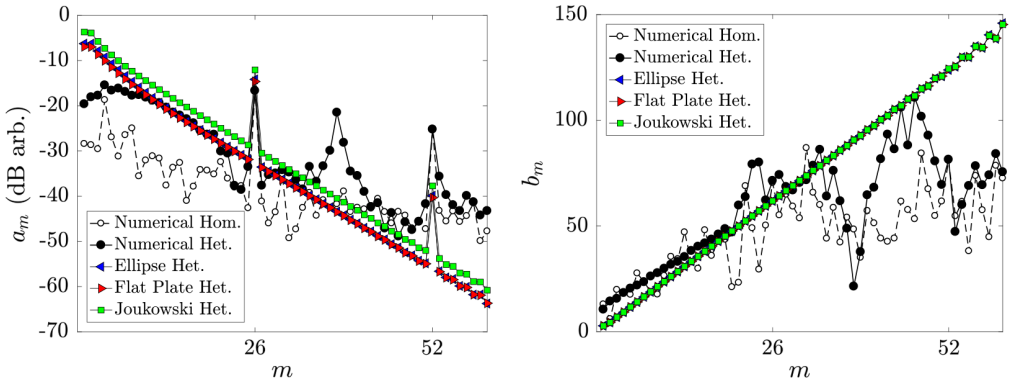

a) a_m coefficients as a function of the order **b) b_m coefficients as a function of the order**

Fig. 13 Exponential-fit parameters of the interpolated Fourier coefficients of the potential upwash velocity for $B = 16$ and $V = 26$.

D. Unsteady Blade Loading

In this section, numerical and analytical unsteady blade loadings are compared. On the one hand, the analytical unsteady lift is given by Parry's model described in Sec. III.D, choosing the flat-plate distortion for its best accuracy. On the other hand, numerical pressure jumps are calculated by a postprocessing of the unsteady numerical simulations with some approximations. To be able to compare both approaches, the numerical pressure jump must be computed at a constant radius and reduced to the one over a flat plate. The first step consists of performing a Fourier transform of the unsteady pressure over the blade surface at the rotational shaft harmonics. Then, a cylindrical cut is unwrapped to reduce the problem to two dimensions. For each isolated airfoil of the cascade, the geometrical leading and trailing edges are determined, and the upper and lower sides of the airfoil are separated. The mean camber line is approximated by the mean vertical coordinate of two points having the same dimensionless curvilinear abscissa on the upper and lower side curves. The pressure jump over the mean camber line is given by the pressure difference between both sides of same curvilinear abscissa. Finally, a simple projection of the mean camber line on the chord-line axis is done to reduce the pressure jump to that of an equivalent flat plate. A comparison of the two approaches for the $V = 14$ heterogeneous configuration is presented in Fig. 15.

The first harmonic is well approximated by the analytical model with a maximum amplitude of 12, as seen in Fig. 16. The chordwise dynamics of the loading is similar and more concentrated in the aft part of the blade, with a drop at the trailing edge, where the Kutta condition is satisfied. In Fig. 15, harmonics of lower orders due to the heterogeneity are reproduced by the analytical model but at much smaller amplitudes. The rate of decrease with the harmonic order is also far more important in the analytical model, leading to negligible lift distributions at the third, fourth, and fifth harmonics. The numerical simulation of the heterogeneous configuration includes minor inhomogeneities that are absent in the analytical model. This could make the harmonic decrease slower. Furthermore, the upstream distortion also affects the blade loading as described in Sec. IV.F. This means that the numerical pressure jump includes an additional contribution not included in the analytical result. It is worth noting that, because of its low-order azimuthal content, the inlet distortion is expected to induce low-order harmonics on the blades as observed in Fig. 15b.

In the second stator configuration ($V = 26$), the numerical pressure jumps are plotted in Fig. 17. The unexpected order $m = 38$ previously observed in Sec. IV.C is still present with the same level as the first and second harmonics. It is also noted that the unsteady lift does not decrease with increasing order. Analytical results are not plotted here because their amplitudes are negligible. In fact, when increasing the number of stator vanes, and according to the distortion field description shown in Fig. 13, loads become negligible. Thus, the high harmonic rate of decrease observed in the previous configuration is emphasized with a higher stator count, leading to a high underestimation of the unsteady lift.

To summarize, Parry's model reproduces some interesting characteristics of the unsteady lift induced by downstream potential perturbations fairly well. However, some unrealistic features such as the harmonic rate of decrease should be investigated, which are directly linked with the distortion field description.

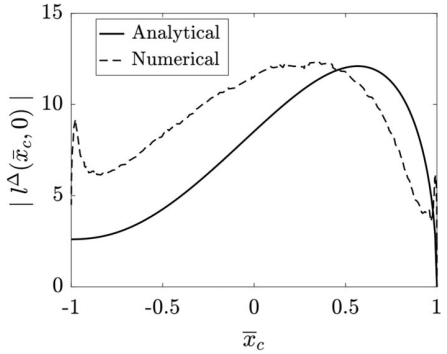

Fig. 16 Compared numerical and analytical pressure jumps at the harmonic order $m = 14$ in the heterogeneous configuration with $V = 14$.

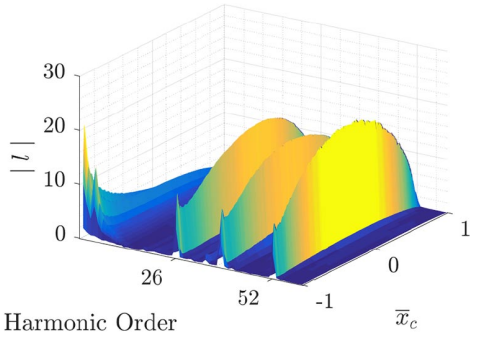

Fig. 17 Numerical rotor loads ($V = 26$).

E. Wake Interaction

From the mean field shown in Fig. 6a, the Fourier coefficients of the absolute velocity can be computed in the interstage region for several axial positions. Results for the two investigated configurations are plotted in Fig. 18. As observed by Jaron et al. [42], the first three harmonics first decrease from the blade trailing edge and then increase.

The higher vane count is also checked to only induce a minor difference in Fig. 18, mostly on the second harmonic, for which it reaches the level of the first harmonic at the stator leading edge. Finally, the heterogeneous vane does not modify the overall axial variation. In all investigated configurations, the wake-induced upwash on the vanes will be similar and could be modeled with the same parameters.

The evolution at different spanwise positions is shown in Fig. 19. The same evolution is obtained close to the hub, but near the casing, the velocity harmonics demonstrate a rapid decay after the interface between the rotor and stator domains and then a new rapid increase. The latter is related to the tip flow that merges with the wake flow.

The rotor-wake impingement will in turn induce unsteady vane loadings, which are plotted in Fig. 20 for the two different stator configurations. As expected, loads concentrate at the leading edge and decrease rapidly toward the trailing edge. The rotor periodicity emerges clearly in the plot, with the principal harmonics being those multiples of the blade number. For the stator configuration with

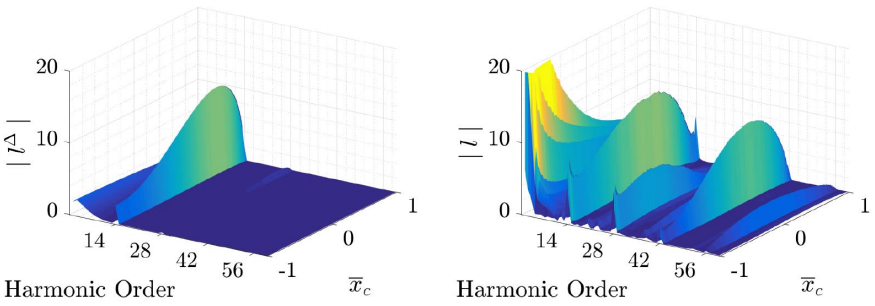

a) Analytical **b) Numerical**

Fig. 15 Comparison of rotor blade loading harmonics as function of harmonic order and chordwise location ($V = 14$).

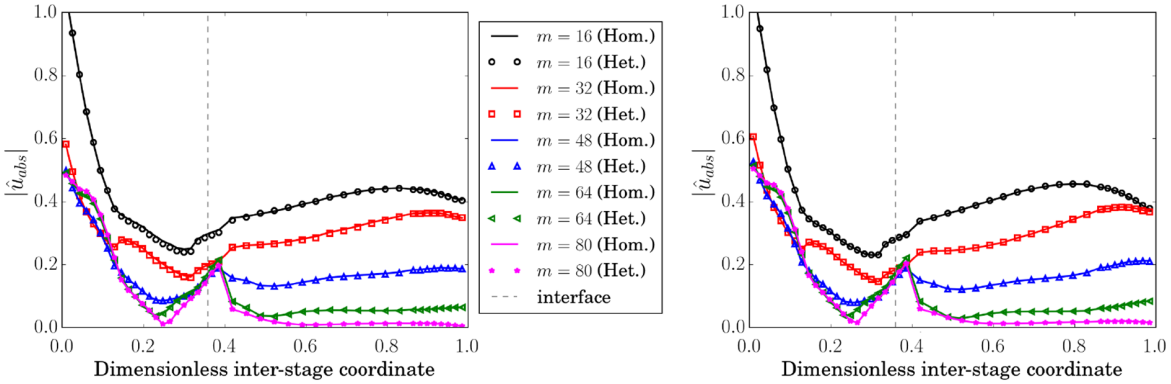

a) $V = 14$ **b) $V = 26$**

Fig. 18 Axial variation of the wake Fourier coefficients for the first five harmonics at midspan.

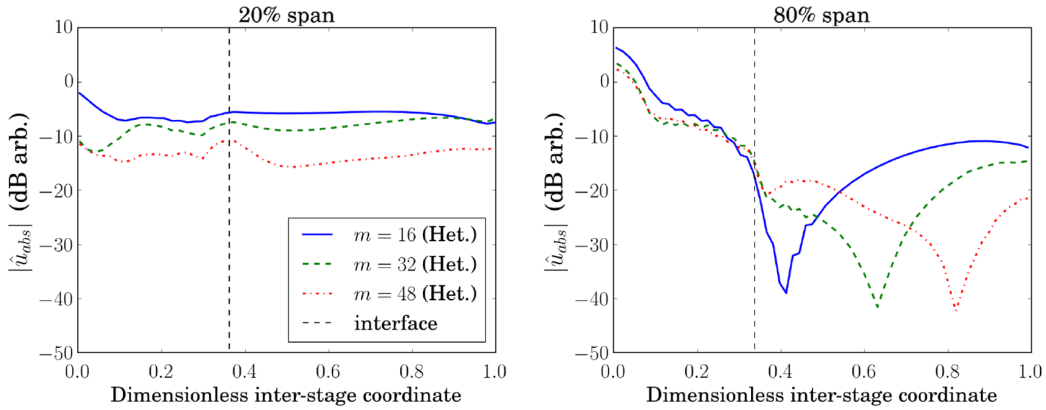

Fig. 19 Axial evolution of the first three harmonics at two other radial positions ($V = 26$ heterogeneous).

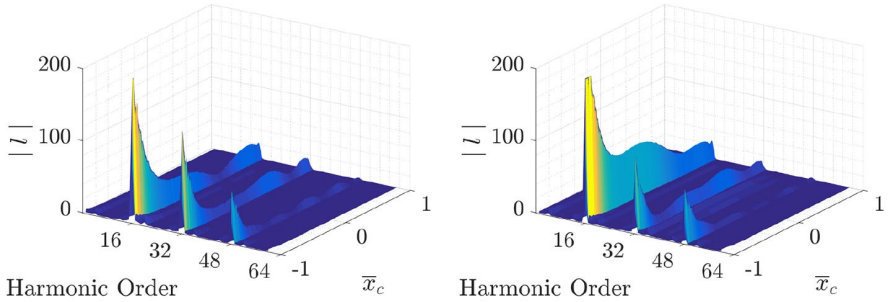

a) $V = 14$ **b) $V = 26$**

Fig. 20 Stator-vane loading distribution as a function of harmonic order and chordwise location for the homogeneous configurations at midspan.

26 vanes, loads can double at midchord, but the maximum value recorded at the leading edge remains the same.

Moreover, numerical loading distributions of the main harmonics $m = 16$ over the vane chord length are shown for all stator vanes in Fig. 21. In green, all vane loadings of the homogeneous configuration are superposed; in both configurations, loads are identical. Despite the geometrical difference of the modified vane, loads close to the leading edge have similar level and shape for all configurations. In fact, the homothetic transformation does not induce a major modification of the leading edge region, with the thickness of the airfoil being hardly modified. Yet, as previously mentioned, because of the higher solidity, loads at midchord are higher for the configuration with a higher stator count $V = 26$ (Fig. 21b). In the heterogeneous configuration with $V = 14$ stator vanes (Fig. 21a), stator loads also remain identical for all unmodified vanes, and the modified vane presents an extended load distribution due to its larger chord only. For the high-count heterogeneous configuration with $V = 26$ stator vanes (Fig. 21b), more variations are seen in the loadings that are about 40% higher than in the homogeneous configuration. Indeed, because the solidity is higher, the adjacent vanes (in red) are strongly perturbed by the modified vane. Finally, for all configurations, the stator-vane loads are much higher than those of the rotor blades, and the noise contribution of the wake impingement is therefore expected to be higher than the potential interaction noise.

F. Upstream Distortion

One competing mechanism of the potential interaction is the upstream distortion interaction. As previously found by Sturm et al. [41,43] with the USI-7 fan mounted in a duct in the Siegen anechoic wind tunnel, LBM simulations accounting for the full test-rig installation can capture the inflow distortion and the distortion noise mechanism accurately. The incoming flowfield is similarly resolved

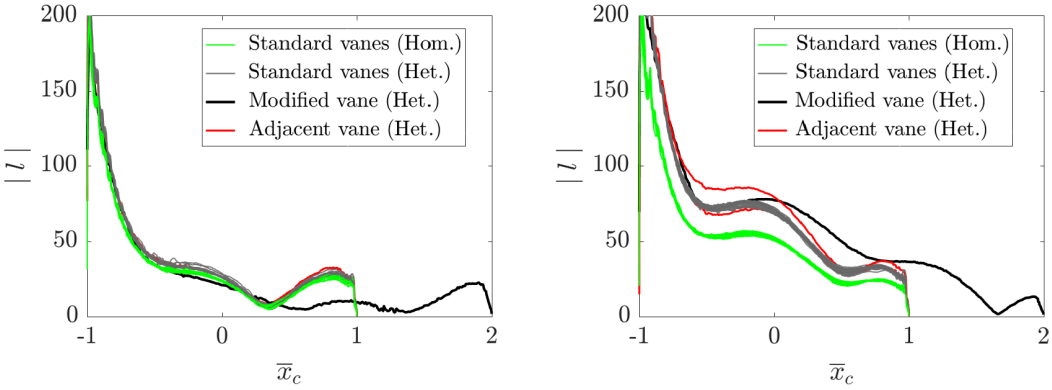

a) $V = 14$ **b) $V = 26$**

Fig. 21 Stator-vane loading distribution for the harmonic order $m = 16$ as a function of the chordwise location at midspan.

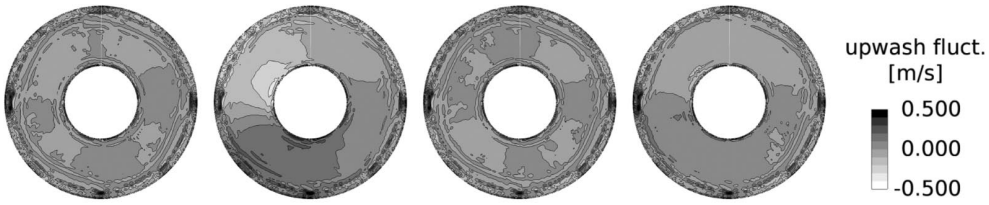

a) V=14 - Hom. **b) V=14 - Het.** **c) V=26 - Hom.** **d) V=26 - Het.**

Fig. 22 Upwash velocity fluctuation seen by the rotor due to the upstream distortion.

in the present LBM simulation setup that accounts for the actual nacelle geometry and the laboratory volume. To evaluate the distortion, a time-averaged field is extracted from the simulations in the duct at $C_R/4$ upstream of the rotor-blade leading edge. The upwash velocity fluctuation seen by the rotor is shown for the four studied configurations in Fig. 22. This fluctuation is obtained by further subtracting the mean tangential field (zero azimuthal harmonic). The distortion is actually hardly noticeable in the time-averaged upwash velocity, demonstrating that the distortion is not as strong as in the USI-7 configuration and that no clear ingested vortex can be observed in the ANCF configurations. The main zones of intense azimuthal variations of the upwash velocity are the areas close to the casing and the hub as a consequence of developing boundary layers on the surface wall. All maps in Fig. 22 exhibit a four-lobe disturbance in the tip region consistent with a square to circular transition from the computational domain to the nacelle geometry. Yet, only for the homogeneous configurations, such a pattern extends over the whole blade span. In the heterogeneous cases, lower orders seem to dominate, and the distortion appears stronger for the 14-vane configurations than for the 26-vane ones.

The resulting azimuthal coefficients of the upwash velocity seen by the rotor are shown in Fig. 23 for three spanwise locations. At midspan, the amplitude of the upwash velocity is clearly increased by the heterogeneity of the configurations that involve lower harmonics, and the distortion is generally lower for the configuration with the higher vane number, consistent with the distortion maps in Fig. 22. In the latter, the distortion is higher close to the casing for all configurations. At this location, the differences between the homogeneous and heterogeneous configurations is therefore mitigated. Moreover, close to the hub and the casing, the harmonics

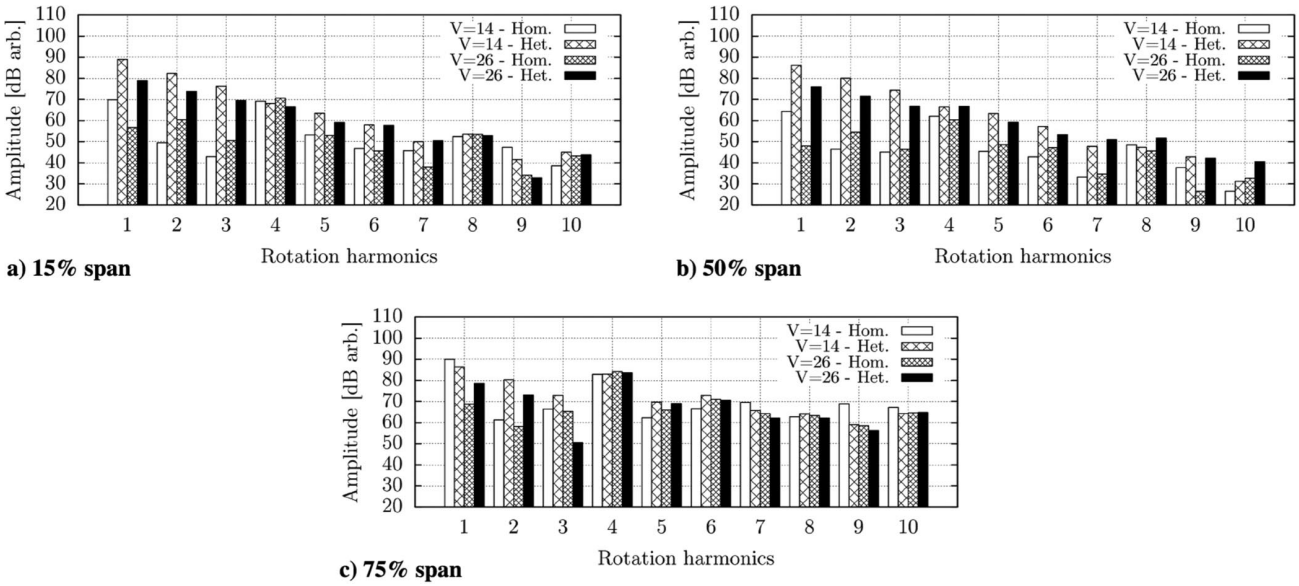

a) 15% span **b) 50% span**

c) 75% span

Fig. 23 Distortion Fourier coefficients of the first 10 harmonics at three span locations with arbitrary decibel scaling.

of orders $p = 4$ and $p = 8$ are noticeably higher than their neighboring harmonics, consistent with the preceding four-lobe distortion pattern. This is more clearly seen in the homogeneous configurations that do not have increased lower harmonics.

The noise from the distortion-interaction mechanism can then be estimated analytically using this upwash velocity extracted from the simulations, shown in Fig. 23. Indeed, the sound power level is calculated by Eq. (4) for a homogeneous rotor, with Amiet's flat-plate response to evaluate the unsteady lift from this leading-edge excitation.

V. Sound Predictions: Analytical Modeling Versus Lattice Boltzmann Method

A. Potential-Interaction Noise

The rotor-noise contribution due to the stator heterogeneity is investigated in this section using Parry's blade response extension computed by Eq. (13) with Goldstein's analogy given in Eqs. (3) and (4). As mentioned previously, the rotor blades are divided into 19 strips, on which the velocity perturbation from the flat-plate cascade given by Eq. (16) (modeling the stator as detailed in Sec. IV.C) is used to compute the isolated blade response given by Eqs. (11) and (12), which is then integrated over the blade span. For the four configurations, the upstream and downstream acoustic powers obtained for the first 10 blade-passing frequencies are shown in Fig. 24. With $V = 14$ vanes, the acoustic powers for the homogeneous and heterogeneous configurations are identical or show less than 2 dB differences. With $V = 26$ vanes, the BPF is cut off in the homogeneous configuration according to Tyler and Sofrin's rule (because the excitation is V-periodic) and cut on in the heterogeneous configuration. All other harmonics are of similar amplitudes with slightly higher differences than in the low-count configuration. The maximum difference is obtained for the third harmonics, with up to 5 dB differences downstream.

The detailed distribution over azimuthal orders of the first three blade-passing frequencies is given in Fig. 25. The main contribution comes from the expected Tyler and Sofrin's modes. The excitation is predominant for the loading harmonics multiples of V, as shown in

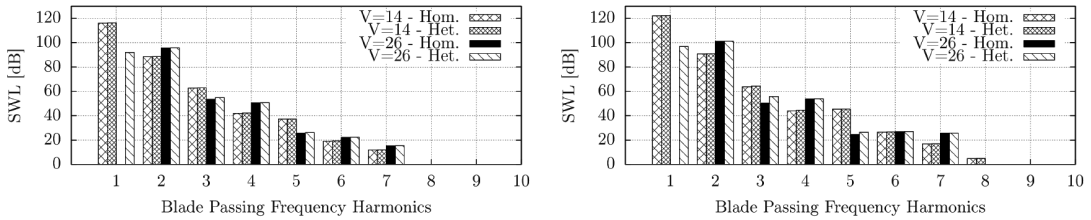

a) Upstream Acoustic Power b) Downstream Acoustic Power

Fig. 24 Acoustic power for the potential distortion noise of the rotor computed from Parry's flat-plate response with Goldstein's analogy.

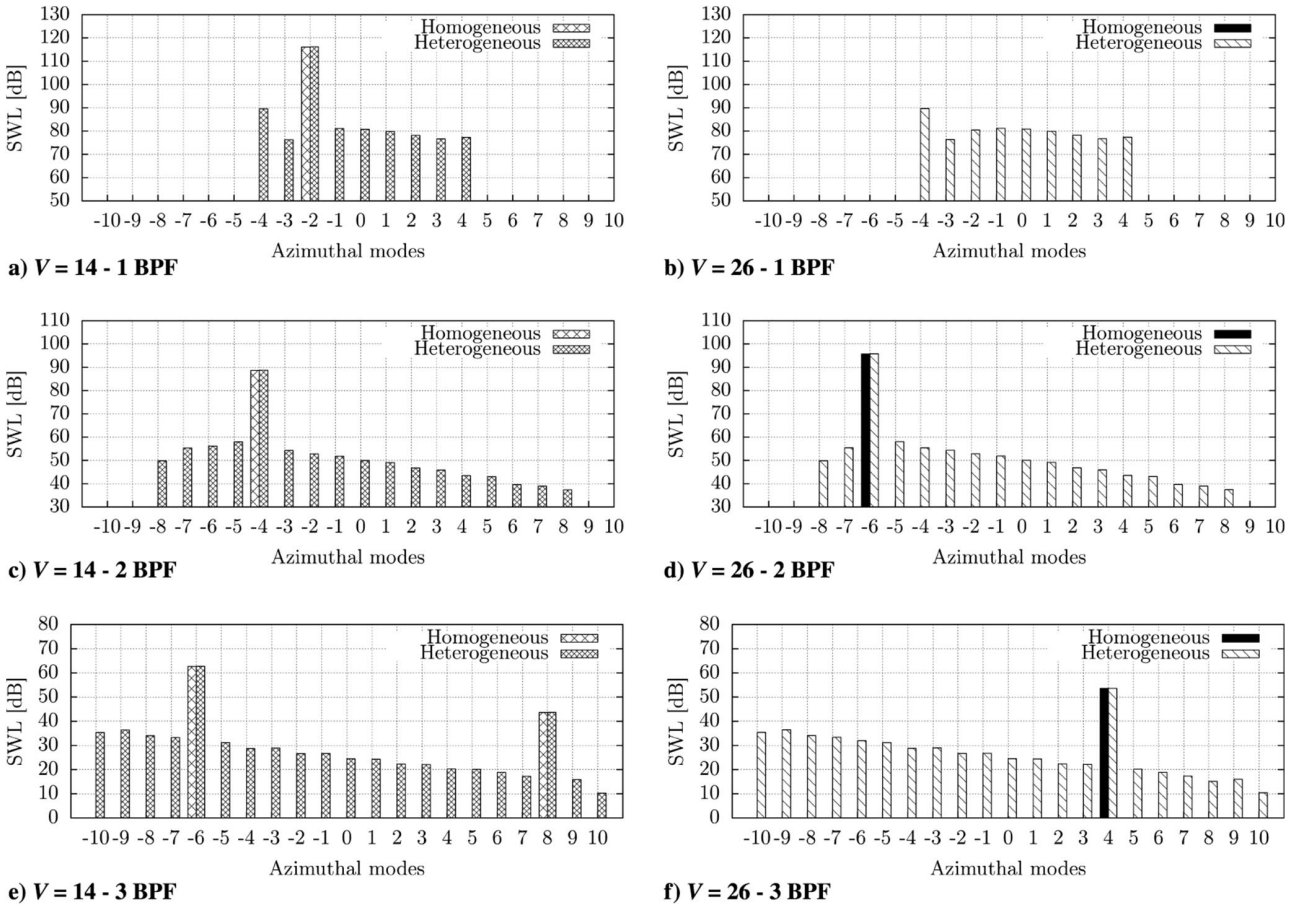

a) V = 14 - 1 BPF b) V = 26 - 1 BPF

c) V = 14 - 2 BPF d) V = 26 - 2 BPF

e) V = 14 - 3 BPF f) V = 26 - 3 BPF

Fig. 25 Upstream acoustic power for the potential interaction noise. Flat-plate cascade computed from Parry's response with Goldstein's analogy.

Figs. 12 and 13. In the heterogeneous configurations, the other azimuthal modes are generated but have a level at least 20 dB lower than the main radiating modes.

B. Wake-Interaction Noise

The stator-noise contribution due to the rotor-wake interactions accounting for heterogeneous vane geometry is investigated using Amiet's blade response computed by Eq. (B4) with Goldstein's analogy given in Eqs. (4) and (5). Similar to previous computations, the stator vanes are divided into 19 strips, on which the excitation from the wake analyzed in Sec. IV.E and extracted at the midsection plane between the rotor and the stator is used to compute the vane response that is then integrated over the vane span. For the four configurations, the upstream and downstream acoustic powers obtained for the same first 10 blade-passing frequencies are shown in Fig. 26. The power contribution is decreasing much more slowly than for the rotor contribution in Fig. 24, making the rotor-wake interaction the dominant noise source, except for the first BPF. This could be questioned were the fast distortion decrease in the analytical model proved to be abusive. The tone-level differences between the homogeneous and heterogeneous configurations is this time stronger with $V = 14$; the levels are about 5 dB higher for the homogeneous configuration on the first five harmonics. For the higher vane number, the amplitudes predicted in the homogeneous and heterogeneous configurations are similar for all tones, except for the first one, which is cut-off in the homogeneous configuration and cut-on in the heterogeneous configuration. Because of the increase of vane number, the configuration $V = 26$ generally produces higher noise levels than the configuration $V = 14$.

The detailed distribution over azimuthal orders of the first three blade-passing frequencies is reported in Fig. 27. As for the previous mechanism, the main contribution comes from Tyler and Sofrin's modes. The other modes are again generated by the heterogeneity but have lower amplitudes by about 20 dB, except for the first harmonics. Apart from Tyler and Sofrin's modes, the modal amplitudes are relatively constant, whereas they were found to decrease for the rotor contribution in Fig. 25.

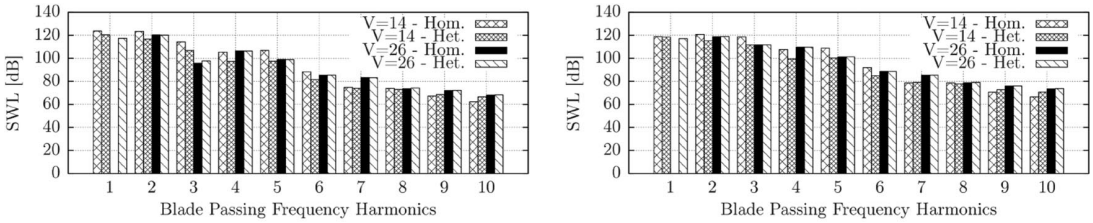

a) Upstream Acoustic Power **b) Downstream Acoustic Power**

Fig. 26 Acoustic power spectra for the rotor-wake interaction noise computed from Amiet's response with Goldstein's analogy.

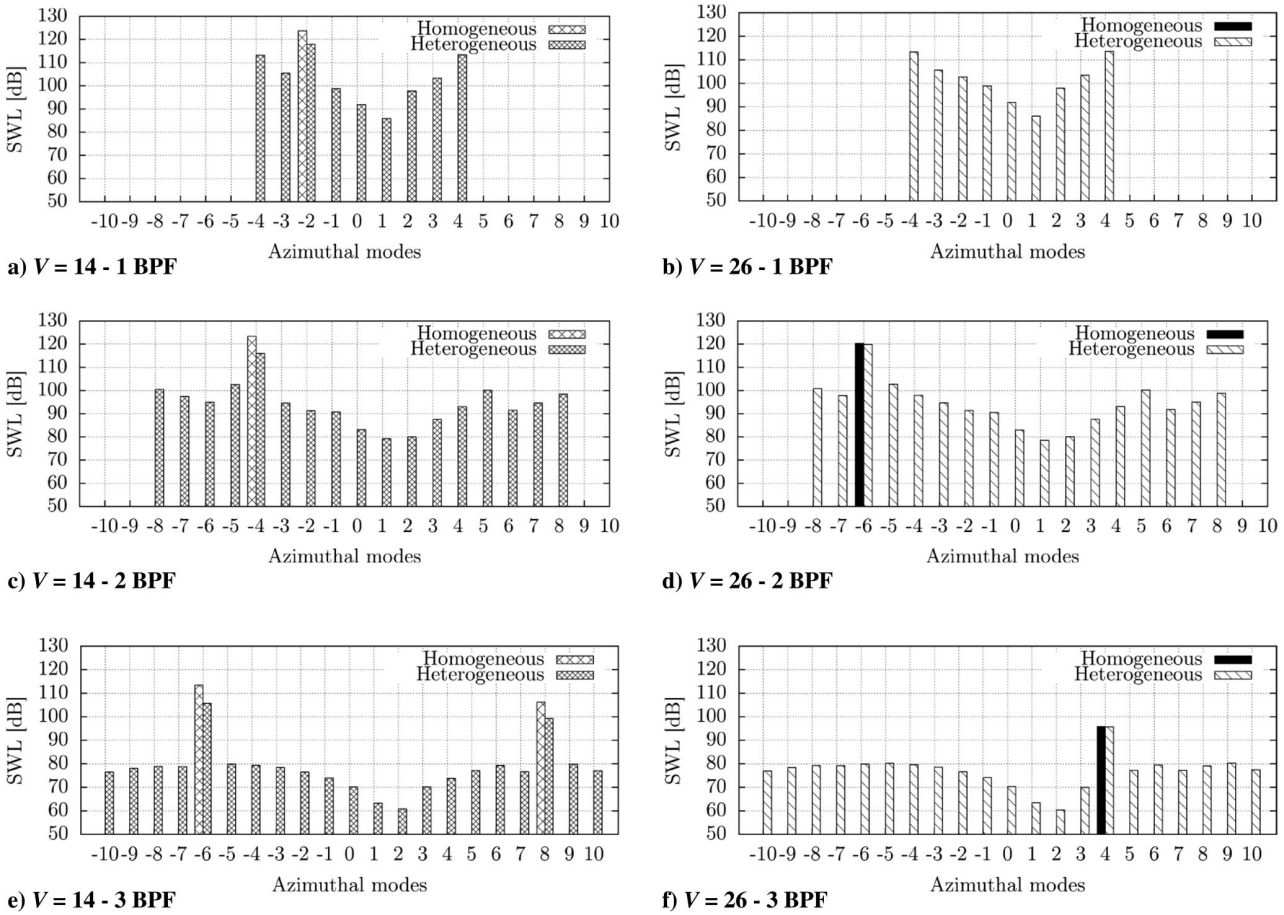

a) V = 14 - 1 BPF **b) V = 26 - 1 BPF**

c) V = 14 - 2 BPF **d) V = 26 - 2 BPF**

e) V = 14 - 3 BPF **f) V = 26 - 3 BPF**

Fig. 27 Upstream acoustic power for the rotor-wake interaction noise computed from Amiet's response with Goldstein's analogy.

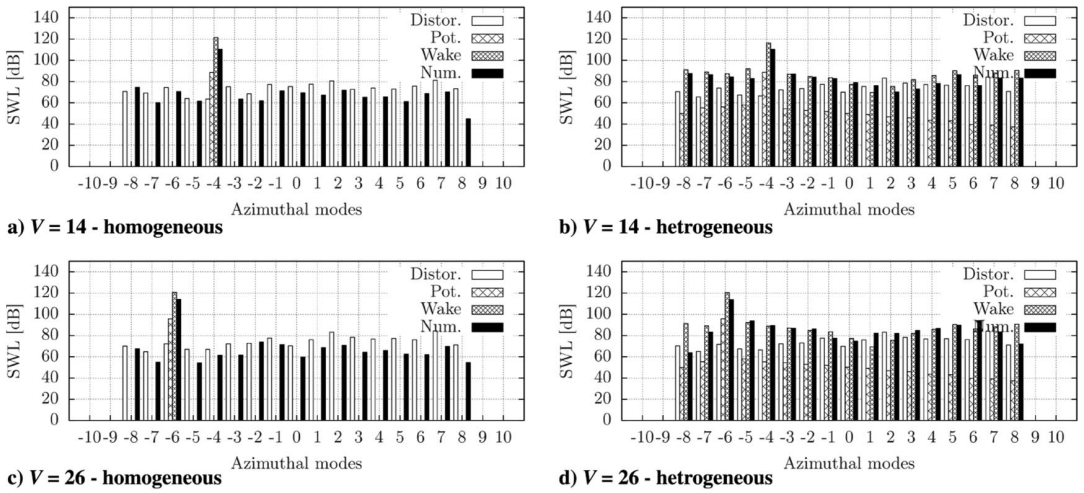

Fig. 28 Upstream modal powers of the second BPF harmonic. Comparison between numerical simulation and analytical predictions for the upstream distortion-interaction noise, the potential-interaction noise, and the wake-interaction noise.

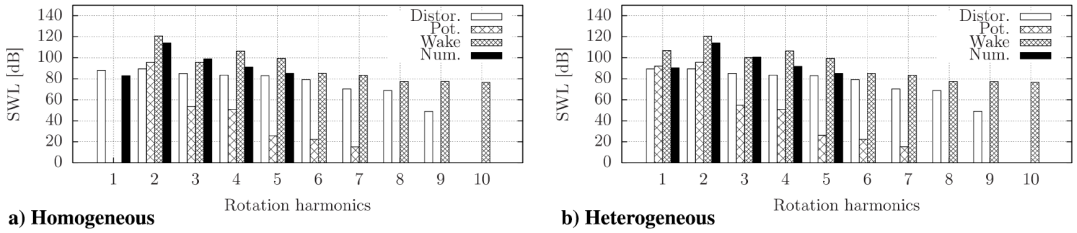

Fig. 29 Upstream acoustic power spectra for all noise mechanisms in the configuration $V = 26$.

C. Comparison with Direct Acoustic Simulations

The acoustic modal distribution is extracted from the simulation by projecting the azimuthal pressure coefficient recorded on a regular grid onto the radial shape functions of the infinite duct [11,13]. The extraction at high-frequency sampling recorded upstream of the rotor is interpolated onto a regular grid of 180×50 points in azimuthal and radial directions respectively. The Moore–Penrose pseudoinverse algorithm as implemented in Matlab is used for least-square analysis of the overdetermined system.

In Fig. 28, the modal power distribution over the azimuthal orders is shown at the second blade-passing frequency for the four configurations. The contributions from the wake-interaction noise and the potential-interaction noise according to the analytical modeling are shown separately. The wake contribution is largely prevailing. In the numerical simulations, the radiating modes appear above 60 dB, with the remaining amplitudes in the homogeneous configurations being due to the inflow distortion as clearly recovered by the analytical calculations. For heterogeneous configurations, the amplitudes of modes other than Tyler and Sofrin's modes are largely higher than the level of inflow distortion noise. This is a clear demonstration of the impact of the heterogeneity on the acoustic radiation as resolved by the simulations. Despite the increase in distortion in the heterogeneous configuration, the resulting increase in acoustic power is negligible. The acoustic power related to the effect of the stator potential field on the rotor is negligible compared with the upstream distortion contribution, as illustrated for instance for both configurations $V = 26$ in the upstream direction in Fig. 29. But it should be stressed again that the amount of potential distortion is quite moderate in the present study. The analytical prediction for the wake-interaction noise overestimates the modes detected in the simulation by 5 to 10 dB, in agreement with previous comparisons for other homogeneous configurations [13]. Nevertheless, the overall distribution and evolution of the modal spectrum for the wake interaction is in good agreement with the numerical extractions.

VI. Conclusions

Simulations using the lattice Boltzmann method as implemented in Powerflow 5.0 have been successfully performed on the baseline and modified configurations of the NASA Active Noise Control Fan (ANCF) test rig. This fan–outlet guiding vane mockup is used as a reference case typical of low-speed high-bypass-ratio engines. Four configurations have been simulated: two homogeneous with 14 and 26 identical vanes, and two heterogeneous in which a single vane of the stator is enlarged by a scale factor of 1.5. The noise originating from the potential effect induced on the rotor by the stator heterogeneity, from the upstream distortion, and from the homogeneous rotor-wake interaction with the heterogeneous stator has been investigated and compared with predictions using analytical aeroacoustic models with in-duct propagation. The classical Amiet's response for the wake impingement on the stator and the upstream distortion interaction with the rotor is used, whereas Parry's response for the impact of the potential field on the rotor row has been reformulated using Schwarzschild's technique. For the latter, the previously developed reversed Sears analytical model for the potential interaction has been extended to account for the Kutta condition at the rotor trailing edges and shown to be equivalent to Parry's approach based on the Wiener–Hopf technique. The three distinct excitations are extracted from the numerical simulations and compared with simplified analytical excitation models. The inviscid theory for two-dimensional uniform flow past flat plates is sufficient to predict the main trends of the evolution of the potential excitation seen by the rotor, and Jaron's wake model provides a good understanding of the wake evolution in the simulated configurations. The modeled potential harmonics show the same axial variations with mode order as Parker's model and measurements for all configurations. Only the saturation of some harmonics of the potential distortion attributed to nonlinear interaction between the stator potential field and the rotor wakes is missed by the proposed linear model, which is also consistent with Parker's previous experimental and numerical results. Finally, the acoustic predictions and the distribution of the

acoustic modal power over the azimuthal mode orders are compared with direct acoustic information extracted from the simulation and decomposed in acoustic duct modes. The wake contribution is the dominant noise source in the present configurations. The heterogeneity strongly affects the distribution of the acoustic power on azimuthal orders by relaxing Tyler and Sofrin's rule. The analytical predictions overestimate the numerical simulations, but the relative amplitudes of the dominant and secondary modes are well captured, providing a simplified tool to estimate the acoustic levels and their distribution over modes in complex configurations. Finally, an acoustic resonance (Parker's β mode) has been evidenced in a coupled simulation for the first time.

Appendix A: In-Duct Green Function

Green's function in the time domain for an infinite annular duct can be expanded on the duct mode basis from that for the Helmholtz equation in the frequency domain using the indices n and j for the circumferential and radial modes, respectively:

$$G(\boldsymbol{x},t|\boldsymbol{x}',\tau)=\frac{i}{4\pi}\sum_{n=-\infty}^{+\infty}\sum_{j=0}^{+\infty}\frac{E_{nj}(r')E_{nj}(r)\mathrm{e}^{in(\theta-\theta')}}{\Gamma_{nj}}\times\int_{-\infty}^{\infty}\frac{\mathrm{e}^{-i(\gamma_{nj}^{\pm}(x-x')+\omega(t-\tau))}}{\kappa_{nj}}\,\mathrm{d}\omega \tag{A1}$$

where $k_0=\omega/c_0$, and $E_{nj}(r)=N_{nj}(\cos\tau_{nj}J_n(\chi_{nj}r)-\sin\tau_{nj}Y_n(\chi_{nj}r))$ is the duct radial function defined by Rienstra and Hirschberg [44] depending on the eigenvalue χ_{nj} and of norm $\Gamma_{nj}=2\pi R_T^2$, where

$$\tau_{nj}=\arctan\left(\frac{J_n(\chi_{nj}R_H)}{Y_n(\chi_{nj}R_H)}\right) \tag{A2}$$

$$N_{nj}=\frac{\sqrt{2}}{2}\pi\chi_{nj}R_T\left(\frac{1-n^2/(\chi_{nj}^2R_T^2)}{J_n(\chi_{nj}R_T)^2+Y_n(\chi_{nj}R_T)^2}-\frac{1-n^2/(\chi_{nj}^2R_H^2)}{J_n(\chi_{nj}R_H)^2+Y_n(\chi_{nj}R_H)^2}\right)^{-1} \tag{A3}$$

$\gamma_{nj}^{\pm}=(M_ak_0\pm\kappa_{nj})/\beta^2$ is the axial acoustic wave number, and $\kappa_{nj}^2=k_0^2-\beta^2\chi_{nj}^2$. The superscript $\pm$ is related to the direction of propagation for $x>x_0$ and $x<x_0$, respectively. x_0 is the position of the source plane.

Appendix B: Amiet's Blade Response

For low frequencies such that $\overline{\mu}<0.4$, the normalized pressure jump follows Sears's compressible response:

$$g^\star(\overline{x}_c,\overline{k}_x,0,M)=\frac{1}{\pi\beta}\sqrt{\frac{1-\overline{x}_c}{1+\overline{x}_c}}\mathcal{S}^\star\left(\frac{\overline{k}_x}{\beta^2}\right)\mathrm{e}^{-i(\overline{k}_x/\beta^2)(M^2\overline{x}_c+f(M))} \tag{B1}$$

where $f(M)=(1-\beta)\,\ell\mathrm{n}\,M+\beta\,\ell\mathrm{n}(1+\beta)-\ell\mathrm{n}\,2$, and the complex conjugate of Sears's function defined as

$$\mathcal{S}^\star(X)=\frac{2}{\pi X[(J_0(X)-Y_1(X))-i(J_1(X)+Y_0(X))]} \tag{B2}$$

At higher frequencies for which the chord is not compact, Amiet's response [27] is used instead:

$$g^\star(\overline{x}_c,\overline{k}_x,0,M)=\frac{\mathrm{e}^{i(\pi/4)}\mathrm{e}^{i\overline{\mu}(1-M)(1-\overline{x}_c)-\overline{k}_x}}{\pi\sqrt{2\pi(1+M)\overline{k}_x}}\times\left(\sqrt{\frac{2}{1+\overline{x}_c}}-1+(1-i)E(2\overline{\mu}(1-\overline{x}_c))\right) \tag{B3}$$

The chordwise integral

$$\mathcal{L}=\int_{-1}^{1}\mathrm{e}^{-i\mathcal{B}\overline{x}_c}l(\overline{x}_c)\,\mathrm{d}\overline{x}_c$$

with $\mathcal{B}=b(\gamma_{nj}^{\pm}\cos\chi-(n/r')\sin\chi)$ for Amiet's response is given as

$$\mathcal{L}=2\pi\rho_0Uw_0(I_1+I_2) \tag{B4}$$

with:

$$I_1=\frac{2\mathrm{e}^{i\Theta_2}}{\pi\sqrt{(1+M)\overline{k}_x}}ES(2\Theta_1) \tag{B5}$$

$$I_2=\frac{2\mathrm{e}^{i\Theta_2}}{\pi\Theta_1\sqrt{2\pi(1+M)\overline{k}_x}}\Big\{i(1-\mathrm{e}^{-i2\Theta_1})+i(1-i)[\sqrt{4\overline{\mu}}\mathrm{e}^{-i2\Theta_1}Es(2(\overline{\mu}(1+M)+\mathcal{B}))-E(4\overline{\mu})]\Big\} \tag{B6}$$

where $\Theta_1=\mathcal{B}-\overline{\mu}(1-M)$, and $\Theta_2=\mathcal{B}-\overline{k}_x+(\pi/4)$. The functions ES and ES that are providing stable computations with complex arguments [32] are related to the complex error function $\Phi^{(0)}$ as

$$ES(z)=\frac{E^\star(z)}{\sqrt{z}}=\frac{1-i}{2}\frac{\Phi^{(0)}(\sqrt{iz}\,)}{\sqrt{z}}$$
$$Es(z)=\frac{E(z)}{\sqrt{z}}=\frac{1+i}{2}\frac{\Phi^{(0)}(\sqrt{-iz}\,)}{\sqrt{z}} \tag{B7}$$

Acknowledgments

The authors acknowledge the Réseau Québécois de Calcul de Haute Performance/Compute Canada for providing technical support and necessary computational resources for this research as well as the Exa Corporation for providing licenses and technical support. The authors also thank A. Mann and F. Pérot from Exa for fruitful discussions and technical support and for providing the initial simulation. This research was funded through the Aeroacoustic Industrial Chair of the Université de Sherbrooke and the ANR Industrial Chair ADOPSYS.

References

[1] de Laborderie, J., Moreau, S., Berry, A., and Posson, H., "Several Technological Effects on Tonal Fan Noise Prediction," *18th AIAA/CEAS Aeroacoustics Conference*, AIAA Paper 2012-2131, June 2012.

[2] de Laborderie, J., and Moreau, S., "Evaluation of a Cascade-Based Acoustic Model for Fan Tonal Noise Prediction," *AIAA Journal*, Vol. 52, No. 12, 2014, pp. 2877–2890. doi:10.2514/1.J053008

[3] de Laborderie, J., Blandeau, V., Node-Langlois, T., and Moreau, S., "Extension of a Fan Tonal Noise Cascade Model for Camber Effects," *AIAA Journal*, Vol. 53, No. 4, 2015, pp. 863–876. doi:10.2514/1.J053266

[4] Holewa, A., Weckmüller, C., and Guérin, S., "Impact of Bypass-Duct Bifurcations on Fan Noise," *18th AIAA/CEAS Aeroacoustics Conference*, AIAA Paper 2012-2129, June 2012.

[5] Bonneau, V., Polacsek, C., Barrier, R., Lewy, S., Roux, J.-M., and Gervais, Y., "Tonal Noise Prediction of a Turbofan with Heterogeneous Stator and Bifurcations," *AIAA Journal*, Vol. 53, No. 11, 2015,

pp. 3354–3369.
doi:10.2514/1.J053970
[6] Daroukh, M., Moreau, S., Gourdain, N., Boussuge, J., and Sensiau, C., "Influence of Distortion on Fan Tonal Noise," *22th AIAA/CEAS Aeroacoustics Conference*, AIAA Paper 2016-2818, 2016.
[7] Sutliff, D. L., Heidelberg, L. J., Elliott, D. M., and Nallasamy, M., "Baseline Acoustic Levels of the NASA Active Noise Control Fan Rig," *2nd AIAA/CEAS Aeroacoustics Conference*, AIAA Paper 1996-1745, May 1996.
[8] Heidelberg, L. J., Hall, D. G., Bridges, J. E., and Nallasamy, M., "A Unique Ducted Fan Test Bed for Active Noise Control and Aeroacoustics Research," *2nd AIAA/CEAS Aeroacoustics Conference*, AIAA Paper 1996-1740, May 1996.
[9] McAllister, J., Loew, R. A., Lauer, J. T., and Sutliff, D. L., "The Advanced Noise Control Fan Baseline Measurements," *47th Aerospace Science Meeting*, AIAA Paper 2009-0624, Jan. 2009.
[10] Pasco, Y., Guedeney, T., Leung-Tak, A., Berry, A., Moreau, S., and Masson, P., "Active Noise Control Simulation of Tonal Turbofan Noise in Aero Engines," *20th AIAA/CEAS Aeroacoustics Conference*, AIAA Paper 2014-3187, 2014.
[11] Mann, A., Pérot, F., Kim, M.-S., Casalino, D., and Fares, E., "Advanced Noise Control Fan Direct Aeroacoustics Predictions Using a Lattice-Boltzmann Method," *18th AIAA/CEAS Aeroacoustics Conference*, AIAA Paper 2012-2287, June 2012.
[12] Maldonado, A. L. P., Miserda, R. F. B., and Pimenta, B. G., "Computational Tonal Noise Prediction for the Advanced Noise Control Fan," *18th AIAA/CEAS Aeroacoustics Conference*, AIAA Paper 2012-2128, June 2012.
[13] Sanjose, M., Daroukh, M., de Laborderie, J., Moreau, S., and Mann, A., "Tonal Noise Prediction and Validation on the ANCF Rotor–Stator Conuration," *Noise Control Engineering Journal*, Vol. 63, No. 6, 2015, pp. 552–562.
doi:10.3397/1/376349
[14] Frisch, U., D'Humiéres, D., Hasslacher, B., Lallemend, P., Pomeau, Y., and Rivet, J.-P., "Lattice Gas Hydrodynamics in Two and Three Dimensions," *Complex Systems*, Vol. 1, No. 4, 1987, pp. 649–707.
[15] Chen, S., and Dooler, G. D., "Lattice Boltzmann Method for Fluid Flows," *Annual Review of Fluid Mechanics*, Vol. 30, 1998, pp. 329–364.
doi:10.1146/annurev.fluid.30.1.329
[16] Marié, S., Ricot, D., and Sagaut, P., "Comparison Between Lattice Boltzmann Method and Navier–Stokes High Order Schemes for Computational Aeroacoustics," *Journal of Computational Physics*, Vol. 228, No. 4, 2009, pp. 1056–1070.
doi:10.1016/j.jcp.2008.10.021
[17] Vergnault, E., Malaspinas, O., and Sagaut, P., "A lattice Boltzmann Method for Nonlinear Disturbances Around an Arbitrary Base Flow," *Journal of Computational Physics*, Vol. 231, No. 24, 2012, pp. 8070–8082.
doi:10.1016/j.jcp.2012.07.021
[18] Chen, H., Orszag, S. A., Staroselsky, I., and Succi, S., "Expanded Analogy Between Boltzmann Kinetic Theory of Fluids and Turbulence," *Journal of Fluid Mechanics*, Vol. 519, Nov. 2004, pp. 301–314.
doi:10.1017/S0022112004001211
[19] Chen, H., Teixeira, C., and Molvig, K., "Realization of Fluid Boundary Conditions via Discrete Boltzmann Dynamics," *International Journal of Modern Physics C*, Vol. 9, No. 8, 1998, pp. 1281–1292.
doi:10.1142/S0129183198001151
[20] Zhang, R., Sun, C., Li, Y., Satti, R., Shock, R., Hoch, J., and Chen, H., "Lattice Boltzmann Approach for Local Reference Frames," *Communications in Computational Physics*, Vol. 9, No. 5, 2011, pp. 1193–1205.
doi:10.4208/cicp.021109.111110s
[21] Masson, V., Posson, H., Sanjose, M., Moreau, S., and Roger, M., "Fan-OGV Interaction Broadband Noise Prediction in a Rigid Annular Duct with Swirling and Sheared Mean Flow," *22th AIAA/CEAS Aeroacoustics Conference*, AIAA Paper 2016-2944, 2016.
[22] Goldstein, M. E., *Aeroacoustics*, McGraw–Hill, New York, 1976, Chap. 4.
[23] Cantrell, R. H., and Hart, R. W., "Interaction Between Sound and Flow in Acoustic Cavities: Mass, Momentum, and Energy Considerations," *Journal of the Acoustical Society of America*, Vol. 36, No. 4, 1964, pp. 697–706.
doi:10.1121/1.1919047
[24] Morfey, C. L., "Acoustic Energy in Non-Uniform Flows," *Journal of Sound and Vibration*, Vol. 14, No. 2, 1971, pp. 159–170.
doi:10.1016/0022-460X(71)90381-6
[25] Tyler, J. M., and Sofrin, T. G., "Axial Flow Compressor Noise Studies," *Society of Automotive Engineers Transactions*, Vol. 70, 1962, pp. 309–332.
[26] de Laborderie, J., "Approches Analytiques et Numériques Pour la Prédiction du Bruit Tonal et Large Bande de Soufflantes de Turboréacteurs," Ph.D. Thesis, Université de Sherbrooke, Sherbrooke, QC, Canada, 2013.
[27] Amiet, R. K., "Noise Produced by Turbulent Flow into a Rotor: Theory Manual for Noise Calculation," NASA CR-181788, 1989.
[28] Roger, M., Moreau, S., and Guédel, A., "Vortex-Shedding Noise and Potential-Interaction Noise Modeling by a Reversed Sears' Problem," *12th AIAA/CEAS Aeroacoustics Conference and Exhibit*, AIAA Paper 2006-2607, 2006.
[29] Parry, A. B., "Theoretical Prediction of Counter-Rotating Propeller Noise," Ph.D. Thesis, University of Leeds, Leeds, England, U.K., 1988.
[30] Amiet, R. K., "Acoustic Radiation from an Airfoil in a Turbulent Stream," *Journal of Sound and Vibration*, Vol. 41, No. 4, 1975, pp. 407–420.
doi:10.1016/S0022-460X(75)80105-2
[31] Amiet, R. K., "Noise Due to Turbulent Flow Past a Trailing-Edge," *Journal of Sound and Vibration*, Vol. 47, No. 3, 1976, pp. 387–393.
doi:10.1016/0022-460X(76)90948-2
[32] Roger, M., and Moreau, S., "Addendum to the Back-Scattering Correction of Amiet's Trailing-Edge Noise Model," *Journal of Sound and Vibration*, Vol. 331, No. 24, 2012, pp. 5383–5385.
doi:10.1016/j.jsv.2012.06.019
[33] Roger, M., François, B., and Moreau, S., "Cascade Trailing-Edge Noise Modeling Using a Mode-Matching Technique and the Edge-Dipole Theory," *Journal of Sound and Vibration*, Vol. 382, 2016, pp. 310–327.
doi:10.1016/j.jsv.2016.06.035
[34] Panton, R. L., *Incompressible Flow*, Wiley, Hoboken, NJ, 2013, Chap. 18.
[35] Parker, R., "Resonant Effects in Wake Shedding from Parallel Plates: Calculation of Resonant Frequencies," *Journal of Sound and Vibration*, Vol. 5, No. 2, 1967, pp. 330–343.
doi:10.1016/0022-460X(67)90113-7
[36] Parker, R., "Relation Between Blade Row Spacing and Potential Flow Interaction Effects in Turbomachines," *Proceedings of the Institution of Mechanical Engineers*, Vol. 184, No. 7, 1969, pp. 1–8.
[37] Gomar, A., , and Léonard, T., et al., "Antares: Python Post-Processing Library," 2012, http://www.cerfacs.fr/antares/, 2012. CERFACS.
[38] Guedeney, T., and Moreau, S., "Unsteady RANS Simulations of a Low Speed Fan for Analytical Tonal Noise Prediction," *11th European Turbomachinery Conference*, Madrid, 2015.
[39] Parker, R., "Pressure Fluctuations Due to Interaction Between Blade Rows in Axial Flow Compressors," *Proceedings of the Institution of Mechanical Engineers*, Vol. 183, No. 1, 1968, pp. 153–164.
doi:10.1243/PIME_PROC_1968_183_016_02
[40] Parker, R., "Resonance Effects in Wake Shedding from Compressor Blading," *Journal of Sound and Vibration*, Vol. 6, No. 3, 1967, pp. 302–309.
doi:10.1016/0022-460X(67)90202-7
[41] Sturm, M., Sanjose, M., Moreau, S., and Carolus, T., "Aeroacoustic Simulation of an Axial Fan Including the Full Test Rig by Using the Lattice Boltzmann Method," *FAN 2015, International Conference on Fan Noise, Technology and Numerical Methods*, Lyon, France, 2015.
[42] Jaron, R., Moreau, A., and Guerin, S., "RANS-Informed Fan Noise Prediction: Separation and Extrapolation of Rotor Wake and Potential Field," *20th AIAA/CEAS Aeroacoustics Conference*, AIAA Paper 2014-2946, 2014.
doi:10.2514/6.2014-2946
[43] Sturm, M., Sanjose, M., Moreau, S., and Carolus, T., "Application of Analytical Noise Models using Numerical and Experimental Fan Data," *11th European Conference on Turbomachinery Fluid Dynamics and Thermodynamics*, Madrid, 2015.
[44] Rienstra, S. W., and Hirschberg, A., *An Introduction to Acoustics*, Eindhoven Univ. of Technology, 2004, Chap. 7, https://www.win.tue.nl/~sjoerdr/papers/boek.pdf.

C. Bailly
Associate Editor